

Alma Mater Studiorum – Università di Bologna

DOTTORATO DI RICERCA IN

CHIMICA

Ciclo XXXV

Settore Concorsuale: 03/C1

Settore Scientifico Disciplinare: CHIM/06

**Radical chemistry of the catechol/quinone system
and its role in the control of lipid peroxidation and melanin biosynthesis**

Presentata da: **Alice Cariola**

Coordinatore Dottorato

Prof. Luca Prodi

Supervisore

Prof. Luca Valgimigli

Esame finale anno 2023

*A scientist lives with all reality. There is nothing better.
To know reality is to accept it, and eventually to love it.*
(George Wald)

Table of contents

CHAPTER 1	9
THE ANTIOXIDANT CHEMISTRY OF SEMIQUINONE AS A RADICAL INTERMEDIATE. KINETIC AND MECHANISTIC STUDIES.....	9
INTRODUCTION.....	12
1.1. Autoxidation and oxidative stress	11
1.1.1 Autoxidation reaction mechanism.....	11
1.2. Antioxidants and inhibition.....	15
1.3. How to test antioxidant activity	17
1.3.1 Data Analysis.....	18
1.4. Antioxidant activity of catechol and hydroquinone.....	20
1.4.1 Antioxidant chemistry of semiquinone, Nitroxides RTA inhibitors-like mechanism hypothesis	22
1.5. Antioxidant activity of ortho and para quinones in the presence of HOO•	24
1.6. Antioxidant activity of lipophilic catechol/quinone redox couples in biomimetic heterogeneous systems	27
1.6.1 Catalytic radical-trapping antioxidants in the presence of HOO• in heterogeneous system	28
RESEARCH OBJECTIVES.....	32
RESULTS AND DISCUSSION.....	32
1.7 Antioxidant activity of lipophilic catechol/quinone redox couples in micelles and biomimetic liposomal systems.	30
1.7.2 Egg yolk phosphatidylcholine (EggPC) unilamellar liposomes as model biomimetic lipid system.	35
1.7.3 Monitoring the autoxidation by the FENIX method	35

1.7.4 Autoxidation of (EggPC) unilamellar liposomes inhibited by the redox couple 3,5-DTBC and 3,5-DTBQ in the absence and presence of a source of superoxide	38
1.7.5 Autoxidation of (EggPC) unilamellar liposomes inhibited by the redox couple C8-DHCA and Ox-C8-DHCA in the absence and presence of a source of superoxide	41
EXPERIMENTAL PART.....	45
1.8 Materials and methods	43
1.8.1 Materials	43
1.8.2 General methods.....	43
1.8.3 Synthesis of C2-DHCA.....	44
1.8.4 Synthesis of C4-DHCA	44
1.8.5 Synthesis of C8-DHCA.....	45
1.8.6 Synthesis of C12-DHCA	45
1.8.7 Synthesis of C14-DHCA	46
1.8.8 Synthesis of C16-DHCA	46
1.8.9 Synthesis of quinones: ox-C2-DHCA, ox-C4-DHCA, ox-C8-DHCA, ox-C12-DHCA, ox-C14-DHCA and C16-DHCA	47
1.8.10 Autoxidation kinetics in MeLin micelles	47
1.8.11 Autoxidation studies in Egg-Yolk unilamellar liposomes (performed during a visiting period at the University of Ottawa)	48
Appendix to Chapter 1	49
CHAPTER 2.....	82
THE ANOMALOUS REGIOCHEMISTRY OF THIOL ADDITION TO O-QUINONES EXPLAINED BY A FREE RADICAL MECHANISM.....	82
INTRODUCTION.....	90
2.1 Thiol-o-quinone reaction.....	84

RESULTS AND DISCUSSION.....	91
2.2 Investigations of free radical intermediates	86
2.3 DFT calculations	93
CONCLUTIONS AND PERSPECTIVES	97
EXPERIMENTAL PART.....	104
2.4 Materials and methods.....	97
2.4.1 Materials	97
2.4.2 General methods.....	98
2.4.3 Synthesis of 4-methyl-o-quinone (4-MBQ).....	98
2.4.4 GC-MS analysis of stilbene isomerization.....	99
2.4.5 HPLC-Q-TOF(MS) analysis of quinone/thiol reactions.....	99
2.4.6 Reaction of 4-MBQ with cysteine	100
2.4.7 Reaction of 4-MBQ with thiophenol.....	100
2.4.8 Synthesis of Cys-NO and NAC-NO [78]	101
2.4.9 EPR spin-trapping experiments	102
2.4.10 Computational analysis.....	103
Appendix to Chapter 2	105
CHAPTER 3.....	122
OXYGEN UPTAKE KINETICS AS A POWERFUL TOOL TO INVESTIGATE POLYPHENOL-OXIDASE (PPO) REACTION AND ITS INHIBITION. NATURAL PHENOLS AS POTENT ANTI-MELANOGENIC AGENTS.....	122
INTRODUCTION.....	124
3.1 Tyrosinase enzyme and its inhibition.....	124
3.1.1 Inhibition of melanin biosynthesis in the biomedical, cosmetic and food- safety fields	124

3.1.2 Tyrosinase enzyme	125
3.1.3 Enzyme inhibition mechanism.....	127
3.1.4 Types of reversible enzyme inhibitors.....	130
REASERCH OBJECTIVES	133
RESULTS AND DISCUSSION.....	136
3.2 Matching the results from two different methodologies: parallel monitoring of the tyrosinase reaction by oximetry and spectrophotometry.....	136
3.3 Inhibition kinetics by glabridin	145
3.4 Anti-tyrosinase and antioxidant activity of Bakuchiol	155
3.4.1 Kinetics of mTYR inhibition	156
3.4.2 Fluorescence quenching study	161
3.4.3 EPR and ReqEPR spectroscopy of bakuchiol phenoxyl radical.....	162
3.4.4 Antioxidant activity of bakuchiol in solution and in micelles	165
3.4.5 Antioxidant activity of bakuchiol O-methyl derivative MeOBak	167
3.4.6 Discussion	168
EXPERIMENTAL PART.....	171
3.5 Materials and methods	171
3.5.1 Materials	171
3.5.2 kinetics evaluation of tyrosinase reaction by UV-Vis spectrophotomete	172
3.5.3 kinetic evaluation of tyrosinase reaction by oximetry	173
3.5.4 Setup of the real-time oxygen sensing equipment.....	176
3.5.5 Autoxidation studies in homogenous solution.....	178

CHAPTER 1

The Antioxidant Chemistry of semiquinone as a radical intermediate.

Kinetic and mechanistic studies.

Abstract

Ferroptosis is a recently identified form of non-apoptotic programmed cell death mediated by peroxidation of phospholipid membranes, which can be counteracted by lipophilic antioxidants confined into the lipophilic bilayer. Although antioxidants represent a mature field of research, their application in biomedicine still requires efforts in rationalizing their dual antioxidant and prooxidant roles. In this conjunction, the recent discovery by our group of a non-conventional antioxidant system based on the catalytic redox cycling of catechol/semiquinone/quinone (QH₂/QH•/Q) of polyphenols in the presence of superoxide or its neutral form, the hydroperoxyl radical, which serves as a sacrificial reducing agent, in spite of its established role as a detrimental biological oxidant, opens the way to unexplored applications of such redox-active systems in biology. To this end, we prepared a series of lipophilic catechols by derivatization of natural dihydrocaffeic acid, and their corresponding oxidized quinones, and we investigated for the first time their antioxidant chemistry in a heterogeneous biomimetic system, namely methyl lineolate micelles in phosphate buffer and unilamellar liposomes of egg phosphatidylcholine. Our preliminary results indicate that depending on their lipophilicity, in the presence of a source of HOO• radicals, some of these compounds can afford unprecedented protection both to micelles and liposomes, outperforming Nature's premier antioxidant alpha-tocopherol. Most interestingly, the antioxidant chemistry is shared both by the catechols and the corresponding quinones and was rationalized as a "radical export" mechanism in which the QH₂/QH•/Q redox system catalyzes the cross-dismutation of alkylperoxyl (ROO•) and hydroperoxyl (HOO•) radicals at the water/lipid interface, causing the export of the unpaired electron outside the lipid particle. Although preliminary, the relevance and potential of these findings in fighting ferroptosis is discussed.

INTRODUCTION

1.1. Autoxidation and oxidative stress

Foods, plastics, gasoline, lubricating and edible oils, fats, rubber, cosmetics, medicines, or other organic materials that are exposed to air are subjected to spontaneous oxidation that leads to degradation and the loss of their physical-chemical, organoleptic nutritional, or medicinal qualities. This process has a great economic impact, it can be triggered by UV radiation, transition metals, high temperatures, mechanical stress, etc. and it occurs at even at moderate temperatures in the presence of molecular oxygen in its triplet ground state ($^3\text{O}_2$). The process is known as autoxidation or peroxidation. Although almost all organic materials are susceptible to air oxidation, some types are more vulnerable than others, especially molecules with weak C-H bonds, such as allylic and benzylic compounds and other unsaturated derivatives. Autoxidation initially produces hydroperoxides (ROOH), which are then transformed into various oxygenated species like alcohols, ketones, aldehydes, acids, and esters called carbonyl compounds. The formation of hydroperoxides goes along with the formation of dialkylperoxides (ROOR) and is intermediated by transient peroxy radicals ROO^\bullet . These and other oxygen-centred radicals that can form in biological systems from peroxides hydroperoxides and oxygen, namely hydroxyl radicals (HO^\bullet), alkoxy radicals (RO^\bullet) and hydroperoxy radicals/superoxide ($\text{HOO}^\bullet / \text{O}_2^{\bullet -}$) are called reactive oxygen species, ROS [1]. ROS cause oxidative stress in cell, they are important in redox signalling and regulation at low concentration, but at higher concentration they could initiate and propagate disruptive radical oxidative chains and bring to tissue damage and death cell death [2]. Antioxidant enzymes and other antioxidant systems are necessary to protect against the growing levels of oxidative damage to living systems [3].

1.1.1 Autoxidation reaction mechanism

In general, oxidative degradation of organic compounds in air involves a free radical chain. A heat or photochemical process that releases an initiating radical, In^\bullet , starts the

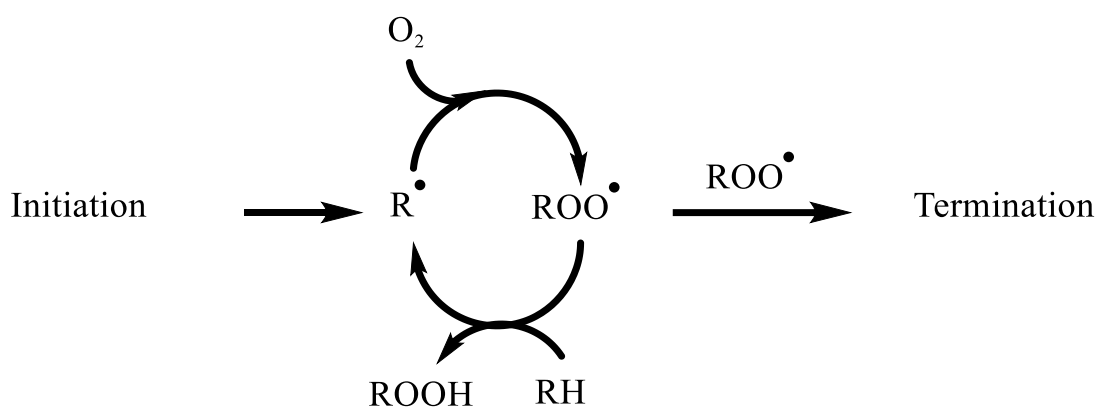
chain reaction. The fast addition of molecular oxygen to create a chain-initiating peroxy radical, InOO^\bullet which is ROO^\bullet , usually occurs if In^\bullet is, or rapidly forms, a carbon-centred radical, R^\bullet [4]. The resulting peroxy radicals (ROO^\bullet) typically go through two types of reactions [5]: (1) they quench their own free valence by stealing a hydrogen from the hydrocarbon substrate, generating another radical:



or terminate with another peroxy radicals losing the free valence:



To sum up, hydrocarbon oxidation involves three different phases: chain initiation, chain propagation and chain termination as shown in Scheme 1.1.



Scheme 1.1 Autoxidation reaction mechanism

As the preservation of organic materials is one of the most important goals of our work, we will go deeply into the knowledge of autoxidation mechanism and discuss kinetics step by step [6]. We will focus on lipid oxidation in heterogenous multi-components systems, a particular yet common case in real-life conditions. The kinetics process is affected by the interactions between the oxidizing lipids and water phase, stressing the interface between them. The differences in antioxidant efficiency between solution and emulsion systems are not predicted by the traditional mechanism of inhibited lipid oxidation. Prooxidant metal catalysts, which can exist in free form or as complexes with proteins, are subjected to the same interfacial phenomena. In studies on lipid

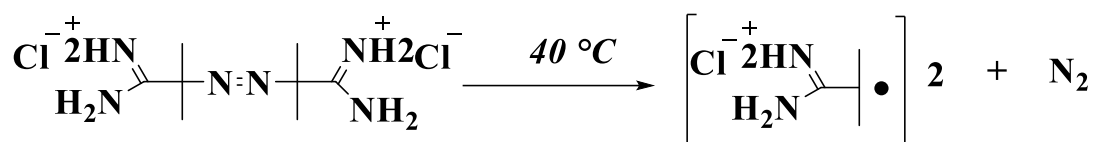
oxidation and its control, model systems have been utilized extensively to simulate biological samples. Working with a variety of model systems could be misleading compare the “real” foods degradation. Since it oversimplifies the interfacial interactions of numerous components, although research on model systems is essential for the successful establishing of the chemical principles that would be relevant to many foods [7].

The *initiation* process is usually spontaneous due to air exposition, UV light or pro-oxidant components. Initiator molecules are used to set up a kinetically controlled autoxidation. They generate radical species because of their weak molecular bond with a BDE (bonding dissociation energy) around 100-200 kJ mol⁻¹ [8].



The most common initiators are peresters or (hydro)peroxides breaking O-O bonds and generating alkoxy radicals (RO•) or hydroxyl radicals (HO•). Azo-initiators are largely used at certain temperatures, splitting two sigma bonds and forming 2 equivalents of alkyl radicals (R•) and N₂.

In the presence of an initiator R_i represents the decomposition rate constant. In practice, the decomposition rate of initiator is usually given by the half-life ($t_{1/2}$), the time necessary to consume half of their initial concentration at a certain temperature, and it depends on temperature, the viscosity of the solvent and the intrinsic characteristics of the initiator itself. 2,2-Azobis(2-amidinopropane) dihydrochloride (AAPH) is degraded at 40°C in aqueous solutions over a wide pH range [9], the thermal decomposition rate constant of AAPH to form radical species averages at $2.1 \times 10^{-6} \text{ s}^{-1}$ and thanks this propriety it is useful in different circumstances. It's possible to calculate the R_i from the thermal decomposition rate of AAPH, multiplying the value by the concentration of the initiator.



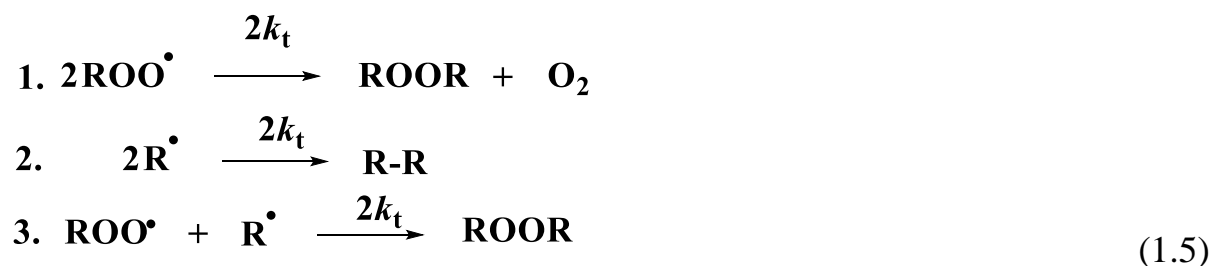
Scheme 1.2. AAPH decomposition to nitrogen and two alkyl radicals

At this stage the *propagation* of alkyl radicals generated from the initiator occurs and they usually react rapidly ($k \sim 10^9 \text{ M}^{-1}\text{s}^{-1}$) with oxygen, forming peroxy radicals ($\text{ROO}\bullet$), which react with the substrate [10]. $\text{ROO}\bullet$ abstracts an H-atom releasing another alkyl radical, which takes into the first initiating phase and propagates the radical chain [11].



The propagation rate constant, k_p , is therefore specific to each oxidizable substrate because of the structures of the substrates. As the C-H bond strength weakens, oxidation becomes easier. Therefore, depending on the substrate's structure and the temperature of the autoxidation, the propagation rate constant, k_p will vary for each oxidizable substrate [12].

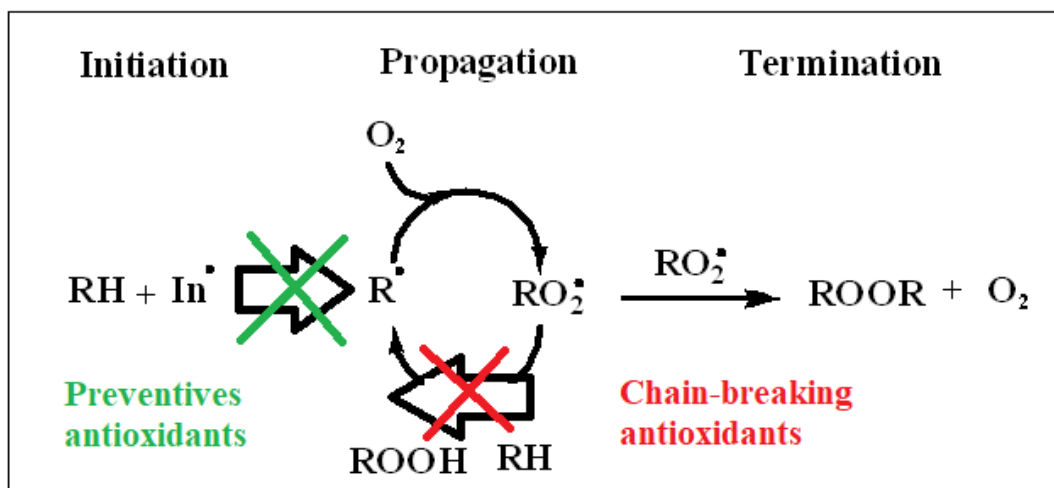
The *termination* of the radical chain turns out when two radical species react with each other to give a non-radical product. There could be three possibilities: (1) a combination of two peroxy radical, (2) the combination of two carbon-centered radical or (3) a mixture of both.



Generally, the more substituted the alkyl group the slower the termination rate constant ($2k_t$), due to increasing steric effects. [13]

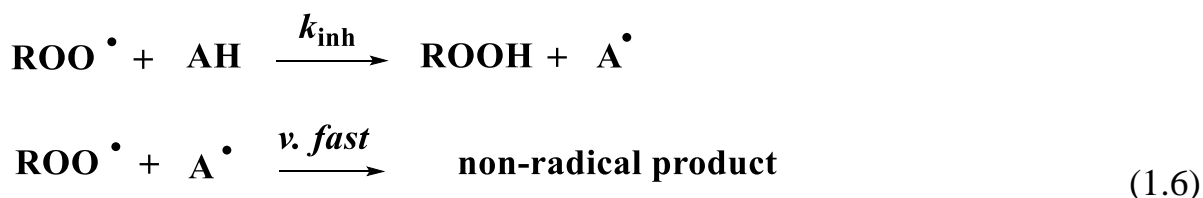
1.2. Antioxidants and inhibition

Numerous studies have been done to learn how to limit the autoxidation process. Antioxidants (AH) have been the subject of much multidisciplinary research over the past 60 years to better understand their activity. *Direct antioxidants* are substances that can directly inhibit the generation of free radicals and the chain reaction of oxidation. These substances can be either natural or synthetic, and they have been the focus of many studies [14]. In the last decades of 20th century it was established that there are two main groups of direct antioxidants [15]: (1) *Radical-Trapping Antioxidants* (RTAs), also known as chain-breaking antioxidants, capture chain-carrying radicals and thus break the oxidation chain. (2) *Preventive Antioxidants*, instead, reduce the rate at which new radical chains are started [4,14]. Chain-breaking antioxidants react with peroxy radicals quickly and more effectively than oxidative chain propagation to create new inactive radicals that do not propagate the autoxidation chain [16]. Preventive antioxidants include compounds like UV filters, which stop the photochemical breakdown of biomolecules like melanin in mammals' skin, metal (copper and iron) chelators, that inhibit the Fenton reactions from producing HO• and RO• radicals, and some ROS decomposers like superoxide dismutase (SOD), catalase (CAT), glutathione peroxidase (GPx) and related enzymes [17].



Scheme 1.3 Mechanism of different types of antioxidants interfering with free radical autoxidation. In green preventives antioxidants blocking the initiation process and in red chain-breaking antioxidants interrupting the propagation state.

The most widely used RTAs are phenols and aromatic amines, they must outcompete the substrate for chain-carrying peroxy radicals, both the relative reactivities and the concentrations of the RTA and substrate are key, hence it should be $k_{inh}[A-H] \gg k_p[R-H]$ [18].



Molecules such as tocopherol (vitamin E), flavonoids, and ubiquinol (CoQH₂) set the basis for the study of more innovative aza-derivatives. The O-H BDE of phenols is directly influenced by the substituents on the aromatic ring. Generally, electron donating substituents (e.g. 4-Ome) lower the O-H BDE, inversely, electron withdrawing substituents (e.g. 4-NO₂) increase the O-H BDE [19]. The growing biological significance of lipid autoxidation and its possible role in the pathophysiology of several diseases boosted the interest, although efforts to develop optimized RTAs date back to the 1950s. Interest in this field has grown beyond a specific area of industrial chemistry, due to its involvement in degenerative diseases and aging. In fact, Burton and Ingold's efforts to comprehend the structure-activity

connections in charge of α -tocopherol (α -TOH), the most biologically active form of vitamin E, were what actually made a difference [20]. Both catechol and hydroquinone are well known biological antioxidants with a k_{inh} close to that of α -TOH but their chemistry is still controversial [21]. This work wants to elucidate different aspects of the antioxidant proprieties of the catechol/quinone redox couple to get a better picture of such complex compounds and help design novel optimized antioxidant systems.

1.3. How to test antioxidant activity

Numerous techniques have been developed to assess the antioxidant activity of distinct samples from various study areas [22]. Our group built up an oximetry apparatus where autoxidations of kinetically well characterized oxidizable substrates initiated by azo compounds are performed and monitored. The instrument consists in a differential oxygen uptake apparatus, formed by two identical thermostated and closed reaction vessels, connected to a differential pressure transducer [23]. The same reaction mixture is placed in both vessels: in the reference flask we block any the autoxidation with a large excess of a reference antioxidant like α -TOH while in the sample flask the autoxidation is allowed to proceed uninhibited or is controlled by a modest concentration of the antioxidant to test, so to allow some oxygen consumption.

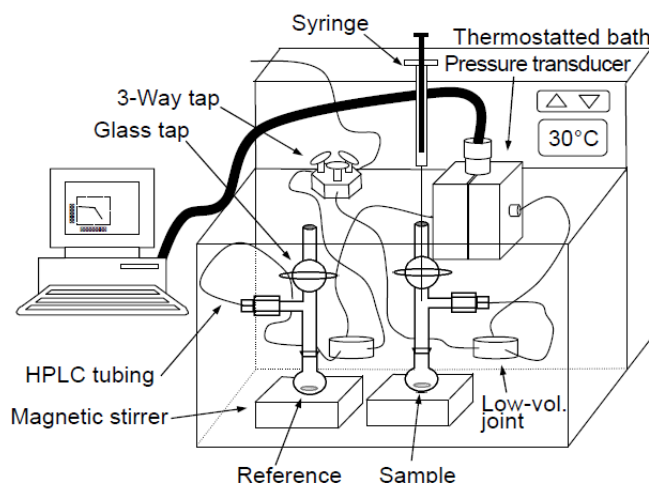


Figure 1.1 Differential oxygen uptake apparatus set in our lab for autoxidation kinetics.

Under standardized condition any difference in pressure is converted in mole of oxygen consumed in the sample, which we monitor over time. Kinetic analysis of the oxygen consumption plots affords both the rate constant for trapping chain carrying peroxy radicals by the antioxidant and the stoichiometry of radical trapping, respectively from the slope and from the length of the inhibited period.

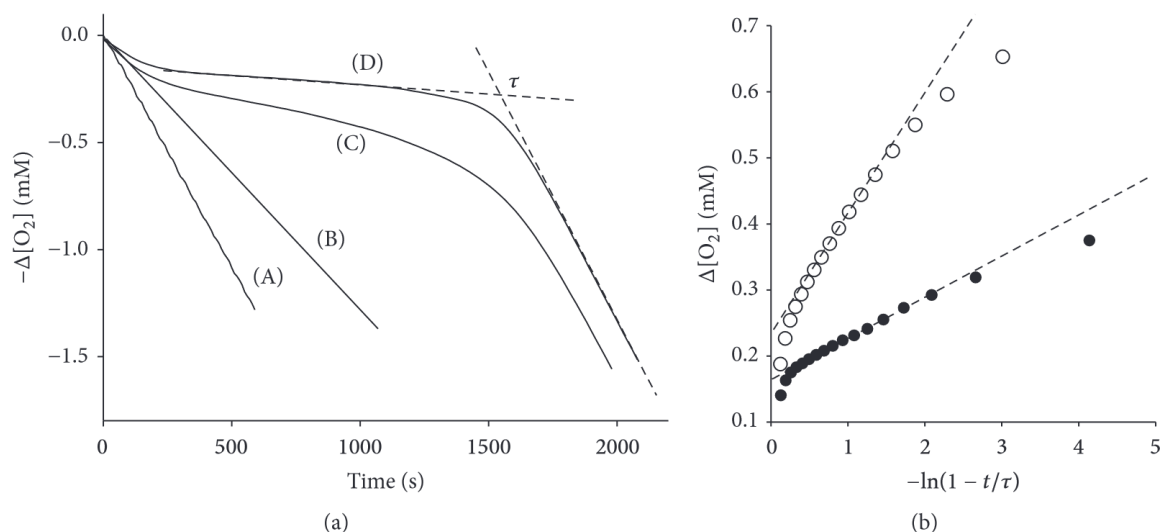


Figure 1.2 From ref. 23 (a) Typical O_2 consumption traces observed during the autoxidation of an organic substrate in the absence (A) or in the presence of antioxidants with low (B), intermediate (C), and high (D) k_{inh} values. (b) Analysis of the O_2 consumption for the antioxidants having intermediate (\circ) and high (\bullet) k_{inh} .

1.3.1 Data Analysis

In practice, oxygen consumption in the sample flask measures how fast the substrate oxidation process is advancing. The introduction of an azo initiator at the beginning of autoxidation, when there are no antioxidants present, removes the kinetic complications of spontaneous oxidation and produces a linear plot of oxygen consumption (plot A in figure 1.2). For transient radical species like $R\bullet$ and $ROO\bullet$, the steady-state approximation is used in kinetic analysis.

$$D[R\bullet]/dt = 0 \quad (1.7)$$

$$d[ROO\bullet]/dt = 0 \quad (1.8)$$

When the autoxidation chain is sufficiently long, the autoxidation kinetics of the substrate could be calculated as follows (1.9), since the consumption of the reactants (O_2 and RH) and the formation of products ($ROOH$) with time is numerically identical.

$$\frac{-d[O_2]}{dt} = \frac{-d[RH]}{dt} = \frac{d[ROOH]}{dt} = \frac{k_p}{\sqrt{2k_t}} \sqrt{R_i} [RH]_0 + R_i \quad (1.9)$$

In 1.9 $[RH]_0$ is the starting concentration of oxidizable substrate, R_i is the initiation rate, and $k_p/(2k_t)^{1/2}$ is the oxidizability of substrates (the substrate consumption during the initial phases of autoxidation is assumed to be small).

According to plot D in Figure 1.2, an efficient antioxidant can prevent the oxygen from being consumed almost entirely up to the point where the antioxidant is completely consumed. At that point, an uninhibited autoxidation, identical to the one achieved without the antioxidant, will then restart.

The length of the inhibition periods (Figure 1.2) can be analyzed with equation 1.10 to establish the stoichiometric factors n because antioxidants quench the peroxy radicals created by the initiators (or from substrate oxidation) during the inhibited period [14].

$$R_i = \frac{n[AH]}{\tau} \quad (1.10)$$

$[AH]_0$ is the antioxidant's initial concentration, and τ is the duration of the inhibition period. The initiation rate (R_i) of an autoxidation that has been inhibited by a known quantity of an effective antioxidant, such as α -TOH, whose stoichiometric coefficient is well known ($n = 2$), might also be calculated using this equation. By assuming that each $ROO\cdot$ radical is trapped by the antioxidant and its corresponding radical, equation 1.11, which uses the initial slope of oxygen consumption during the inhibited period, may be used to calculate the inhibition rate constant k_{inh} .

$$-\frac{d[O_2]}{dt} = \frac{k_p}{nk_{inh}} \frac{[RH]R_i}{[AH]} + R_i \quad (1.11)$$

Equation 1.12 can be applied if the inhibited period in Figure 1.2 is not as easily distinguished as in plot D, or if the first portion of the plot cannot be used to calculate the oxygen consumption rate (plot C).

$$\Delta[O_2]t = \frac{k_p[RH]R_i}{k_{inh}} \ln \left(1 - \frac{t}{\tau} \right) \quad (1.12)$$

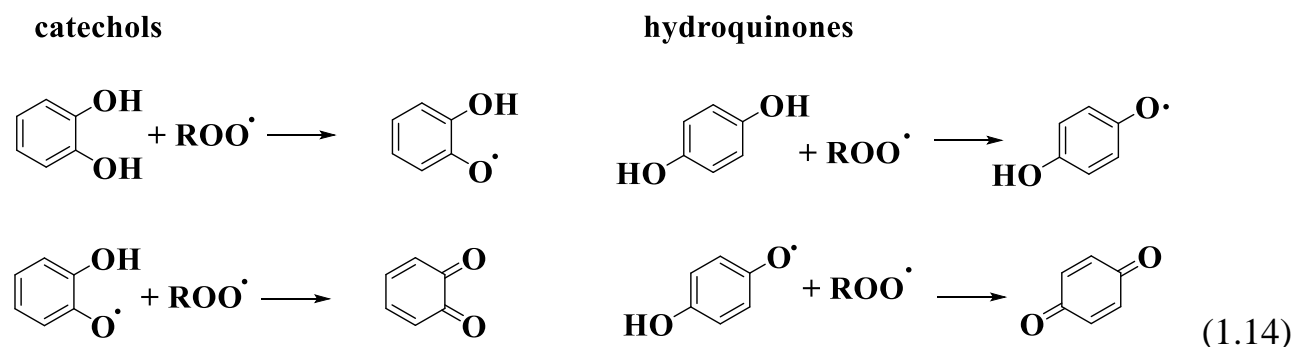
Equation 1.13 was used by Denisov and Khudyakov to determine k_{inh} in circumstances where the antioxidant's efficacy is too low to allow for a clear observation of the inhibition time, as in plot B [24].

$$\frac{R_{ox,0}}{R_{ox}} - \frac{R_{ox}}{R_{ox,0}} = \frac{nk_{inh}[AH]_0}{\sqrt{R_i 2k_t}} \quad (1.13)$$

In Eq. 1.13, R_{ox} and $R_{ox,0}$ are the oxygen consumption rates ($d[O_2]/dt$) in the presence and absence of the antioxidant, respectively, as determined by the plots under similar experimental conditions. Additionally, kinetic information and changes in reactants and products could be obtained using computer simulations of the oxygen-uptake trace (using, for example, the Copasi software).

1.4. Antioxidant activity of catechol and hydroquinone

Both catechols and hydroquinones are known antioxidants, formally able to trap two alkylperoxyl radical to form the corresponding quinones. But, while 1,2-isomers trap two peroxy radicals as expected, 1,4-hydroquinones show formally a low value of n , the so-called stoichiometric factor, corresponding the number of peroxy radicals trapped by one antioxidant molecule.



Wondering about the nature of this behavior our group started to investigate the reactivity of those systems [16]. Their high reactivity depends on the low value of OH bond dissociation energy, which is due to the electron donating contribution of the second OH group in conjugated position. However, we notice for catechol also the formation of an intramolecular hydrogen bond, which significantly boosts the reactivity. In fact, while the intramolecular hydrogen bonds stabilize the starting

catechol it provides higher stabilization of the semiquinone radical, thereby decreasing the energy gap, which means it decreases the BDE of the unbound OH group (Fig.1.3)

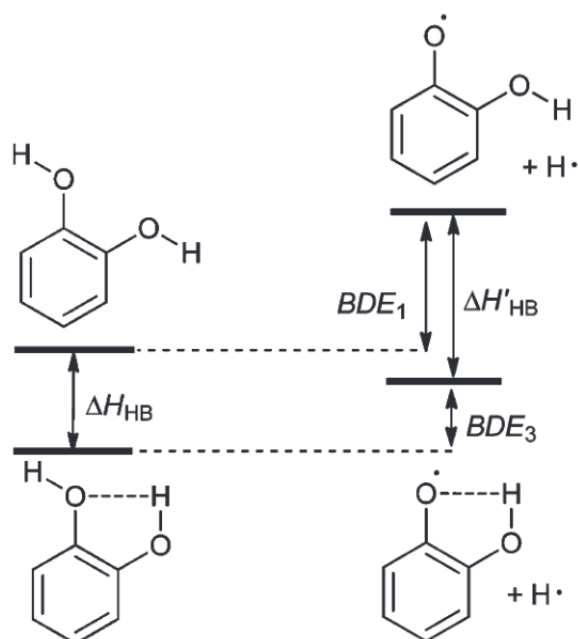
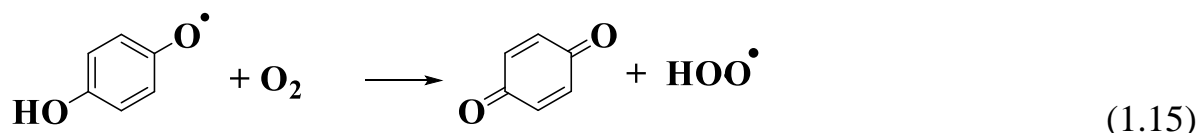


Figure 1.3 From ref. 16 an ortho hydroxyl group stabilizes both the phenol and (to a larger extent) the radical ($BDE_3 < BDE_1$) by donating an intramolecular H-bond

Additionally, *para*-semiquinones react rapidly with oxygen to form the hydroperoxyl radical, which starts a new oxidative chain; therefore, the apparent stoichiometric factor for 1,4-isomers decreases, as it is the results of the oxidative chains that are broken minus the oxidative chains that are started.

para- semiquinone oxidation

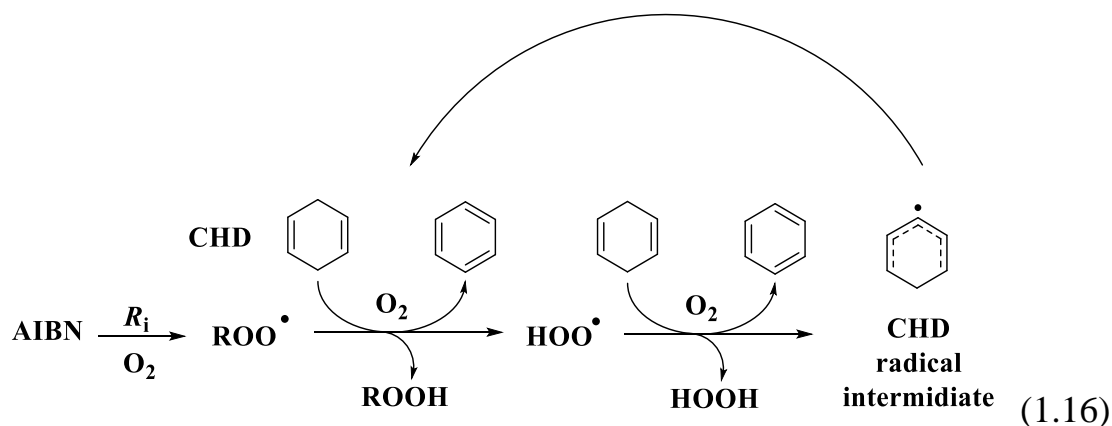


This is normally not observed or not relevant with *ortho*-semiquinone due to their stabilization by the intramolecular H-bond. As a result, catechols are far better antioxidants reacting faster with chain carrying peroxy radicals and trapping two of them, while hydroquinones have much lower apparent stoichiometric factor due to the generation of new chain propagating species. The reaction of semiquinone radicals

with oxygen to afford the quinone and $\text{HOO}\cdot$ is well known, but much less is known on the back reaction.

1.4.1 Antioxidant chemistry of semiquinone, Nitroxides RTA inhibitors-like mechanism hypothesis

Previous work from our group revealed that phenols could react with the phenoxyl radical of vitamin E and regenerate it, behaving as co-antioxidants to increase the antioxidant activity [25]. At the same time it is known that the hydroperoxyl radical has an exceptionally weak H-OO• BDE (49.2 kcal/mol), [26], which allows one to consider H-OO• as potentially good H-atom donating agent. Starting from these two points our collaborators, Prof. Riccardo Amorati with the group of Prof. Greg Litwinienko, created a new protocol to measure the reactivity of phenolic antioxidants in the presence of hydroperoxyl radicals [27]. They added cyclohexadiene (CHD) to autoxidizing styrene. CHD act as hydrogen atom donor (HAT) due to aromatization driving force and as its co-oxidation is a well-known source of hydroperoxyl radicals as the propagating radical.



The chain-breaking effect of TOH was more clearly visible in styrene because this substrate has a lower propagation rate constant than CHD (41[27] vs. 1400 $\text{M}^{-1}\text{s}^{-1}$ in chlorobenzene, respectively). In CHD, however, the length of the inhibition period was up to 10 times longer (corresponding to nearly 20 radicals quenched by each TOH molecules) than in styrene. as it shown in figure 1.4. Therefore they attributed the enhanced antioxidant activity of α -TOH to its regeneration from the phenoxyl radical, due to its reduction by H-atom transfer (HAT) from the hydroperoxyl radicals itself.

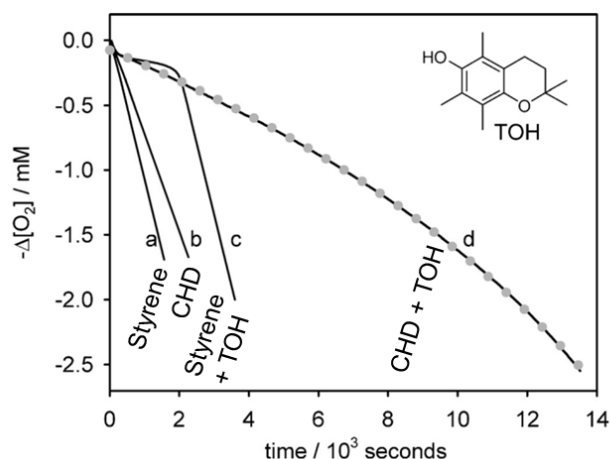
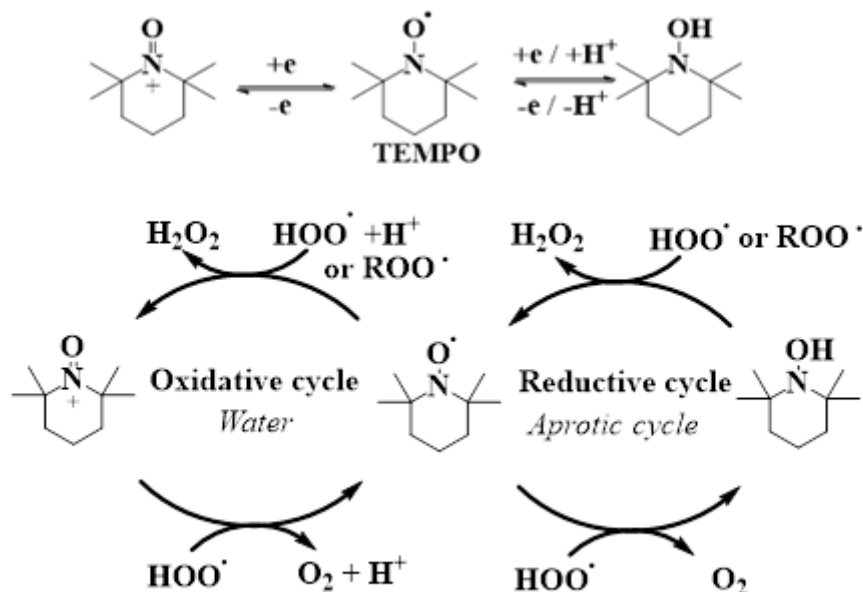


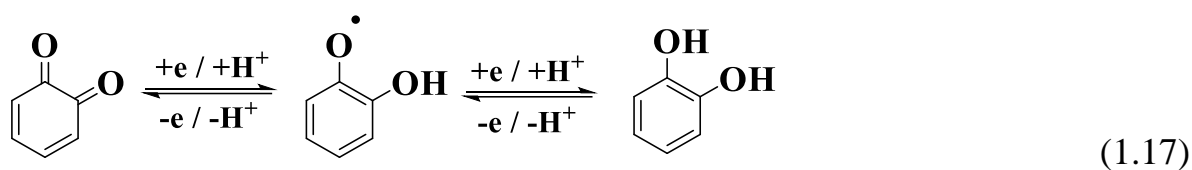
Figure 1.4 From ref. 27, autoxidation experiments in chlorobenzene supporting the hydroperoxyl radical co-participation theory.

This chemistry was somehow reminiscent of the behavior of nitroxides which our research group was investigating as non-conventional antioxidants in the same period [28]. In the presence of a source of hydroperoxyl radicals nitroxides can undergo two redox cycles. The oxidative one, which is relevant only in protic media, and a reductive one observed in aprotic media, in which the nitroxide is reduced to the parent hydroxylamine by HAT from the hydroperoxyl radical.



Scheme 1. 4 Catalytic Quenching of HOO· by TEMPO.

The hydroxylamine is then oxidized back by another hydroperoxyl radical or by alkylperoxyl radicals, so in this way nitroxides acts as catalytic antioxidants, affording very efficient and extended protection of lipids. We asked ourselves if the same chemistry occurs with semiquinone radical intermediates in the presence of $\text{HOO}\cdot$, given their similar electronic position compared to nitroxides.



1.5. Antioxidant activity of ortho and para quinones in the presence of $\text{HOO}\cdot$

Our group nicely demonstrated that 1-methyl-1,4-cyclohexadiene (MeCHD) could serve as reducing agent for quinones to synthesize the corresponding hydroquinones [29]. Based on a somewhat similar chemistry, the group also demonstrated that MeCHD and the natural γ -terpinene sharing the same pre-aromatic structure, could extend the antioxidant activity of catechols and hydroquinones and turn into good antioxidants even the corresponding quinones. MeCHD and the natural γ -terpinene was used as the first time of a good H-atom source generating the short-lived $\text{HOO}\cdot$ radical and giving rise a catalytic antioxidant cycle [30, 31]. 3,5-Di-*tert*-butyl-1,2-benzoquinone (1) and 2,5-di-*tert*-butyl-1,4-benzoquinone (2) have been taken as model compounds to test the theory and in fig.1.5 are represented the keys mechanistic step of the catalytic antioxidant behaviour.

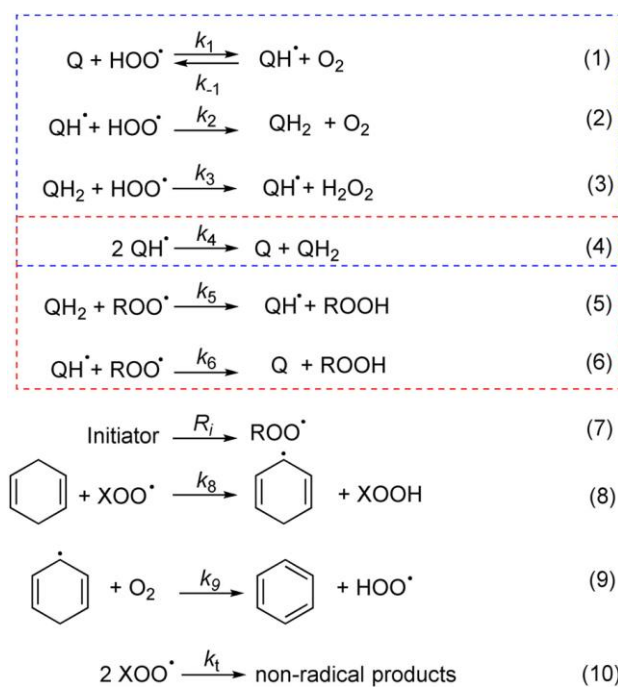


Figure 1.5. From rif. 30, key reactions explaining the antioxidant activity of ortho and para-quinones, Q, in the presence of 1,4-cyclohexadiene (X=H or R).

An interesting finding was that, while neither *ortho* or *para*-quinone have any antioxidant activity in the absence of cyclohexadiene; however, the addition of the same excess of cyclohexadiene to the quinones produce somewhat different outcomes with the *ortho* versus the *para* quinone. The *para*-quinone forms a far less effective antioxidant system than the *ortho*, which might be due to less efficient reduction to the hydroquinone or to the lower antioxidant activity of the hydroquinone compared to the catechol or both [30]. They studied the autoxidation process inhibited by compounds **1**, **1H₂**, **2**, **2H₂**. The chain-breaking antioxidant activity of **1** and **2** was evaluated by measuring, at 30 °C and in a low-polarity solvent (chlorobenzene), the rate of O₂ consumption during the azobis(isobutyronitrile) (AIBN) initiated oxidation of styrene, a reference organic substrate whose autoxidation at low temperature is propagated by ROO•. MeCHD was used as oxidizable co-substrate to produce HOO•.

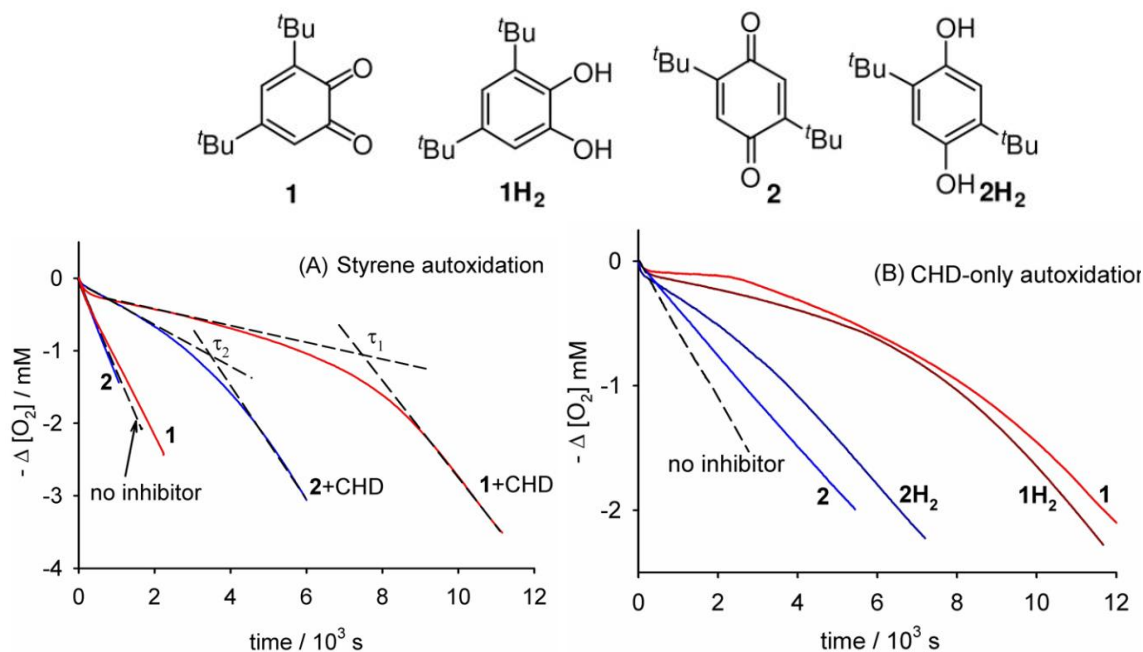


Figure 1.6 From rif. 31, O_2 consumption during the autoxidation of styrene in chlorobenzene at 30°C initiated with 25 mM AIBN in the absence of inhibitors (dashed line), and in the presence of quinones **1** and **2** (5 mM) with or without 0.023 M CHD. B) O_2 consumption during the autoxidation of CHD (0.23 M) initiated by 25 mM AIBN at 30°C in chlorobenzene with no antioxidants (dashed line), or with added 40 mM of **2** or **2H₂**, and with 5 mM **1H₂** or **1**.

The rate constants for the reaction between *ortho*-benzoquinone and $\text{HOO}\cdot$ was calculated by using equation 1.13, which relates the rates of the inhibited and non-inhibited autoxidation (R_{inh} and R_0 , respectively) to the rate constant for the reaction of the antioxidant with the chain-carrying radicals and the stoichiometry of radical trapping (n). The rate of initiation (R_i) was determined experimentally as $3.1 \times 10^{-9} \text{ M s}^{-1}$, while $2k_t$ for CHD in chlorobenzene is $1.2 \times 10^9 \text{ M}^{-1} \text{ s}^{-1}$ [12]. With the assumptions that $n = 2$, k_{inh} was obtained as $(1.4 \pm 0.2) \times 10^7 \text{ M}^{-1} \text{ s}^{-1}$. It was found that oxidized quinone **1** is a far better antioxidant than catechol **1H₂**, but only in the presence of $\text{HOO}\cdot$. Results also show that a substantial quantity of catechol **1H₂** is formed from **1**, in line with previous hypothesis (Fig 1.6), although somewhat counterintuitive, and it means that the antioxidant **1** is being reduced, at least transiently, during the inhibition of CHD autoxidation. This characteristic of *ortho*-quinone could explain why redox system formed by $\text{HOO}\cdot$ with $\text{Q}/\text{QH}\cdot/\text{QH}_2$ is so important to protect dietary lipids [31]

and has also been proposed as main contributor of the antioxidant behavior of biological macromolecules like melanin [30]. There is an open window on the possible application of this kind of chemistry and the aim of this research project was to investigate different aspects, using such an interesting antioxidant model. We started with testing the protection from oxidative damage of micelles and phospholipid bilayers as a model for future studies on cells to evaluate their protection from ferroptosis, as the cause of different neurological pathologies.

1.6. Antioxidant activity of lipophilic catechol/quinone redox couples in biomimetic heterogeneous systems

Ferroptosis was first recognized in 2012 as an iron-dependent form of nonapoptotic cell death [32]. Although distinct from apoptosis, necrosis and autophagy, cells undergoing ferroptosis undergo similar morphological changes [33]. Recent studies have shown that ferroptosis is closely related to the pathophysiological processes of many diseases, particularly tumours, nervous system diseases, cardiovascular diseases and kidney injury [34]. Therefore, regulating cell ferroptosis (in both directions) has become an important strategy to target the related diseases [35]. It is becoming clear that lipid peroxidation (LPO), the oxidative degradation of lipids by free radicals' chain reaction, is the main biochemical event triggering ferroptosis [36]. Iron is involved in initiating LPO by the decomposition of phospholipid hydroperoxides (LOOH) in biomembranes (Fenton reaction), which is described as the main trigger for ferroptosis [37]. However, work in Pratt's group pointed toward membrane damage as the main causative event, regardless of it being triggered by iron [38]. Interestingly, a recent work proved a significant positive correlation between the antioxidant activity of molecules in a model liposome system and their anti-ferroptosis activity in cells [39]. This prompts research on novel redox-active systems to target ferroptosis as a key modulator of the related diseases. Research on antioxidants remain to be addressed adequately in particular for the applications in biomedicine, in part owing to incomplete understanding of the dualistic antioxidant and prooxidant roles of antioxidants [40]. An important issue on ferroptosis that certainly deserves better

understanding is the role of superoxide. While superoxide can induce ferroptosis by increasing the release of (Fe^{2+}) and initiating LPO [41], it might paradoxically protect the cell under some settings [42]. The mechanism might rely on the two-faced behaviour of superoxide, that can work both as oxidant and reductant. The hydroperoxyl radical ($\text{HOO}\cdot$), the neutral form of superoxide ($\text{O}_2^{\cdot-}$) produced in the mitochondrial respiratory chain, is universally considered a detrimental oxidizing species, responsible for the oxidative damage of membranes and biomolecules [3]. Yet, our group has shown that it can play a role in the opposite direction, reducing rather than oxidizing biomolecules. $\text{HOO}\cdot$ rapidly reduces by Hydrogen Atom Transfer (HAT) nitroxides ($>\text{NO}\cdot$) to hydroxylamines ($>\text{NOH}$) [28], and nitroxides, in the presence of a source of $\text{HOO}\cdot$ radicals, efficiently catalyse the cross dismutation of alkylperoxyl radicals, thereby acting as an extremely effective catalytic antioxidant system [43], [44]. In more recent work the group has shown that a similar chemistry would occur with the quinone (Q)/ semiquinone ($\text{QH}\cdot$)/catechol (QH_2) redox system in organic solvent, as discussed in paragraph 1.5. The aim of future project in collaboration with Pratt's researchers will be study the (Q)/ semiquinone ($\text{QH}\cdot$)/catechol (QH_2) redox system in biomimetic solvent

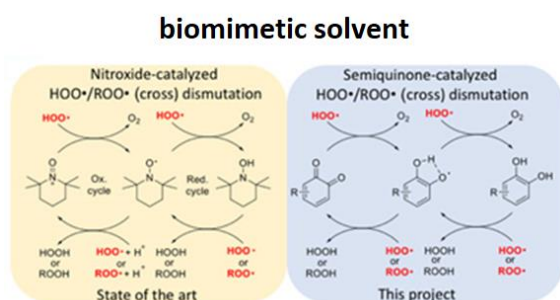


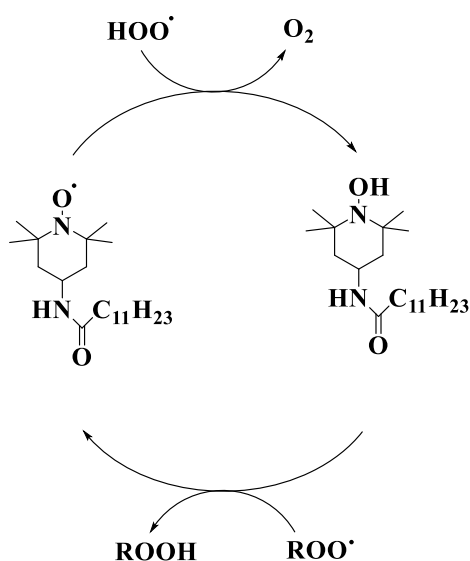
Figure 1.7 Scheme of catalyzed cross-dismutation of hydroperoxyl and alkyl peroxyl radicals by nitroxides (left) and quinone/catechol system (right) in biomimetic solvent

1.6.1 Catalytic radical-trapping antioxidants in the presence of $\text{HOO}\cdot$ in heterogeneous system

Nitroxides are forming a catalytic antioxidant cycle when $\text{HOO}\cdot$ sources (e.g. cyclohexadienes, triethylamine, 1,4-hydroquinones, or benzyl alcohol) are present during the oxidation of styrene in organic solvent. This chemistry was demonstrated by our group during inhibited autoxidations in solution [28]. Pratt's group in Ottawa

recently investigated the antioxidant behavior of lipophilic nitroxides localized in autoxidizing liposomes and reported an increase of the antioxidant protection by the nitroxide in the presence of a thermal source of superoxide radical (SOTS) in the aqueous phase. The behavior was explained by the reduction of nitroxide to the hydroxylamine by $O_2^{\cdot-}$ followed by protonation or concerted with protonation, thereby paralleling the mechanism our group identified in solution [42].

The study aimed at identifying of non-conventional antioxidant systems that could work combination with sources of $HOO\cdot/O_2^{\cdot-}$ radicals to target ferroptosis, with focus on their therapeutic potential against neurodegenerative conditions. Stepping from the combination of such results in liposomes and our results in homogenous solution both using nitroxides or catechol/quinone systems, we aimed at investigating the ortho-quinone systems (Q/QH \cdot /QH $_2$ system) as potential catalytic redox system in biomimetic conditions, *i.e.* in heterogeneous lipid systems like micelles and liposomes.



Scheme 1.5 Proposed mechanisms of co-antioxidant activity of lipophilic nitroxides in heterogeneous systems in the presence of $HOO\cdot$ in the aqueous phase (ref.42).

RESEARCH OBJECTIVES

With the semiquinone chemistry in mind, my research objectives were to dig into a specific aspect of semiquinone as radical intermediate in specific reaction conditions. The antioxidant characterization of ortho-quinone/catechol redox system was be extended to heterogeneous systems to deeply understand the fundamental interaction

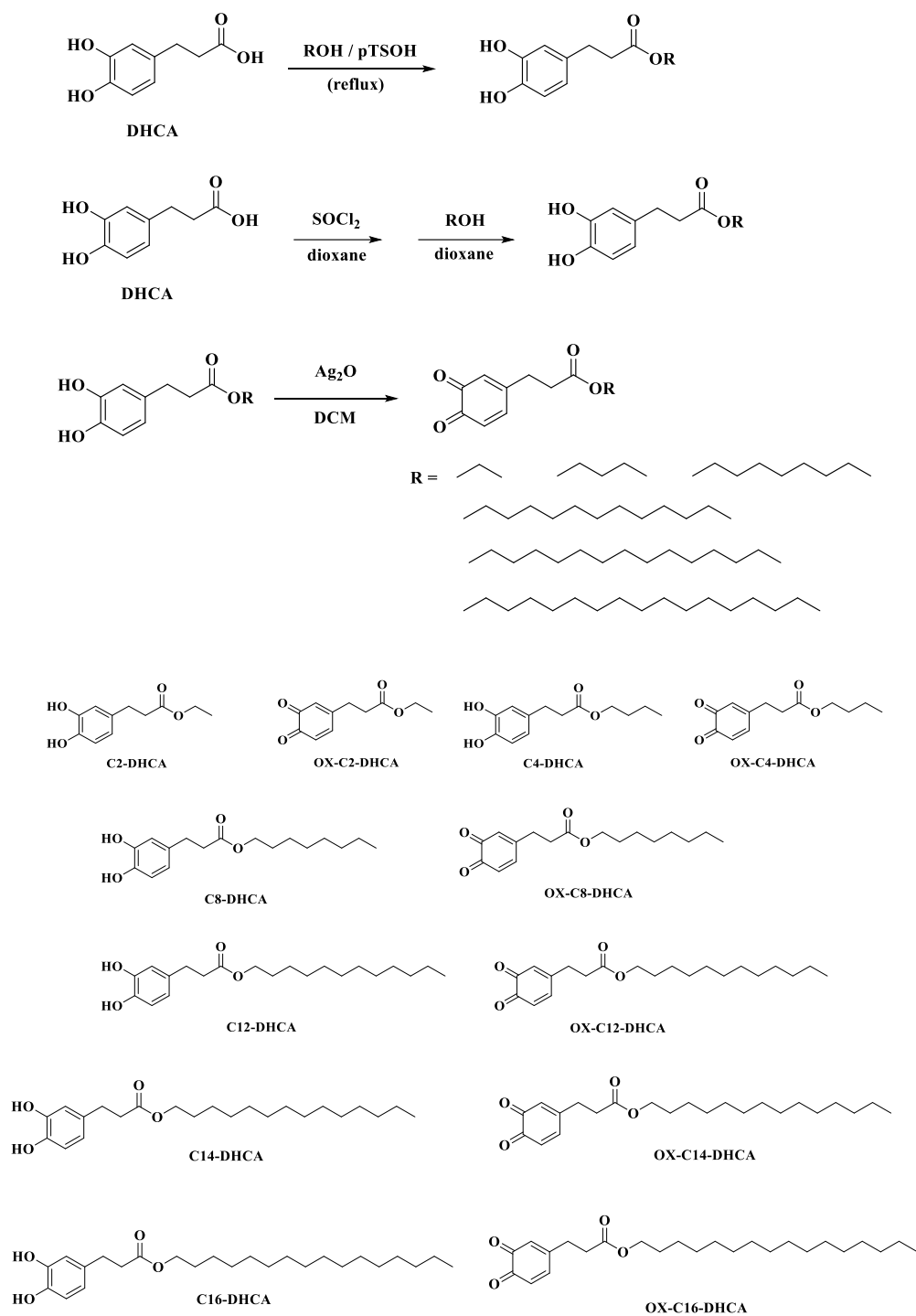
between semiquinone/HOO• and oxidable substrate dispersed in aqueous environments. The result will trigger the research for biological studies and pave the way to the use of these catalytic antioxidant systems as remedy for pathologies produced by lipids peroxidation. To do that a collaboration between our group and Prof. Pratt's research group at the Ottawa University has been established because of their findings about antioxidant chemistry in liposomes system. Theoretically, a source of hydroperoxyl radicals in combination with the redox catalytic couple would cause dismutation of HOO• in the aqueous phase and cross-dismutation of ROO• and HOO• in the lipid phase, mimicking the “radical export” behavior of the known synergic antioxidant couple Vitamin E/Vitamin C.

RESULTS AND DISCUSSION

1.7 Antioxidant activity of lipophilic catechol/quinone redox couples in micelles and biomimetic liposomal systems.

Polyphenolic secondary plant metabolites, such as flavonoids, chalcones, and caffeic acid esters, have been the subject of much research due to their various biochemical properties. These compounds are known for a variety of beneficial properties, most many of which are associated to their antioxidant activity [52]. Many such compounds share the catechol function. Research on Q/QH•/QH₂ system had previously focused on a limited number of catechols (1,2-di-hydroxybenzenes) and hydroquinones (1,4-di-hydroxybenzenes), and has demonstrated that the *ortho*-benzoquinone moiety is essential for efficient catalytic reaction with hydroperoxyl radicals (HOO•) [29]. So, dihydrocaffeic acid (DHCA) was selected as lead structure in our study. It was functionalized with suitable lipophilic chains to modulate the affinity for the phospholipid membranes. The aim was to force the localization of the antioxidant in the lipid phase and investigate its interplay with HOO•/ O₂^{-•} radicals produced in the aqueous phase, so to fully mimic the scenario found in cells. Along with DHCA derivatives, the (commercially available) lipophilic catechol/quinone couple, 3,5-di-

tert-butyl-catechol (3,5-DTBC) and 3,5-di-*tert*-butyl-benzoquinone (3,5-DTBQ), was first used as experimental model to gain proof-of-concept that the chemistry observed in solution could also be relevant in liposomes. Other studies have been made in micelles to investigate the behavior of lipophilic catechols and quinones in a different kind of heterogeneous system. The synthesis of the DHCA derivatives follows the procedures previously reported in literature [53-56] with some modifications. Briefly, a one-pot Fisher esterification using para-toluenesulfonic acid as the catalyst (*method 1*) was chosen to create shorter chain derivatives (*ethanol* and *butanol* derivatives), while a two steps synthesis (*method 2*) consisting first in the formation of the acyl chloride then on its reaction with the desired alcohols was preferred for longer chain derivatives (*1-octanol*, *1-dodecanol*, *1-tetradecanol* and *1-esadecanol*), to avoid the very difficult removal of the large excess of non-volatile alcohol from the reaction mixture, which was necessary to achieve satisfactory yields with *method 1*. The lipophilic catechols have then been oxidized using silver oxide (Ag₂O) [57] to afford the corresponding *ortho*-quinones. Briefly, to a solution of the lipophilic catechol was added Ag₂O powder. The mixture was vigorously stirred at room temperature to maintain the suspension of the Ag₂O. Then after nearly one hour the green solution shift to red and was filtrated with 0.7 μm porosity paper filter. The solution changing coloured was the oxidation eye-sign started and the low porosity of the filter was calculated to better remove the silver oxide particles. The organic solution was evaporated under reduced pressure to afford the desired quinone in nearly quantitative amount (from a range of 65.13 %, to 99 %). The product was used without further purification. Overall, the following molecules were prepared for testing in heterogenous systems.



Scheme 1.6 Synthetic procedures for lipophilic catechol and quinone DHCA derivatives.

1.7.1 Autoxidation of methyl linoleate micelles in phosphate buffer inhibited by lipophilic catechol C2-DHCA, C4-DHCA, C8-DHCA, C12-DHCA, C14-DHCA, C16-DHCA and the corresponding quinones.

Autoxidation studies were performed by monitoring the oxygen consumption in closed systems using miniaturized oxygen sensors based on NIR fluorescence quenching. The instrumental settings and apparatus was identical to that described in detail Chapter 3 and we refer to that discussion for details. The autoxidizing systems consisted in micelles of methyl linoleate (MeLin, 2.74 mM) in Triton™ X-100 neutral micelles (8 mM), initiated by water soluble AAPH at 37 °C, which is a well-validated kinetic model [59]. Preliminary results are summarized in Figure 1.8. Tocopherol was used as antioxidant standard to test the credit of the new analytical method.

Although these are just partial and preliminary results, which were obtained in the last period of my project and would certainly require further effort for confirmation and full rationalization, some interesting observations are already possible. All catechols showed good to excellent antioxidant activity in micelles, which appeared to depend on the size of the lipophilic chain. DHCA derivatives bearing C2, C4 or C8 tails had much improved antioxidant activities (Fig. 1.8 A-C). C2-DHCA and C4-DHCA afforded neat inhibited periods of reduced slope, indicating a high rate constant for trapping peroxy radicals. Most surprisingly, the duration of inhibition was extended with an apparent stoichiometric factor $n = 5$ for C2-DHCA and $n = 6$ for C4-DHCA. C8-DHCA showed the rate of peroxy radical trapping with an apparent $n = 8$. Instead, C12-DHCA has slightly higher slope of the inhibited period indicating lower rate of peroxy radical trapping compared to C8-DHCA, which however it outperformed in terms of duration of inhibition, with approximately double apparent stoichiometric factor ($n = 4$). C14-DHCA has a hallow reactivity in trapping peroxy radicals but similar stoichiometric factor ($n = 2$). Only C16-DHCA had modest antioxidant activity with lack of a distinct inhibition period which did not allow to determine the stoichiometric factor. Since a catechol can trap on two peroxy radicals of stoichiometric basis, the larger apparent n value recorded for all lipophilic DHCA derivatives (except C14 and C16) suggests their regeneration from the oxidized (quinone form). We hypothesize that regeneration occurs by the $\text{HOO}\cdot$ produced as a side event during the autoxidation of methyl linoleate. To gain confirmation in this

regard parallel autoxidation experiments were conducted using the corresponding oxidized forms, the quinones in place of the catechols. As it can be judged in figure 1.8, the quinones from C2 to C8 gave clear inhibition of the autoxidation albeit more modest the corresponding catechols. Measurements could not per performed with the quinones from C12 to C16 as we were unable to incorporate them into the micelles owing to their waxy high melting nature, and we believe that the high melting point with limited mobility inside the micelles also explains the more modest antioxidant activity of C14-DHCA and C16-DHCA catechol, which were also difficult to incorporate into the micelles.

Although further studies are necessary, these preliminary findings promise a breakthrough in antioxidant chemistry in biomimetic settings, conforming the expectations arising from previous studies in homogenous solution.

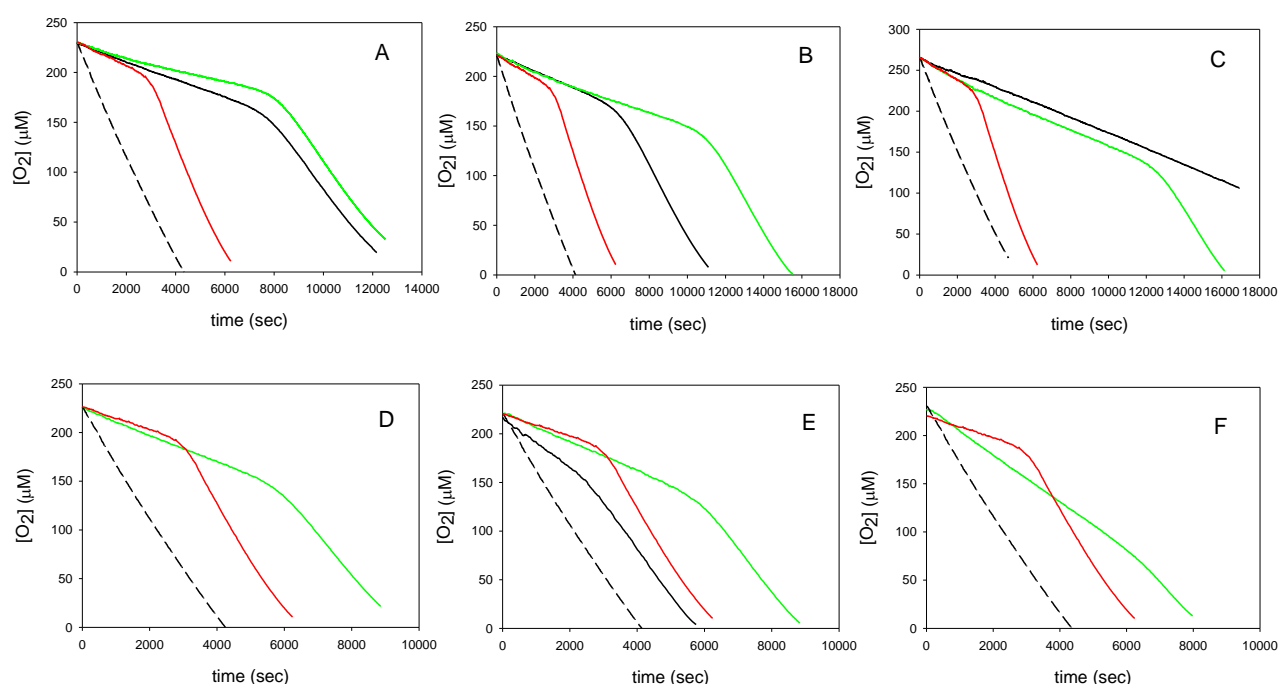
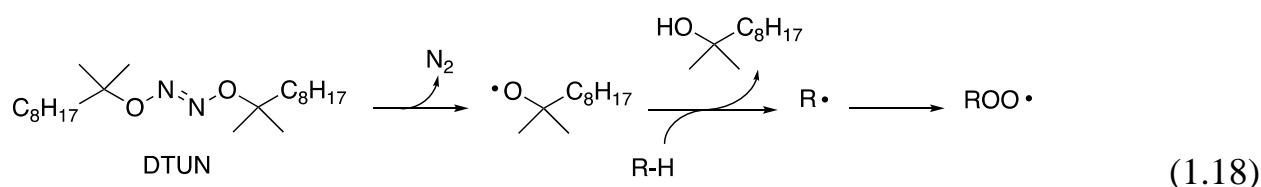


Figure 1.8 . Representative autoxidation of methyl linoleate (2.74 mM) in 8 mM Triton X-100 micelles with AAPH 2.5 mM at 37°C: (A) with 2.5 µM C2-DHCA (green), 2.5 µM Ox-C2-DHCA (black), 2.5 µM α -tocopherol reference (red), or uninhibited (dotted black), (B) with 2.5 µM C4-DHCA (green), 2.5 µM Ox-C4-DHCA (black), 2.5 µM α -tocopherol reference (red), or uninhibited (dotted black), (C) with 2.5 µM C8-DHCA (green), 2.5 µM Ox-C8-DHCA (black), 2.5 µM α -tocopherol reference (red), or uninhibited (dotted black), (D) with 2.5 µM C12-DHCA (green), 2.5

μM α -tocopherol reference (red), or uninhibited (dotted black), (E) with $5.0 \mu\text{M}$ C14-DHCA (green), $2.5 \mu\text{M}$ C14-DHCA (black), $2.5 \mu\text{M}$ α -tocopherol reference (red), or uninhibited (dotted black), (F) with $2.5 \mu\text{M}$ C16-DHCA (green), $2.5 \mu\text{M}$ α -tocopherol reference (red), or uninhibited (dotted black). N.B: autoxidation plots for ox-C12-DHCA, ox-C14-DHCA, ox-C16-DHCA aren't showed in the figures because of difficult incorporation into micelles.

1.7.2 Egg yolk phosphatidylcholine (EggPC) unilamellar liposomes as model biomimetic lipid system.

Pratt's group has previously validated a liposomal lipid model to investigate antioxidants under biomimetic settings. It consists of unilamellar liposomes with diameter of 100 nm in phosphate buffer (pH 7.4) prepared from 1 mM L- α -phosphatidylcholine from egg yolk (EggPC), by the extrusion technique. The lipid matrix can incorporate the lipophilic antioxidant and a lipophilic initiator of the autoxidation. To guarantee the localization of the initiator within the lipid bilayer and improve the control of autoxidation kinetics, we used the very lipophilic di-*tert*-undecyl hyponitrite (DTUN) as thermal initiator. Owing to its lipophilicity, upon suspension in the phosphate buffer the initiator is incorporated in the lipid matrix, where it thermally decomposes as illustrate in eq 1.18 starting the radical chain reaction [39].



This previously validated model [39,42] was used for our studies.

1.7.3 Monitoring the autoxidation by the FENIX method

A reliable method to study antioxidants under biomimetic settings is the FENIX method, which enables accurate quantification of radical trapping and antioxidant activity in the phospholipid bilayers. Pratt research group developed the FENIX method (Fluorescence-Enabled Inhibited Autoxidation) to quantify the radical-trapping antioxidant activity of compounds in phospholipid bilayers as a step forward over existing methods, such as the DPPH (2,2-diphenyl-1-picrylhydrazyl) assay,

because it is more accurate and allows for the reliable prediction of the antiferroptotic potency of redox-active compounds. [39]. The lipid peroxidation kinetic was studied by using the autoxidation reaction at the non-chain radical condition of 1 mM L- α -Phosphatidylcholine from egg yolk (EggPC) liposomes, which were extruded to 100 nm. The reaction was initialized by 0.2 mM di-*tert*-undecyl hyponitrite (DTUN) thermal initiator, suspended in phosphate buffer solution at pH 7.4. The reaction monitoring relies on the use of the fluorescent probe STY-BODIPY included in the lipid matrix. The probe carries a styryl moiety conjugated with the BODIPY π -system, which can be oxidized (by radical addition) by chain-carrying peroxy radicals with a rate constant $k = 894 \text{ M}^{-1}\text{s}^{-1}$ at 37°C . Upon attack by peroxy radicals the probe changes its spectroscopic properties, hence its oxidation can be monitored either spectrophotometrically by following the decrease of absorbance at λ_{max} 565 nm, or by monitoring the increase of its fluorescence at λ_{max} 512 nm upon excitation at λ_{max} 488 nm. If appropriately dosed the oxidation of the probe can compete with that of the lipids, progressing in parallel, thereby allowing the monitoring of autoxidation progress by spectrophotometry or spectrofluorimetry, as illustrated in Figure 1.9.

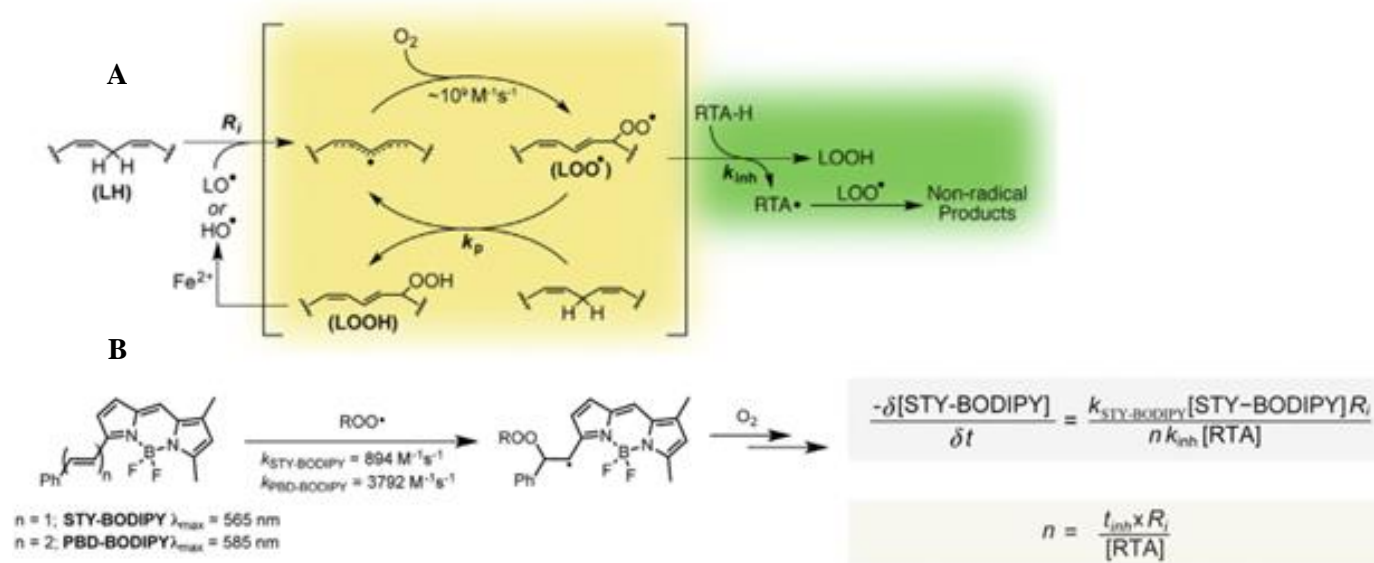


Figure 1.9. From ref. 39, A) Simplified mechanism of lipid peroxidation (autoxidation) and its inhibition by RTAs. The reaction of STY-BODIPY and PBD-BODIPY with peroxy radicals can be used as a signal carrier in inhibited co-oxidations to obtain inhibition rate constants (k_{inh}) and

stoichiometries (n) of added RTAs. [BODIPY] = dye concentration at $t = 0$ (M); n = stoichiometry; [RTA] = antioxidant concentration (M); R_i = rate of initiation; k_{BODIPY} = rate constant of propagation; t_{inh} = inhibition time (s).

Under our settings, the method was implemented to be suited for a microplate-based assay. Upon addition of 1 μM STY-BODIPY probe, the reaction kinetics was monitored by fluorescence set on excitation at 488 nm and emission at 518 nm. The data were analyzed by dividing the raw response units (y-axis values) by the response factor of $5.46 \times 10^4 \text{ RFU}/\mu\text{M}$ for ST-BODIPY, which was calculated for radical-chain condition carrying out a preliminary set of uninhibited autoxidations, with varying concentration of the probe (1, 2 and 4 μM). The inhibition rate constant (k_{inh}) and stoichiometry (n) were determined for each experiment (repeated three times). The second-order rate constant for the dye is $k_{\text{STY-BODIPY}} = 894 \text{ M}^{-1}\text{s}^{-1}$ for non-chain conditions was used in calculations. The rate of initiation (R_i) was determined using 2,2,5,7,8-Pentamethyl-6-chromanol (PMHC) as a reference antioxidant, which has a well-known stoichiometry of $n = 2$.

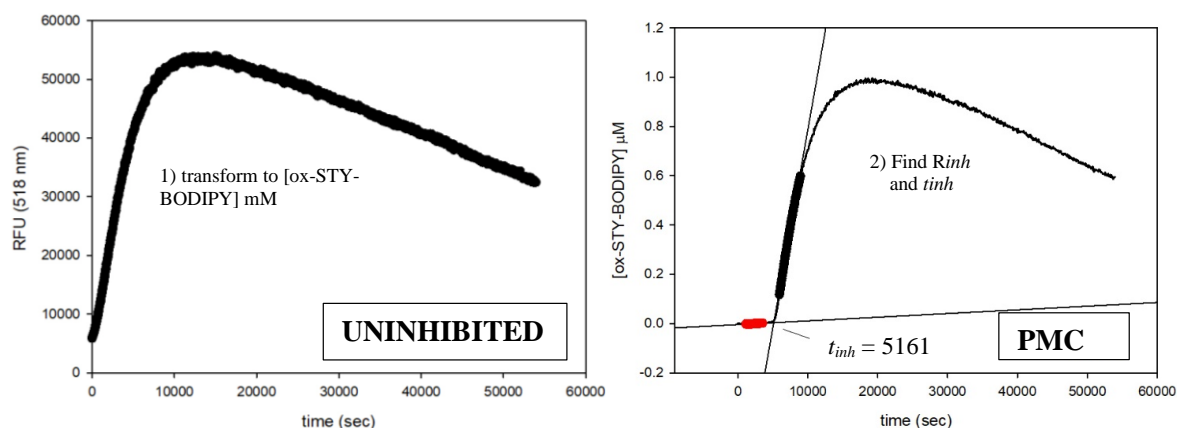


Figure 1.10 Example of calculation for R_i , n , R_{inh}

Once PMC's data was reproducible, the FENIX method was used to determinate the k_{inh} and n the model compounds 3,5-DTBC and 3,5-DTBQ, which were initially used to set the optimal experimental conditions.

1.7.4 Autoxidation of (EggPC) unilamellar liposomes inhibited by the redox couple 3,5-DTBC and 3,5-DTBQ in the absence and presence of a source of superoxide

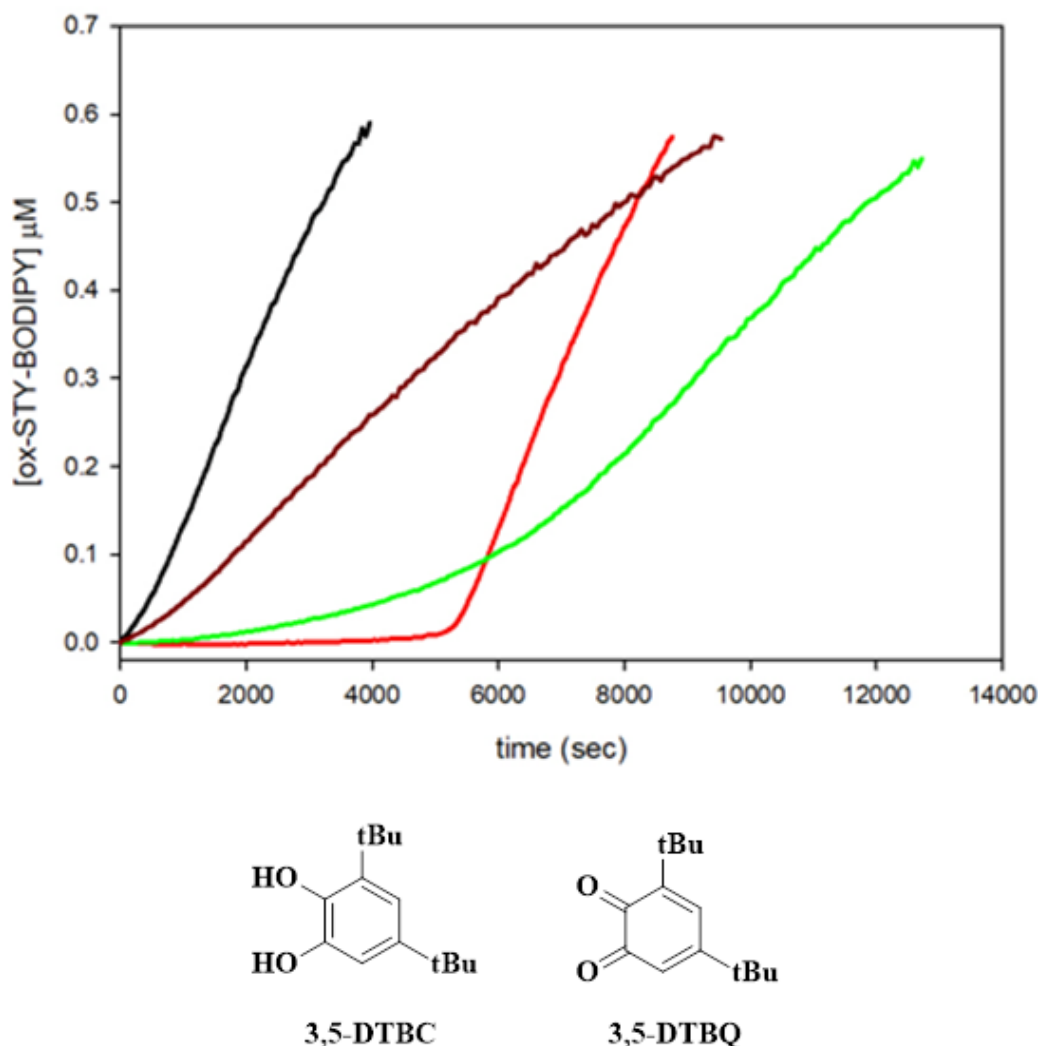


Figure 1.11. Representative co-oxidation of STY-BODIPY (1 μM), 1 mM Egg PC liposomes and 0.2 mM DTUN with 2 μM 3,5-DTBC (green), 2 μM 3,5-DTBBQ (dark red), 2 μM PMHC reference (red), or uninhibited (black).

As can be observed in figure 1.11, under our settings the catechol 3,5-DTBC produced a marked inhibition of liposomes autoxidation, with a duration similar to that of PMHC, however at the formal end of the inhibited period the catechol maintained some retarding of the autoxidation (reduced rate compared to uninhibited).

The calculated R_i using PMHC inhibition as reference was $7.7 \times 10^{-10} \text{ s}^{-1}$ hence the value of k_{inh} for 3,5-DTBC could be determined as $1.53 \times 10^4 \text{ M}^{-1} \text{ s}^{-1}$ with an experimental rate of inhibited autoxidation, R_{inh} of $1.073 \times 10^{-11} \text{ M/s}$ and a stoichiometric factor n

corresponding to 2.1. 3,5-DTBQ shows an antioxidant behavior, but no clear inhibition period is observed. Its apparent stoichiometric factor is too low to determine precisely the k_{inh} . Interestingly, however, its autoxidation plot runs parallel to the final portion of the plot obtained with 3,5-DTBC, suggesting that the residual inhibition of 3,5-DTBC is due to radical trapping by its oxidation product, the quinone, or to the generation of some hydroperoxyl radicals as side event during the autoxidation of phosphatidylcholine. HOO^\bullet could then reduce the quinone back to the starting catechol, reviving its antioxidant activity, as previously observed in homogenous solution [27]. To prove the engagement of hydroperoxyl radicals in the cross-dismutation quinone/catechol reaction, Ingold's superoxide thermal source of $O_2^{\bullet-}$, SOTS has been used. As shown in Figure 1.12 SOTS is water soluble, hence it would thermally decompose outside the lipi bilayer to form $O_2^{\bullet-}$, which might then react with the antioxidant system at the interface. SOD, superoxide dismutase enzyme, has also been added in matched experiments, to prove that any effect observed upon addition of SOTS was due to the formation of superoxide, so to achieve unambiguous clarification of the main role of $HOO^\bullet/O_2^{\bullet-}$.

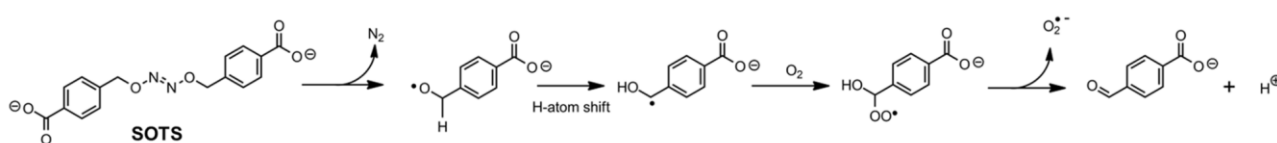


Figure 1.12. From “Potent Ferroptosis Inhibitors Can Catalyze the Cross-Dismutation of Phospholipid-Derived Peroxyl Radicals and Hydroperoxyl Radicals” by J.F. Poon et al. Represent a super oxide thermal source (SOTS) was used to produce superoxide

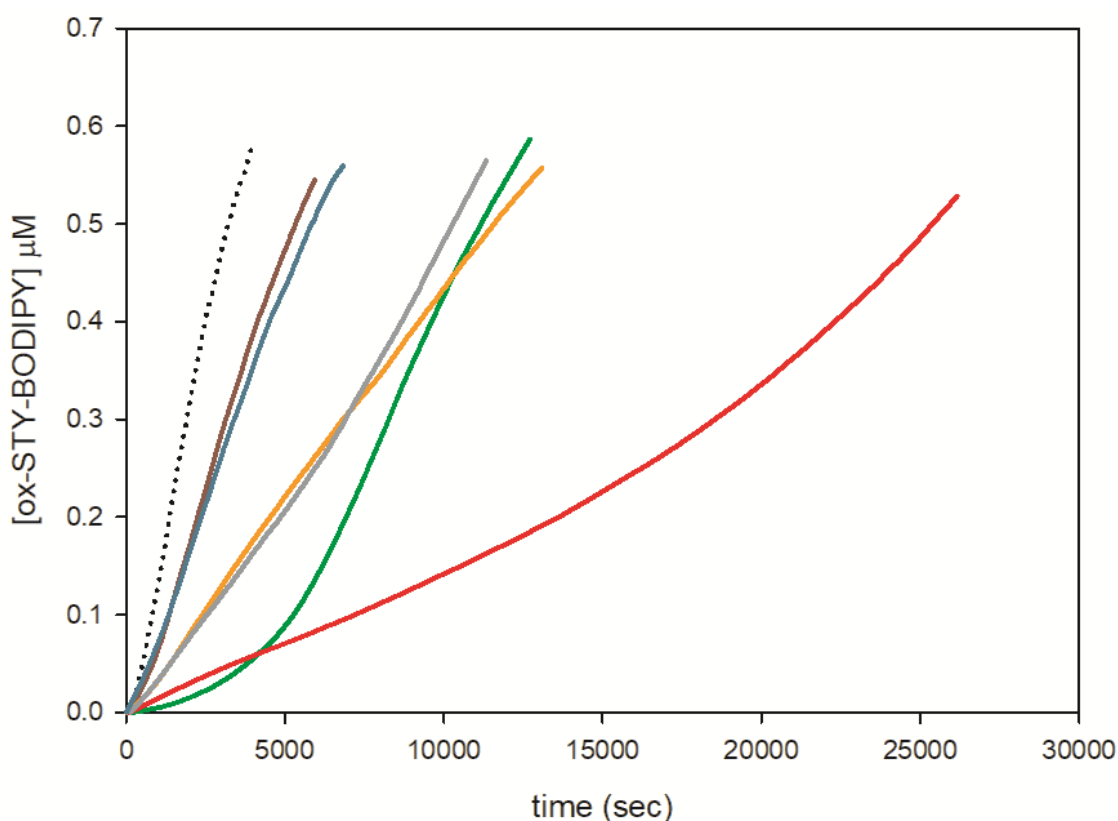


Figure 1.13. Representative co-oxidation of STY-BODIPY (1 μM) and 1 mM Egg PC liposomes at 37°C, with 0.2 mM DTUN, in the presence of 2 μM 3,5-DTBC (green), 2 μM 3,5-DTBBQ (dark red), 2 μM 3,5-DTBBQ and 25 μM SOTS (orange), 2 μM 3,5-DTBBQ and 50 μM SOTS (red), 2 μM 3,5-DTBBQ, 50 μM SOTS and 2 U/mL SOD (light gray), 2 μM 3,5-DTBBQ, 50 μM SOTS and 10 U/mL SOD (dark grey), or uninhibited (dotted).

As can be seen in Figure 1.13, the addition of increasing doses of SOTS from 12.5 to 50 μM progressively increased the *n* value of the quinone and the simultaneous addition of 1-10 U/mL of SOD reverted the activity.

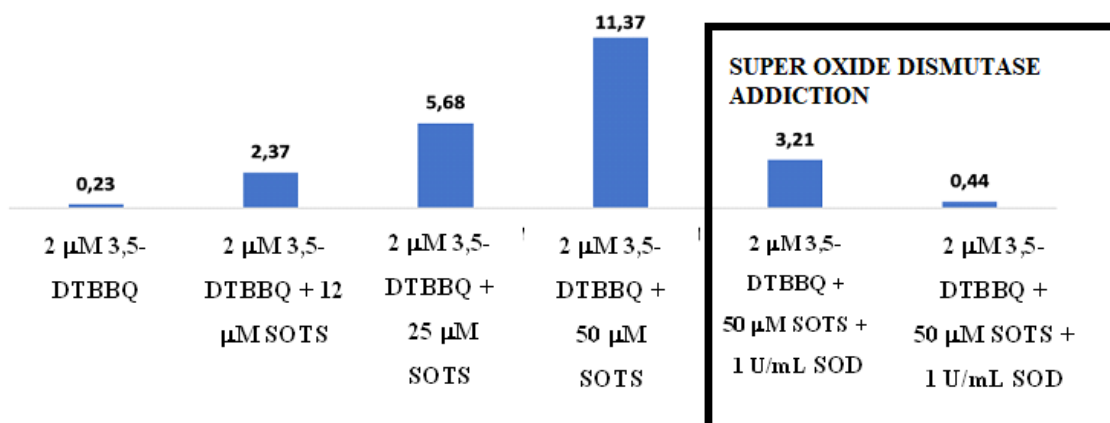


Figure 1.14. Histogram showing *n* values of 2 μM 3,5-DTBBQ upon the addition of different concentrations of SOTS and SOD.

This provides clear evidence that the chemistry previously observed in homogenous solution, *i.e.* the reduction of the quinone to the parent catechol by $\text{HOO}^\bullet/\text{O}_2^{\bullet-}$ can occur at the water/lipid interface of biomimetic liposomes, and this chemistry is able to establish a synergic antioxidant system based on $\text{Q}/\text{QH}^\bullet/\text{QH}_2$ and $\text{HOO}^\bullet/\text{O}_2^{\bullet-}$ which works as sacrificial reducing agent.

Figure 1.14 shows the apparent stoichiometric factor of 3,5-DTBQ as a function of the added SOTS and/or SOD, clearly proving the establishing of the antioxidant catalytic cycle $\text{Q}/\text{QH}^\bullet/\text{QH}_2$ as the maximum value of n recorded for the quinone largely exceeds both the negligible initial value and the value determined for the corresponding catechol ($n = 2$), a behavior that is abolished by removing $\text{O}_2^{\bullet-}$ upon addition of SOD.

1.7.5 Autoxidation of (EggPC) unilamellar liposomes inhibited by the redox couple C8-DHCA and Ox-C8-DHCA in the absence and presence of a source of superoxide

Once we had obtained these encouraging results as good proof of our theory, *n*-octyl dihydro caffeate (C8-DHCA) and its benzoquinone derivative (ox--C8DHCA) were investigated as a lipophilic antioxidant catechol/quinone couple. C8-DHCA has been synthesized as previously described (section 1.8). Although other lipophilic homologues were also prepared, time was not sufficient to investigate the entire series, hence studies are currently in progress and the C8 derivative is illustrated as prototype. The two molecules were tested as previously described, with microplate FENIX assay.

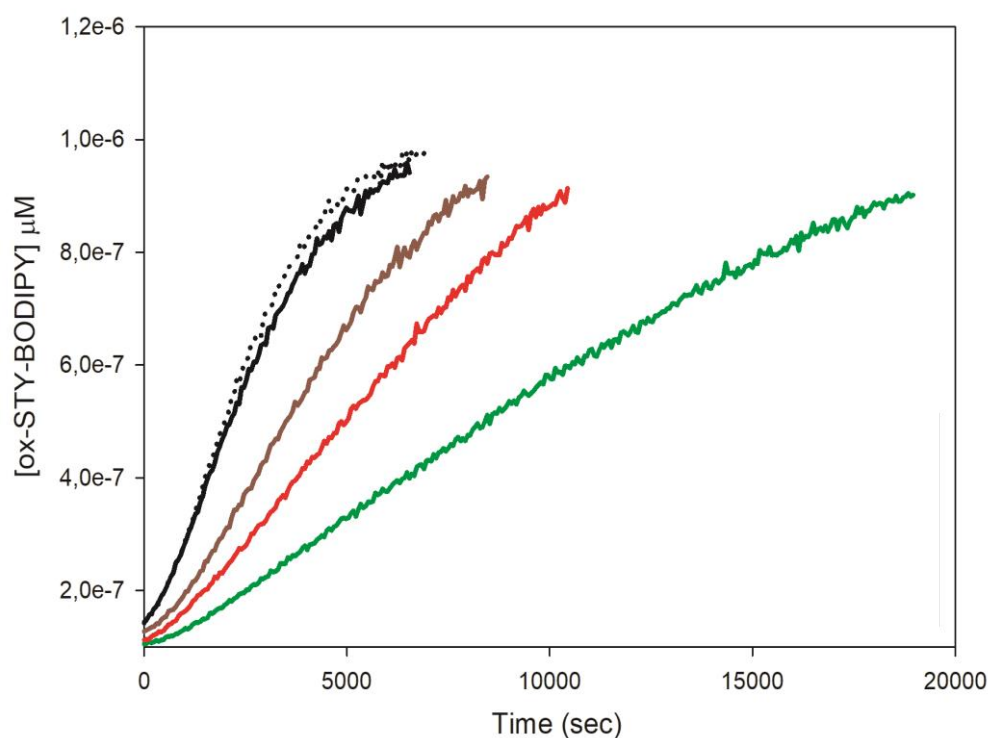


Fig. 1.15 Representative co-oxidation of STY-BODIPY (1 μM) and 1 mM Egg PC liposomes with 0.2 mM DTUN, in the presence of 2 μM C8-DHCA (green), 2 μM ox-C8-DHCA (dark red), 2 μM ox-C8-DHCA and 50 μM SOTS (red), 2 μM DHCA (black), or uninhibited (dotted).

From these preliminary results, it is possible to deduce that C8-DHCA has a higher antioxidant activity than DHCA and the benzoquinone form (ox-C8-DHCA) shows some retardation of the autoxidation process. Of interest, upon addition of SOTS in the aqueous phase the antioxidant activity of ox-C8-DHCA is significantly increased, supporting the reduction of the quinone to the parent semiquinone and catechol by superoxide, thereby paralleling the behavior shown by the couple 3,5-DTBC and 3,5-DTBQ.

The higher activity of C8-DHCA compared to more hydrophilic DHCA is explained by the higher incorporation into the lipid bilayer. In this picture, the antioxidant performance of quinone derivatives in our model system is expected to depend on their lipophilicity.

As localization of the quinone in the bilayer is key to its protective activity toward the bilayer itself, we it would be important to complete the investigation using the other

derivatives of DHCA with variable lipophilicity, which we have prepared for the purpose. This would allow establishing the optimal lipophilicity for maximum protection of the lipid bilayer and for the highest efficiency of the regeneration of the antioxidant by superoxide at the water/lipid interface.

The experiments with SOD aren't shown in the picture because of the limited time of the internship. but in conclusion, the positive results put down the basic knowledge to move forward in this research, finding the optimal catechol/quinone couple with the purpose of identifying effective non-conventional antioxidant systems to be used as inhibitors of ferroptosis.

EXPERIMENTAL PART

1.8 Materials and methods

1.8.1 Materials

Dihydrocaffeic acid (DHCA), ethanol, butanol, 1-octanol, 1-dodecanol, 1-tetradecanol, 1-esadecanol, p-toluensulfonic acid (pTSA), thionyl dichloride (SOCl₂), α -tocopherol, silver oxide, AAPH (2,2'-azobis(2-methylpropionamidine) dihydrochloride), methyl linoleate (MeLin) ($\geq 98\%$) and TritonTM X-100, were used as received from Sigma Aldrich (Milan, Italy). Di-*tert*-undecyl Hyponitrite (DTUN), Superoxide thermal source (SOTS) and STY-BODIPY were available at the host laboratory (Derek Pratt's group a University of Ottawa) from previous studies [60]. Stock solutions of AAPH in the desired solvents were prepared immediately prior to use and/or maintained for maximum 2h or 4h, respectively, at 4°C between subsequent uses, to avoid significant decomposition. Solvents and other chemicals were of the highest grade commercially available (Sigma-Aldrich, Merck, VWR; Milan, Italy) and were used as received.

1.8.2 General methods

¹H NMR spectra were recorded in deuterated chloroform CDCl₃, in deuterated water D₂O, or in dimethyl sulphoxide DMSO at 400 MHz on a Bruker spectrometer. ¹³C

NMR spectra were recorded in CDCl₃ at 400 MHz on a Bruker 400 MHz spectrometer. Analytical and preparative TLC were carried out on silica gel plates (0.25 and 0.50 mm, respectively) from Merck using hexane/ethyl acetate in different proportions as the eluant. InfinityLab LC/MSD Series and 6100 Series LC/MS single quadrupole (SQ) instrument was used for HPLC-ESI-MS analysis. Detection wavelength was set at 240 nm, 254 nm and 280 nm. Eluant system: 0.1 % formic acid – water and acetonitrile (ACN) starting from 30:70 to 10:90 v/v. The gradient is 30:70 for 10 minutes, 50:50 for 10 minutes, 70:30 for 10 minutes and 10:90 in 15 minutes. ESI source used the following conditions: nebulizer pressure 35 psig; drying gas (nitrogen) flushed at 12.0 L / min at a temperature of 350 °C; capillary voltage 3000 V. An Eclipse Plus C18 column (150 × 4.6 mm, 5 μm) at a flow rate of 0.7 mL / min was used, using the same eluant as above at 40 °C.

1.83 Synthesis of C2-DHCA

The title compound was prepared following a procedure previously reported with modifications [53]. 1 g DHCA (molecular weight -m.w-: 182.17 g/mol, 5.5 mmol), ethanol (m.w: 46,07 g/mol, 1 mmol) 40 mL and 0.2 pTSA was mixed and refluxed in a round bottom flask immerse in silicon bath at 120 °C degree equipped with a refrigerator for 2 hours and then heatless only stirred for 18 hours, under nitrogen. The reaction was stopped and work up was executed with 5 % bicarbonate solution, brine and extraction with dicloromethane (DCM). The product was purified by columns chromatography on silica gel eluting with 50:50 ACN/hexane. Yield: 0.60 g C2-DHCA (MW: 210.09 g/mol, 2.87 mmol), 52.2 %. HPLC-ESI-MS analysis (see Appendix) and ¹H-NMR (see Appendix) confirmed the identity.

1.8.4 Synthesis of C4-DHCA

The title compound was prepared following a procedure previously reported with modifications [53]. 1 g DHCA (5.5 mmol), butanol (74,121 g/mol, 1 mmol) 30 mL and 0.2 pTSA was mixed refluxed in a round bottom flask immerse in silicon bath at 120 °C degree equipped with a refrigerator for 2 hours and then heatless only stirred for 18

hours, under nitrogen. The reaction was stopped and work up was executed with 5 % bicarbonate solution, brine and extraction with DCM. The product was purified by columns chromatography on silica gel eluting with 50:50 ACN/hexane. Yield: 0.85 g C4-DHCA (MW: 238.12 g/mol, 3.55 mmol), 64.6 %. HPLC-ESI-MS analysis (see Appendix) and ¹H-NMR (see Appendix) confirmed the identity.

1.8.5 Synthesis of C8-DHCA

The title compound was prepared following a procedure previously reported with modifications [55]. 1 g DHCA (5.5 mmol), was reacted with 0.6 mL SOCl₂ (1.5 eq) in 25 mL of anhydrous dioxane in a 3-neck round bottom flask equipped with refrigerator. The reaction mixture was stirred under nitrogen and heating at 200°C for one hour. 1.3 mL octanol (m.w.: 130,23 g/mol, 1.5 eq) was added and the mixture was stirred at 200°C for 18 hours, then allowed to reach room temperature and quenched with brine and 5 % bicarbonate solution. The product was extracted in DCM and evaporated to afford a viscous oil which was purified by column chromatography on silica gel eluting with 75:25 hexane/ethyl acetate (EtOAc). Yield: 0.13 g (MW: 294.18 g/mol, 0.44 mmol) 8%. HPLC-ESI-MS analysis (see Appendix) and ¹H-NMR (see Appendix) confirmed the identity.

1.8.6 Synthesis of C12-DHCA

The title compound was prepared following a procedure previously reported with modifications [55]. 1 g DHCA (5.5 mmol), was reacted with 0.6 mL SOCl₂ (1.5 eq) in 25 mL of anhydrous dioxane in a 3-neck round bottom flask equipped with refrigerator. The reaction mixture was stirred under nitrogen and heating at 200 °C for one hour. 1.84 mL dodecanol (m.w.: 186.33 g/mol, 1.5 eq) was added and the mixture was stirred at 200 °C for 16 hours, then allowed to reach room temperature and quenched with brine and 5 % bicarbonate solution. The product was extracted in DCM and evaporated to afford a viscous oil which was purified by column chromatography on silica gel eluting with 75:25 hexane/EtOAc. Yield: 0.75g C12-DHCA (MW: 350.25 g/mol, 2.14 mmol)

35.19%. HPLC-ESI-MS analysis (see Appendix) and ¹H-NMR (see Appendix) confirmed the identity.

1.8.7 Synthesis of C14-DHCA

The title compound was prepared following a procedure previously reported with modifications [55]. 1 g DHCA (5.5 mmol), was reacted with 0.6 mL SOCl₂ (1.5 eq) in 25 mL of anhydrous dioxane in a 3-neck round bottom flask equipped with refrigerator. The reaction mixture was stirred under nitrogen and heating at 200 °C for one hour. 1.8 g g tetradecanol (m. w.: 214.39 g/mol, 1.5 eq) was added and the mixture was stirred at 200 °C for 24 hours, then allowed to reach room temperature and quenched with brine and 5 % bicarbonate solution. The product was extracted in DCM and evaporated to afford a viscous oil which was purified by column chromatography on silica gel eluting with 75:25 hexane/EtOAc. Yield: 0.68 g C14-DHCA (PM: 378.28 g/mol, 1.79 mmol) 41.2%. HPLC-ESI-MS analysis (see Appendix) and ¹H-NMR (see Appendix) confirmed the identity.

1.8.8 Synthesis of C16-DHCA

The title compound was prepared following a procedure previously reported with modifications [55]. 1g DHCA (5.5 mmol), was reacted with 0.6 mL SOCl₂ (1.5 eq) in 25 mL of anhydrous dioxane in a 3-neck round bottom flask equipped with refrigerator. The reaction mixture was stirred under nitrogen and heating at 200 °C for one hour. 2 g g hexadecanol (m. w.: 242,44 g/mol, 1.5 eq) added and the mixture was stirred at 200 °C for 20 hours, then allowed to reach room temperature and quenched with brine and 5 % bicarbonate solution. The product was extracted in DCM and evaporated to afford a viscous oil which was purified by column chromatography on silica gel eluting with 80:20 hexane/EtOAc.. Yield: 0.64 g C16-DHCA (MW: 406.31 g/mol, 1.57 mmol) 48.6%. HPLC-ESI-MS analysis (see Appendix) and ¹H-NMR (see Appendix) confirmed the identity.

1.8.9 Synthesis of quinones: ox-C2-DHCA, ox-C4-DHCA, ox-C8-DHCA, ox-C12-DHCA, ox-C14-DHCA and C16-DHCA

The quinones were prepared from the corresponding catechols following a procedure previously reported with modifications [57]. To a stirred solution of the lipophilic catechol in DCM was added 5 equivalents of silver oxide powder. The mixture was vigorously stirred at room temperature to maintain the suspension of the Ag₂O. Then after nearly one hour the green solution shift to red and was filtrated with 0.7 μm porosity paper filter. The solution changing coloured was the oxidation eye-sign started and the low porosity of the filter was calculated to better remove the silver oxide particles. The organic solution was evaporated under reduced pressure to afford the desired quinone in nearly quantitative amount (from a range of 65.13 %, to 99 %). The product was used without further purification. HPLC-ESI-MS analysis (see Appendix), ¹H-NMR and ¹³C-NMR (see Appendix) confirmed the identity, showing variable amounts of impurities arising from oligomerization and polymerization of the quinones.

1.8.10 Autoxidation kinetics in MeLin micelles

The micelles model used in this investigation was similar to that previously described and validated by Konopko and Litwinienko [59]. In a typical experiment, 2.5 mL of air-saturated buffered (PBS, 50 mM, pH 7.4) aqueous dispersion of MeLin (final concentration 2.74 mM) in Triton™ X-100 (final concentration 8 mM) micelles were prepared by vortex mixing, then adding a freshly prepared stock solution of AAPH (final concentration 2.5-5 mM), immediately followed by addition 4–16 μL of a (0.5–1 mM) stock solution of the antioxidant in acetonitrile (final concentration of 2.5–10 μM) at room temperature. After brief additional vortex stirring (5–10 sec.) the mixture was used to fill in a sealed 2.4 mL glass vial provided with a PTFE-coated stirring bar. The sample was equilibrated at 37 °C in a thermostatted bath equipped with a sealed

magnetic stirrer and O₂ consumption was recorded. Oxygen concentration was monitored with the same equipment described for mTYR kinetics and data were similarly treated by the equation: $V \text{ (M/s)} = V \text{ (}\Delta P/\Delta t) \times 0.210 \times 10^{-3}/P_0$, where P₀ is the initial 20 % O₂ saturation reading that corresponds to 0.210 mM at 37 °C. Oxygen consumption in the presence of the antioxidant was compared with that recorded with identical reference mixtures lacking the antioxidant. Different initiator concentrations were used to find the optimal experimental condition to test the antioxidant molecules and the best settings with the oxygen sensor was with AAPH 2.5 mM. The theoretical R_i calculated with equation 1.10 was 1.88 x 10⁻⁹ M/s, which was confirmed by monitoring the oxygen consumption during the thermal degradation of AAPH in buffer solution in the absence of micelles and antioxidants.

1.8.11 Autoxidation studies in Egg-Yolk unilamellar liposomes (performed during a visiting period at the University of Ottawa)

Measurements were performed according to the previously published protocol by Pratt's group [60]. Briefly, to a black 96-well polypropylene plate, was added a solution containing liposomes (1 mM) and STY-BODIPY (1 mM) in PBS at pH 7.4 to a final volume of 295 μL. EggPC liposomes were prepared by the extrusion techniques according to literature [61], followed by the addition of inhibitors (2 μL aliquots) at desired concentrations to the appropriate wells. The plate was incubated for 10 minutes at 37°C in the BioTek Synergy H1 plate reader followed by a vigorous mixing protocol for 5 minutes. The plate was ejected from the plate reader and the autoxidation was initiated by the addition of a 3 μL aliquot of DTUN (0.2 mM in EtOH), followed by another mixing protocol for 5 minutes. The plate was incubated for an additional 10 minutes to equilibrate at 37°C before data was acquired by excitation of the probes at 488 nm and emission was measured at 518 nm (gain: 70). The data was transformed by dividing the raw RFU values by the response factor of 7.49x10⁴ RFU/mM. The data shown is an average of three independent experiments. Data analysis followed the published procedure [60].

Appendix to Chapter 1

HPLC-ESI-MS chromatogram

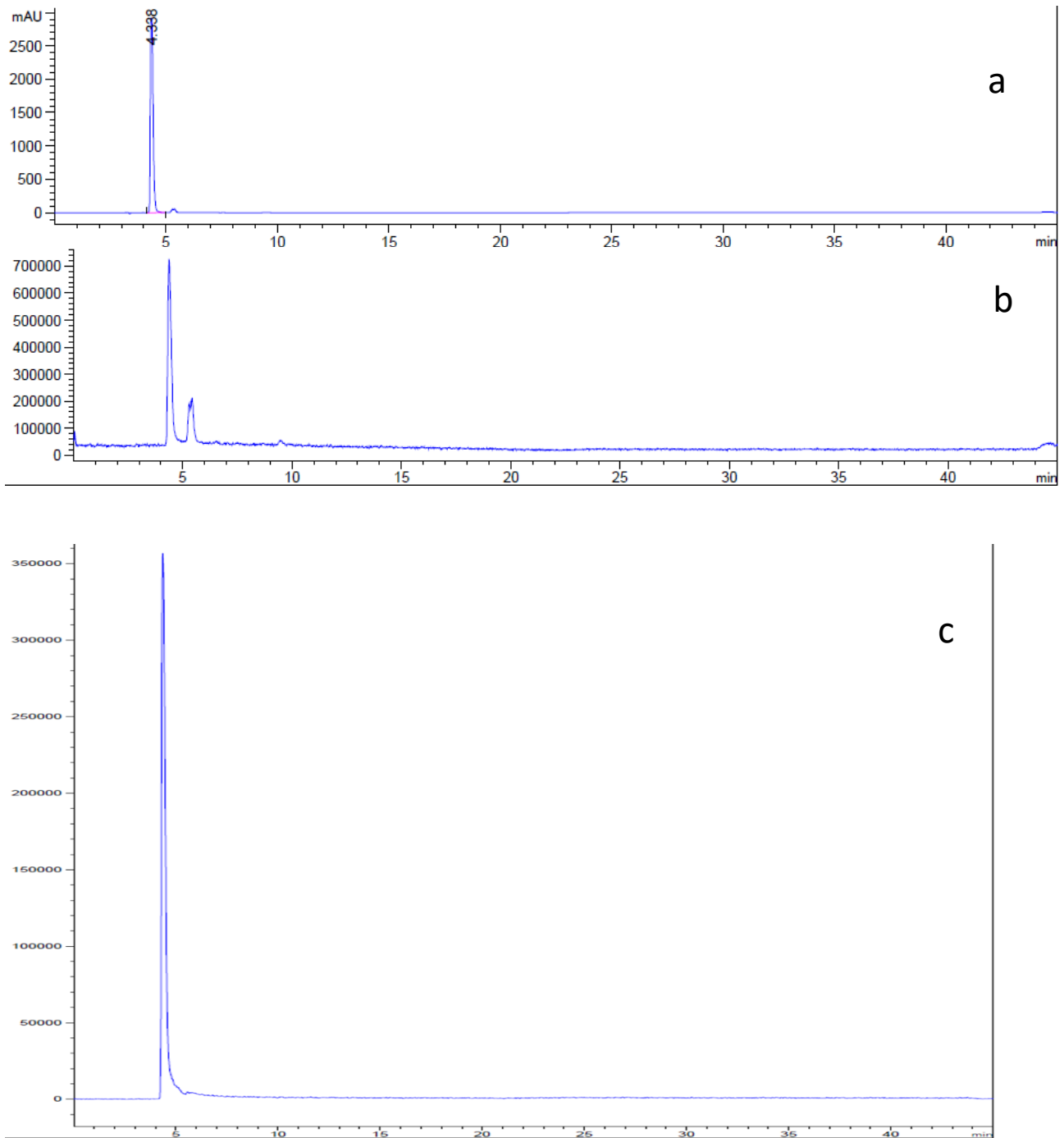


Figure A 1.1 Chromatogram of C2-DHCA r.t.(4.38 min), in acetonitrile a) DAD 210 nm b) MS FULL SCAN NEGATIVE principle mass peaks: 209.1, 210, 245, 419, 420 c) MS EXTRACTED NEG ION 209

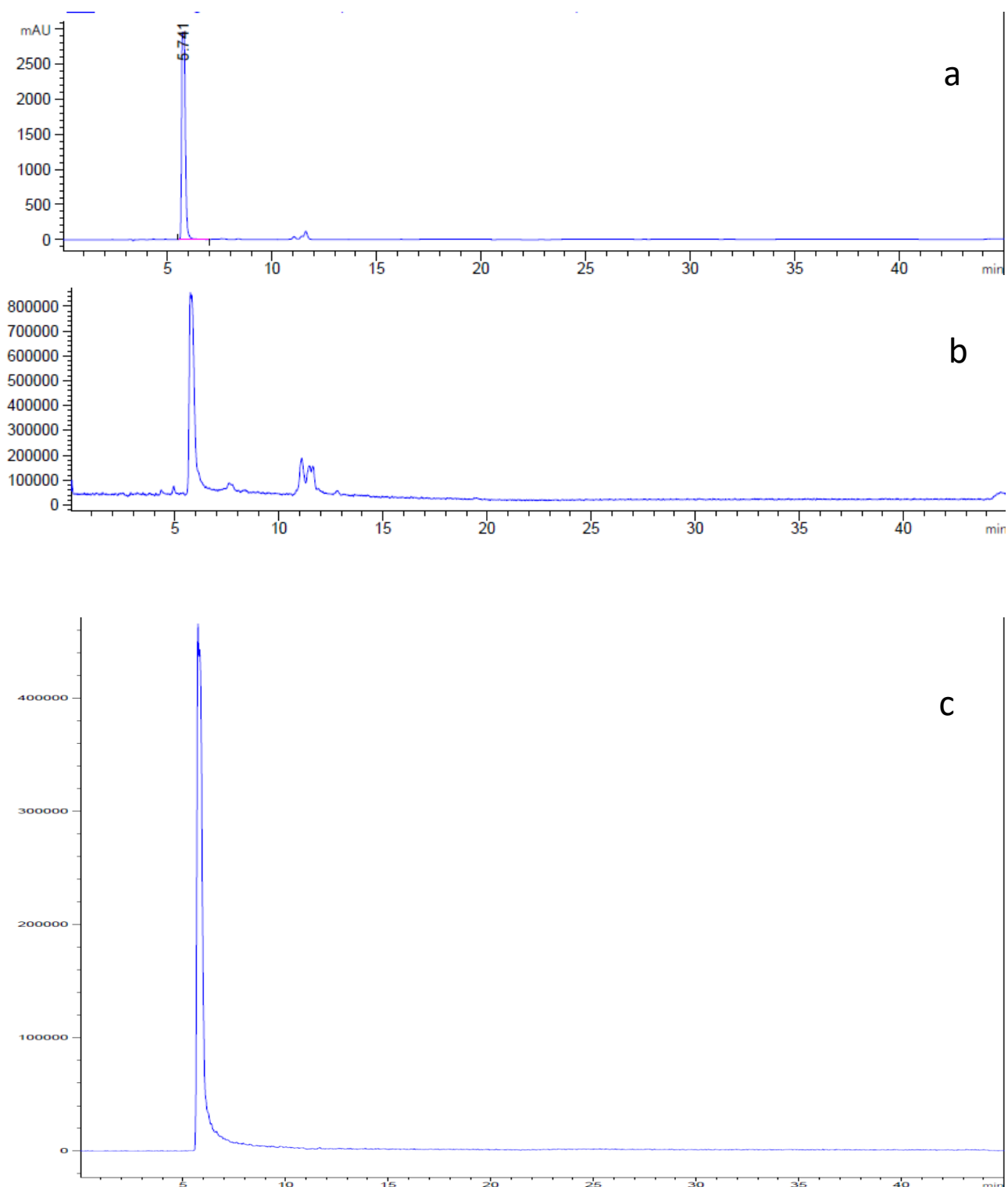


Figure A 1.2 Chromatogram of C4-DHCA r.t.(5.74 min), in acetonitrile a) DAD 210 nm b) MS FULL SCAN NEGATIVE principle mass peaks: 237.1, 238.1, 475.2,476.2 c) MS EXTRACTED NEG ION 237

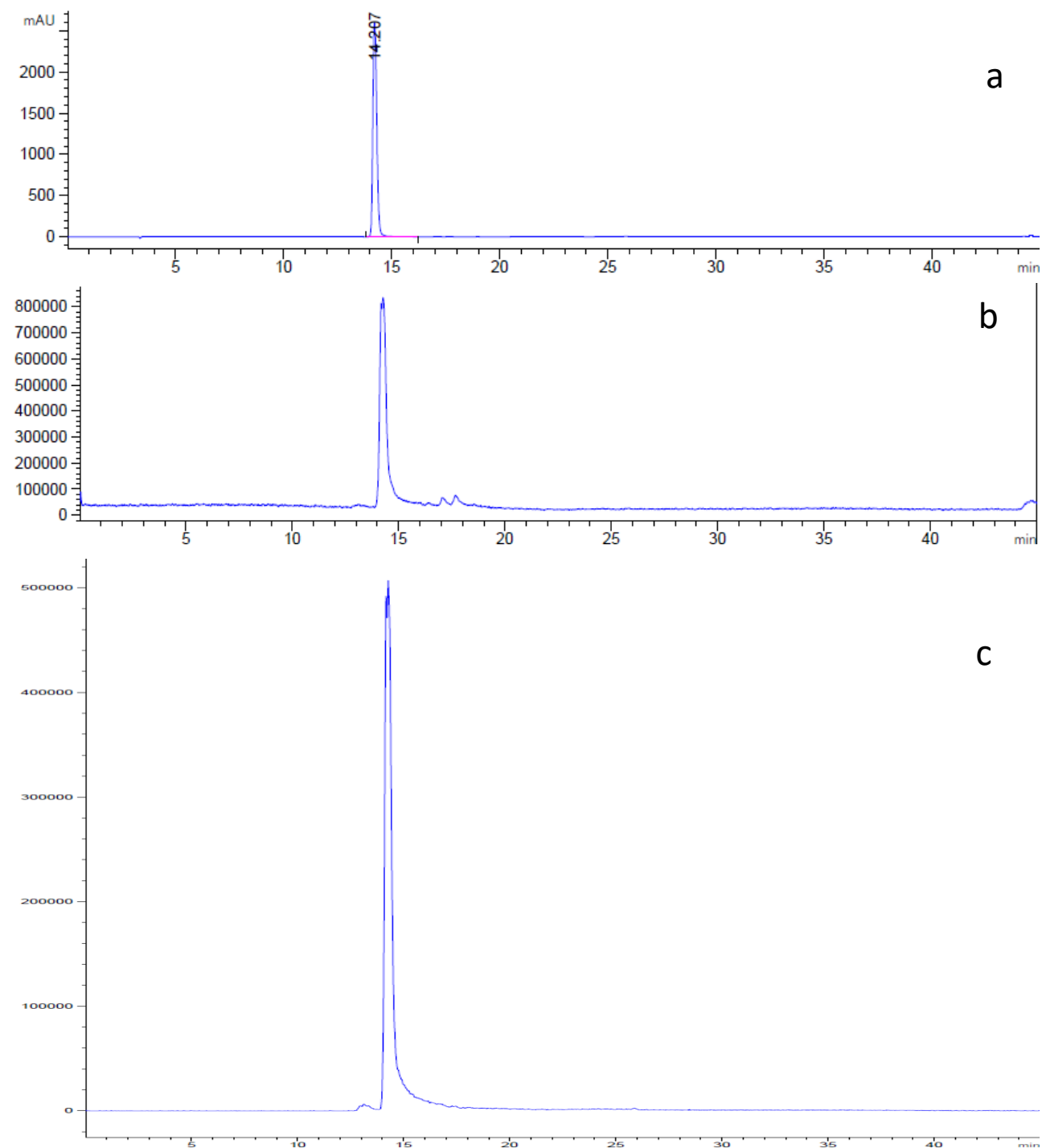


Figure A 1.3 Chromatogram of C8-DHCA r.t.(14.29 min), in acetonitrile, a) DAD 210 nm b) MS FULL SCAN NEGATIVE principle mass peaks: 293, 294, 329, 582; c) MS EXTRACTED NEG ION 293

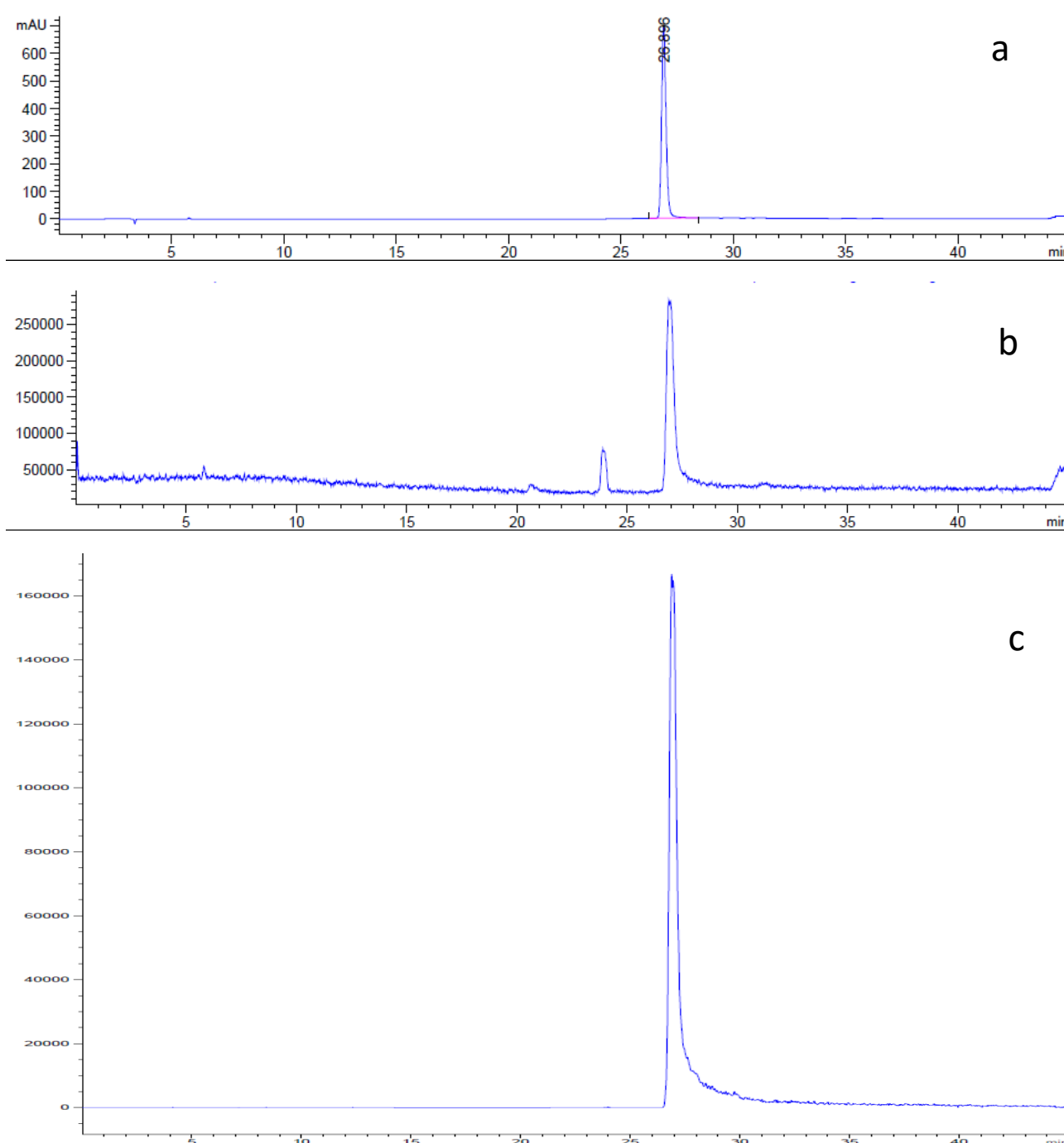


Figure A 1.4 Chromatogram of C12-DHCA r.t.(26.99 min), in acetonitrile a) DAD 210 nm b) MS FULL SCAN NEGATIVE principle mass peaks: 349, 350, 385, 386; c) MS EXTRACTED NEG ION 349

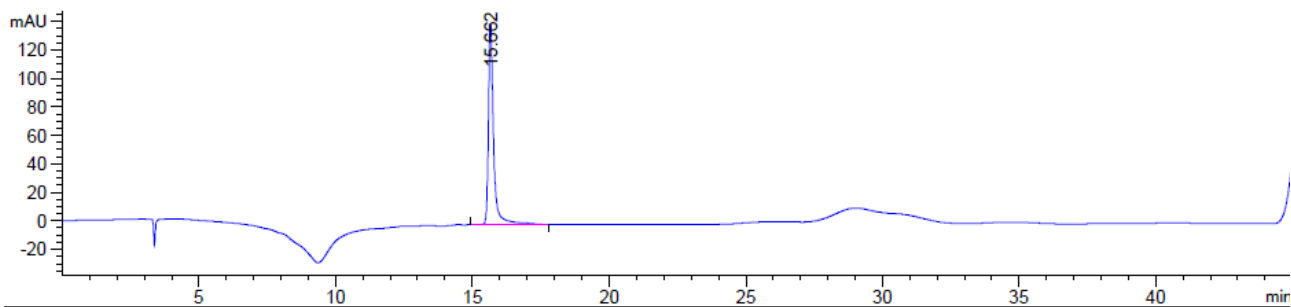


Figure A 1.5 Chromatogram of C14-DHCA r.t.(15.62 min), in acetonitrile DAD 210 nm

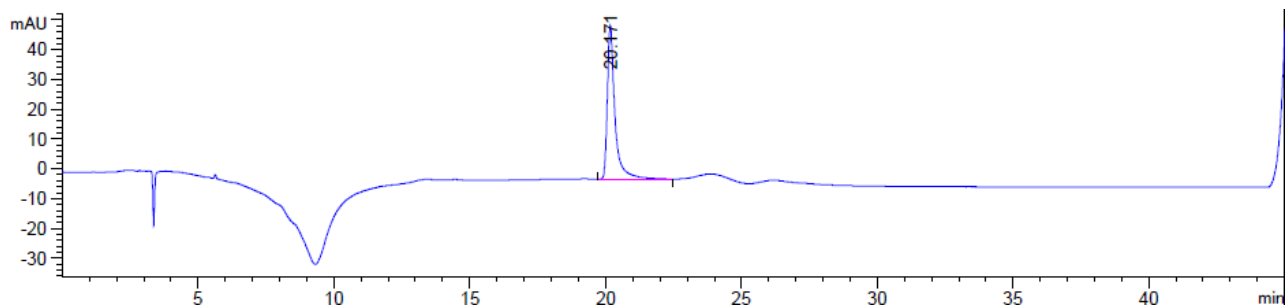
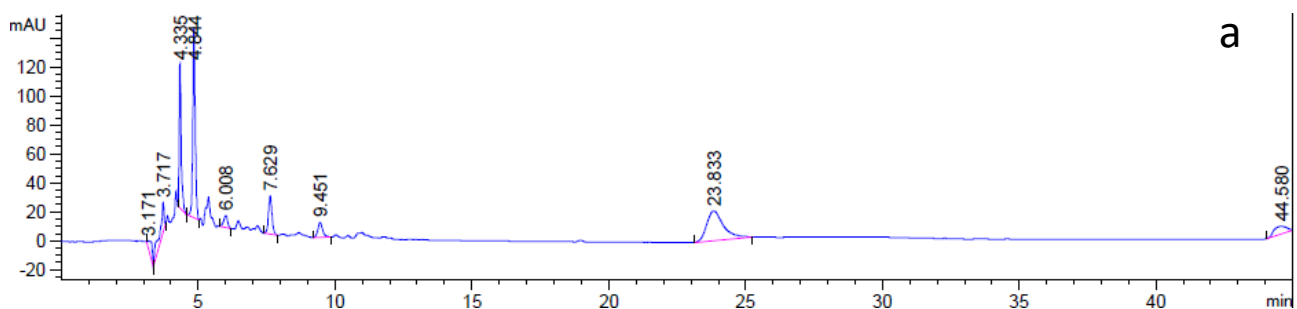
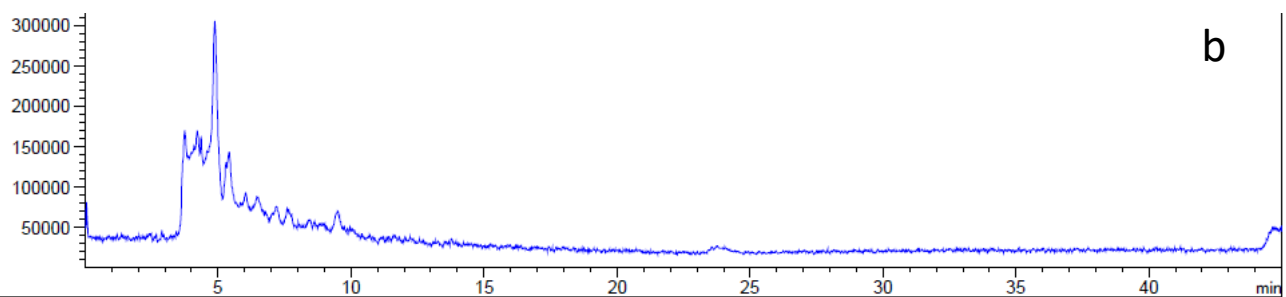


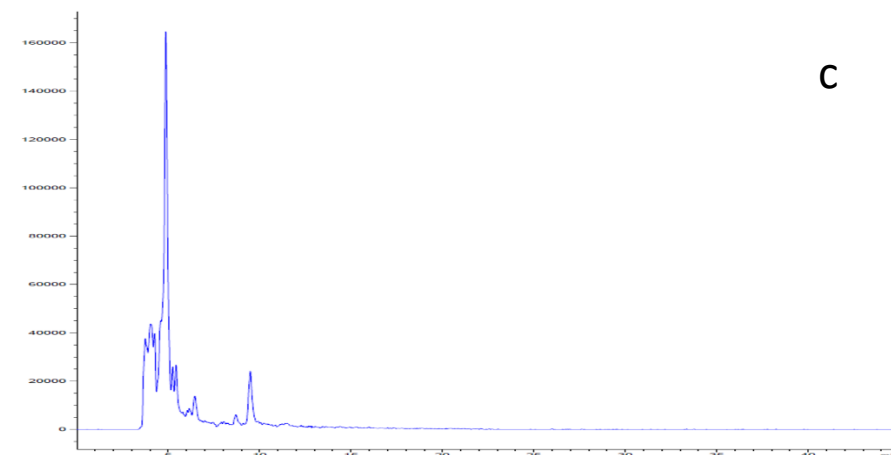
Figure A 1.6 Chromatogram of C16-DHCA r.t.(20.17 min), in acetonitrile DAD 210 nm



a



b



c

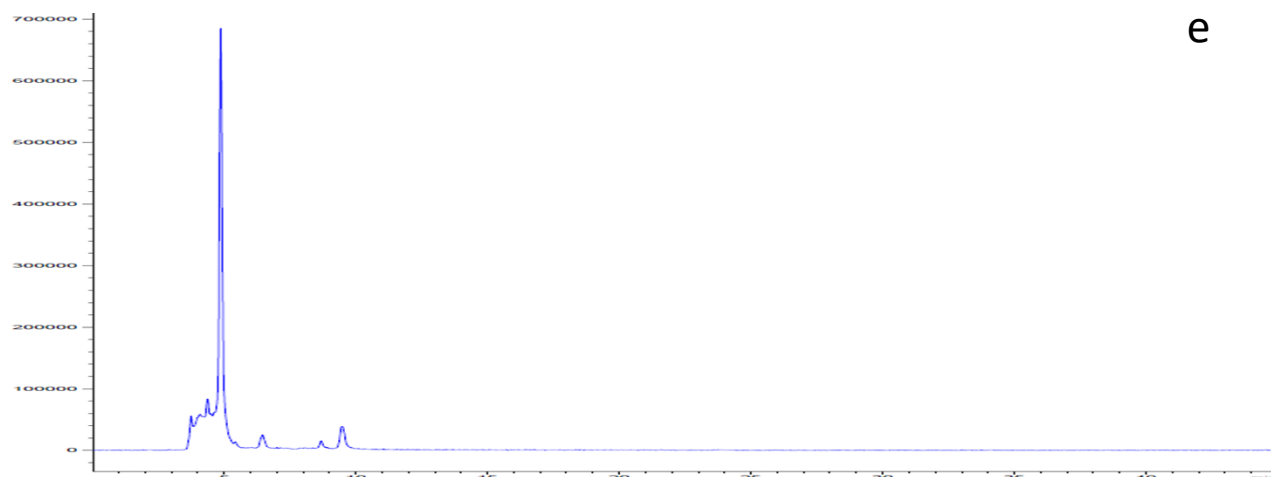
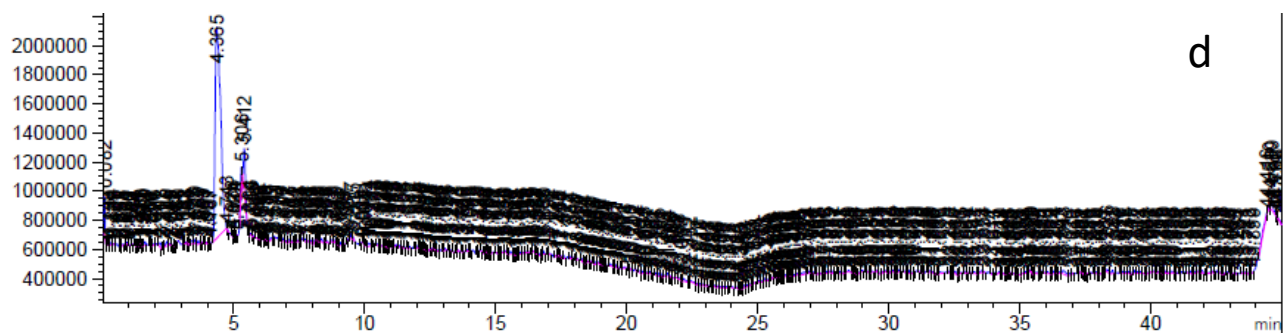
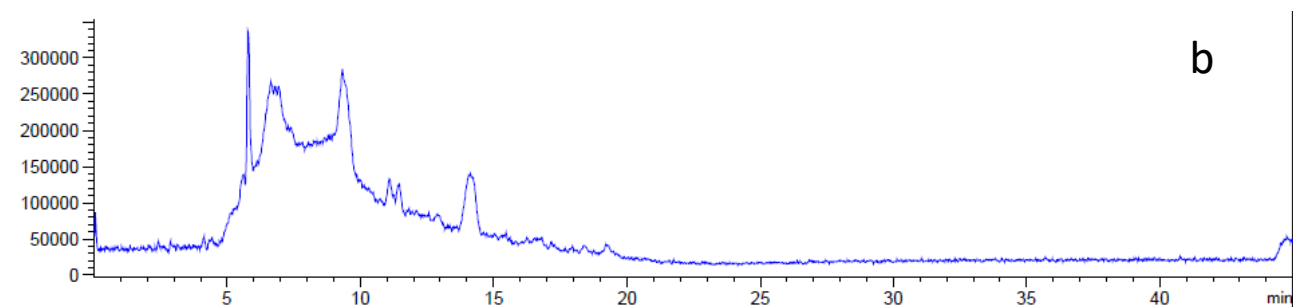
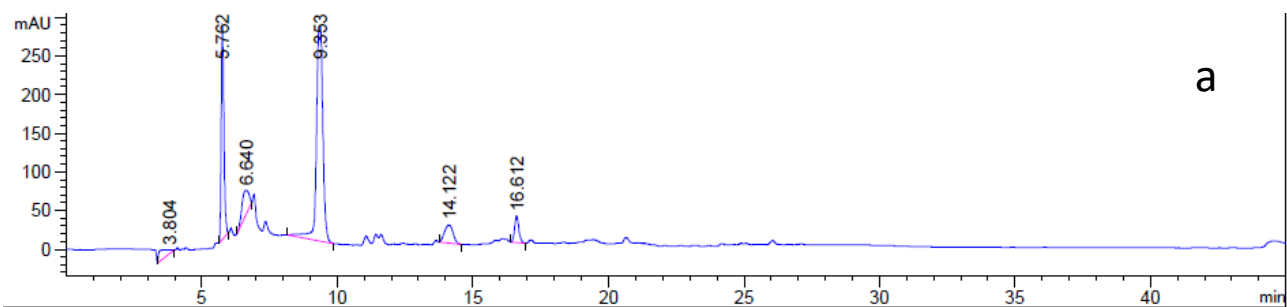
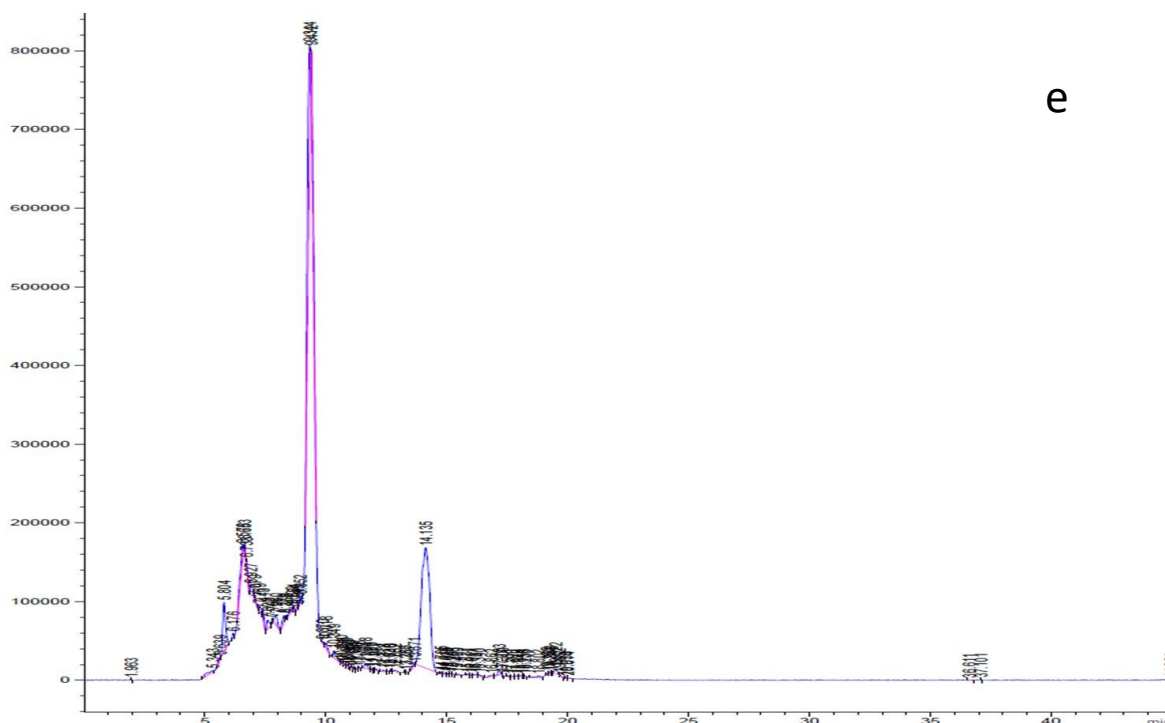
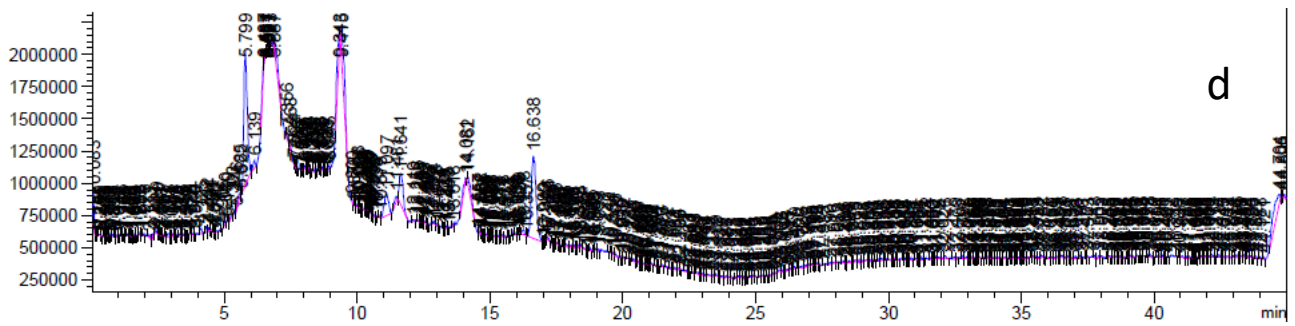
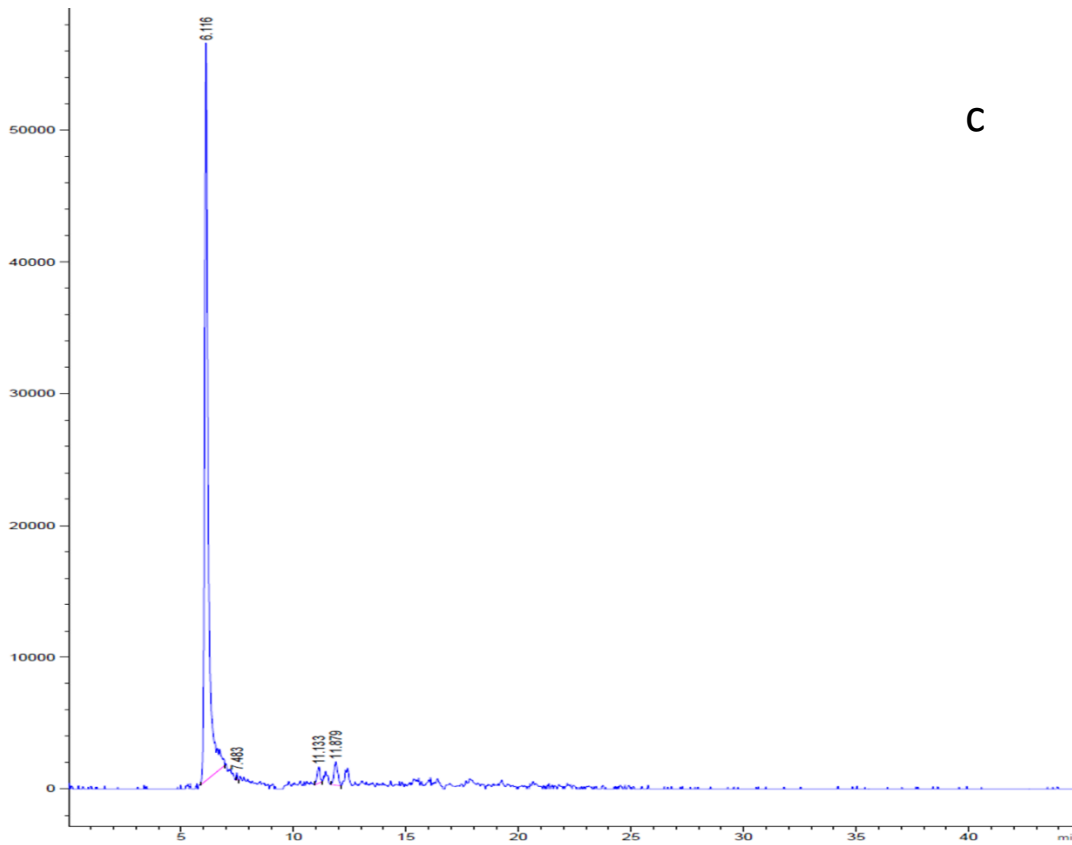


Figure A 1.7 Chromatogram of ox-C2-DHCA r.t.(4.33 min), in acetonitrile a) DAD 210 nm b) MS FULL SCAN NEGATIVE principle mass peaks: 415,416, 478, 529, 831; c) MS EXTRACTED NEG ION 415 d) MS FULL SCAN POSITIVE e) MS EXTRACTED POS ION 439





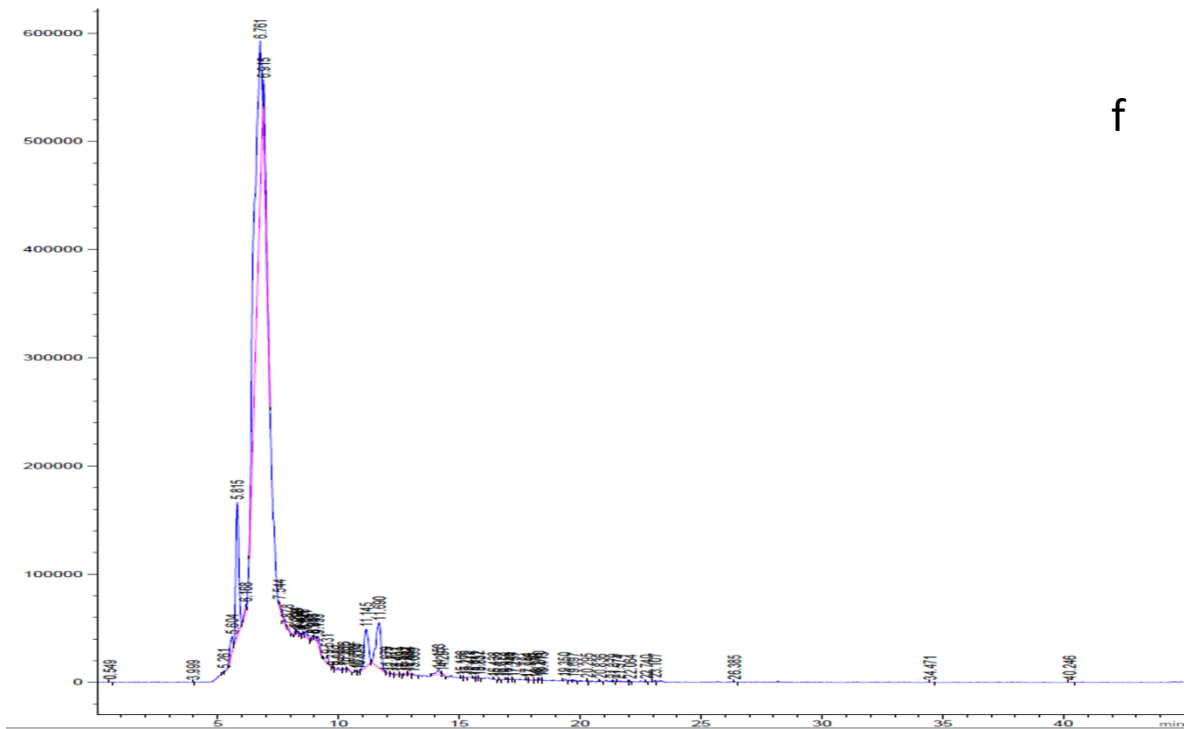
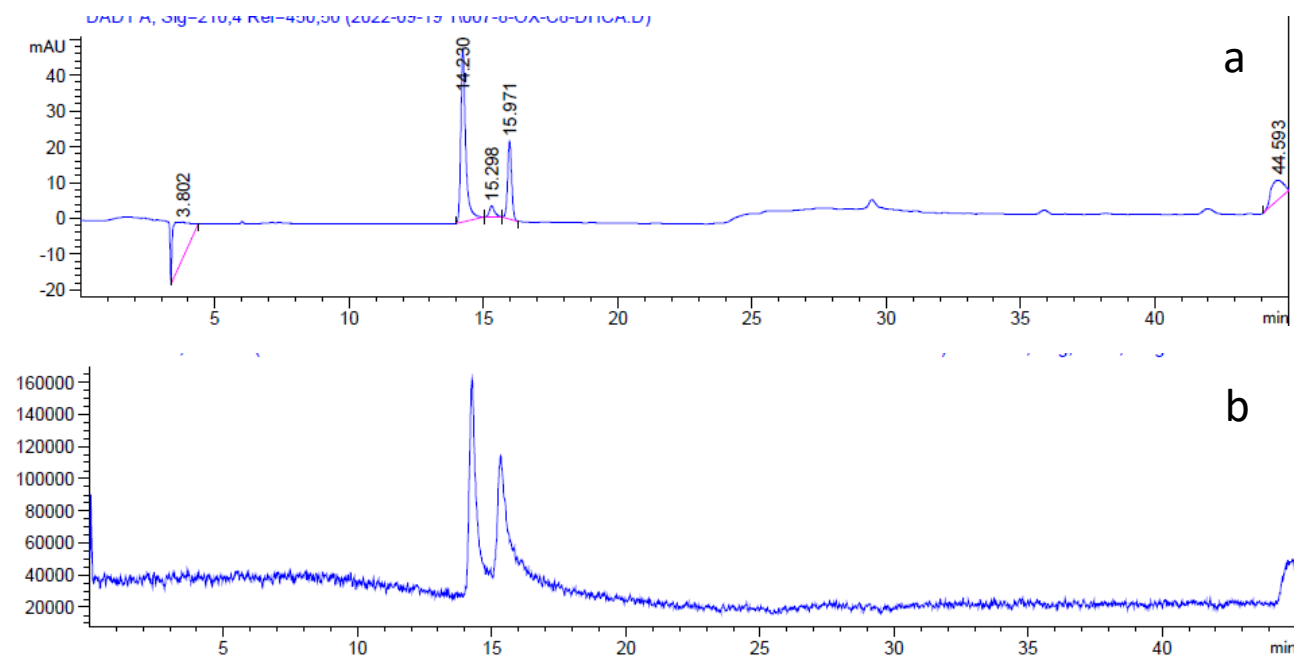


Figure A 1.8 Chromatogram of ox-C4-DHCA r.t.(6.64 min), in acetonitrile a) DAD 210 nm b) MS FULL SCAN NEGATIVE principle mass peaks: 235, 471 c) MS EXTRACTED NEG ION 235 d) MS FULL SCAN POSITIVE principle mass peaks: 473, 495, 513 e) MS EXTRACTED POS ION 295 f) MS EXTRACTED POS ION 513



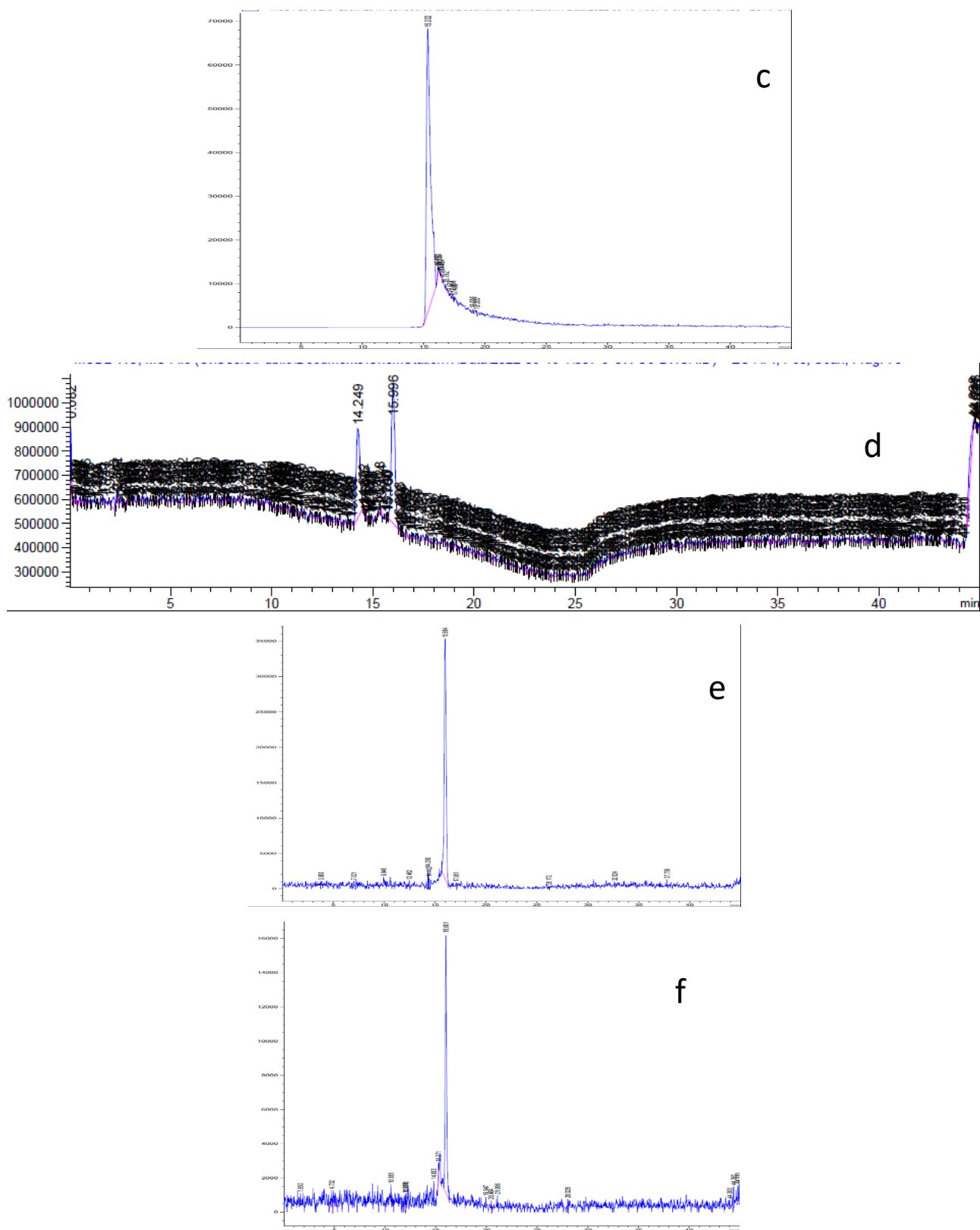


Figure A 1.9 Chromatogram of ox-C8-DHCA r.t.(14.20 min), in acetonitrile a) DAD 210 nm b) MS FULL SCAN NEGATIVE principle mass peaks: 293, 325 c) MS EXTRACTED NEG ION 291 d) MS FULL SCAN POSITIVE e) MS EXTRACTED POS ION 293 f) MS EXTRACTED POS ION 316

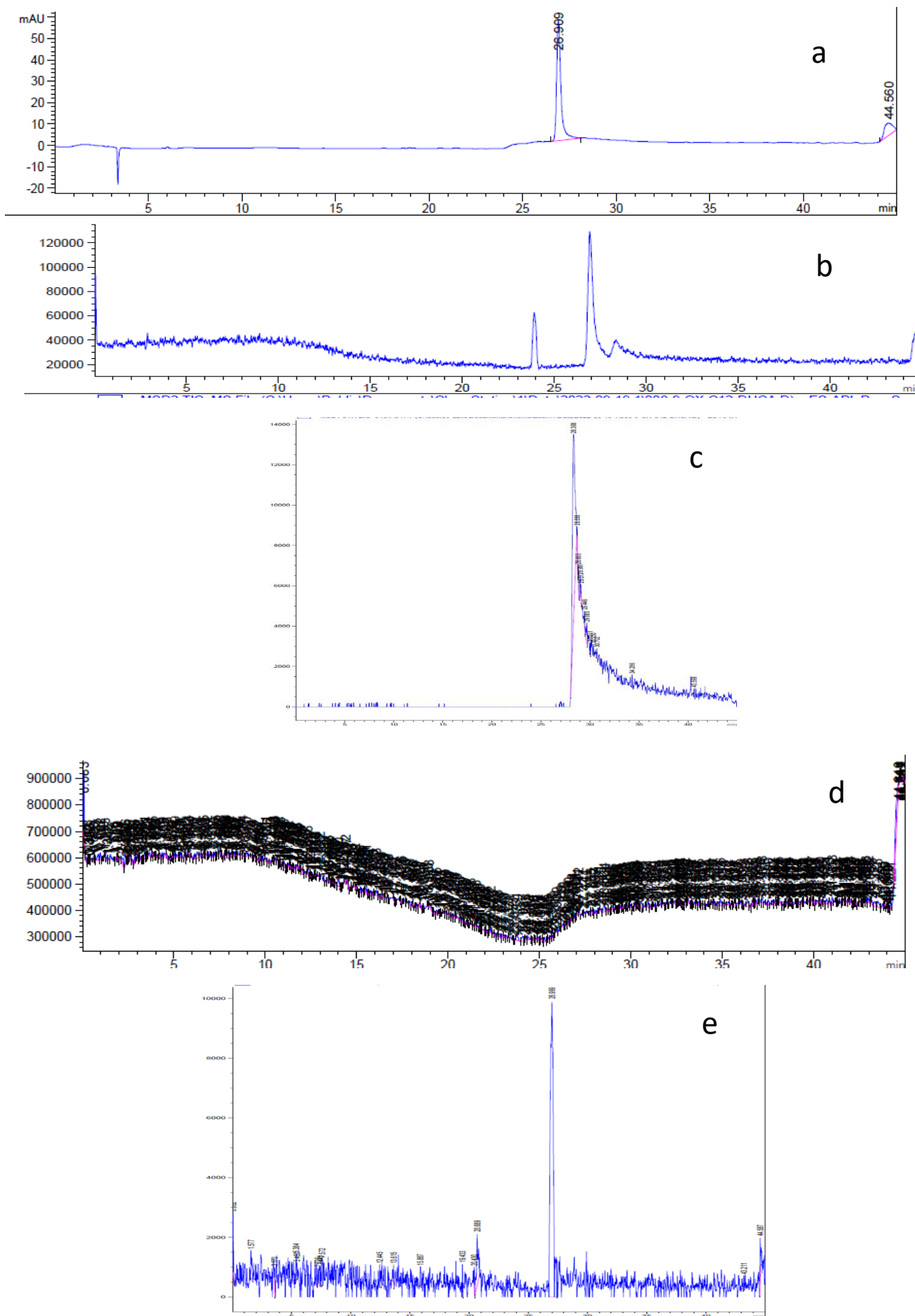


Figure A 1.9 Chromatogram of ox-C12-DHCA r.t.(26.99 min), in acetonitrile a) DAD 210 nm b) MS FULL SCAN NEGATIVE principle mass peaks: 293, 325 c) MS EXTRACTED NEG ION 291 d) MS FULL SCAN POSITIVE e) MS EXTRACTED POS ION 293

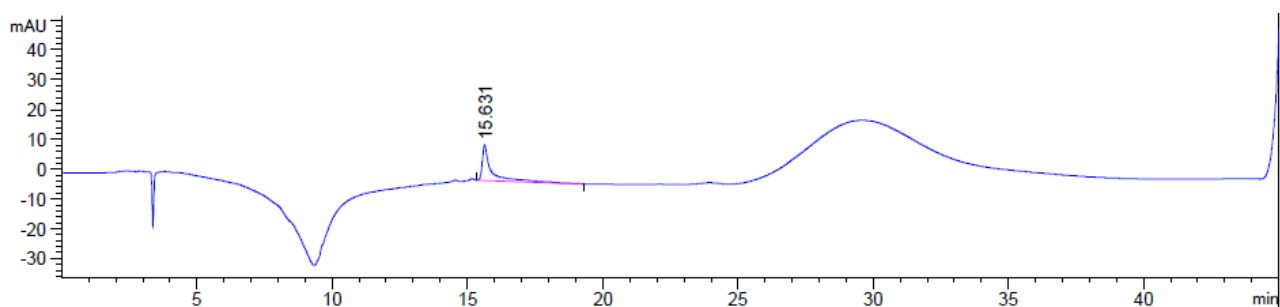


Figure A 1.10 Chromatogram of OX-C14-DHCA r.t.(15.63 min), in acetonitrile DAD 210 nm

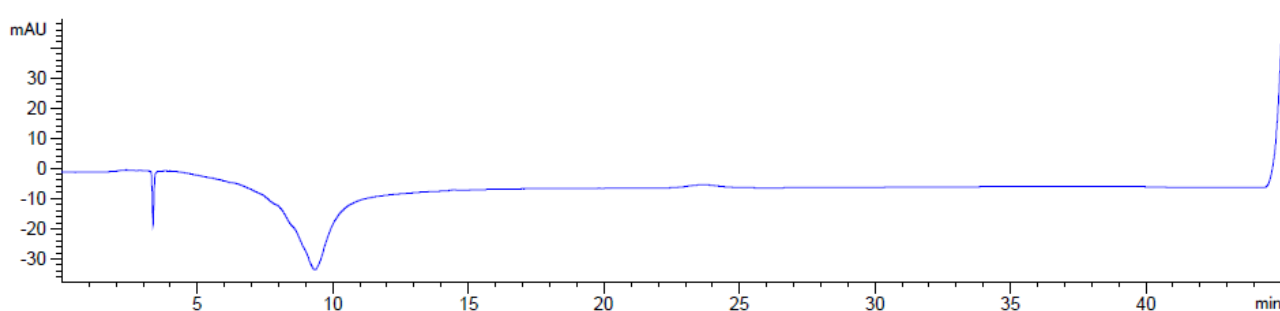


Figure A 1.11 Chromatogram of OX-C16-DHCA r.t.(24 min), in acetonitrile DAD 210 nm

NMR spectra

Sample 1
1H-NMR
CDCl₃
NT= 16

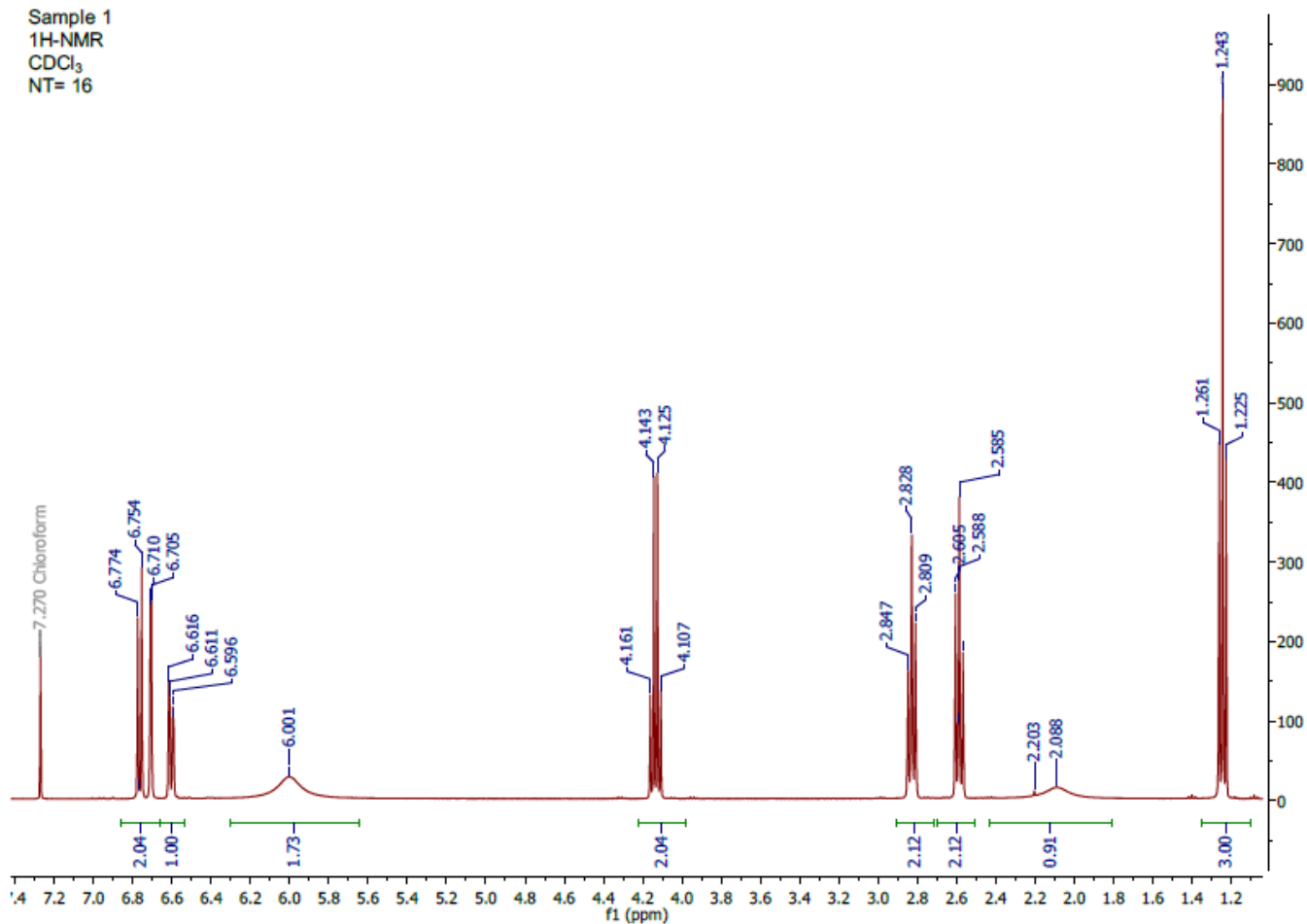


Figure A 1.12 ¹H-NMR spectrum of C2-DHCA (400 MHz, CDCl₃)

Sample 3
1H-NMR
CDCl₃
NT= 16

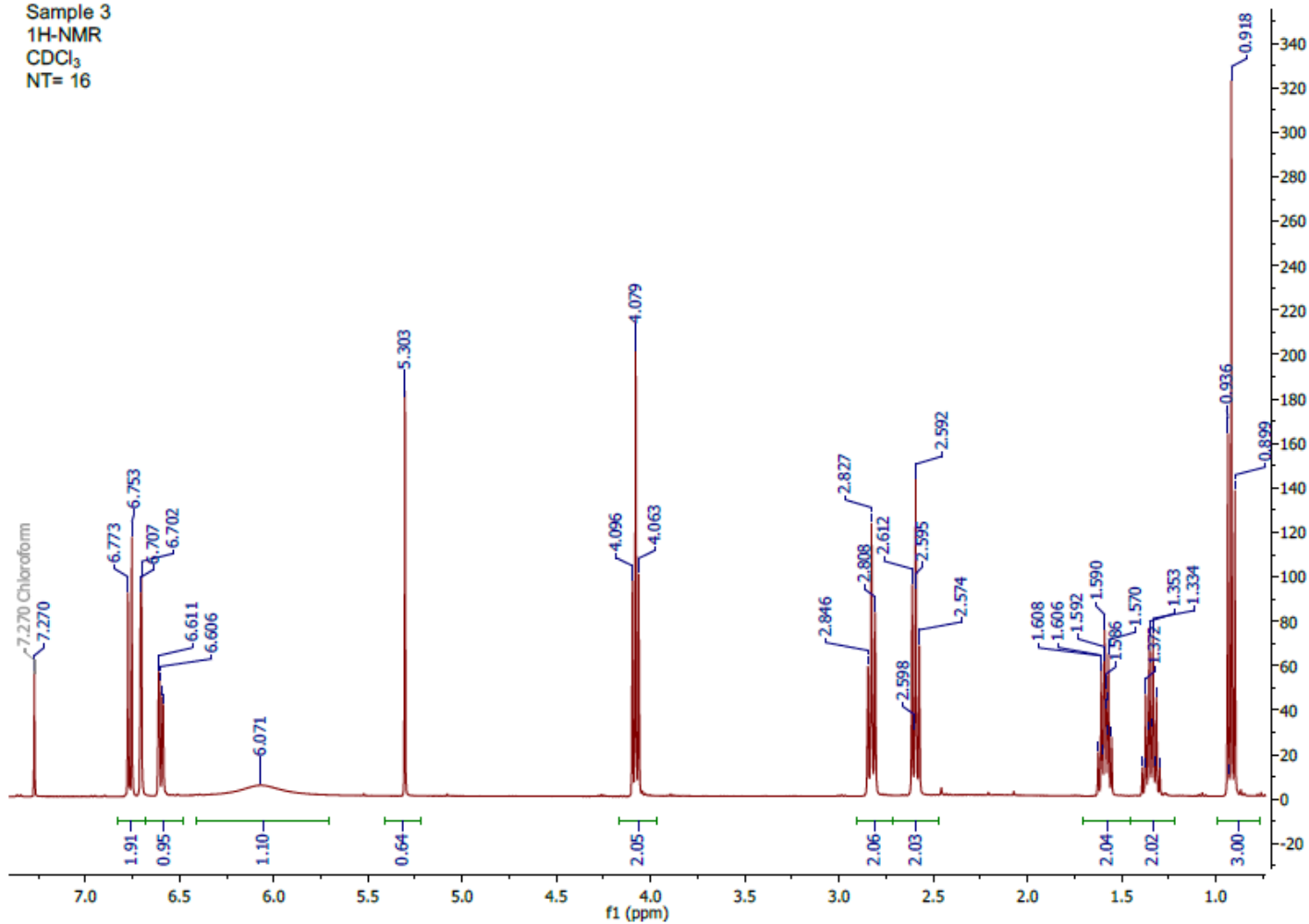


Figure A 1.13 ¹H-NMR spectrum of C4-DHCA (400 MHz, CDCl₃)

Sample 5
1H-NMR
CDCl₃
NT= 16

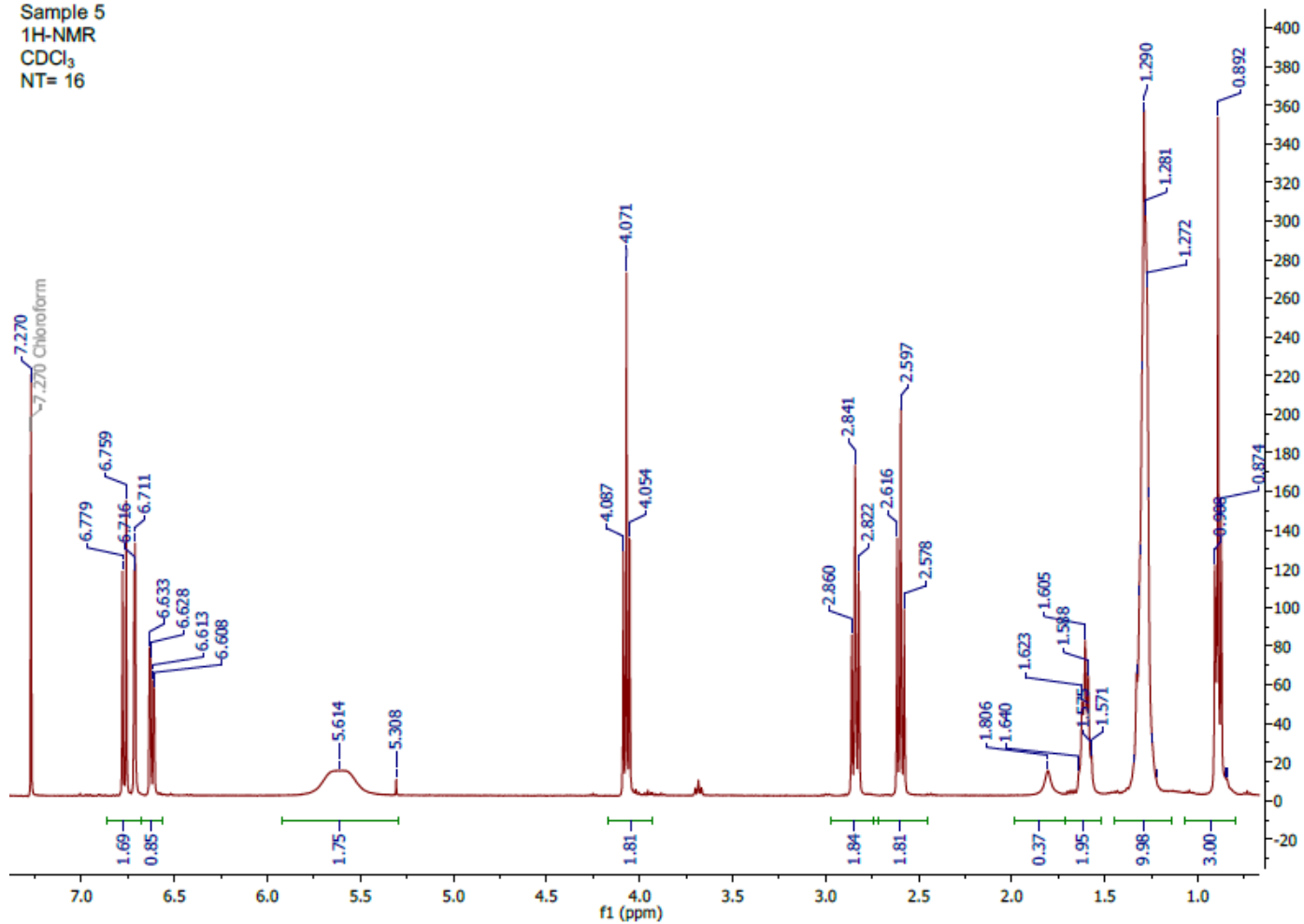


Figure A 1.14 ¹H-NMR spectrum of C8-DHCA (400 MHz, CDCl₃)

Sample 7
1H-NMR
CDCl₃
NT= 16

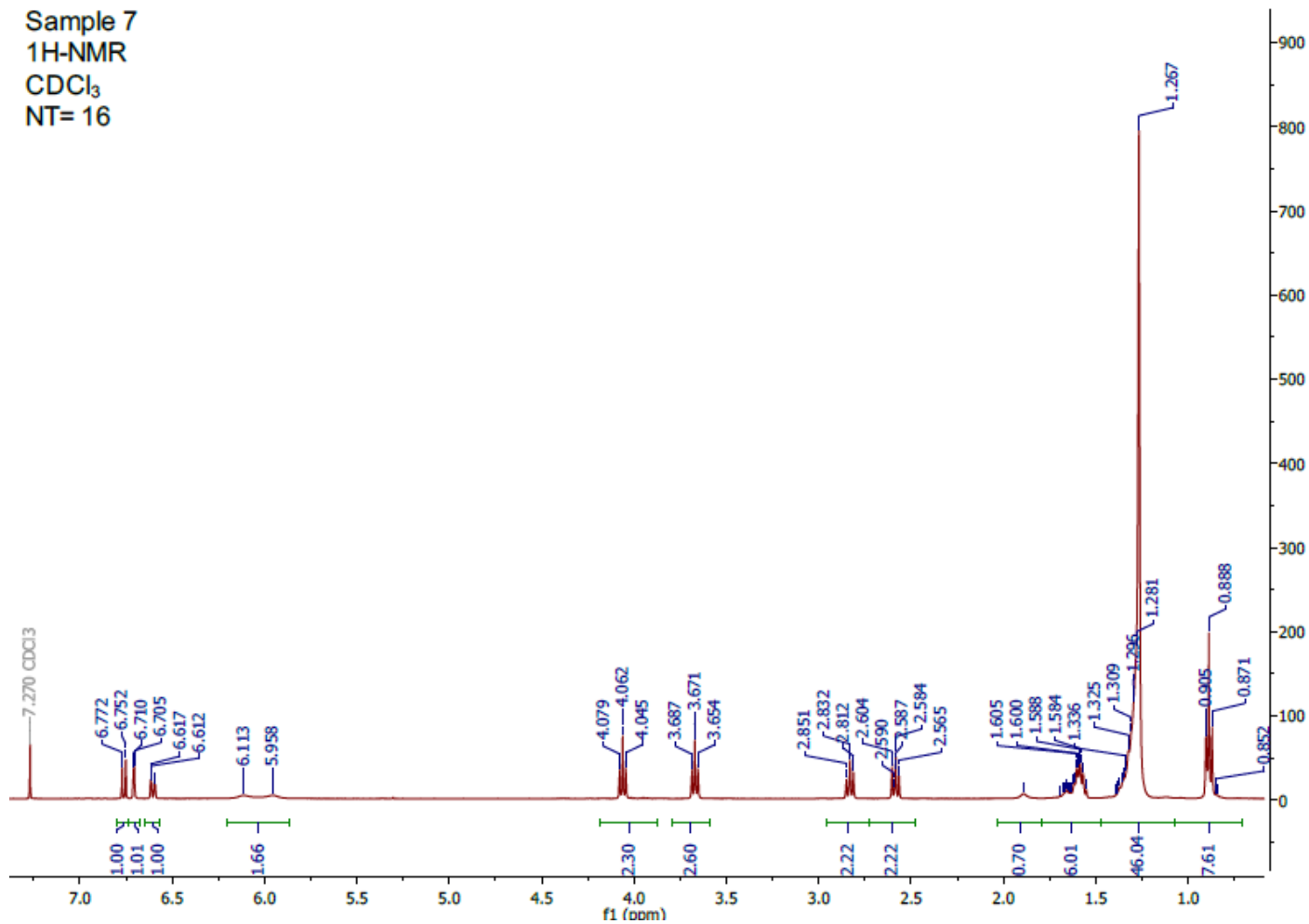


Figure A 1.15 ¹H-NMR spectrum of C12-DHCA (400 MHz, CDCl₃)

Sample 9
1H-NMR
CDCl₃
NT= 16

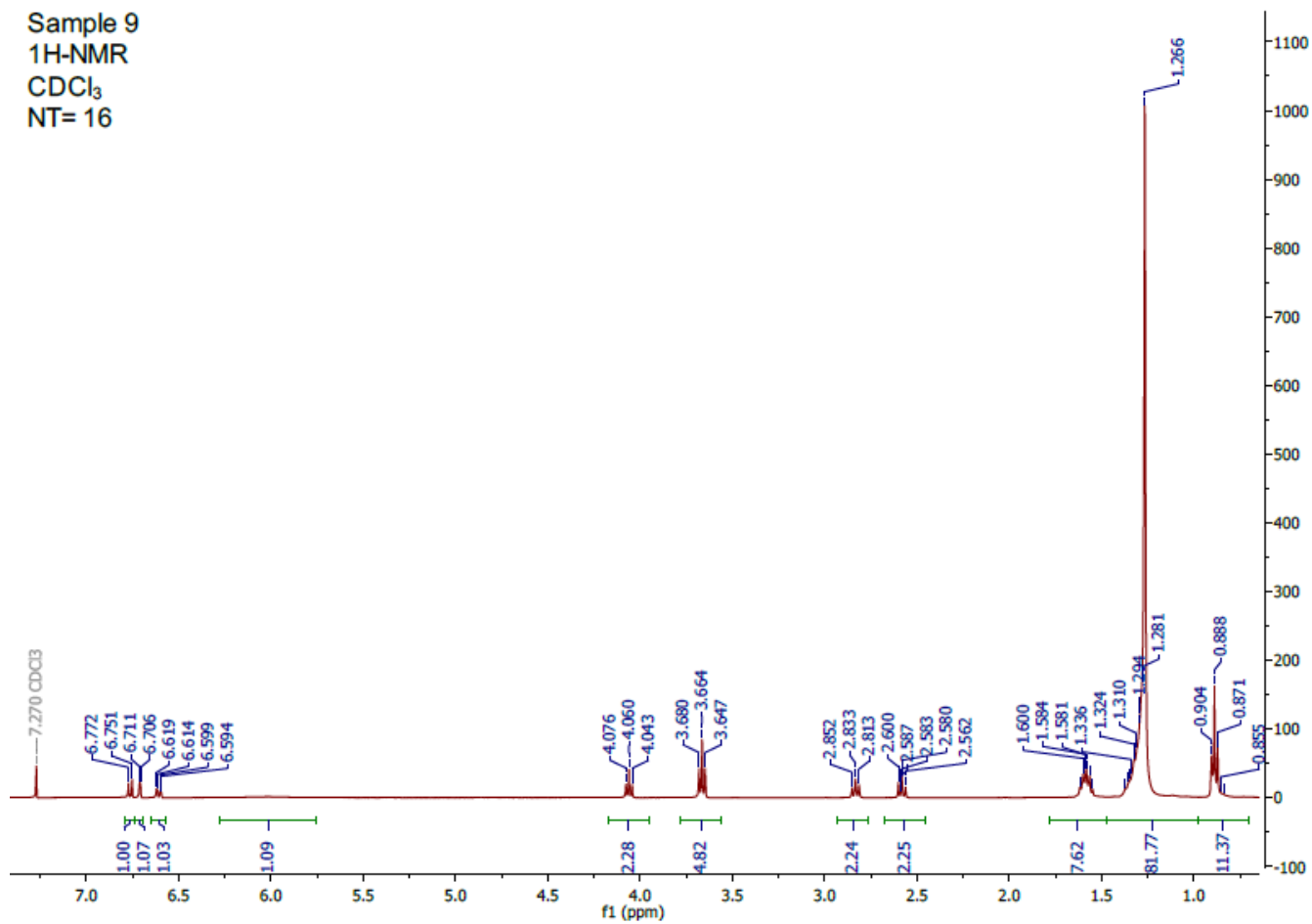


Figure A 1.16 ¹H-NMR spectrum of C14-DHCA (400 MHz, CDCl₃)

Sample 11
1H-NMR
CDCl₃
NT= 16

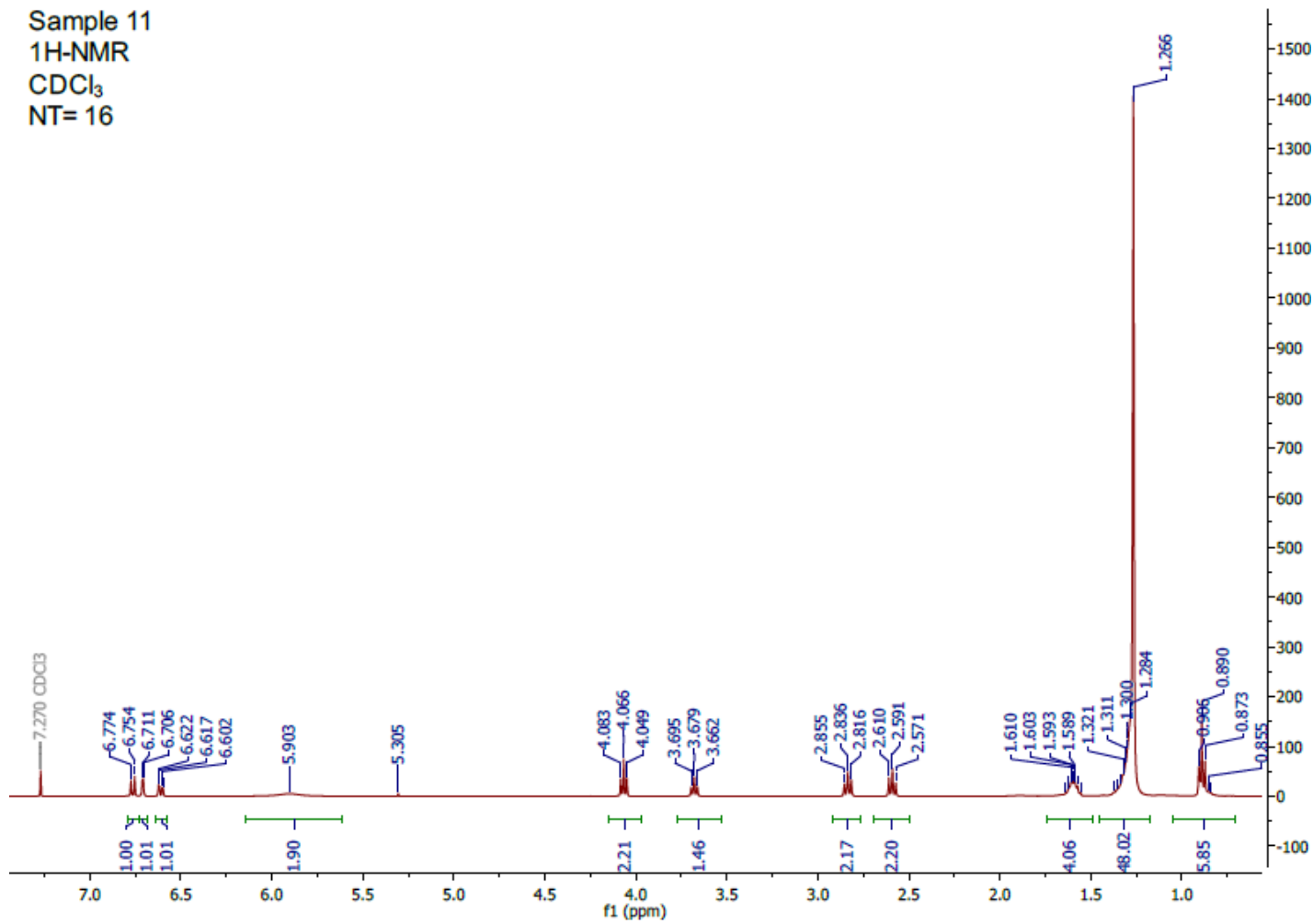


Figure A 1.17 ¹H-NMR spectrum of C16-DHCA (400 MHz, CDCl₃)

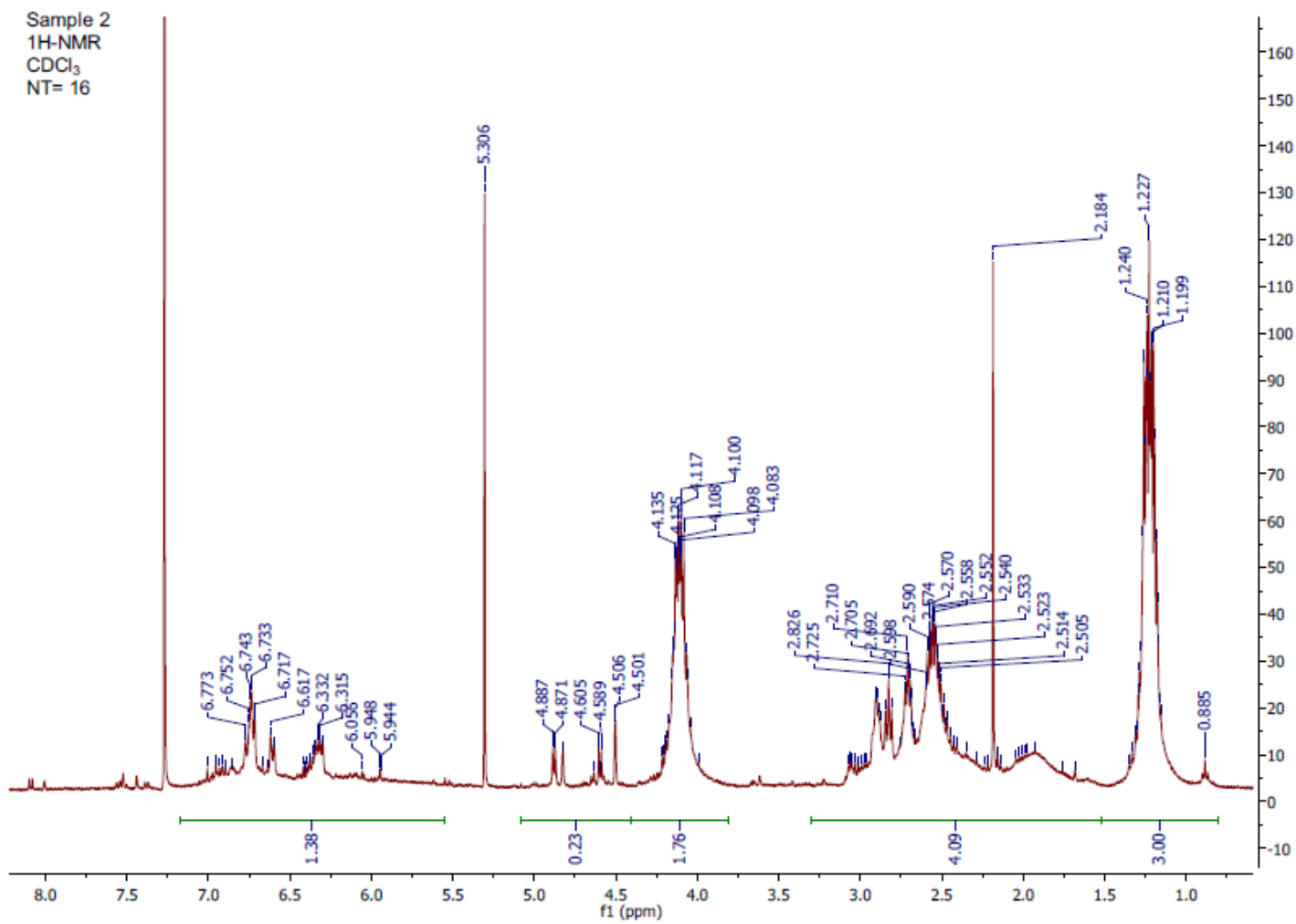


Figure A 1.18 ¹H-NMR spectrum of OX-C2-DHCA (400 MHz, CDCl₃)

Sample 2
13C-
NMR
CDCl₃
NT= 512

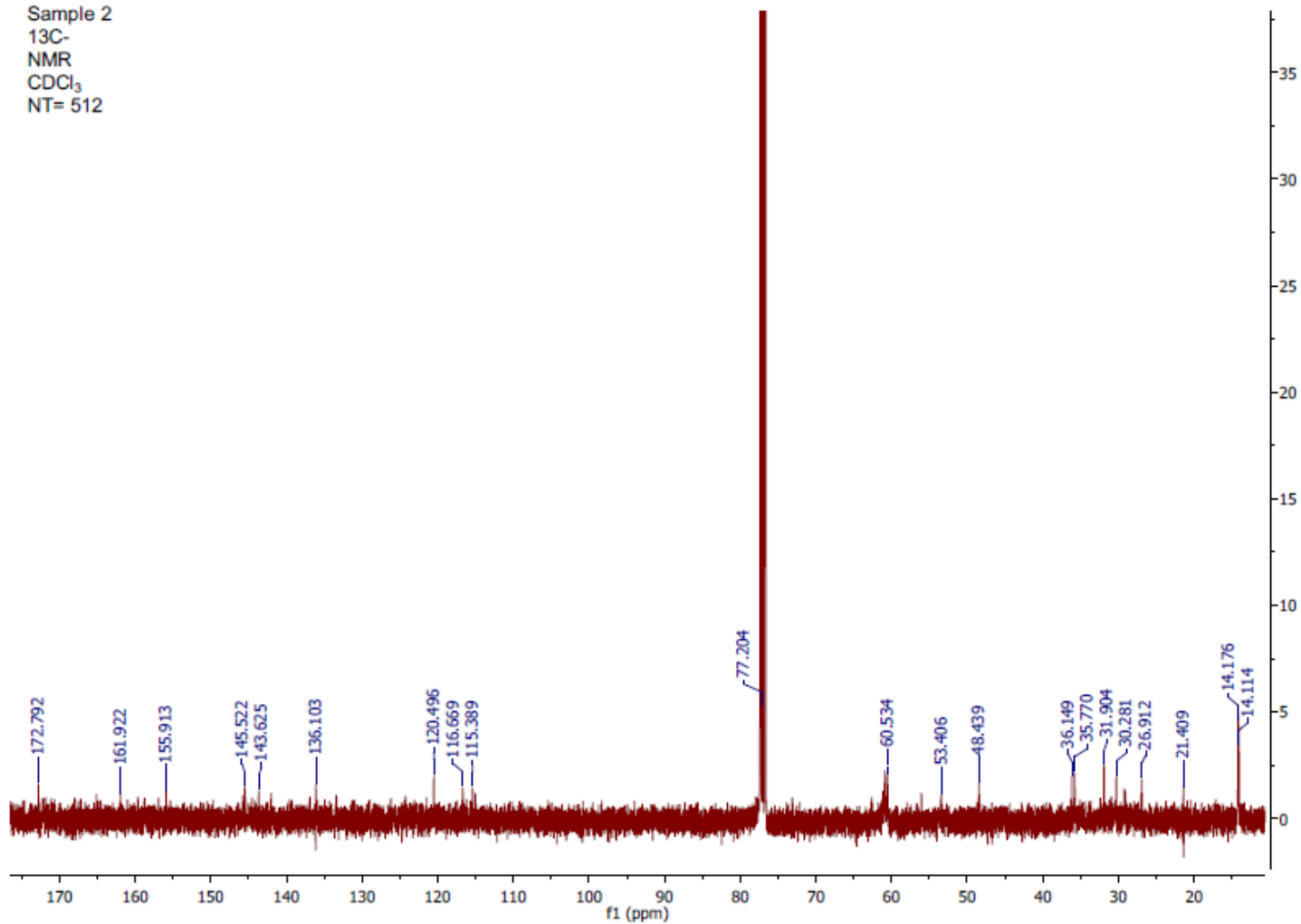


Figure A 1.19 ¹³C-NMR spectrum of OX-C2-DHCA (400 MHz, CDCl₃)

Sample 4
1H-NMR
CDCl₃
NT= 16

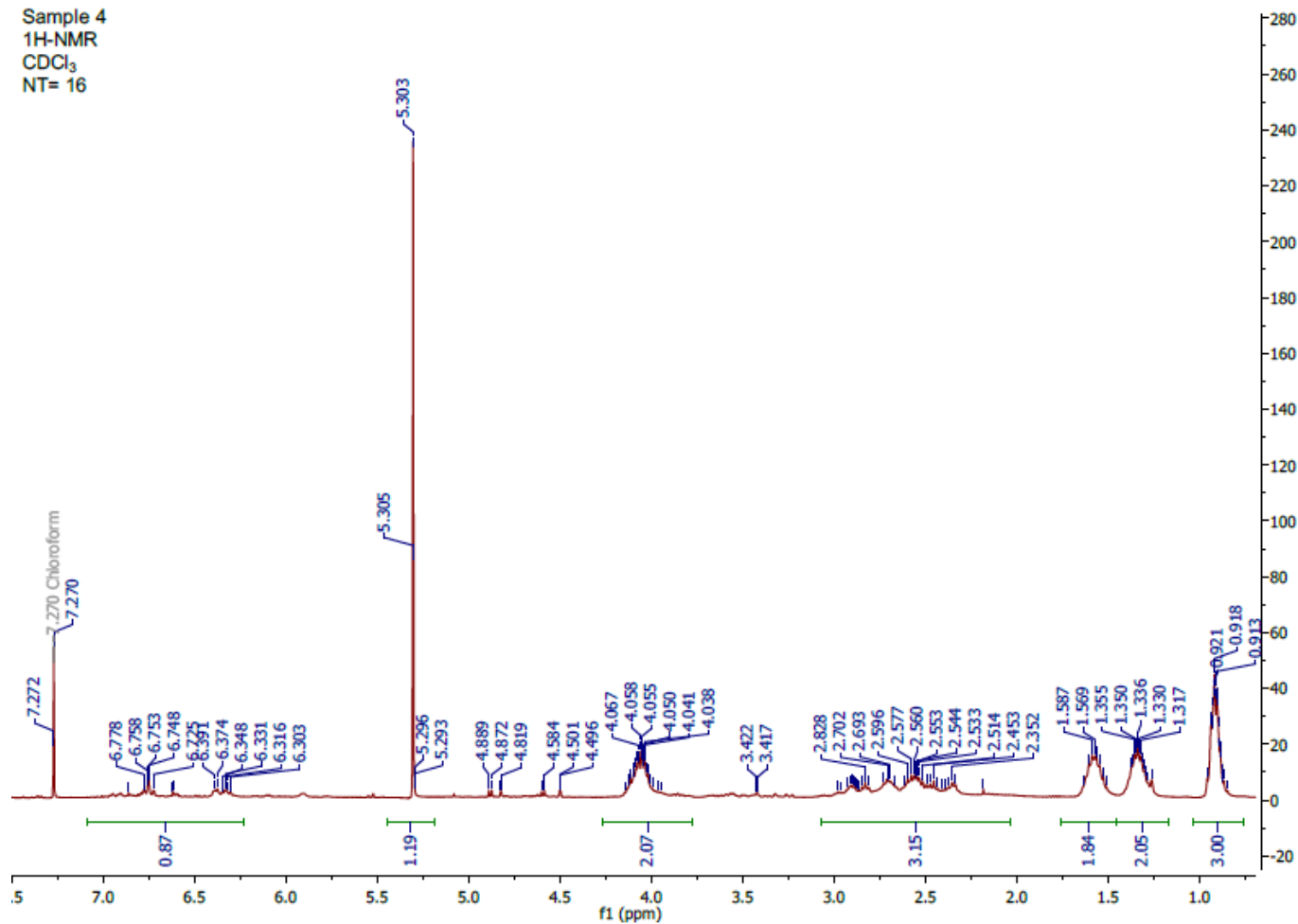


Figure A 1.20 ¹H-NMR spectrum of OX-C4-DHCA (400 MHz, CDCl₃)

Sample 4
13C-
NMR
CDCl₃
NT= 512

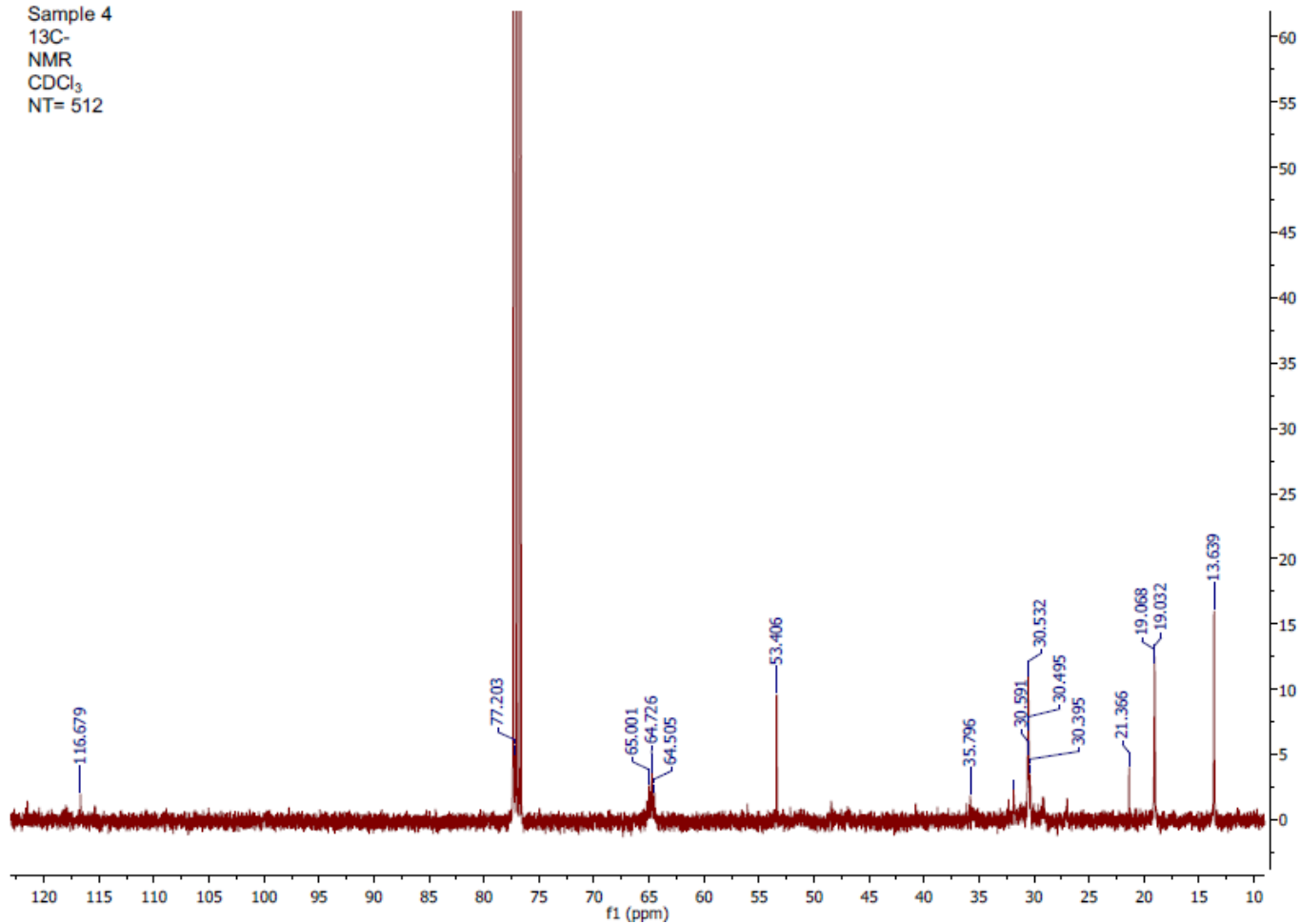


Figure A 1.21 13C-NMR spectrum of OX-C4-DHCA (400 MHz, CDCl₃)

Sample 6
1H-NMR
CDCl₃
NT= 16

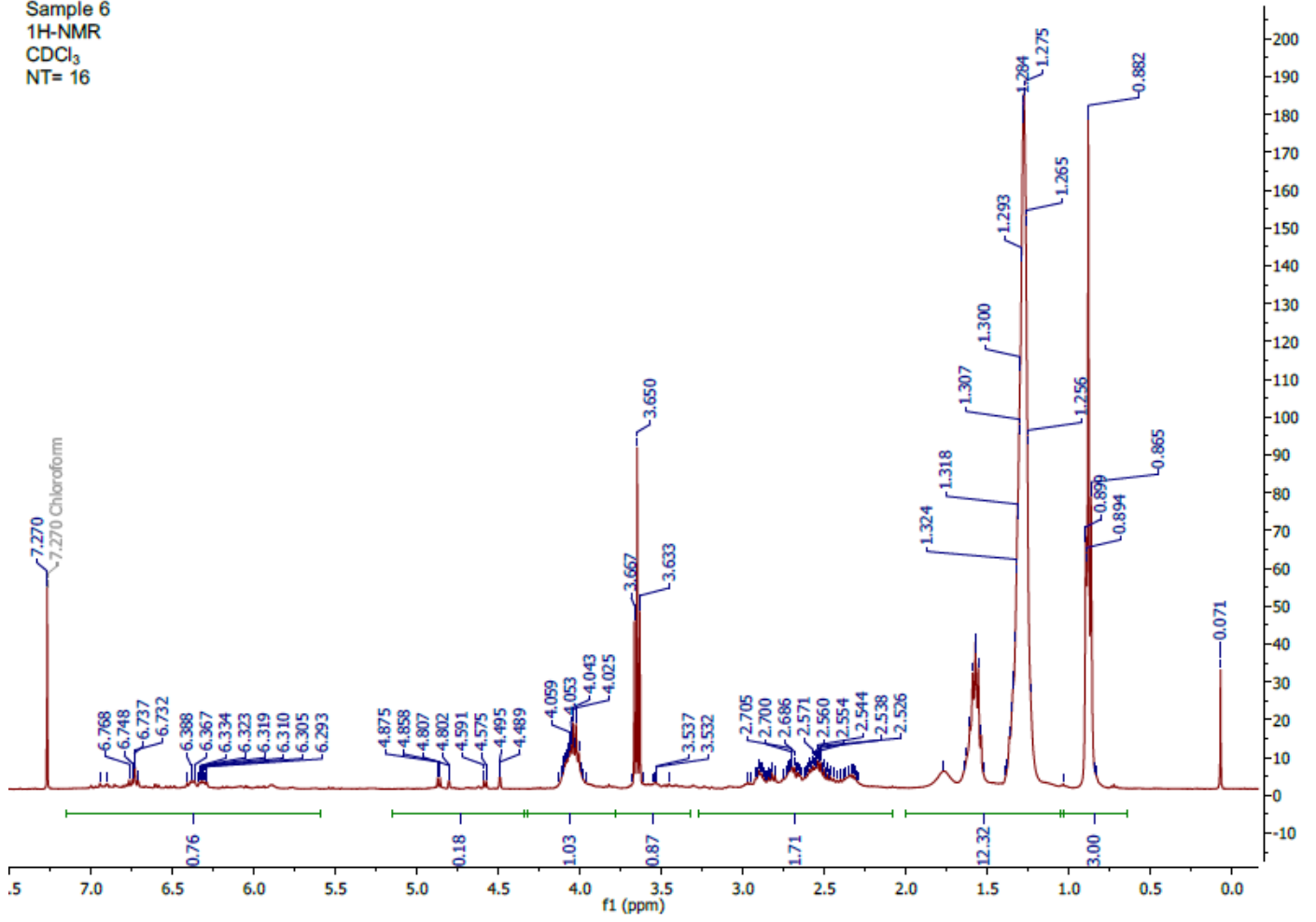


Figure A 1.22 ¹H-NMR spectrum of OX-C8-DHCA (400 MHz, CDCl₃)

Sample 6
13C-
NMR
CDCl₃
NT= 512

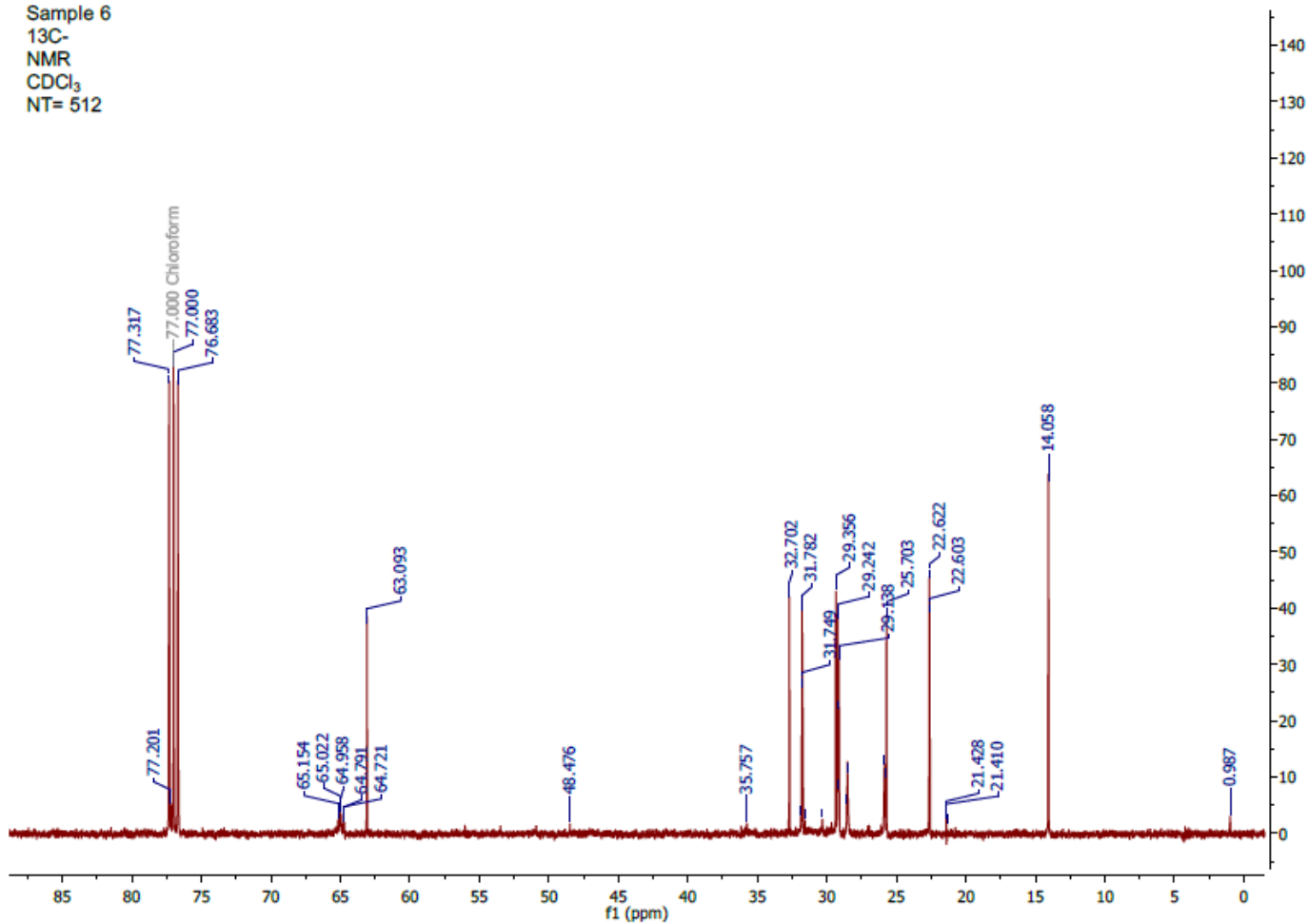


Figure A 1.23 13C-NMR spectrum of OX-C8-DHCA (400 MHz, CDCl₃)

Sample 8
1H-NMR
CDCl₃
NT= 16

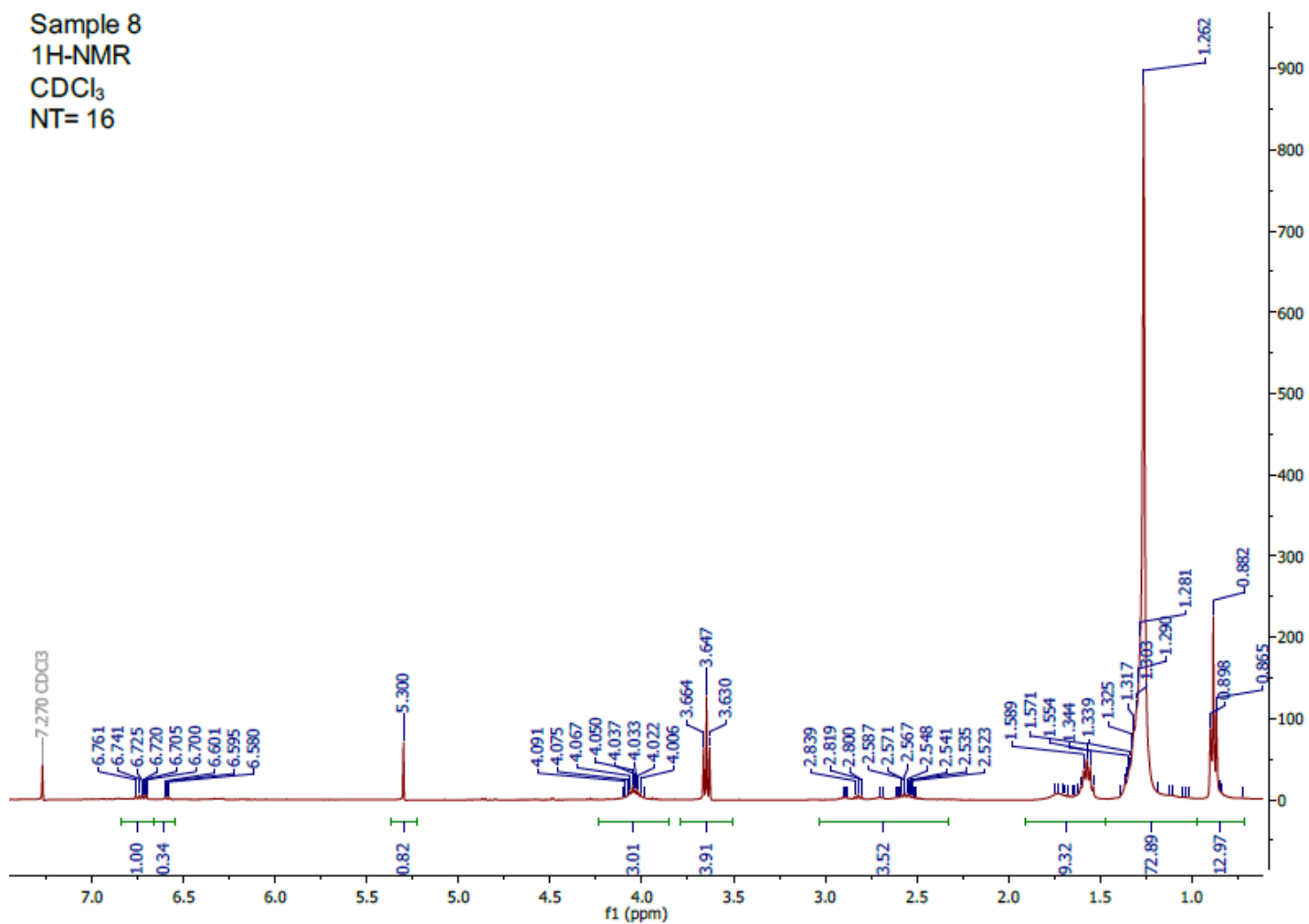


Figure A 1.24 ¹H-NMR spectrum of OX-C12-DHCA (400 MHz, CDCl₃)

Sample 8
13C-NMR
CDCl₃
NT= 512

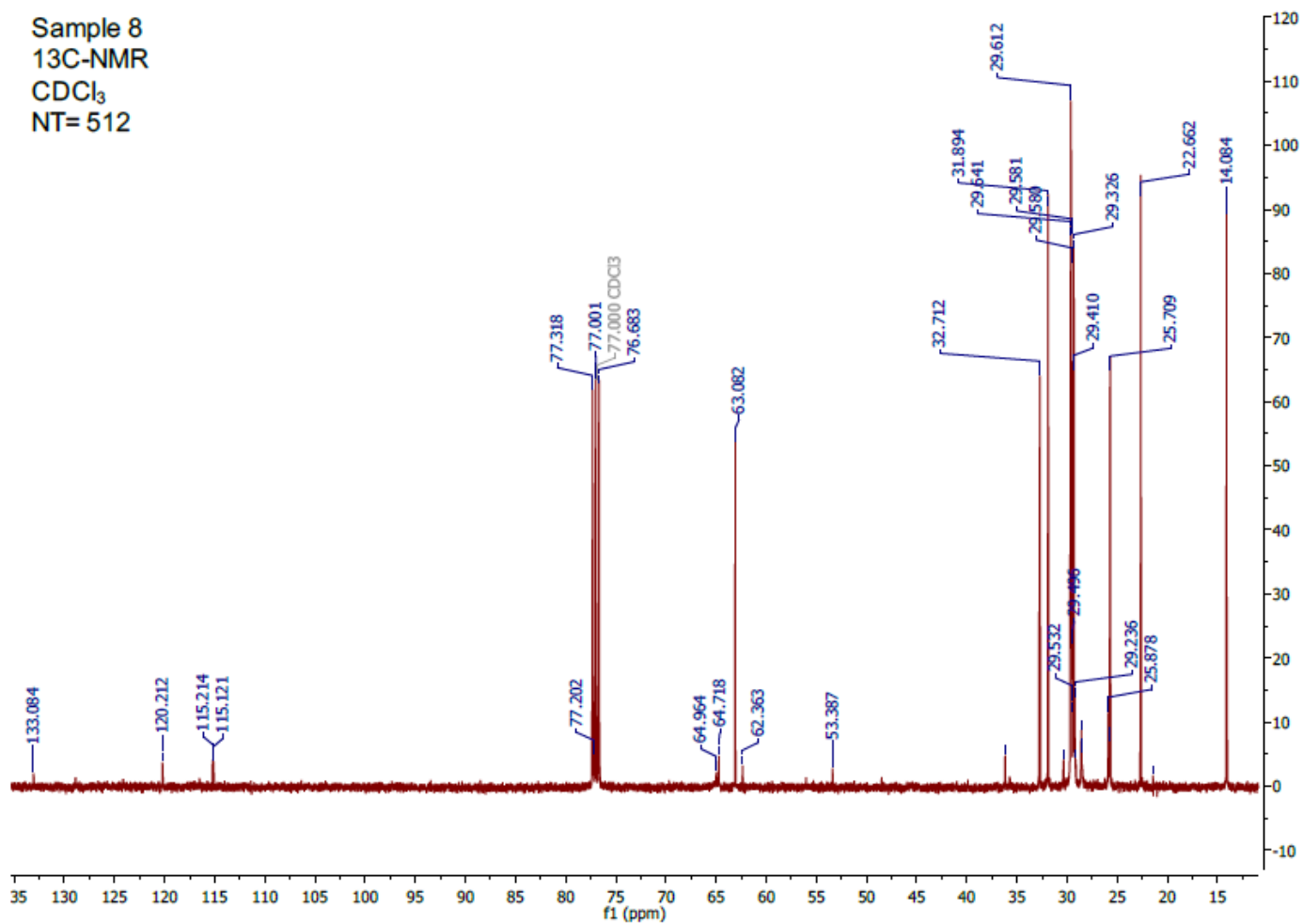


Figure A 1.25 13C-NMR spectrum of OX-C12-DHCA (400 MHz, CDCl₃)

Sample 10
1H-NMR
CDCl₃
NT= 16

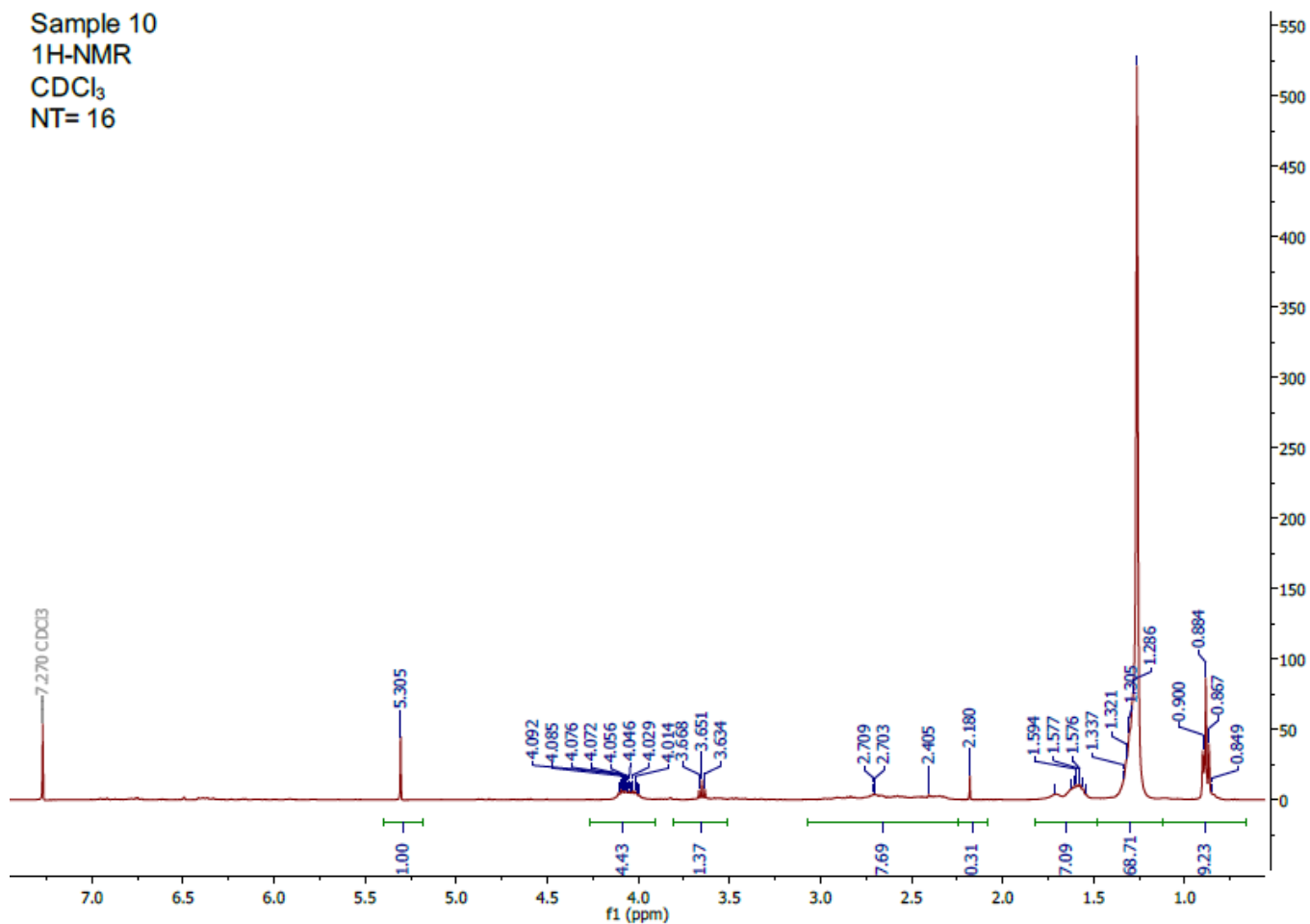


Figure A 1.26 ¹H-NMR spectrum of OX-C14-DHCA (400 MHz, CDCl₃)

Sample 10
13C-NMR
CDCl₃
NT= 512

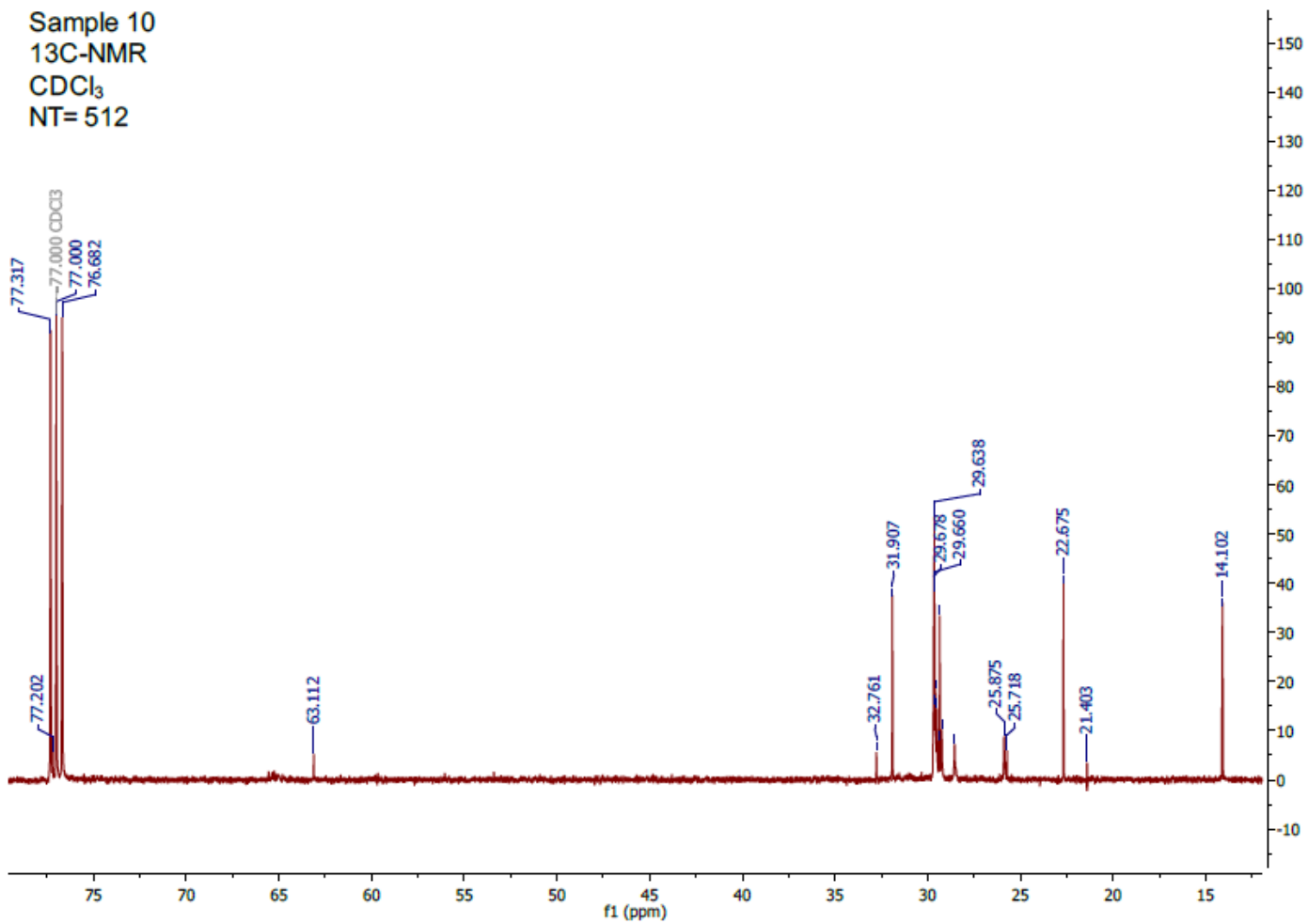


Figure A 1.27 13C-NMR spectrum of OX-C14-DHCA (400 MHz, CDCl₃)

Sample 12
1H-NMR
CDCl₃
NT= 16

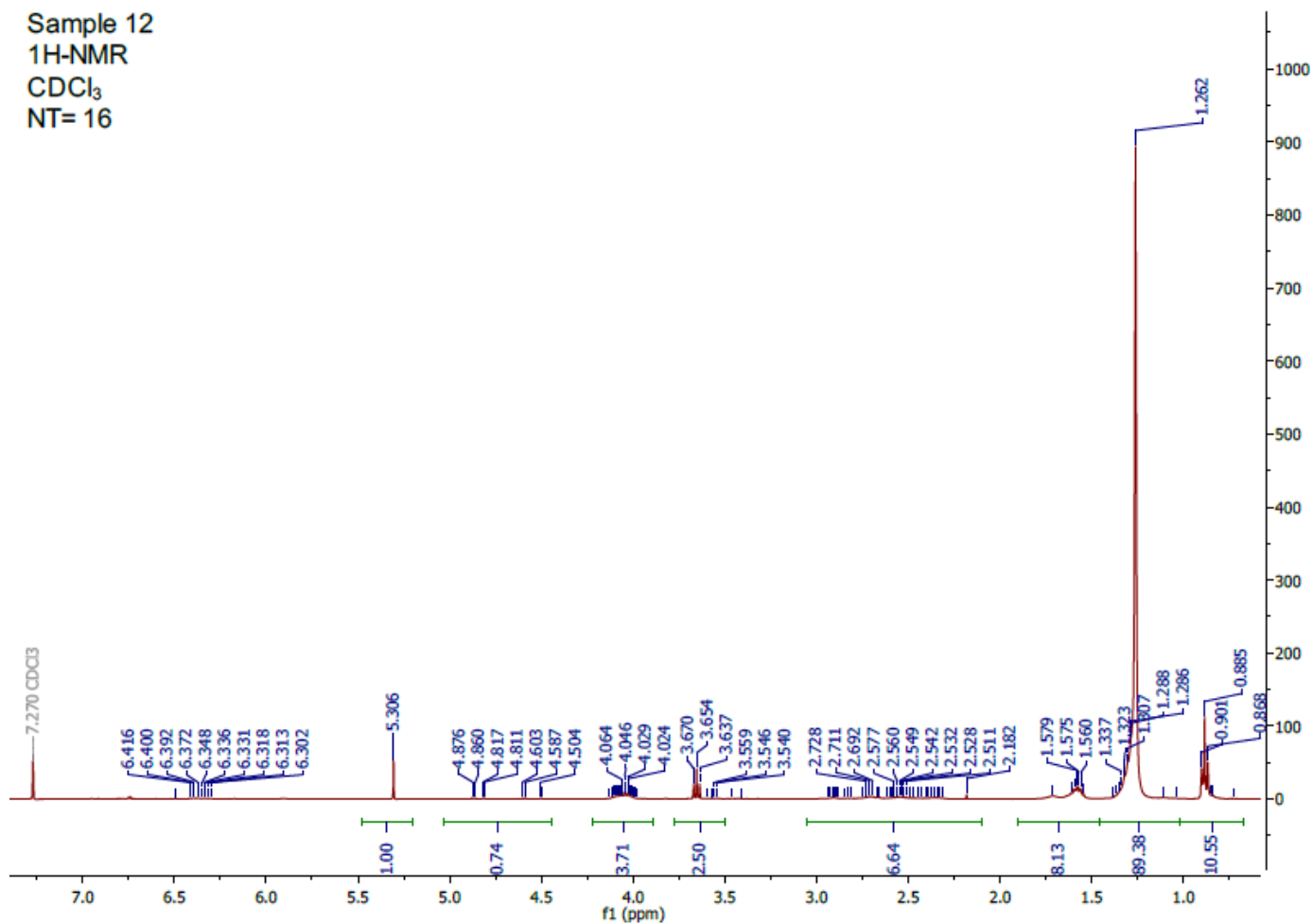


Figure A 1.28 ¹H-NMR spectrum of OX-C16-DHCA (400 MHz, CDCl₃)

Sample 12
13C-NMR
CDCl₃
NT= 512

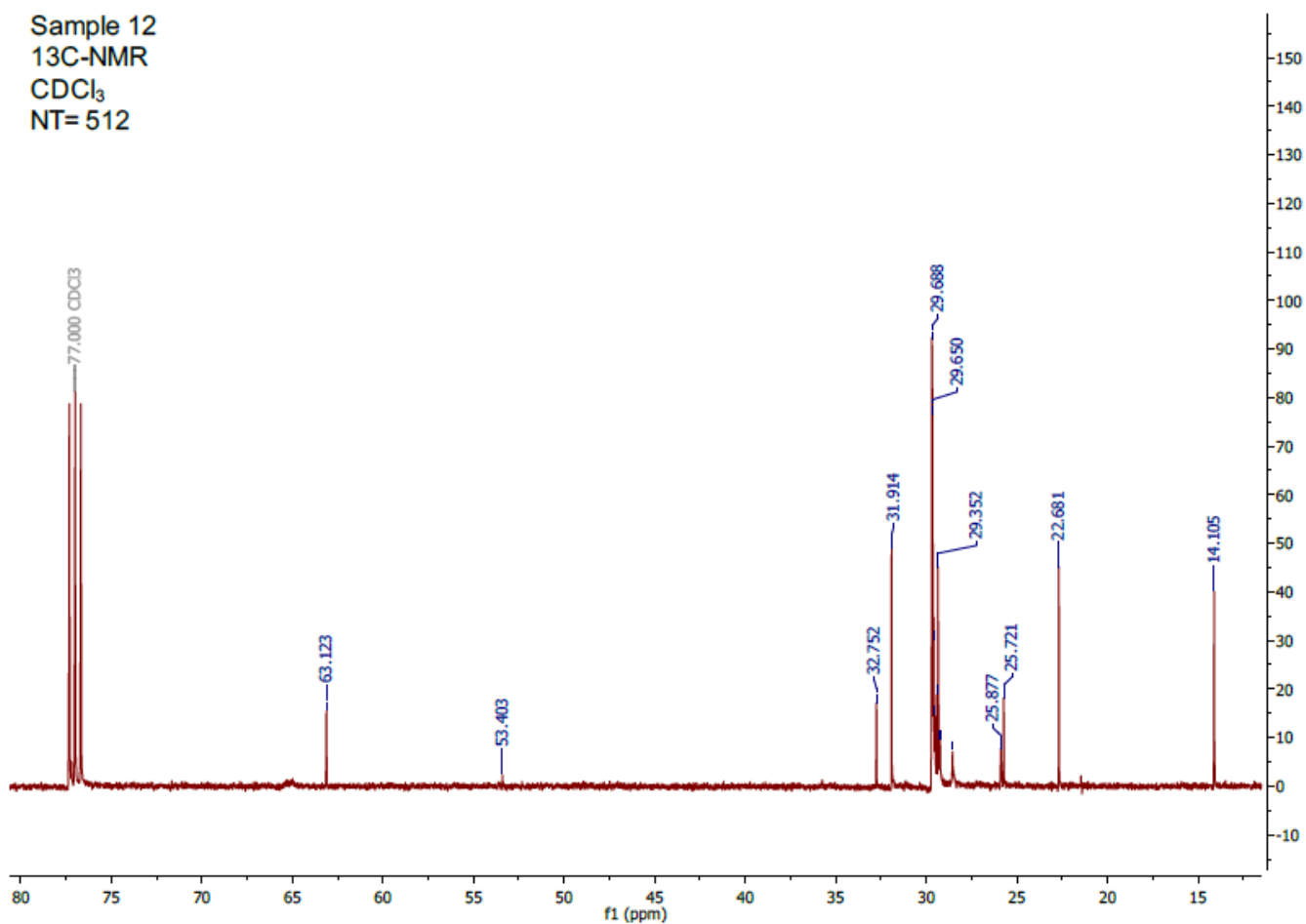


Figure A 1.29 13C-NMR spectrum of OX-C16-DHCA (400 MHz, CDCl₃)

References

- [1] M. Lucarini, G.F. Pedulli, Free radical intermediates in the inhibition of the autoxidation reaction, *Chem. Soc. Rev.* 39 (2010) 2106–2119. <https://doi.org/10.1039/B901838G>.
- [2] H. Sies, Hydrogen peroxide as a central redox signaling molecule in physiological oxidative stress: Oxidative eustress, *Redox Biology.* 11 (2017). <https://doi.org/10.1016/j.redox.2016.12.035>.
- [3] Y. Sheng, I.A. Abreu, D.E. Cabelli, M.J. Maroney, A.-F. Miller, M. Teixeira, J.S. Valentine, Superoxide Dismutases and Superoxide Reductases, *Chem. Rev.* 114 (2014) 3854–3918. <https://doi.org/10.1021/cr4005296>.
- [4] K.U. Ingold, D.A. Pratt, Advances in Radical-Trapping Antioxidant Chemistry in the 21st Century: A Kinetics and Mechanisms Perspective, *Chem. Rev.* 114 (2014) 9022–9046. <https://doi.org/10.1021/cr500226n>.
- [5] Peroxy radicals | Accounts of Chemical Research, (n.d.). <https://pubs.acs.org/doi/10.1021/ar50013a001> (accessed November 29, 2022).
- [6] C. Walling, Autoxidation, in: C.S. Foote, J.S. Valentine, A. Greenberg, J.F. Liebman (Eds.), *Active Oxygen in Chemistry*, Springer Netherlands, Dordrecht, 1995: pp. 24–65. https://doi.org/10.1007/978-94-007-0874-7_2.
- [7] E.N. Frankel, Chapter 10 - Oxidation in multiphase systems, in: E.N. Frankel (Ed.), *Lipid Oxidation (Second Edition)*, Woodhead Publishing, 2012: pp. 259–297. <https://doi.org/10.1533/9780857097927.259>.
- [8] Mechanisms of Decomposition of Initiators, in: *Handbook of Free Radical Initiators*, John Wiley & Sons, Ltd, 2003: pp. 1–15. <https://doi.org/10.1002/0471721476.ch1>.
- [9] J. Werber, Y.J. Wang, M. Milligan, X. Li, J.A. Ji, Analysis of 2,2'-Azobis (2-Amidinopropane) Dihydrochloride Degradation and Hydrolysis in Aqueous Solutions, *JPharmSci.* 100 (2011) 3307–3315. <https://doi.org/10.1002/jps.22578>.
- [10] B. Maillard, K.U. Ingold, J.C. Scaiano, Rate constants for the reactions of free radicals with oxygen in solution, *J. Am. Chem. Soc.* 105 (1983) 5095–5099. <https://doi.org/10.1021/ja00353a039>.
- [11] M. Lucarini, G.F. Pedulli, L. Valgimigli, Do Peroxyl Radicals Obey the Principle That Kinetic Solvent Effects on H-Atom Abstraction Are Independent of the Nature of the Abstracting Radical?, *J. Org. Chem.* 63 (1998) 4497–4499. <https://doi.org/10.1021/jo971944i>.
- [12] Absolute Rate Constants for Hydrocarbon Autoxidation. XXI. Activation Energies for Propagation and the Correlation of Propagation Rate Constants with Carbon–Hydrogen Bond Strengths, (n.d.). <https://cdnsiencepub.com/doi/abs/10.1139/v72-365> (accessed December 2, 2022).
- [13] K.U. Ingold, Rate constants for some reactions of oxy radicals, *Pure and Applied Chemistry.* 15 (1967) 49–68. <https://doi.org/10.1351/pac196715010049>.
- [14] L. Valgimigli, D.A. Pratt, Antioxidants in Chemistry and Biology, in: *Encyclopedia of Radicals in Chemistry, Biology and Materials*, John Wiley & Sons, Ltd, 2012. <https://doi.org/10.1002/9781119953678.rad055>.
- [15] K.U. Ingold, Inhibition of the Autoxidation of Organic Substances in the Liquid Phase., *Chem. Rev.* 61 (1961) 563–589. <https://doi.org/10.1021/cr60214a002>.
- [16] R. Amorati, L. Valgimigli, Modulation of the antioxidant activity of phenols by non-covalent interactions, *Org. Biomol. Chem.* 10 (2012) 4147–4158. <https://doi.org/10.1039/C2OB25174D>.
- [17] J.D. Lambert, R.J. Elias, The antioxidant and pro-oxidant activities of green tea polyphenols: a role in cancer prevention, *Arch Biochem Biophys.* 501 (2010) 65–72. <https://doi.org/10.1016/j.abb.2010.06.013>.
- [18] L. Valgimigli, D.A. Pratt, Maximizing the Reactivity of Phenolic and Aminic Radical-Trapping Antioxidants: Just Add Nitrogen!, *Acc. Chem. Res.* 48 (2015) 966–975. <https://doi.org/10.1021/acs.accounts.5b00035>.
- [19] D.A. Pratt, G.A. DiLabio, G. Brigati, G.F. Pedulli, L. Valgimigli, 5-Pyrimidinols: Novel Chain-Breaking Antioxidants More Effective than Phenols, *J. Am. Chem. Soc.* 123 (2001) 4625–4626. <https://doi.org/10.1021/ja005679l>.
- [20] G.W. Burton, K.U. Ingold, Vitamin E: application of the principles of physical organic chemistry to the exploration of its structure and function, *Acc. Chem. Res.* 19 (1986) 194–201. <https://doi.org/10.1021/ar00127a001>.

- [21] L. Valgimigli, R. Amorati, M.G. Fumo, G.A. DiLabio, G.F. Pedulli, K.U. Ingold, D.A. Pratt, The Unusual Reaction of Semiquinone Radicals with Molecular Oxygen, *J. Org. Chem.* 73 (2008) 1830–1841. <https://doi.org/10.1021/jo7024543>.
- [22] R. Amorati, L. Valgimigli, Advantages and limitations of common testing methods for antioxidants, *Free Radical Research.* 49 (2015) 633–649. <https://doi.org/10.3109/10715762.2014.996146>.
- [23] R. Amorati, A. Baschieri, L. Valgimigli, Measuring Antioxidant Activity in Bioorganic Samples by the Differential Oxygen Uptake Apparatus: Recent Advances, *Journal of Chemistry.* 2017 (2017) e6369358. <https://doi.org/10.1155/2017/6369358>.
- [24] E.T. Denisov, I.V. Khudyakov, Mechanisms of action and reactivities of the free radicals of inhibitors, *Chem. Rev.* 87 (1987) 1313–1357. <https://doi.org/10.1021/cr00082a003>.
- [25] R. Amorati, F. Ferroni, M. Lucarini, G.F. Pedulli, L. Valgimigli, A Quantitative Approach to the Recycling of α -Tocopherol by Coantioxidants, *J. Org. Chem.* 67 (2002) 9295–9303. <https://doi.org/10.1021/jo026501f>.
- [26] J.J. Warren, T.A. Tronic, J.M. Mayer, The Thermochemistry of Proton-Coupled Electron Transfer Reagents and its Implications, *Chem Rev.* 110 (2010) 6961–7001. <https://doi.org/10.1021/cr100085k>.
- [27] J. Cedrowski, G. Litwinienko, A. Baschieri, R. Amorati, Hydroperoxyl Radicals (HOO \cdot): Vitamin E Regeneration and H-Bond Effects on the Hydrogen Atom Transfer, *Chemistry – A European Journal.* 22 (2016) 16441–16445. <https://doi.org/10.1002/chem.201603722>.
- [28] A. Baschieri, L. Valgimigli, S. Gabbanini, G.A. DiLabio, E. Romero-Montalvo, R. Amorati, Extremely Fast Hydrogen Atom Transfer between Nitroxides and HOO \cdot Radicals and Implication for Catalytic Coantioxidant Systems, *J. Am. Chem. Soc.* 140 (2018) 10354–10362. <https://doi.org/10.1021/jacs.8b06336>.
- [29] A. Baschieri, R. Amorati, L. Valgimigli, L. Sambri, 1-Methyl-1,4-cyclohexadiene as a Traceless Reducing Agent for the Synthesis of Catechols and Hydroquinones, *J. Org. Chem.* 84 (2019) 13655–13664. <https://doi.org/10.1021/acs.joc.9b01898>.
- [30] Hydrogen Atom Transfer from HOO \cdot to ortho-Quinones Explains the Antioxidant Activity of Polydopamine - Guo - 2021 - *Angewandte Chemie International Edition - Wiley Online Library*, (n.d.). <https://onlinelibrary-wiley-com.ezproxy.unibo.it/doi/full/10.1002/anie.202101033> (accessed December 9, 2022).
- [31] Y. Guo, A. Baschieri, R. Amorati, L. Valgimigli, Synergic antioxidant activity of γ -terpinene with phenols and polyphenols enabled by hydroperoxyl radicals, *Food Chemistry.* 345 (2021) 128468. <https://doi.org/10.1016/j.foodchem.2020.128468>.
- [32] S.J. Dixon, K.M. Lemberg, M.R. Lamprecht, R. Skouta, E.M. Zaitsev, C.E. Gleason, D.N. Patel, A.J. Bauer, A.M. Cantley, W.S. Yang, B. Morrison, B.R. Stockwell, Ferroptosis: an iron-dependent form of nonapoptotic cell death, *Cell.* 149 (2012) 1060–1072. <https://doi.org/10.1016/j.cell.2012.03.042>.
- [33] D. Tang, X. Chen, R. Kang, G. Kroemer, Ferroptosis: molecular mechanisms and health implications, *Cell Res.* 31 (2021) 107–125. <https://doi.org/10.1038/s41422-020-00441-1>.
- [34] X. Jiang, B.R. Stockwell, M. Conrad, Ferroptosis: mechanisms, biology and role in disease, *Nat Rev Mol Cell Biol.* 22 (2021) 266–282. <https://doi.org/10.1038/s41580-020-00324-8>.
- [35] J. Li, F. Cao, H. Yin, Z. Huang, Z. Lin, N. Mao, B. Sun, G. Wang, Ferroptosis: past, present and future, *Cell Death Dis.* 11 (2020) 1–13. <https://doi.org/10.1038/s41419-020-2298-2>.
- [36] D. Tang, G. Kroemer, Ferroptosis, *Current Biology.* 30 (2020) R1292–R1297. <https://doi.org/10.1016/j.cub.2020.09.068>.
- [37] B.R. Stockwell, X. Jiang, The Chemistry and Biology of Ferroptosis, *Cell Chem Biol.* 27 (2020) 365–375. <https://doi.org/10.1016/j.chembiol.2020.03.013>.
- [38] R. Shah, K. Margison, D.A. Pratt, The Potency of Diarylamine Radical-Trapping Antioxidants as Inhibitors of Ferroptosis Underscores the Role of Autoxidation in the Mechanism of Cell Death, *ACS Chem. Biol.* 12 (2017) 2538–2545. <https://doi.org/10.1021/acscchembio.7b00730>.
- [39] S. R, F. La, Z. O, V.K. Atm, P. Da, Beyond DPPH: Use of Fluorescence-Enabled Inhibited Autoxidation to Predict Oxidative Cell Death Rescue, *Cell Chemical Biology.* 26 (2019). <https://doi.org/10.1016/j.chembiol.2019.09.007>.
- [40] J. Helberg, D.A. Pratt, Autoxidation vs. antioxidants – the fight for forever, *Chem. Soc. Rev.* 50 (2021) 7343–7358. <https://doi.org/10.1039/D1CS00265A>.
- [41] A.-M. Vučković, R. Venerando, E. Tibaldi, V. Bosello Travain, A. Roveri, L. Bordin, G. Miotto, G. Cozza, S. Toppo, M. Maiorino, F. Ursini, Aerobic pyruvate metabolism sensitizes cells to ferroptosis

- primed by GSH depletion, *Free Radical Biology and Medicine*. 167 (2021) 45–53. <https://doi.org/10.1016/j.freeradbiomed.2021.02.045>.
- [42] J.-F. Poon, O. Zilka, D.A. Pratt, Potent Ferroptosis Inhibitors Can Catalyze the Cross-Dismutation of Phospholipid-Derived Peroxyl Radicals and Hydroperoxyl Radicals, *J. Am. Chem. Soc.* 142 (2020) 14331–14342. <https://doi.org/10.1021/jacs.0c06379>.
- [43] K.A. Harrison, E.A. Haidasz, M. Griesser, D.A. Pratt, Inhibition of hydrocarbon autoxidation by nitroxide-catalyzed cross-dismutation of hydroperoxyl and alkylperoxyl radicals, *Chem. Sci.* 9 (2018) 6068–6079. <https://doi.org/10.1039/C8SC01575A>.
- [44] M. Griesser, R. Shah, A.T. Van Kessel, O. Zilka, E.A. Haidasz, D.A. Pratt, The Catalytic Reaction of Nitroxides with Peroxyl Radicals and Its Relevance to Their Cytoprotective Properties, *J. Am. Chem. Soc.* 140 (2018) 3798–3808. <https://doi.org/10.1021/jacs.8b00998>.
- [45] D.B. Zorov, M. Juhaszova, S.J. Sollott, Mitochondrial reactive oxygen species (ROS) and ROS-induced ROS release, *Physiol Rev.* 94 (2014) 909–950. <https://doi.org/10.1152/physrev.00026.2013>.
- [46] D.T. Sawyer, J.S. Valentine, How super is superoxide?, *Acc. Chem. Res.* 14 (1981) 393–400. <https://doi.org/10.1021/ar00072a005>.
- [47] Y.A. Ilan, G. Czapski, D. Meisel, The one-electron transfer redox potentials of free radicals. I. The oxygen/superoxide system, *Biochim Biophys Acta.* 430 (1976) 209–224. [https://doi.org/10.1016/0005-2728\(76\)90080-3](https://doi.org/10.1016/0005-2728(76)90080-3).
- [48] B.H.J. Bielski, D.E. Cabelli, R.L. Arudi, A.B. Ross, Reactivity of HO₂/O₂⁻ Radicals in Aqueous Solution, *Journal of Physical and Chemical Reference Data.* 14 (2009) 1041. <https://doi.org/10.1063/1.555739>.
- [49] B.H.J. Bielski, A.O. Allen, Mechanism of the disproportionation of superoxide radicals, *J. Phys. Chem.* 81 (1977) 1048–1050. <https://doi.org/10.1021/j100526a005>.
- [50] B.H. Bielski, R.L. Arudi, M.W. Sutherland, A study of the reactivity of HO₂/O₂⁻ with unsaturated fatty acids, *J Biol Chem.* 258 (1983) 4759–4761.
- [51] Z.A.M. Zielinski, D.A. Pratt, Lipid Peroxidation: Kinetics, Mechanisms, and Products, *J. Org. Chem.* 82 (2017) 2817–2825. <https://doi.org/10.1021/acs.joc.7b00152>.
- [52] R. P, V. I, C. P, B. Dv, A. K, H. A, Synthesis and evaluation of caffeic acid amides as antioxidants, *Bioorganic & Medicinal Chemistry Letters.* 11 (2001). [https://doi.org/10.1016/s0960-894x\(00\)00630-2](https://doi.org/10.1016/s0960-894x(00)00630-2).
- [53] B. Etzenhouser, C. Hansch, S. Kapur, C.D. Selassie, Mechanism of toxicity of esters of caffeic and dihydrocaffeic acids, *Bioorg Med Chem.* 9 (2001) 199–209. [https://doi.org/10.1016/s0968-0896\(00\)00238-8](https://doi.org/10.1016/s0968-0896(00)00238-8).
- [54] P. Zhang, Y. Tang, N.-G. Li, Y. Zhu, J.-A. Duan, Bioactivity and chemical synthesis of caffeic acid phenethyl ester and its derivatives, *Molecules.* 19 (2014) 16458–16476. <https://doi.org/10.3390/molecules191016458>.
- [55] K. Uwai, Y. Osanai, T. Imaizumi, S. Kanno, M. Takeshita, M. Ishikawa, Inhibitory effect of the alkyl side chain of caffeic acid analogues on lipopolysaccharide-induced nitric oxide production in RAW264.7 macrophages, *Bioorganic & Medicinal Chemistry.* 16 (2008) 7795–7803. <https://doi.org/10.1016/j.bmc.2008.07.006>.
- [56] H. Shi, D. Xie, R. Yang, Y. Cheng, Synthesis of Caffeic Acid Phenethyl Ester Derivatives, and Their Cytoprotective and Neuritogenic Activities in PC12 Cells, *J. Agric. Food Chem.* 62 (2014) 5046–5053. <https://doi.org/10.1021/jf500464k>.
- [57] L. Valgimigli, G.F. Pedulli, S. Cabiddu, E. Sanjust, A. Rescigno, Formation of a Blue Adduct between 4-tert-Butyl-1,2-benzoquinone and 4-Amino-N,N-diethylaniline, *Tetrahedron.* 56 (2000) 659–662. [https://doi.org/10.1016/S0040-4020\(99\)01036-4](https://doi.org/10.1016/S0040-4020(99)01036-4).
- [58] D.E. Pennington, D.M. Ritter, PERIODATE OXIDATION OF PHENOLS, *J. Am. Chem. Soc.* 69 (1947) 187–188. <https://doi.org/10.1021/ja01193a507>.
- [59] A. Konopko, G. Litwinienko, Unexpected Role of pH and Microenvironment on the Antioxidant and Synergistic Activity of Resveratrol in Model Micellar and Liposomal Systems, *J Org Chem.* 87 (2022) 1698–1709. <https://doi.org/10.1021/acs.joc.1c01801>.
- [60] R. Shah, L. A. Farmer, O. Zilka, A. T.M. Van Kessel, D. A. Pratt. Beyond DPPH: Use of Fluorescence-Enabled Inhibited Autoxidation to Predict Oxidative Cell Death Rescue. *Cell Chem. Biol.* 26 (2019), 1594–1607.

- [61] Li, B., Harjani, J.R., Cormier, N.S., Madarati, H., Atkinson, J., Cosa, G., and Pratt, D.A. Besting vitamin E: sidechain substitution is key to the reactivity of naphthyridinol antioxidants in lipid bilayers. *J. Am. Chem. Soc.* 135 (2013), 1394–1405.

CHAPTER 2

The anomalous regiochemistry of thiol addition to *o*-quinones explained by a free radical mechanism

(Published on The Journal of Organic Chemistry 2022 as DOI: 10.1021/acs.joc.1c02911) The research was carried on in collaboration with the research group of Prof. Alessandra Napolitano (University of Naples, Federico II)

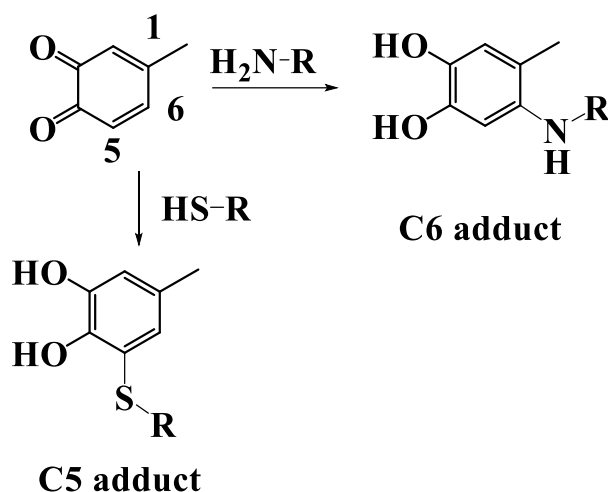
Abstract

During an investigation on the synthesis of novel catechol/quinone type antioxidants containing chalcogens like sulphur as substituents in the ring, a work which the research group of Prof. Alessandra Napolitano (University of Naples) has been carrying on in collaboration with our research group, it was observed an anomalous regiochemistry of formal “nucleophilic addition” of thiols to o-quinones. We set to investigate in detail the mechanism at the basis of this unusual behaviour as a collaborative project between the research groups. It was discovered that the addition of thiol compounds, such as cysteine or benzenethiol, to o-quinones, such as dopaquinone, proceeds through a free radical chain mechanism triggered by the addition of thiyl radicals to the o-quinone. This contrasts with the usual 1,4-nucleophilic addition mechanism, which is typically seen in the addition of amines to o-quinones. The proposed mechanism has been supported by density functional theory (DFT) calculations, which consistently predicted the correct regiochemistry only for the thiyl radical-quinone addition pathway. These findings suggest that the commonly accepted mechanisms for thiol-o-quinone conjugation may need to be revised and that further work is needed to assess the impact of free radical processes in biologically relevant thiol-quinone interactions.

INTRODUCTION

2.1 Thiol-o-quinone reaction

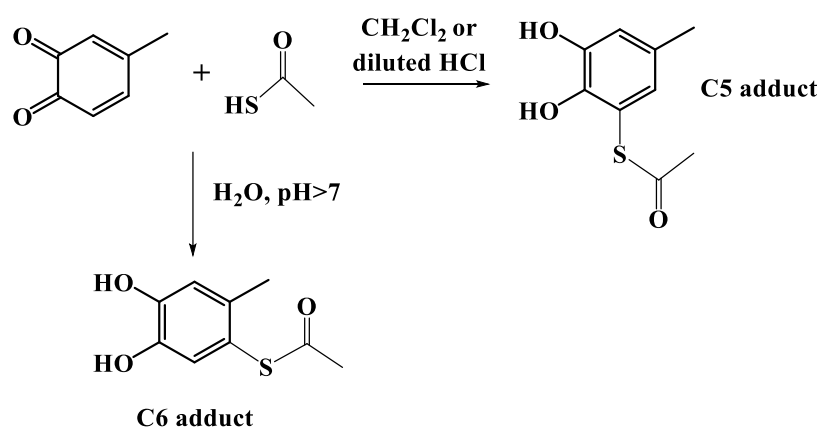
The reactions of o-quinones with natural thiol compounds like cysteine or glutathione [1] are important in a variety of biological processes, including pigment synthesis, metabolic transformations, and cross-linking mechanisms. These reactions are also relevant in food, agriculture, materials science, toxicology, and organic synthesis. In our specific case, this reaction was key to the synthesis of novel antioxidants containing both the catechol function and chalcogens (sulfur) as substituents on the ring, since these molecules might offer distinctive advantage to handle oxidative stress in biological systems [2]. However, a distinguishing feature of the thiol-o-quinone reaction is the anomalous regiochemistry of the coupling reaction, which leads mainly to C5-linked adducts, in contrast to the usual C-6 conjugates seen in other nucleophile addition pathways. This regiochemistry has been a puzzle and has prompted intensive investigations.



Scheme 2.1 Coupling reactions of catechols with thiol or amine compounds leading to C-5 or C-6 conjugates, respectively

The anomalous regiochemistry of the thiol-o-quinone reaction, which leads mainly to C5-linked adducts, has been observed in the conjugation of DOPA or catecholamines with cysteine or glutathione [3]. Electron-withdrawing substituents on the alkyl chain

of catecholamines can direct the attack of the thiol toward the more hindered 2-position of the *o*-quinone ring [4] [5]. However, in no case is the typical regiochemistry via 1,4-nucleophilic addition observed. The structural and mechanistic basis for this unusual regiochemistry has not been fully understood. Early studies on the reaction of 4-methyl-*o*-benzoquinone with thioacetic acid showed that the "normal" 6-S-adduct prevails in an aqueous or alkaline medium, while the "anomalous" 5-S-adduct dominates at acidic pH or in organic solvent [6]. This divergent behavior was attributed to the differential reactivity of the thiolate anion versus the thiol, with the thiol being less reactive and expected to react more selectively at the less sterically hindered position, benefitting also from greater resonance stabilization.



Scheme 2.2 Schematic reaction of 4-methyl-*o*-benzoquinone with thioacetic acid under different reaction conditions.

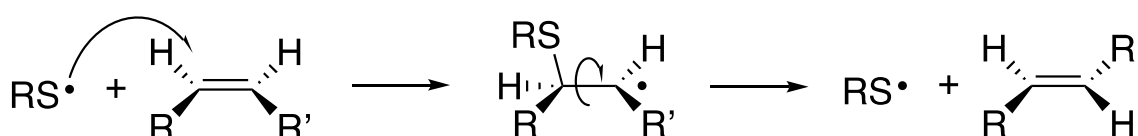
The anomalous regiochemistry of the thiol-*o*-quinone reaction, which leads mainly to C5-linked adducts, has been a subject of investigation for some time. It has been observed that other sulfur nucleophiles, such as thioureas and derivatives, usually add to the "canonical" C-6 position, suggesting that the regiochemistry may be related to the typical reactivity of the thiol group [7]. Studies have suggested that the reaction may involve a free radical pathway, possibly involving the generation of semiquinone radicals or thiyl radicals [8]. Density functional theory (DFT) calculations have suggested that the initial adduct may evolve through the migration of the thiolate to the adjacent 5- or 2-positions through energetically viable reaction channels [9]. Other

studies have suggested a role for thiols as both reactants and catalysts in the rate-determining propagation step of the reaction, and the possibility of a radical chain mechanism triggered by the addition of thiyl radicals to the o-quinone has been proposed [10]. However, the exact mechanisms and factors contributing to the anomalous regiochemistry of the thiol-o-quinone reaction are still not fully understood and require further investigation.

RESULTS AND DISCUSSION

2.2 Investigations of free radical intermediates

Experimental support to the intermediacy of thiyl radicals in the reaction was gained through investigation of *cis-trans* isomerization in olefins due to reversible addition of the thiyl radicals to the C=C double bonds (Scheme 1.8), a reaction that was found to be key to the thiol-mediated isomerization of lipids in bio-membranes, associated with oxidative stress related toxicity.



Scheme 2.3 Thiyl radical-mediated isomerization of olefins.

Since this reaction is specific of thiyl radicals and not observed to any significant extent with other transient or persistent radicals (*e.g.* phenoxyl, aminyl, nitroxyl), we set to exploit this process to selectively detect the formation of thiyl radical during the reaction of thiols with 4-MBQ. (*Z*)-stilbene promptly reacts with thiyl radicals [11] and its *E/Z* isomers are easily distinguished by their UV spectra [12] or by GC-MS analysis, therefore we used the *Z*→*E* isomerization of stilbene as a reporter of the formation of thiyl radicals. In this study, it has been investigated the formation of thiyl radicals in the reaction between 4-methylbenzoquinone (4-MBQ) and various thiols, including

thiophenol (PhSH), mercaptoethanol, *N*-(*tert*-butoxycarbonyl)-(L)-cysteine methyl ester (LipCys), and thioacetic acid. It has been found that when 4-MBQ is incubated with PhSH in the presence of (*Z*)-stilbene, (*E*)-stilbene is formed as a product, but when 4-MBQ is incubated with the other thiols, no isomerization is observed. This suggests that the intermediacy of thiyl radicals is important for the observed isomerization; however, the radicals need to be sufficiently stable to reach a threshold steady-state concentration in order to produce detectable *Z*→*E* isomerization of stilbene.

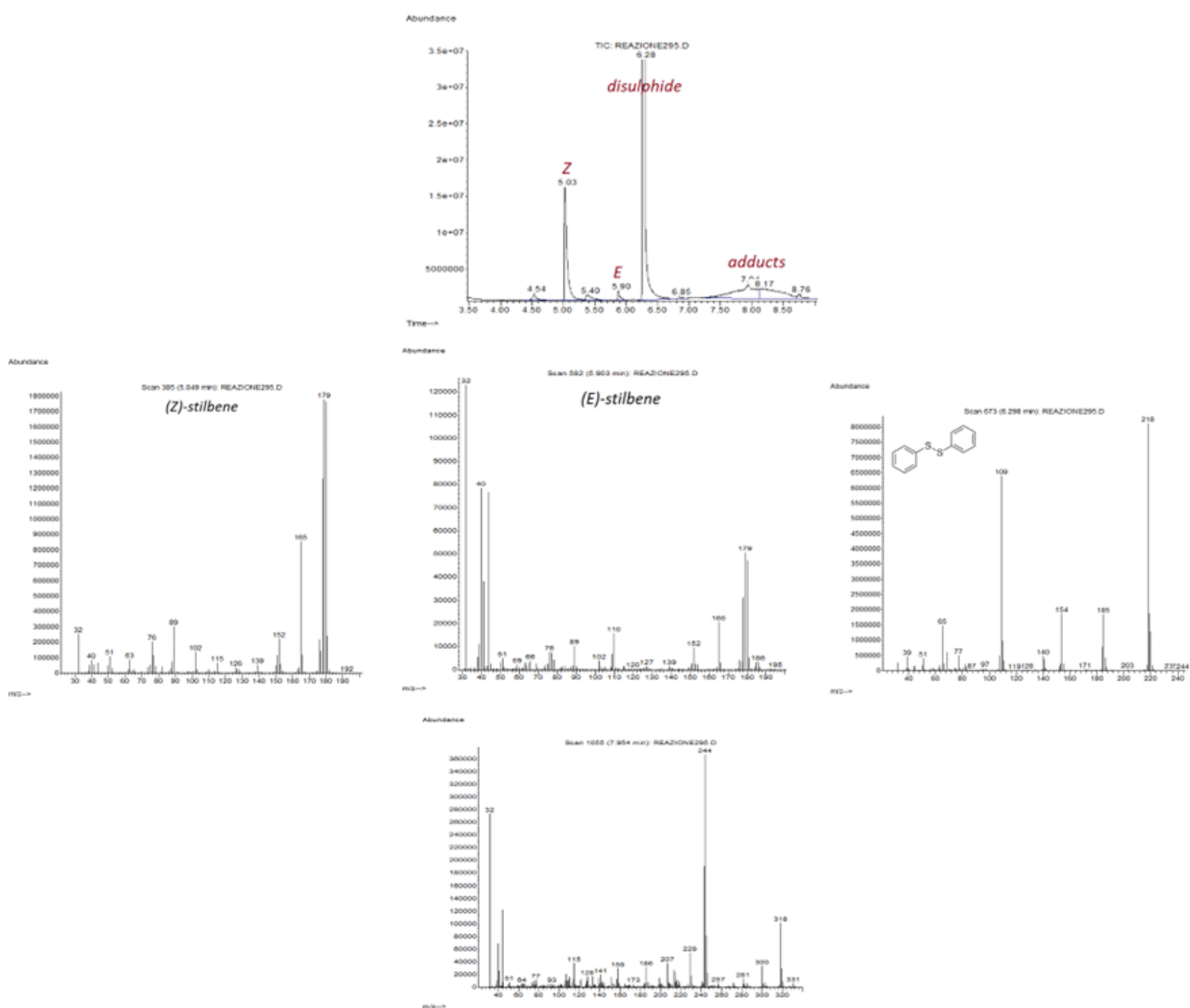


Figure 2.1 (Top) GC-MS analysis of the reaction mixture of PhSH 1 mM, (*Z*)-stilbene 0.1 mM and 4-methylbenzoquinone (4-MBQ) 1 mM in MeCN after 1 hour at 30°C showing isomerization of (*Z*)-stilbene to (*E*)-stilbene (r.t. 5.90 min), formation of phenyldisulphide (r.t. 6.28 min) and of unresolved quinone adducts and dimers; and (middle and bottom) the corresponding mass spectra.

To confirm the intermediacy of thiyl radicals, spin-trapping experiments have been set up with alpha-phenyl-*N*-*tert*-butyl nitron (PBN) and 5-(diethoxyphosphoryl)-5-

methyl-1-pyrroline-*N*-oxide (DEPMPO) as spin-traps, which would allow them to detect the presence of thiyl radicals in the reaction mixture by electron paramagnetic resonance (EPR) spectroscopy. When 4-MBQ was incubated with PhSH in the presence of either PBN or DEPMPO, weak yet detectable signals attributed to the trapping of PhS• radicals were recorded, as shown in figure 2.2, indicating the intermediacy of thiyl radicals in the reaction path.

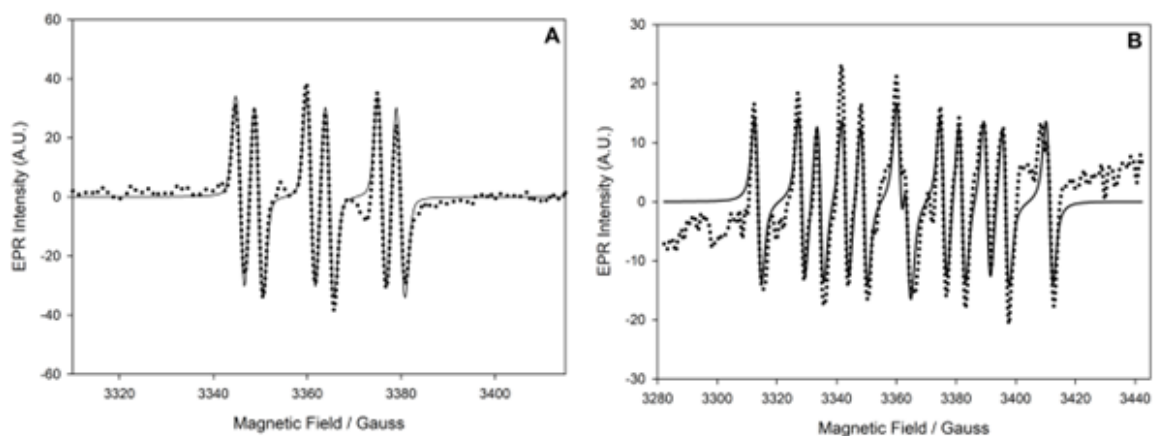


Figure 2.2 EPR spectra (dotted lines) recorded in spin-trapping experiments with (A) PBN 30 mM, PhSH 15 mM, 4-MBQ 15 mM in 1:1 MeCN/acetate buffer (pH = 5.0) or (B) DEPMPO 30 mM, PhSH 15 mM, 4-MBQ 15 mM in 1:1 MeCN/acetate buffer (pH = 5.0). Corresponding computer simulations (full lines) have been obtained with the following parameters: (A) $a_N = 15.1$ G, $a_H = 3.9$ G (2.0067); (B) $a_N = 14.6$ G, $a_H = 20.9$ G, $a_P = 47.4$ G ($g = 2.0064$)

After these encouraging results, we attempted to confirm the intermediacy of thiyl radicals in the reaction between 4-MBQ and cysteine using the same spin-trapping experiments with PBN and DEPMPO. When DEPMPO was used as the spin-trap, weak but reproducible electron paramagnetic resonance (EPR) signals were detected, as shown in figure 2.3 ($a_N = 14.4$ G; $a_H = 19.8$ G; $a_P = 47.0$ G; $g = 2.0064$), which, on the basis of the spectral parameters, are compatible with the trapping of a cysteine derived thiyl radical [12].

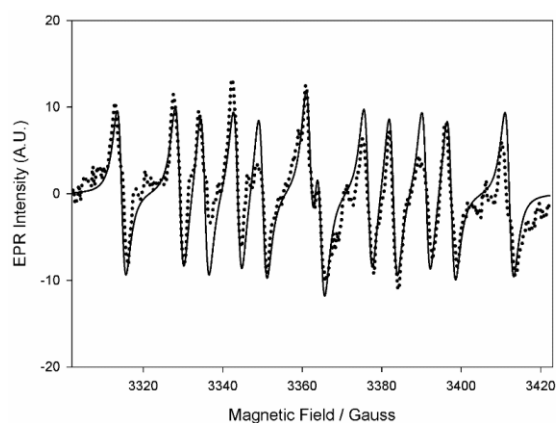


Figure. 2.3 EPR spectrum (dotted lines) and corresponding computer simulation (full line) recorded in spin-trapping experiments with DEPMPO 50 mM, cysteine 8.5 mM, 4-MBQ, 5 mM in 1:1 MeCN/acetate buffer (pH = 5.0), showing the trapping of CyS• radicals.

However, when PBN was used as the spin-trap, we were unable to obtain clear, reproducible EPR signals. Only in one experiment we could obtain a very weak spectrum which might be compatible with the expected adduct, for which there was the good agreement of the spectral parameters ($a_N = 15.1$ G; $a_H = 3.0$ G; $g = 2.0068$) with the literature [13]. However, we were unable to repeat the experiment, possibly due to the instability and high reactivity of cysteine thiyl radicals in solution, which leads to low steady-state concentrations in the reaction mixture

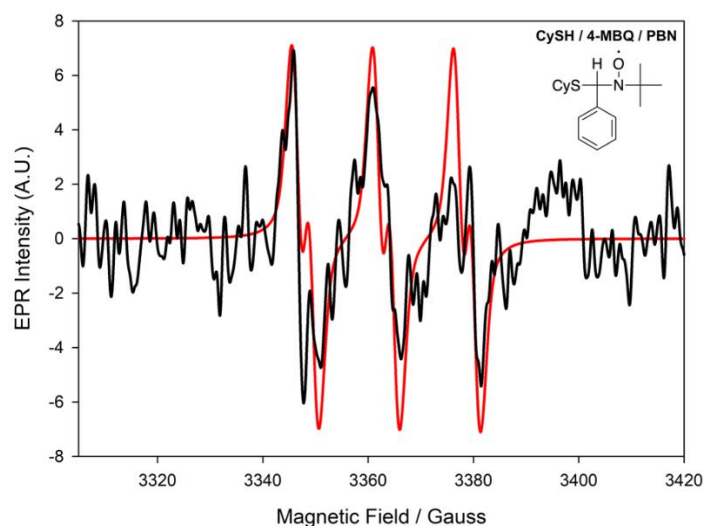


Figure 2.4 Spin adduct obtained by incubating PBN 85 mM, CySH 16 mM, 4-MBQ 16 mM in 1:1 MeCN/acetate buffer (pH = 5). Spectrum (black) was recorded with the following settings: modulation amplitude 1 G, sweep time 60 s, microwave power 10 mW, frequency 9.76 GHz ($g = 2.0068$), while its computer simulation (red) was obtained using the following parameters: $a(N) = 15.1$ G, $a(H) = 3.0$ G.

As for the case of *Z/E* isomerization experiments, we attribute the modest signals obtained with cysteine in spin-trapping experiments to the major instability and high reactivity of CyS• (aliphatic) thiyl radicals in solution which affords only low steady-state concentrations of the thiyl radical, possibly formed as intermediate in the reaction of CySH with 4-MBQ. Given this not fully conclusive result, we decided to revert the experimental approach. To find independent confirmation of the intermediacy of thiyl radicals in the reaction between *ortho*-quinones like 4-MBQ and thiols like cysteine we synthesized nitrosocysteine (CyS-NO) and *N*-acetylcysteine nitroso derivative (NAC-NO), which are known to generate thiyl radicals upon photolysis [14], [15]. We then performed spin-trapping experiments by photolyzing the nitrosothiols in the presence of PBN and found clear evidence of the formation of thiyl radical adducts, starting from either of the two photochemical sources, as can be seen in figure 2.5.

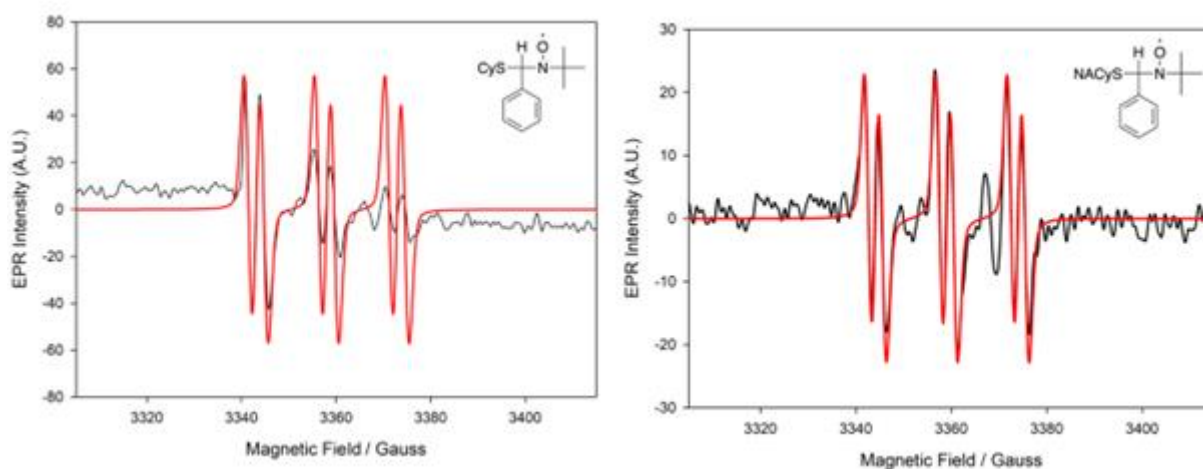
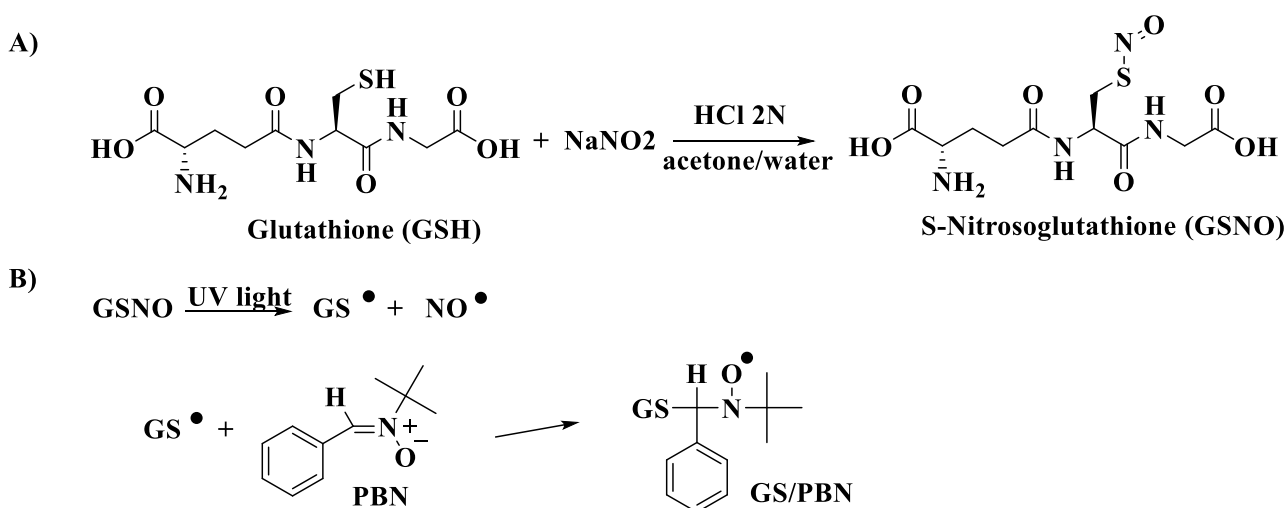


Figure. 2.5 Spin trapping of the thiyl radical from CySH and NACys upon photolyzing in the EPR cavity a solution of the corresponding nitroso CyS-NO and NAC-NO (25 mM) in the presence of PBN (6 mM) in MeCN/acetate buffer (pH = 5.0) 7:3 at 30°C. Photolysis was performed at 240-400 nm (2200-3000 mW/cm²) for 40s. Experimental spectra (black) were recorded with the following settings: modulation amplitude 1 G, sweep time 60 s, microwave power 5 mW, frequency 9.76 GHz ($g = 2.0068$), while their computer simulations (red) were obtained using the following parameters: (CyS-PBN) $a(N) = 15.0$ G, $a(H) = 3.2$ G; (NACyS-PBN) $a(N) = 14.9$ G, $a(H) = 2.9$ G;

Having obtained clear evidence that both CyS-NO and NAC-NO produce detectable levels of thiyl radicals under our setting, we replaced with 4-MBQ and irradiated the

mixture, to verify the formation of the thiyl adduct of the quinone. This would have provided evidence that, under conditions in which there is no thiol and the reaction is certainly carried out by thiyl radicals, the same radical adducts typically observed by reacting 4-MBQ with cysteine or other aliphatic thiols are obtained. However, the analysis of the reaction mixture showed the presence of relevant amounts of the starting thiols and disulfides, owing to the impossibility to better purify the unstable CyS-NO and NAC-NO from the starting thiols. The presence of some starting thiol in the reaction mixture made it difficult to confirm that the observed adducts to the quinone derived from the thiyl radicals rather than the thiols (see Appendix). To circumvent the problem, we turned to glutathione (GS) as a probe thiol and synthesized GS-NO, which (unlike CyS-NO and NAC-NO), we were able to obtain in pure form, without impurities of the starting thiol. Then we repeated the experiments using GS-NO, in an attempt to provide unambiguous evidence for the intermediacy of thiyl radicals in the reaction between 4-MBQ and a cysteine-like thiol. The experiment is illustrated in scheme 2.5.



Scheme 2.4 A) Synthesis of *S*-nitrosoglutathione; B) reaction scheme of spin-trapping experiments by photolyzing the nitrosoglutathione in the cavity of the EPR spectrometer in the presence of PBN.

Spin-trapping with PBN afforded good EPR signals which were unambiguously assigned to the trapped GS• thiyl radical, based on its spectroscopic parameters [16].

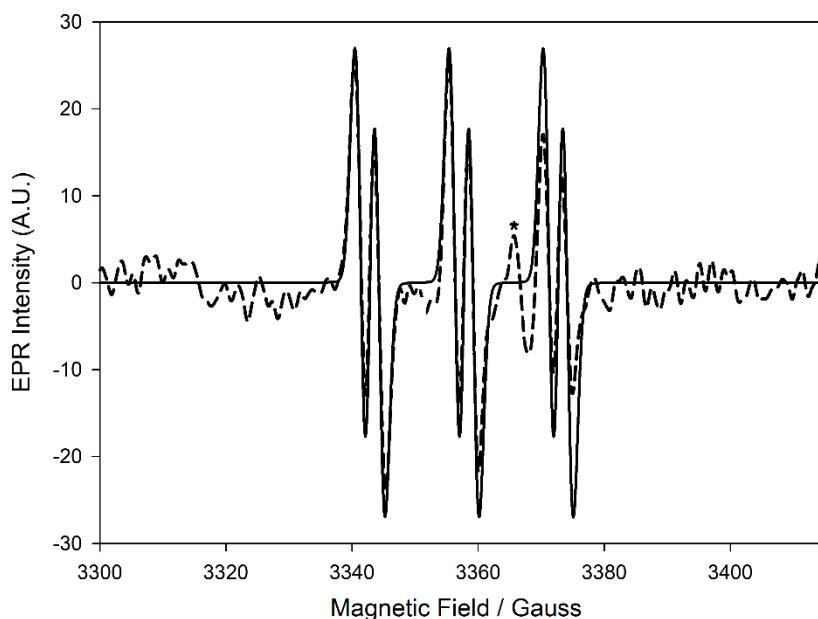
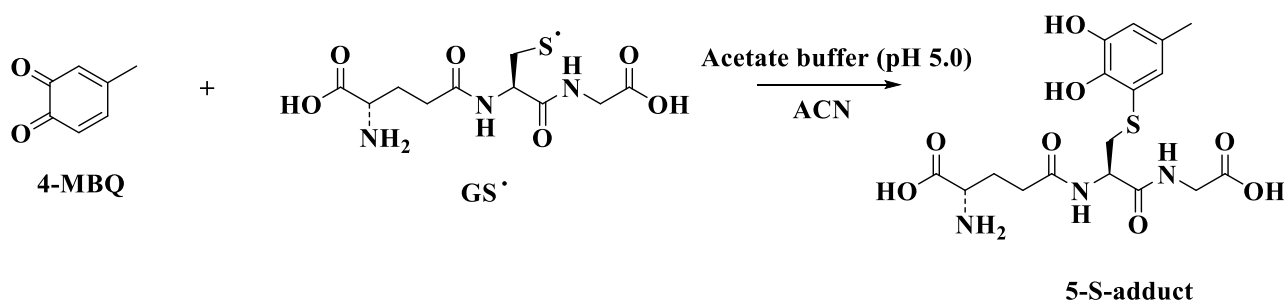


Figure. 2.6 Spin trapping of the thiyl radical GS• upon photolyzing a solution of GS-NO (1.7 mM) in the presence of PBN (9 mM) in MeCN/acetate buffer (pH = 5) at 30°C (dashed line; the asterisk indicates the persistent signal of the EPR cavity Dewar). Simulated spectrum (full line): $a_N = 15.1$ G, $a_H = 3.1$ G, g-factor = 2.0070).

To confirm the generation of 4-MBQ/GS adduct under radical conditions, two matched reaction mixtures were prepared:

- 1) a solution containing 1 mM of 4-MBQ and 1 mM GS-NO in acetate buffer/MeCN (pH 5.0), which was irradiated with a 400 mW Hamamatsu UV- lamp (4500 mW/cm², set at 50%) for 5 minutes at 30°C;
- 2) a solution containing 1 mM of 4-MBQ and 1 mM GSH in acetate buffer/MeCN (pH 5.0) which was incubated in the dark at 30°C for 15 minutes.



Scheme 2.5 Generation of 4-MBQ/GS adduct under radical conditions.

The HPLC-Q-TOF analysis of the two reaction mixtures showed in both cases the formation of an adduct, which was identified as the 5-GS adduct by comparing its

chromatographic behaviour to an authentic sample. The analysis also showed that the adduct had a characteristic ion signal at m/z 430 and a specific fragmentation pattern when subjected to MS/MS analysis. Comparison of the MS spectra and retention time confirmed that the two reaction mixtures had produced the same adduct. This suggests that both reaction must proceed via the transient formation of thiyl radicals [6]. The thiyl radical would then add to the quinone to afford the final adduct, normally attributed to nucleophilic addition of the thiol. We identified that there was the formation of 5-GS because for the reaction regiochemistry similarity using PhSH. Previously was isolated and characterized as the 5-*S*-phenyl adduct (5-methyl-3-(phenylthiol)benzene 1,2-diol) by complete spectral analysis confirming that the reaction with PhSH followed the same regiochemistry observed for L-cysteine and so glutathione. The NMR spectra are shown in Appendix.

2.3 DFT calculations

To support the main conclusions from the above sets of experiments, and to gain a deeper insight into the origin of the anomalous regiochemistry, a systematic computational investigation was carried out at the DFT level of theory. Initially, the relative energies were computed for the various regioisomers that can be formed by reaction of the thiol with the *o*-quinone *via* three alternate pathways: 1a) thiol-quinone and 1b) thiolate-quinone nucleophilic addition; 2a) thiyl radical-phenoxy radical and 2b) thiyl radical-semiquinone radical anion coupling, and 3) thiyl radical-quinone coupling. Coupling pathways 2 and 3 would be consequent to a preliminary electron transfer step between the thiol and the quinone leading to thiyl radicals and semiquinones (see Appendix). The computational work has been carried out at the University of Naples by Prof. Orlando Crescenzi. It has been used a computational method to calculate the free energy of several chemical species in different solvents. The free energy is a measure of the thermodynamic feasibility of a chemical reaction or process, and it can be computed using density functional theory (DFT) and a basis set, which is a set of mathematical functions used to describe the electronic

wavefunction of a molecule. The species being studied include 4-MBQ, phenoxy radical, semiquinone, methanethiol, thiolate, and thiyl radical. The initially formed adducts, or the products of chemical reactions, under the assumption that the reactions were kinetically controlled, meaning that competitive reaction paths are selected on the basis of their relative rate, rather than by their thermodynamic favourability. The results of the calculations are reported in Table 1, and they show the relative free energies of different regioisomers, or isomers that differ in the arrangement of their atoms, produced by different pathways.

Table 2.1. Relative free energies (kcal mol⁻¹) for the regioisomers depicted in Scheme 5 calculated with PBE0 density functional and with ω B97X-D functional (data reported in brackets)

Path	<i>In vacuo</i>		<i>In water</i>	
	Regioisomer	Energy (kcal mol ⁻¹)	Regioisomer	Energy (kcal mol ⁻¹)
1a	I-5	n.d. ^a	I-5	unstable (unstable) ^b
	I-6	n.d. ^a	I-6	unstable (unstable) ^c
1b / 2b	II-5	n.d. ^a	II-5	1.9 (2.6)
	II-6	n.d. ^a	II-6	0.0 (0.0)
2a	III-5	3.7 (3.0)	III-5	4.8 (5.2)
	III-6	0.0 (0.0)	III-6	0.0 (0.0)
3	IV-5	0.0 (0.0)	IV-5	0.0 (0.0)
	IV-6	6.5 (6.2)	IV-6	4.2 (3.2)

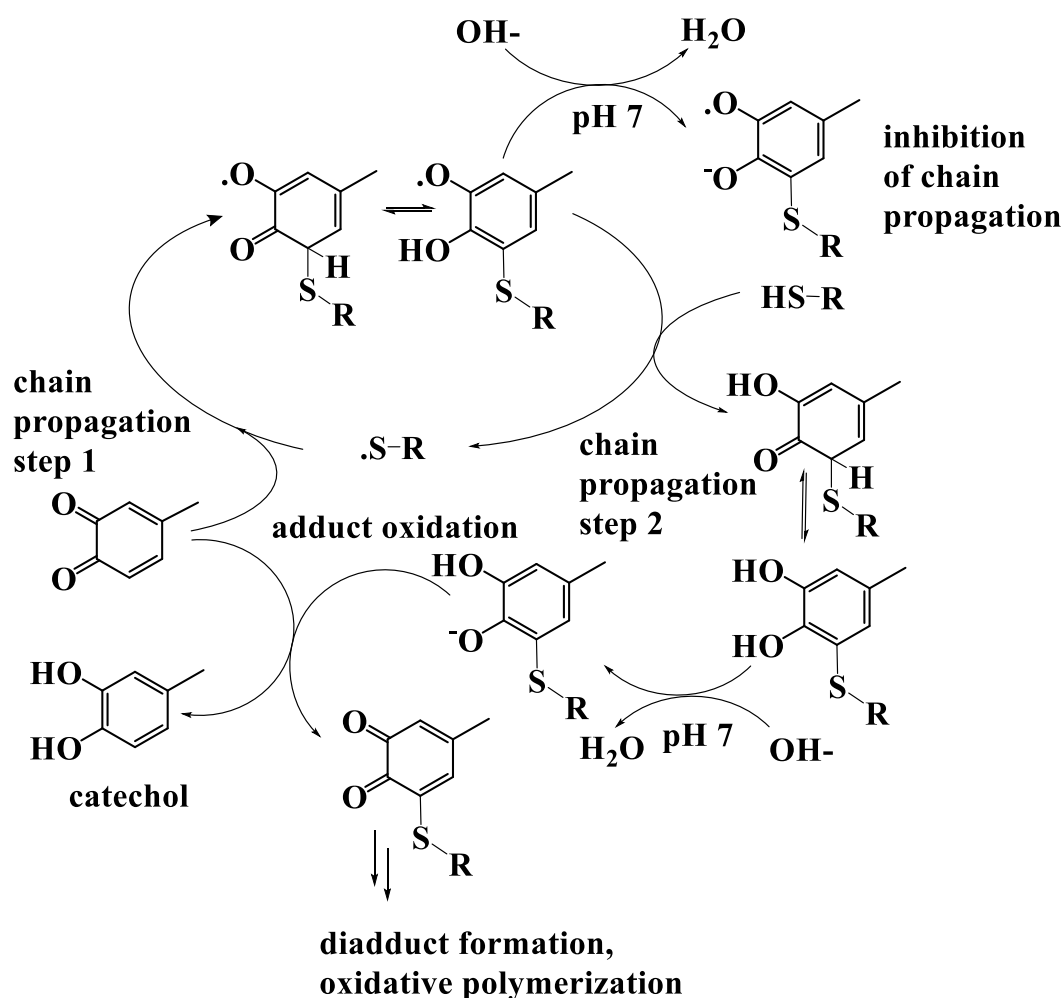
^[a] Charged / zwitterionic species were examined only in water.

^[b] Most starting structures of the zwitterionic adduct dissociate during optimization; only few minima have been identified. The computed $\Delta_r G^0$ for the reaction (PBE0 level) is 22.7 kcal mol⁻¹.

^[c] All starting structure examined dissociate during optimization.

It has been conducted additional computational calculations using a different functional, called ω B97X-D, to validate their results. They found that the ω B97X-D functional, which has been specifically validated for modeling thio-Michael additions, gave the same overall trend as the PBE058 functional. The data from the computational calculations suggest that thiyl radical addition to the quinone is the only mechanism that is compatible with the anomalous regiochemistry that is experimentally observed. However, there is a more complex analysis needed to fully understand the mechanism

of the reaction, taking into account factors such as the role of oxygen, protonation and deprotonation of the substrate and adduct, and redox exchange between the different species. By combining the evidence for the intermediary of thiyl radicals obtained in our previous experiments, the specific regioselectivity observed in the final adduct, and the results of calculations, it is possible to suggest an overall reaction mechanism for the thiol-quinone reaction. It is shown in Scheme 2.7 to account for most of the experimental evidence. For simplicity, only the prevalent 5-S adduct is shown in the scheme.



Scheme 2.6 Proposed mechanism for the 5-S-adduct formation.

In this scheme, a thiyl radical, even if produced in trace amounts by oxidizing agents present in the medium, including the starting quinone, would initiate a free radical chain process hinging on the stronger H-atom abstraction capacity of the intermediate

radical **IV-5** with respect to the semiquinone isomer. Hence, the overall outcome of the reaction would be based on the competition between H-atom abstraction from the thiol and isomerization to semiquinone. Table 2.2 reports computed free energies (kcal mol⁻¹) for the main reaction steps.

Table 2.2. Relative free energies (kcal mol⁻¹) for the reaction steps proposed in Scheme 6.

Step	<i>In vacuo</i>	<i>In water</i>
chain-propagation, step 1	-12.4	-11.8
chain-propagation, step 2	2.4	6.1
rearomatization	-20.3	-19.7

The mechanism depicted in Scheme 2.6 would also be consistent with the following observations:

- 1) At pH 7.0, the first formed free radical adduct or the equivalent phenoxy radical would undergo deprotonation to give a semiquinone radical anion, thus preventing H-atom transfer from the thiol would account for thiol radical-generating chain propagation step 2. Moreover, deprotonation of the resulting adduct would increase its facility to oxidation *via* redox exchange with the starting quinone resulting both in catechol accumulation and adduct conversion to the corresponding quinone. This latter step would account for diadduct formation and the general decrease in adduct yield at pH 7.0.
- 2) At pH 4.0, when both autoxidation and anion formation are minimized, allowance of oxygen into the medium would ensure both a greater efficiency of the thiol radical generating initiation steps and the re-oxidation of any catechol/semiquinone produced by redox exchange thus regenerating the quinone and enhancing the key coupling step.

CONCLUSION AND PERSPECTIVES

The anomalous regiochemistry of the coupling reaction of thiols, *e.g.* cysteine, with *o*-quinones was re-examined in this project by an integrated experimental and computational approach. Both experimental and theoretical results pointed strongly to a mechanism based on generation of thiyl radicals and their subsequent addition to the *o*-quinone. This latter step would promote a free radical chain process in which the initial adduct would continuously produce thiyl radicals from the thiol *via* efficient H-atom abstraction. The proposed free radical mechanism would be compatible with the observed dependence of product yield and distribution on both air and pH and would open new vistas into a range of reactions and processes of biological relevance. Additionally the understanding of the reaction mechanism will allow rational optimization of synthetic strategies to prepare novel chalcogen-containing polyphenolic antioxidants.

EXPERIMENTAL PART

2.4 Materials and methods

2.4.1 Materials

4-methyl-*o*-catechol, L-cysteine, thiophenol (PhSH), 6-hydroxy-2,5,7,8-tetramethylchromane-2-carboxylic acid (Trolox), (*Z*)-stilbene, (*E*)-stilbene, 2,2'-azobisisobutirronitrile (AIBN), mercaptoethanol (HSEtOH), N-(tert-butoxycarbonyl)-(L)-cysteine methyl ester (LipCys), tert-butyl perbenzoate, α -phenyl N-tertiary-butyl nitron (PBN), 5-(diethoxyphosphoryl)-5-methyl-1-pyrroline-N-oxide (DEPMPO), sodium nitrite, N-acetylcysteine and glutathione were purchased from Sigma Aldrich (Milan, Italy), sodium periodate was purchased from Carlo Erba (Milan, Italy). 6-S-cysteinyl isomer was prepared as previously described [17].

2.4.2. General methods

UV-vis spectra were recorded with a Jasco V-560 UV-vis spectrophotometer (Lecco, Italy) or with a Biomate 5 (Thermo Scientific, Milan, Italy) coupled with a Heto DBT Hetotherm (Birkerød, Denmark) thermostating water circulator for temperature control set at 30°C. ¹H NMR spectra were recorded in CDCl₃, in D₂O, or in DMSO at 400 MHz on a Bruker spectrometer. ¹³C NMR spectra were recorded in CDCl₃ at 400 MHz on a Bruker 400 MHz spectrometer. ¹H,¹H COSY, ¹H,¹³C HSQC, and ¹H,¹³C HMBC were run at 400 MHz using Bruker standard pulse programs. Structural assignments were made with additional information from gCOSY, gHSQC, and gHMBC experiments. Analytical and preparative TLC were carried out on silica gel plates (0.25 and 0.50 mm, respectively) from Merck using chloroform/methanol 9:1 v/v as the eluant. HPLC analyses were performed on an Agilent 1100 binary pump instrument (Agilent Technologies, Milan, Italy) equipped with a SPD10AV VP UV-visible detector using a Phenomenex Synergy 4U Hydro-RP column (250 mm × 4.6 mm, 4 μm particle size) at 0.7 mL/min. Detection wavelength was set at 254 nm. Eluant system: 0.1 % formic acid - methanol 75:25 v/v. LC-MS analyses were performed in positive ion mode using an Agilent 1260/6230DA ESI-TOF instrument in the following conditions: nebulizer pressure 35 psig; drying gas (nitrogen) flushed at 5 L / min at a temperature of 325 ° C; capillary voltage 3500 V; fragmentor voltage 175 V. An Eclipse Plus C18 column (150 × 4.6 mm, 5 μm) at a flow rate of 0.4 mL / min was used, using the same eluant as above.

2.4.3 Synthesis of 4-methyl-o-quinone (4-MBQ)

The title compound was prepared following a procedure previously reported with modifications [18]. To a solution of 4-methylcatechol (4 mmol, 40 mL) in cold water, sodium periodate (4.4 mmol), previously dissolved in cold water, was rapidly added, and the mixture was kept under vigorous stirring in an ice bath. After 30 s the mixture was extracted with cold dichloromethane (3×50 mL). The organic layers were dried over anhydrous sodium sulfate and taken to dryness to give a red-brown powder in 96 % yield and pure form as confirmed by UV-vis analysis, HPLC-Q-TOF analysis (see

Appendix) and ¹H-NMR (see Appendix). ¹H NMR (CDCl₃) δ (ppm): 6.72 (d, 1H), 6.33 (d, 1H), 6.20 (s, 1H), 2.21 (s, 3H).

2.4.4 GC-MS analysis of stilbene isomerization

GC-MS analyses were performed in a Agilent 6890N-5973N system equipped with 7683B autosampler (Agilent Technologies, Milan, Italy) mounting a HP-5MS 0.25 mm × 30 m × 0.25 μm column, using He as carrier gas at flow rate 1 mL/min. Temperature programming was: 100°C, hold 1 min, ramp to 270°C at 30°C/min, hold 8 min. Injector and detector temperatures were 250°C and 270°C respectively, injection volume 1 μL, split ratio 20:1. Mass spectra were recorded in EI+ (70 eV) mode in the range 32-800 m/z. For Z→E isomerization studies a mixture of 0.1 mM (Z)-stilbene was incubated with PhSH (1-10 mM) and 1 mM 4-MBQ in MeCN at 30 °C and analyzed at different time-intervals. Control experiments lacking 4-MBQ were performed. Thioacetic acid, HSEtOH and LipCys were also tested as the thiol reactant in place of PhSH. As a positive control 0.1 mM (Z)-stilbene was incubated with a thiol (1-10 mM) and AIBN or tert-butyl perbenzoate (TBPB) (5-10 mM) at 30-70°C.

2.4.5 HPLC-Q-TOF(MS) analysis of quinone/thiol reactions

Analyses were performed on a Acquity UPCL H-Class Plus coupled to a Xevo G2-XS QTOF spectrometer (Waters, Milan Italy) mounting a SepaChrom Adams C18-classic (250 mm × 4.6 mm, 5 μm particle size) column eluted isocratically with 30% A (0.1% trifluoroacetic acid in MeCN) and 70% B (0.1% trifluoroacetic acid in water) at flow rate 0.6 mL/min. ESI+ : cone 30V, capillary 0.8 kV, temp. 120°C, desolv. temp. 600°C, cone gas flow 50 L/h, desolv. flow 1000 L/h. Mass range 50 to 1250 m/z, High CE ramp 20 to 30 eV. MS/MS: CID 20 to 30 eV with Ar. TOF: acceleration 10/100V, pusher/puller 1900V/1400V, flight tube 9 kV, reflectron 1.6 kV. In experiments probing quinone/thiol reaction a mixture of 1 mM 4-MBQ and the S-nitroso thiol (GS-NO, NAC-NO or CyS-NO) at 1 mM contained in a quartz cuvette was irradiated using

Hamamatsu UV - lamp (4500 mW/cm² at 240-400 nm) provided with an optical fiber, at 30-70% power for 5 minutes at 30°C, then immediately subjected to analysis, alternatively a mixture of 4-MBQ 1 mM and glutathione 1 mM was incubated in the dark at 30 °C for 5-15 min then immediately analysed.

2.4.6 Reaction of 4-MBQ with cysteine

To a solution of 10 mM cysteine (0.02 mmol) in 50 mM phosphate buffer (2 mL) at pH 7.0, 4-MBQ dissolved in a minimal amount of acetonitrile was added up final concentration 1 mM, and the mixture was kept in air under stirring (400 rpm). After 15 min aliquots were withdrawn, treated with an excess of solid sodium dithionite and analyzed by HPLC and UV-vis spectrophotometry. The same experiments were also run in 50 mM phosphate buffer at different pHs (in the range 4-7) both in air and under an argon atmosphere. All experiments were run in triplicate. Identification of 4-MBQ-cysteine adducts was achieved by comparison of their chromatographic behavior with those of authentic samples [19]. Control experiments were run in the absence of cysteine. Selected reaction mixtures were analysed by LC-MS under the conditions detailed above. In other experiments to a solution of cysteine and 4-MBQ both at 1 mM, in 50 mM phosphate buffer at pH 4.0, different amounts of trolox (0.5-5 mM) were added and the mixture was kept in air under stirring. After 3 min withdrawn aliquots were analyzed by HPLC as above (see Appendix). The same experiments were also run at 1:5 catecholcysteine/Trolox ratio at different pHs (in the range 4-7) under an argon atmosphere and after 3 min were analyzed as above.

2.4.7 Reaction of 4-MBQ with thiophenol

To a solution of 10 mM PhSH (8.2 mmol) in 50 mM phosphate buffer at pH 4.0, a solution of 4-MBQ (0.82 mmol) in acetonitrile was added and the mixture was kept under stirring (400 rpm) in air. After 15 min the mixture was analyzed by HPLC. The chromatographic profile revealed the presence of a major component eluted at t_R =16

min. The mixture was then extracted with ethyl acetate (3x800 mL), and the combined organic phases were taken to dryness after treatment with anhydrous sodium sulphate. TLC analysis showed the presence of a main product ($R_f = 0.6$, eluant $\text{CHCl}_3/\text{MeOH}$ 9:1 v/v). Purification was run by preparative TLC using CHCl_3 : MeOH 9:1 v/v containing 1 % acetic acid as eluant to give the product (30% yield) in pure form. UV λ_{max} (MeOH): 256 nm (ϵ 3630 $\text{M}^{-1}\text{cm}^{-1}$), 295 nm (ϵ 5899 $\text{M}^{-1}\text{cm}^{-1}$). ^1H NMR (DMSO-d_6) δ (ppm): 2.14 (s, 3H), 6.63 (s, 1H), 7.48 (s, 1H), 7.53 (m, 1H), 7.57 (m, 2H), 7.73 (d, 2H). $^{13}\text{C}\{^1\text{H}\}$ NMR (DMSO-d_6) δ (ppm): 19.27 (CH₃), 116.87 (CH), 119.80 (CH), 127.29 (CH), 128.15 (C), 129.56 (C), 129.86 (CH), 133.40 (CH), 142.39 (C), 143.82 (C), 151.02 (C).

2.4.8 Synthesis of Cys-NO and NAC-NO [78]

The title compounds were prepared accordingly to protocols previously reported with modifications. Briefly, L-cysteine (0.18 mmol) and sodium nitrite (0.18 mmol) were dissolved in 0.5 M HCl (5 mL) and the mixture was kept under stirring in an ice bath. After 30 min a 0.1 M NaOH solution was added to the mixture up to pH 5.0. The concentration of Cys-NO was estimated by measuring absorbance at 332 nm using a molar coefficient of 0.75 $\text{mM}^{-1}\text{cm}^{-1}$ as 15.2 mM, corresponding to a yield of ~50%. Similarly, the concentration of NACNO was estimated from absorbance at 330 nm using a molar coefficient of 0.73 $\text{mM}^{-1}\text{cm}^{-1}$. HPLC-Q-TOF analysis revealed in both cases the presence of the starting thiol and the corresponding disulphide. The solution was used for product study and spin trapping experiments. Synthesis of GS-NO [79],[80] To a stirred ice-cold solution of GSH (500 mg, 1.7 mmol) in water (2.5 mL) NaNO_2 (120 mg, 1.7 mmol) was added and then acidified by adding HCl 2N (0.9 mL). After 40 minutes during which the temperature was maintained from 0 to 5 °C the red solution was treated with acetone (3.5 mL) and stirred for further 10 minutes. The resulting fine pale red precipitate was filtered off and washed successively with ice-cold water (2 mL), acetone (2 mL) and diethyl ether (2 mL) to afford S-nitrosoglutathione (300 mg, 76%), whose identity and purity was assessed by UV-Vis,

^1H NMR (see Appendix), and HPLC-Q-TOF analysis (see Appendix). UV-Vis λ_{max} (H_2O): 335 nm (ϵ 922 $\text{M}^{-1}\text{cm}^{-1}$), 545 nm (ϵ 15.9 $\text{M}^{-1}\text{cm}^{-1}$). ^1H NMR (D_2O) δ (ppm): 4.60–4.50 (m, 1H), 4.10–3.85 (m, 2H), 3.80 (s, 2H), 3.65 (t, 1H), 2.30 (t, 2H), 2.10–1.95 (m, 2H). Q-TOF (ESI⁺) m/z: 337 ($[\text{M}+\text{H}]^+$, 2%), 307, 289 (bp), 232, 118.

2.4.9 EPR spin-trapping experiments

The X-band EPR spectra were collected in 1 mm quartz tubes with Eleksys 500 (Bruker, Milan, Italy) and a MiniScope MS 5000 (Magnettech, Freiberg, Germany), both equipped with temperature control, and all spectra were recorded at 30°C. When needed UV irradiation in cavity was provided by an optical fiber from a mercury-xenon lamp (Hamamatsu Lightningcure LC8, 240-400 nm, max 4500 mW/cm^2). Spectra were analysed by the WinESR program (developed by Prof. Marco Lucarini, University of Bologna) and subjected to iterative simulation-matching based on the systematic application of MonteCarlo method. Measured g-factors were corrected with respect of 2,2,6,6-tetramethylpiperidine-N-oxyl (TEMPO) radical, $g = 2.0061$, [20], [21] and that of 2,2-diphenyl-1-picrylhydrazyl (DPPH) radical in acetonitrile, $g = 2.0036$ [22]. Spectra were recorded with the following settings: modulation amplitude 0.1-0.2 mT, sweep width 12 mT, modulation frequency 100 kHz, frequency 9.76 Hz, sweep time 60s, microwave power 10 mW. For spin-trapping experiments 10-100 mM spin trap (PBN or DEPMPO) was added to a mixture of the thiol 1-20 mM and 4-MBQ 1-20 mM in MeCN/acetate buffer (pH = 5.0) 1:1 in a quartz tube in the cavity of the EPR spectrometer (30°C) and spectra were recorded every 5 minutes. For experiments with S-nitroso derivatives a mixture of Cys-NO, NAC-NO or GS-NO 1-25 mM and PBN 5-10 mM in MeCN/acetate buffer (pH = 5.0) was briefly irradiated (20-40s, 50% power) in the spectrometer cavity (30°C) and the spectra recorded immediately after.

2.4.10 Computational analysis

Calculations were mostly performed by Prof. Orlando Crescenzi with the Gaussian 09 package of programs; [23] only DLPNO-CCSD(T)-F12 calculations were performed with Orca 4.2.1. [24], [25]. The spin-unrestricted formulation was used for open-shell species. All structures were optimized with the PBE0 functional, [26] the PBE hybrid including 25% exact exchange. In several cases, independent optimizations were also carried out with the ω B97X-D functional, [27] a long-range-corrected functional including empirical dispersion, which in a recent study [28] has been specifically validated to model thio-Michael additions. For each species, different tautomers / conformers, as well as different protonation states were explored. In those cases where enantiomers exist, a single enantiomeric series has been explored. All conformers identified were further characterized by single point energy evaluations with the M06-2X functional [29] in conjunction with a much larger basis set, 6-311++G(2d,2p). Reference conventional coupled-cluster singles and doubles calculations were also carried out, [30] [31] including non-iterative treatment of triple excitations, [32] with the cc-pVTZ basis set [33] [34] or with basis sets of the “calendar” series [35]. For open-shell species, a restricted open-shell reference wave function was used. Domain-based local pair natural orbital coupled-cluster (DLPNO-CCSD(T)) calculations with inclusion of explicit correlation (F12) in the wavefunction were performed with the cc-pVTZ-F12 basis set [36] and with a “TightPNO” pair natural orbital setting. For a uniform treatment of open- and closed-shell species, the “UseFullLMP2Guess” keyword was set to “false” for the closed shell calculations. Computations were performed either in vacuo, or by adoption of a polarizable continuum medium (PCM) [37] [38] [39] [40] to account for the influence of the solution environment. In view of the faster convergence, a scaled van der Waals cavity based on universal force field (UFF) radii; [41] [42] [43] non-electrostatic contributions to the solvation free energy were disregarded at this stage: these terms were accounted for in single-point PCM calculations (at the PCM geometries) employing radii and non-electrostatic terms of the SMD solvation model [44]. Vibrational-rotational contributions to the free energy

at 298.15 K were also computed. G values reported in the tables are referred to a 1 atm standard state; however, they were converted to a 1 M standard state in order to compute the reaction free energies discussed in the paper [45].

Appendix to Chapter 2

UPLC-Q-TOF chromatograms and mass spectra, NMR spectra, and mechanistic details.

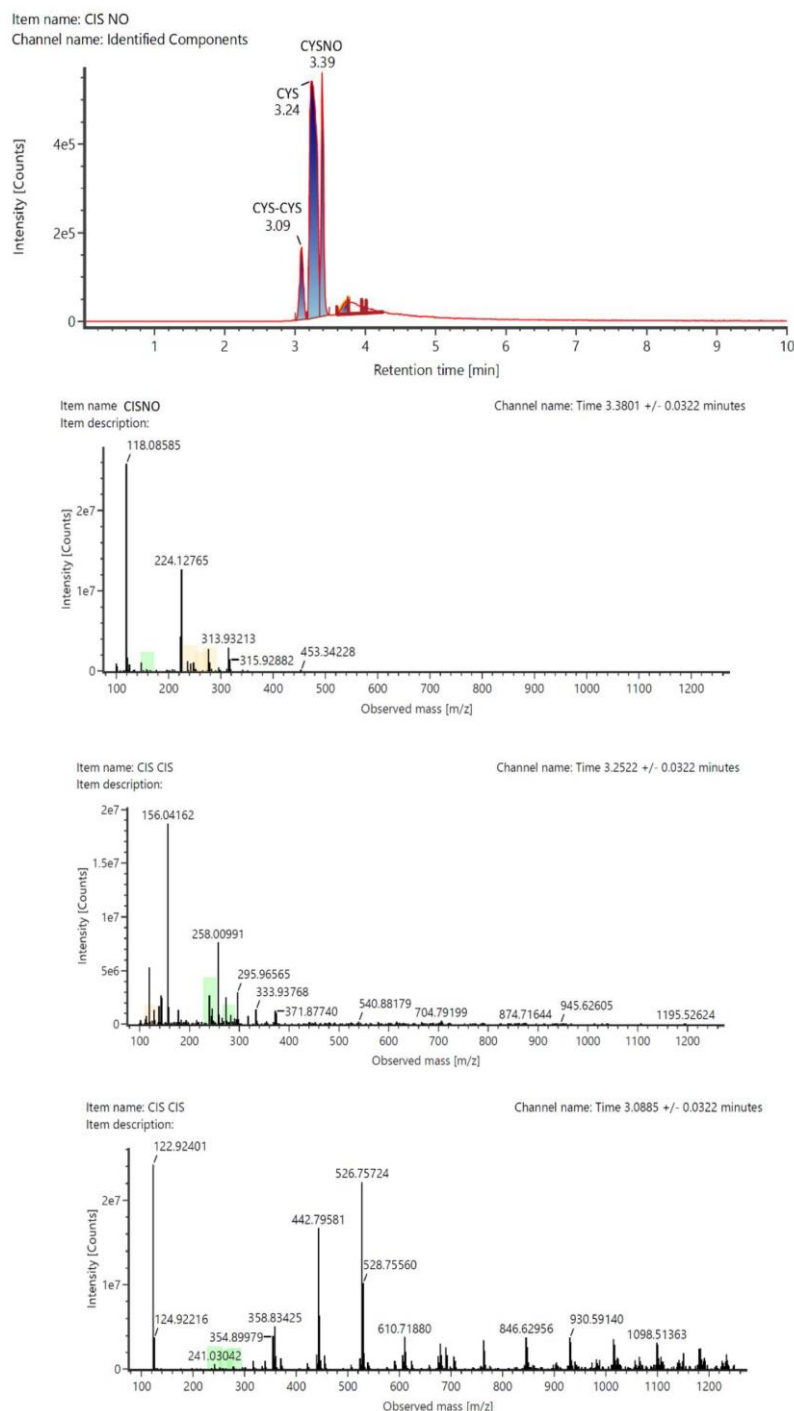


Figure A 2.1 Chromatogram of S-Nitrosocysteine (CYS-NO) (r.t. 3.39 min), in acetate buffer/MeCN (pH 5.0), showing residues of the starting cysteine (CYS) (r.t. 3.24 min) and the disulphide dimer (CYS-CYS) (r.t. 3.09 min) originated from the synthesis. The corresponding mass spectra are shown below the chromatogram.

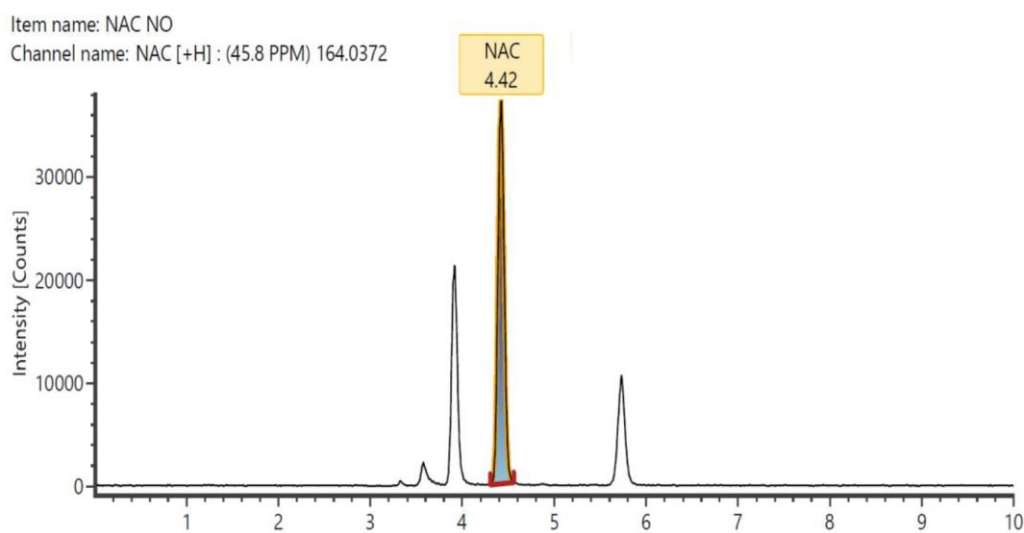
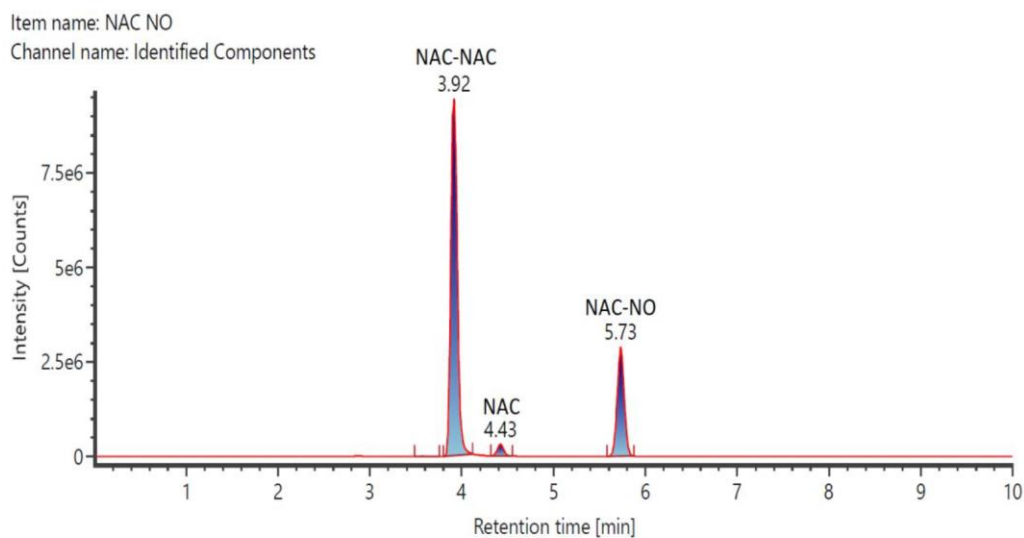
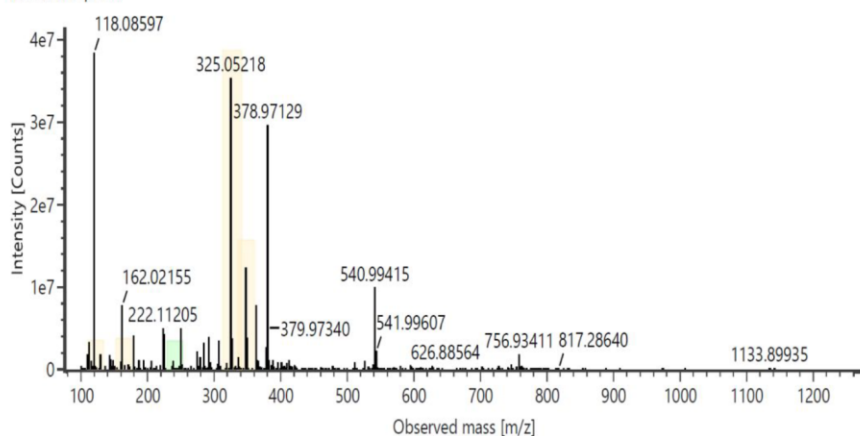
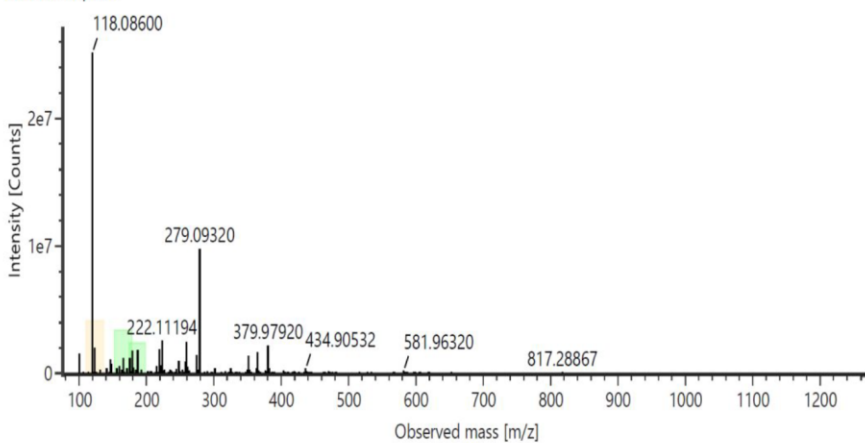


Figure A 2.2 Chromatogram of S-Nitroso-N-acetylcysteine NAC-NO (r.t. 5.73 min), in acetate buffer/MeCN (pH 5.0), showing residues of the starting N-acetylcysteine NAC (r.t. 4.43 min) and the disulphide dimer NAN-NAC (r.t. 3.92 min) originated from the synthesis. (Bottom) Chromatogram built at m/z 164 corresponding to $[M+H]^+$ ion of NAC, proving the relevant impurity of the starting thiol in the synthesized NACNO.

Item name: NAC NO Channel name: Time 5.7308 +/- 0.0405 minutes
Item description:



Item name: NAC NO Channel name: Time 4.4258 +/- 0.0405 minutes
Item description:



Item name: NAC NO Channel name: Time 3.9186 +/- 0.0405 minutes
Item description:

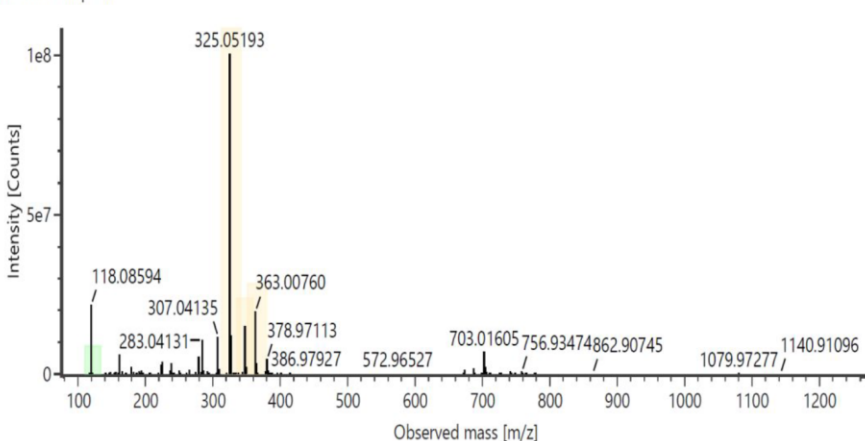
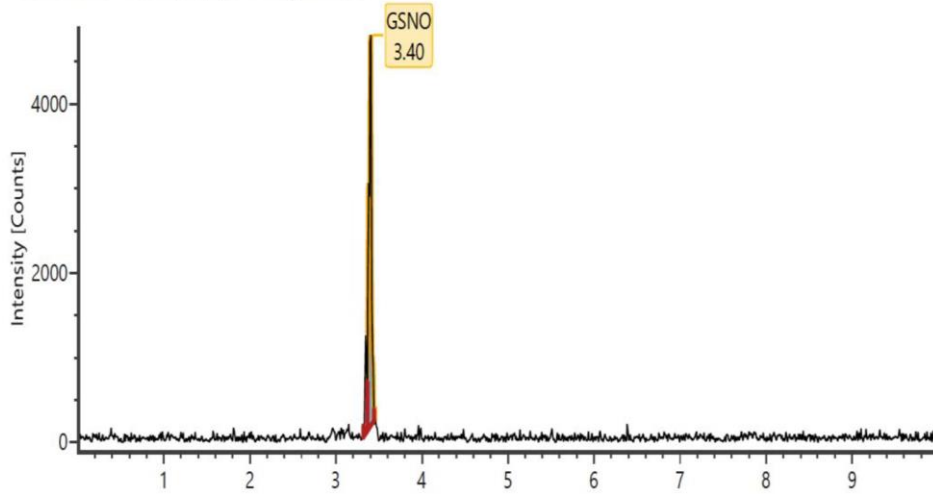


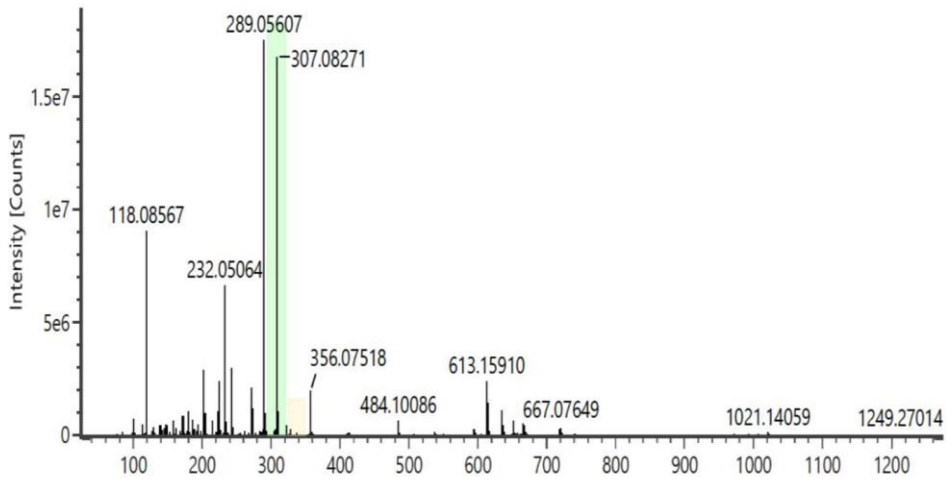
Figure A 2.3 Q-TOF mass spectra of the components identified in fig. A 1.2 (top) S-Nitroso-N-acetylcysteine NAC-NO, (middle) N-acetylcysteine, and (bottom) the corresponding disulphide.

Item name: 4 MBQ + GSNO Pre
Channel name: GSNO [+H] : (37.1 PPM) 337.0814



Item name: 4 MBQ + GSNO Pre 30
Item description:

Channel name: Low energy : Time 3.3904 +/- 0.0281 minutes



Item name: 4 MBQ + GSNO Pre 30
Item description:

Channel name: High energy : Time 3.3904 +/- 0.0281 minutes

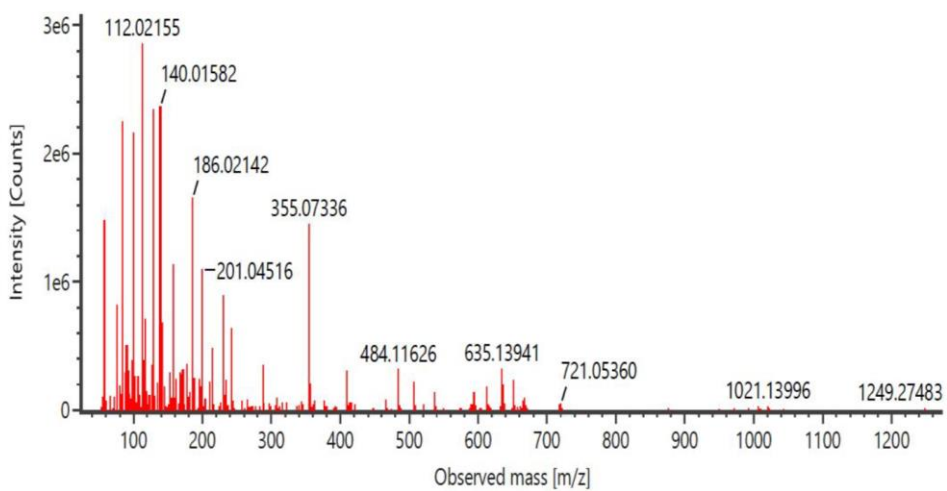
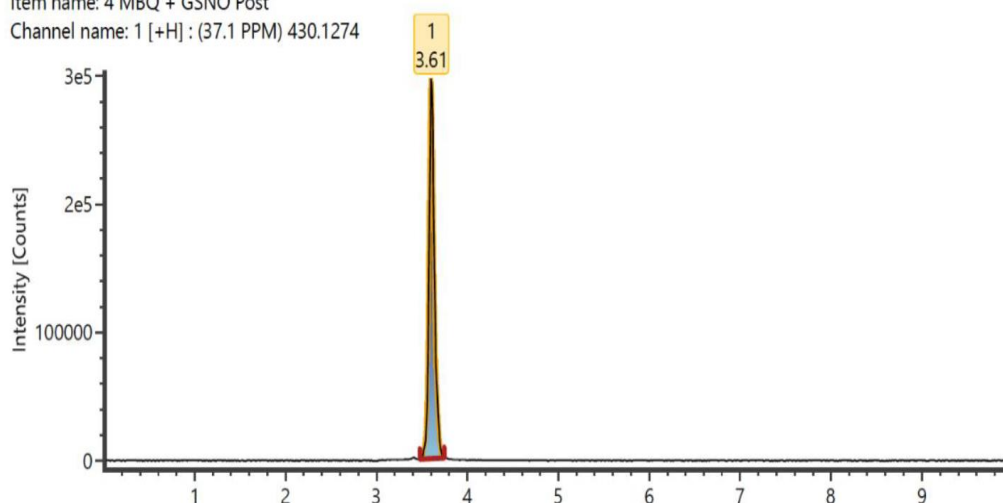


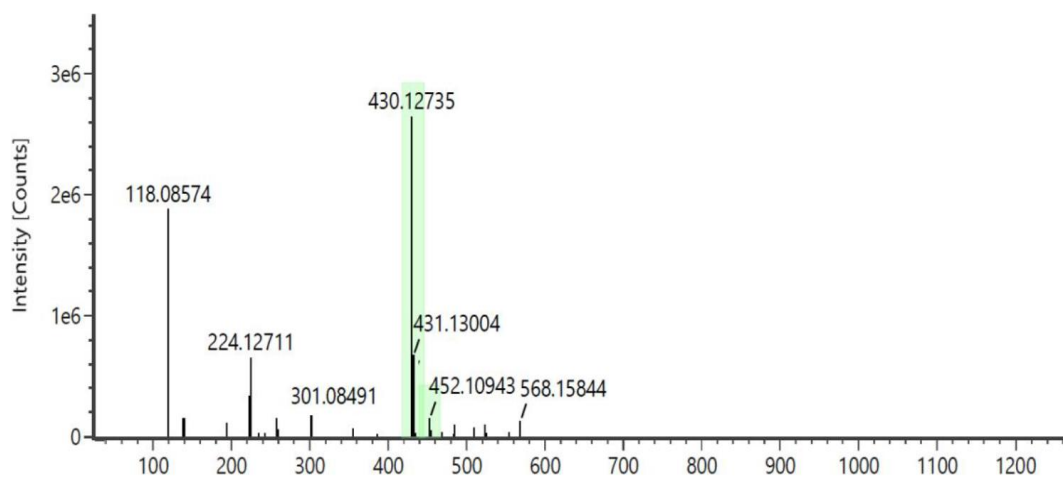
Figure A 2.4 Chromatogram of S-Nitrosoglutathione (GS-NO) $[M+H]^+$, in acetate buffer/MeCN (pH 5.0), before reaction with quinone, (middle) corresponding MS spectrum and (bottom) MS/MS fragmentation pattern of characteristic ion at m/z 307.

Item name: 4 MBQ + GSNO Post
Channel name: 1 [+H] : (37.1 PPM) 430.1274



Item name: 4 MBQ + GSNO Post
Item description:

Channel name: Low energy : Time 3.6098 +/- 0.0342 minutes



Item name: 4 MBQ + GSNO Post 30
Item description:

Channel name: High energy : Time 3.5961 +/- 0.0346 minutes

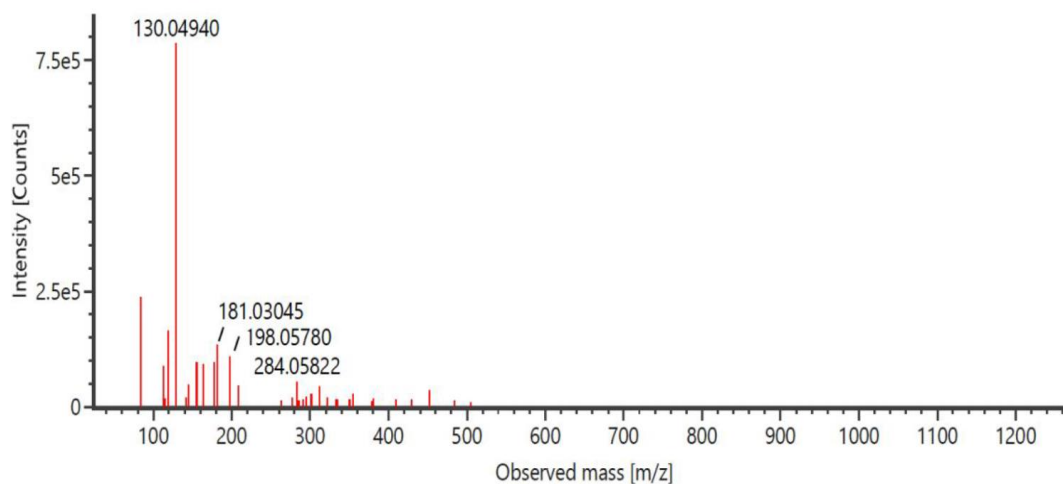
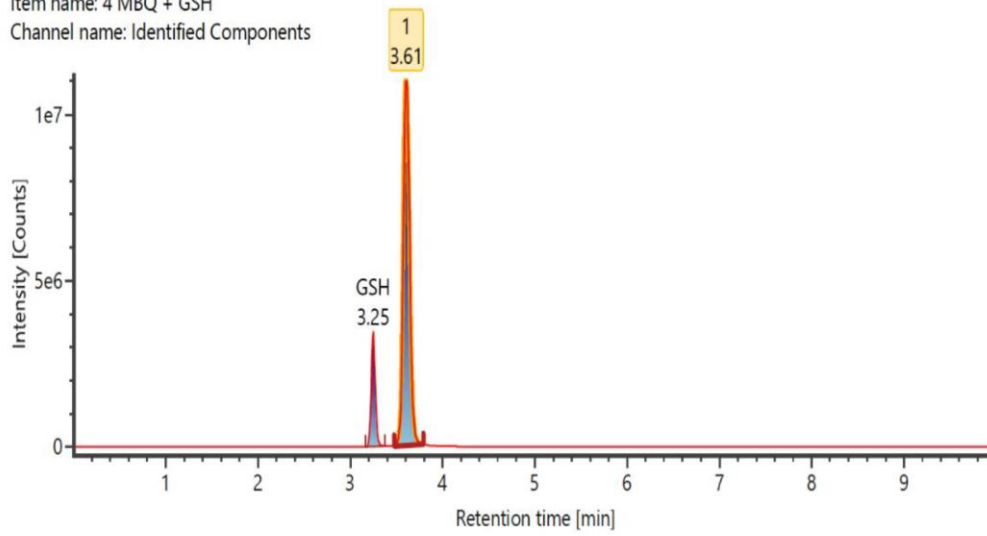


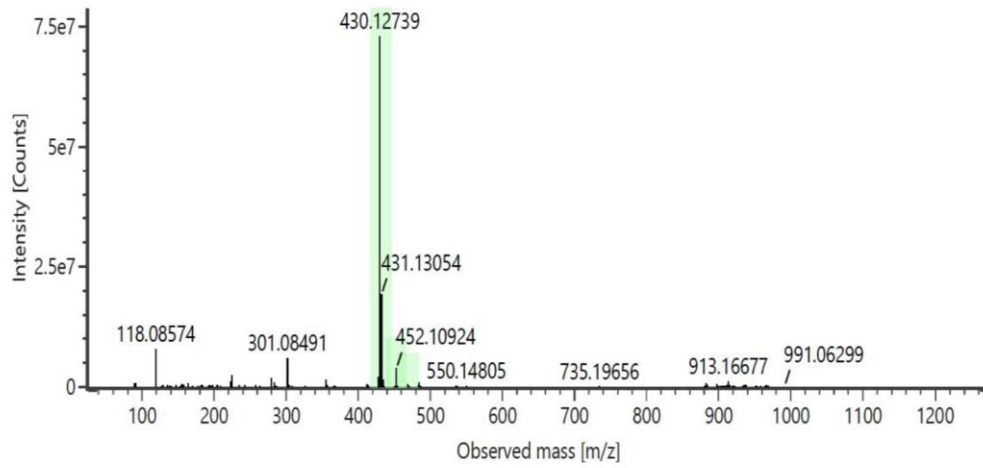
Figure A 2.5 Chromatogram of the adduct obtained by irradiating a solution of 1 mM 4-MBQ and 1 mM GS-NO in acetate buffer/MeCN (pH 5.0), with a Hamamatsu UV - lamp (4500 mW/cm² at 240-400 nm, power 50%) for 5 minutes at 30°C, (middle) corresponding MS spectrum and (bottom) MS/MS fragmentation pattern of characteristic ion at m/z 430.

Item name: 4 MBQ + GSH
Channel name: Identified Components



Item name: 4 MBQ + GSH
Item description:

Channel name: Low energy : Time 3.6123 +/- 0.0948 minutes



Item name: 4 MBQ + GSH
Item description:

Channel name: High energy : Time 3.6123 +/- 0.0948 minutes

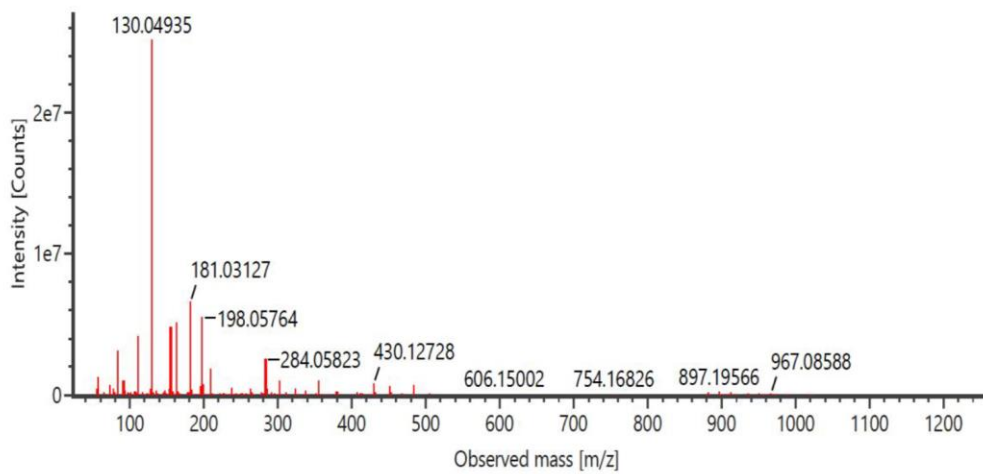


Figure A 2.6 Chromatogram of the adduct obtained by mixing 1 mM 4-MBQ and 1 mM glutathione (GSH) in acetate buffer/MeCN (pH 5.0), and incubation at 30°C for 15 min, (middle)

corresponding MS spectrum and (bottom) MS/MS fragmentation pattern of characteristic ion at m/z 430.

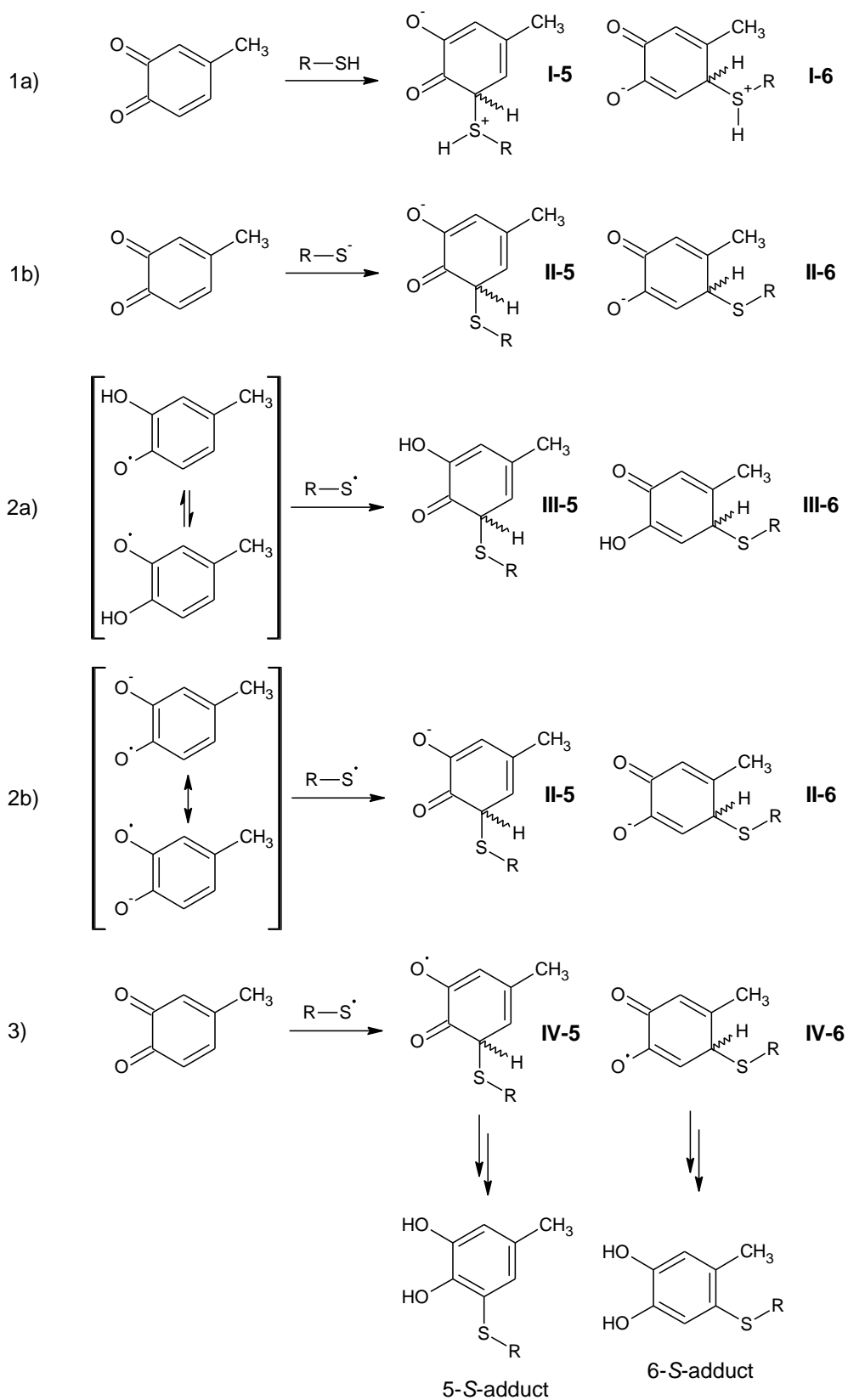


Figure A 2.7. Scheme of the different reaction pathways evaluated by DTF calculations of the reaction of 4-MBQ reactions with thiols, to model the experimentally observed regioselectivity of addition.

NMR spectra

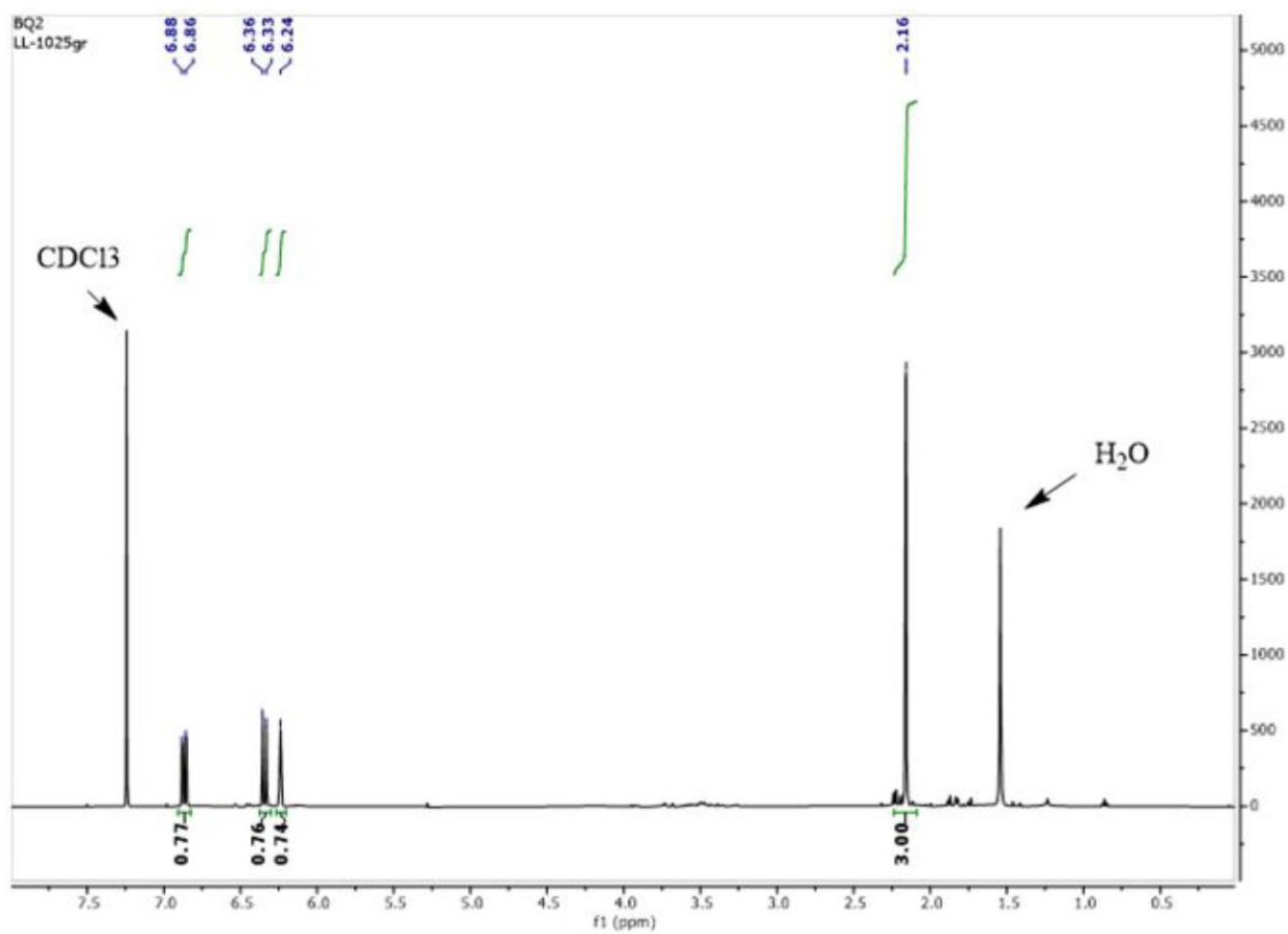


Figure A 2.8 ¹H-NMR spectrum of 4-MBQ (400 MHz, CDCl₃)

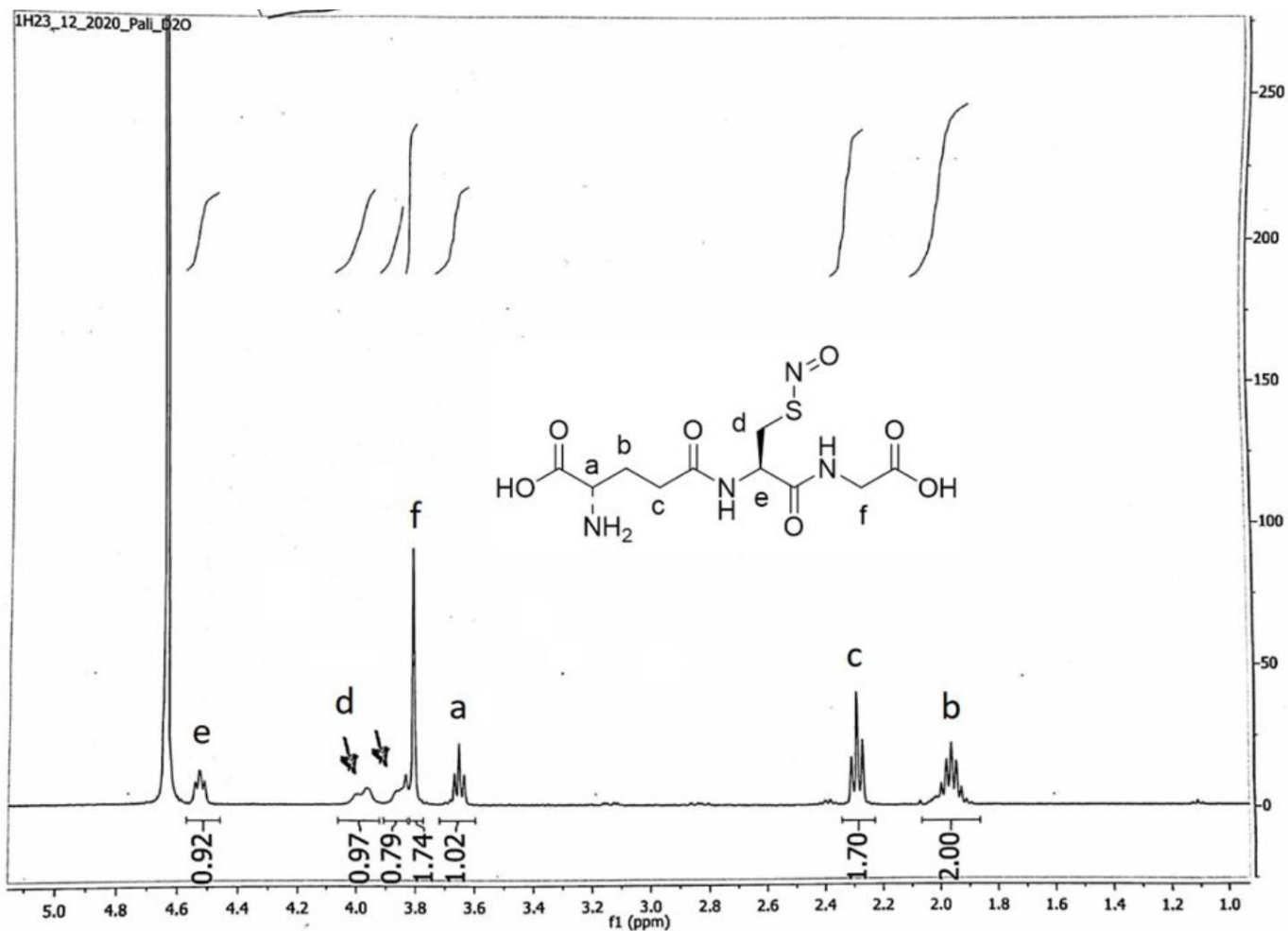


Figure A 2.9 $^1\text{H-NMR}$ spectrum of GS-NO in D_2O at 400 MHz.

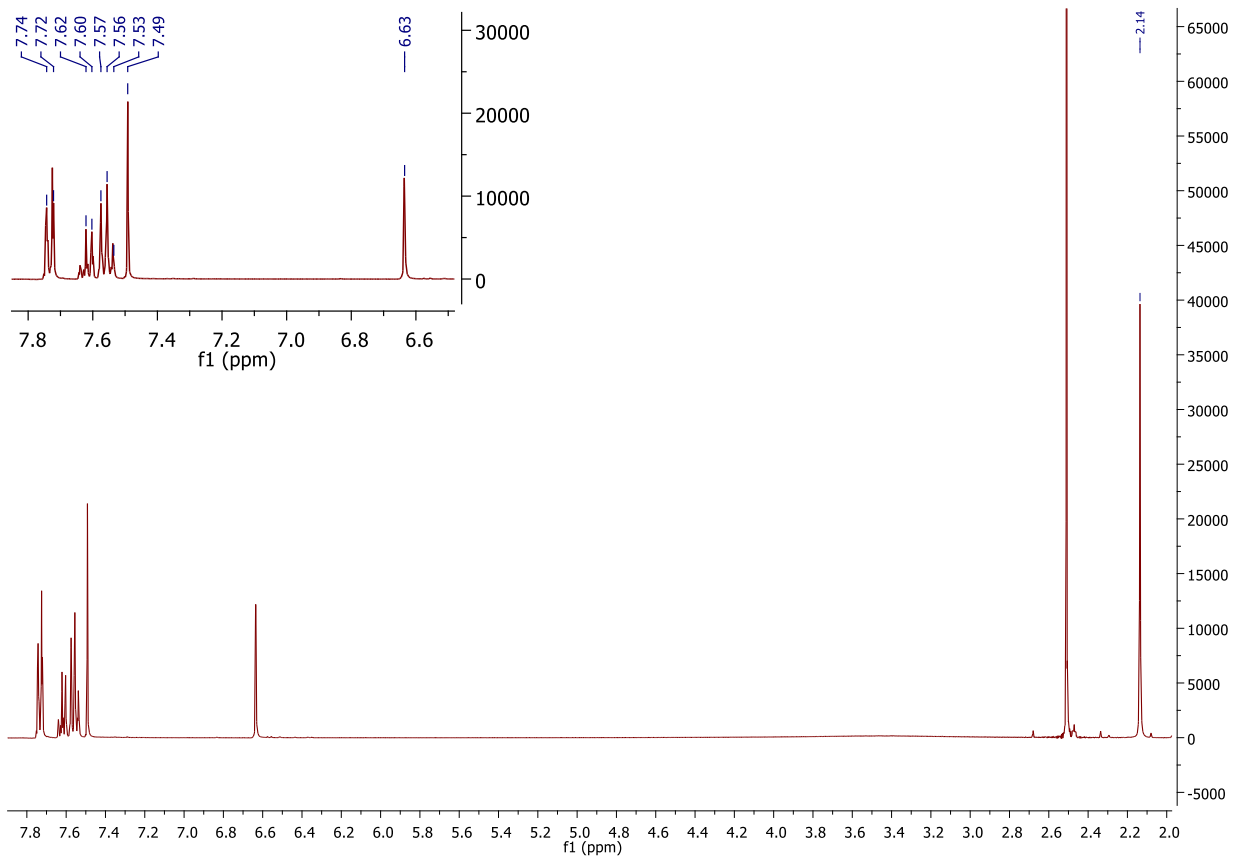


Figure A 2.10 ^1H NMR spectrum of 5-methyl-3-(phenylthiol)benzene 1,2-diol in DMSO-d_6 .

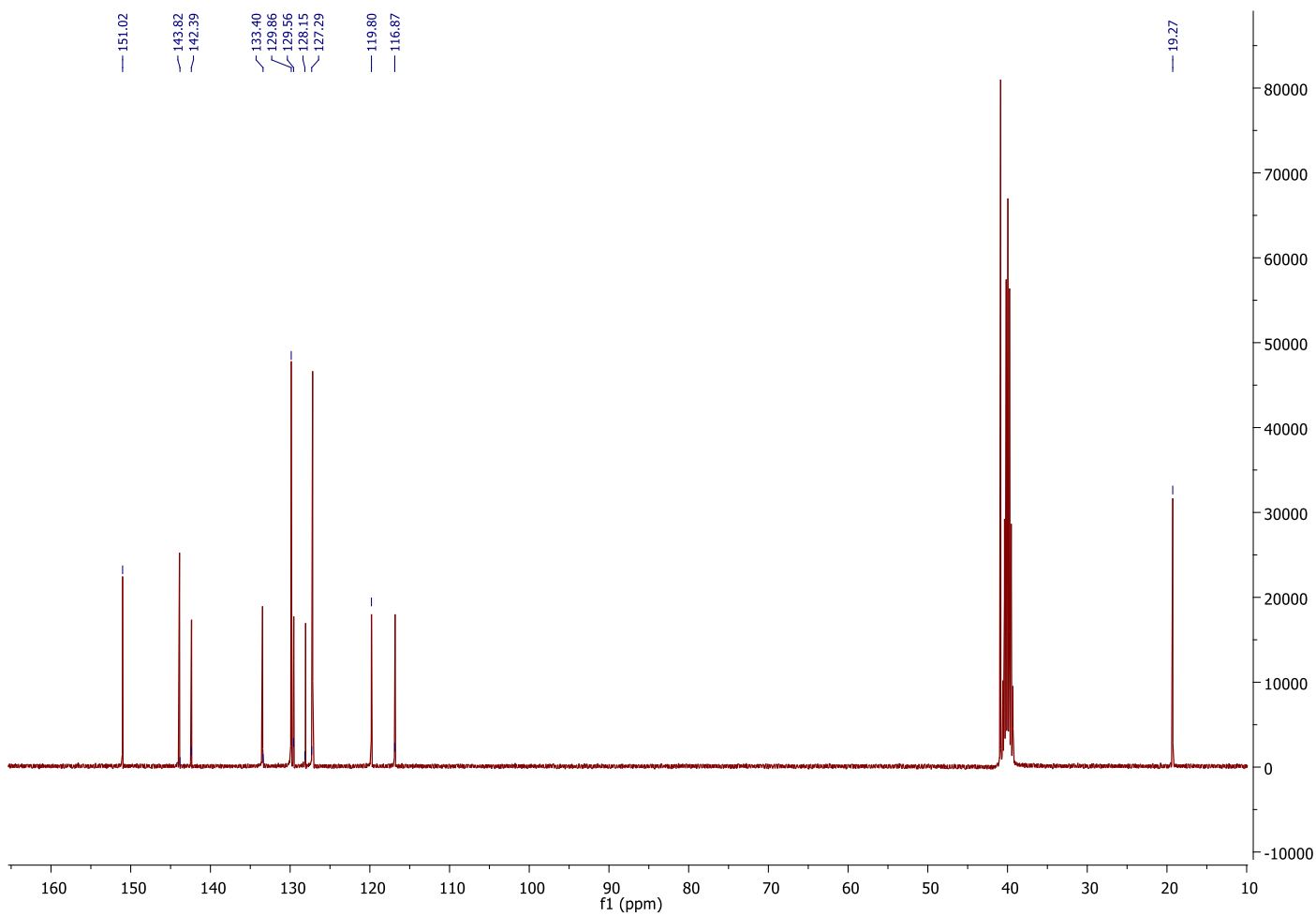


Figure A 2.11. ^{13}C NMR spectrum of 5-methyl-3-(phenylthiol)benzene 1,2-diol in DMSO- d_6 .

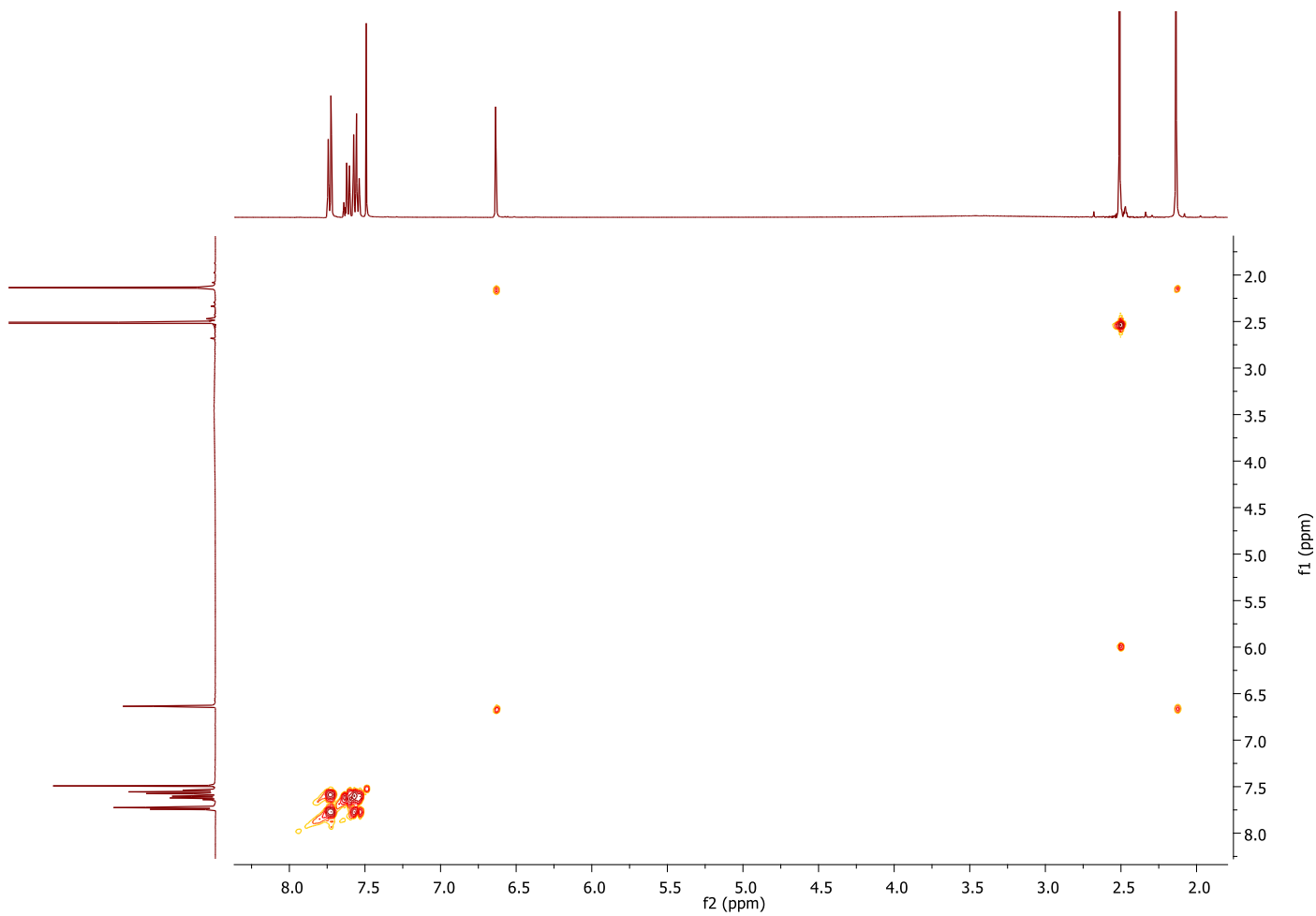


Figure A 2.12. ^1H , ^1H COSY spectrum of 5-methyl-3-(phenylthiol)benzene 1,2-diol in DMSO- d_6 .

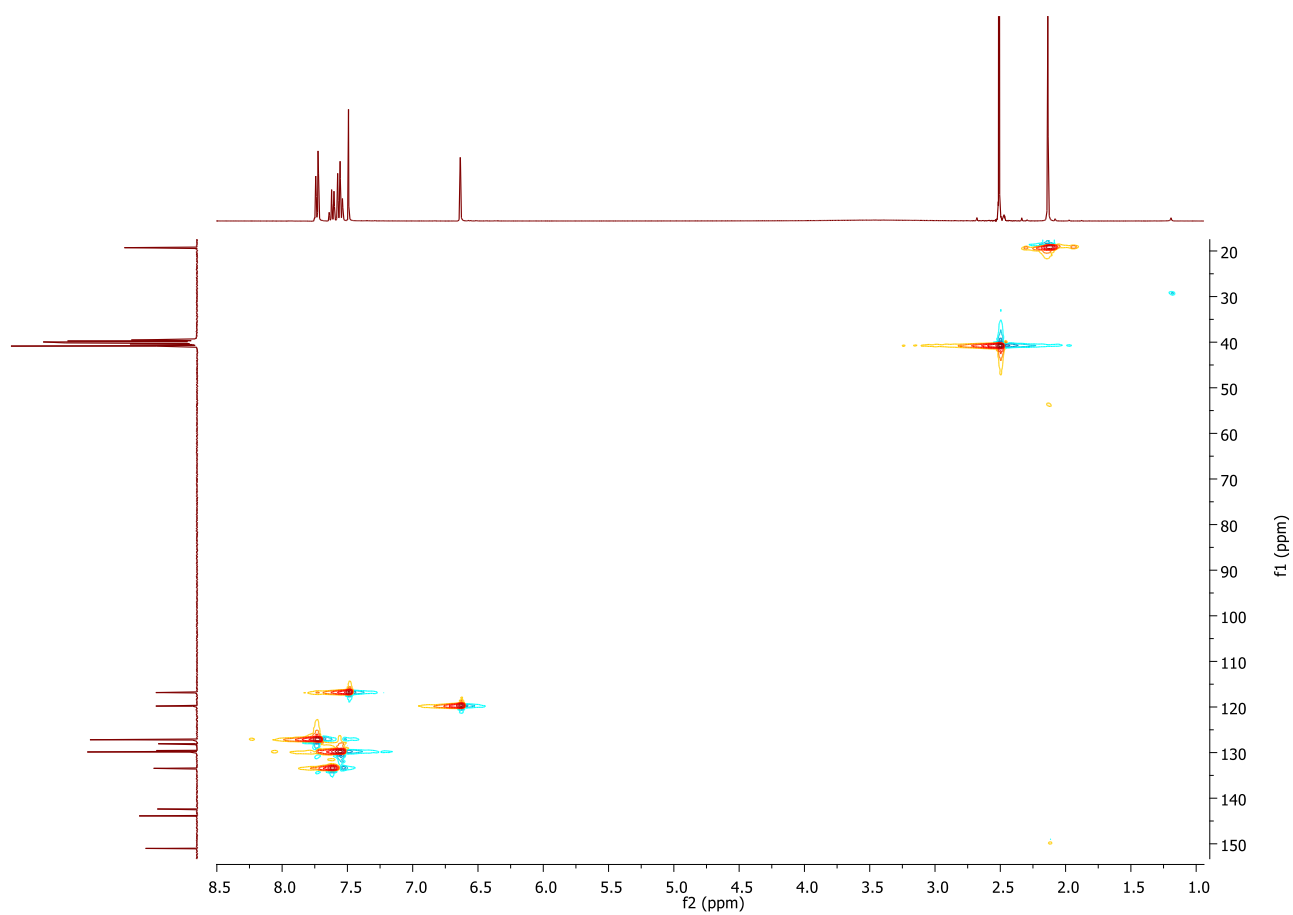


Figure A 2.13. ^1H , ^{13}C HSQC spectrum of 5-methyl-3-(phenylthiol)benzene 1,2-diol in DMSO- d_6 .

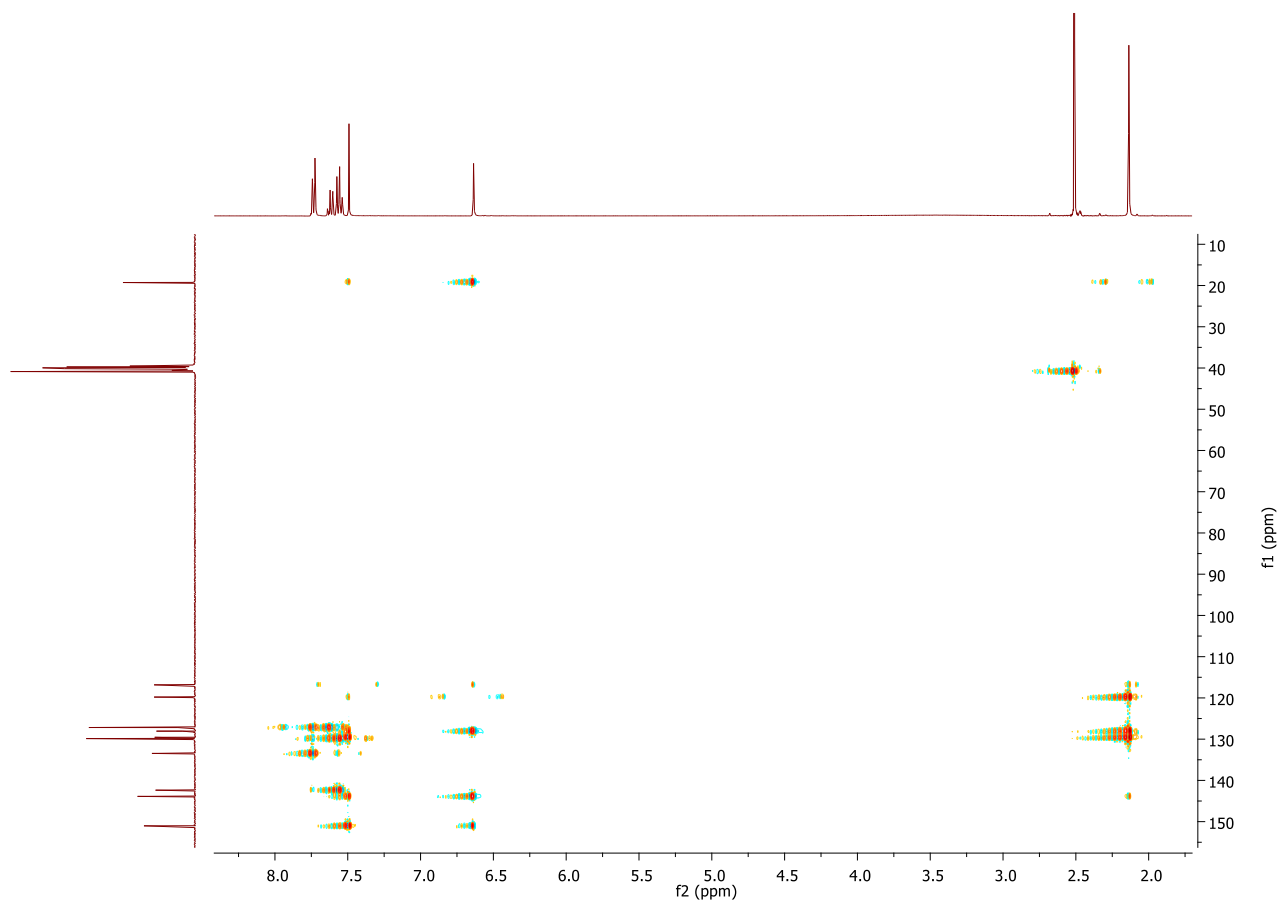


Figure A2.. ^1H , ^{13}C HMBC spectrum of 5-methyl-3-(phenylthiol)benzene 1,2-diol in DMSO- d_6 .

References

- [1] J. Yang, M.A.C. Stuart, M. Kamperman, Jack of all trades: versatile catechol crosslinking mechanisms, *Chem. Soc. Rev.* 43 (2014) 8271–8298. <https://doi.org/10.1039/C4CS00185K>.
- [2] M.L. Alfieri, L. Panzella, R. Amorati, A. Cariola, L. Valgimigli, A. Napolitano. Role of Sulphur and Heavier Chalcogens on the Antioxidant Power and Bioactivity of Natural Phenolic Compounds. *Biomolecules*. 2022 Jan 6;12(1):90. doi: 10.3390/biom12010090.
- [3] A. Napolitano, S. Memoli, G. Prota, A New Insight in the Biosynthesis of Pheomelanins: Characterization of a Labile 1,4-Benzothiazine Intermediate, *J. Org. Chem.* 64 (1999) 3009–3011. <https://doi.org/10.1021/jo981018j>.
- [4] J. Mancebo-Aracil, C. Casagualda, M.Á. Moreno-Villaécija, F. Nador, J. García-Pardo, A. Franconetti-García, F. Busqué, R. Alibés, M.J. Esplandiú, D. Ruiz-Molina, J. Sedó-Vegara, Bioinspired Functional Catechol Derivatives through Simple Thiol Conjugate Addition, *Chemistry – A European Journal*. 25 (2019) 12367–12379. <https://doi.org/10.1002/chem.201901914>.
- [5] A. Napolitano, L. Panzella, L. Leone, M. d’Ischia, Red Hair Benzothiazines and Benzothiazoles: Mutation-Inspired Chemistry in the Quest for Functionality, *Acc. Chem. Res.* 46 (2013) 519–528. <https://doi.org/10.1021/ar300219u>.
- [6] S. Ito, A. Palumbo, G. Prota, Tyrosinase-catalyzed conjugation of dopa with glutathione, *Experientia*. 41 (1985) 960–961. <https://doi.org/10.1007/BF01970033>.
- [7] L. Panzella, A. Napolitano, M. d’Ischia, Oxidative conjugation of chlorogenic acid with glutathione: Structural characterization of addition products and a new nitrite-Promoted pathway, *Bioorganic & Medicinal Chemistry*. 11 (2003) 4797–4805. [https://doi.org/10.1016/S0968-0896\(03\)00460-7](https://doi.org/10.1016/S0968-0896(03)00460-7).
- [8] D. Bassil, D.P. Makris, P. Kefalas, Oxidation of caffeic acid in the presence of l-cysteine: isolation of 2-S-cysteinylcaffeic acid and evaluation of its antioxidant properties, *Food Research International*. 38 (2005) 395–402. <https://doi.org/10.1016/j.foodres.2004.10.009>.
- [9] C. Giulivi, E. Cadenas, One- and two-electron reduction of 2-methyl-1,4-naphthoquinone bioreductive alkylating agents: kinetic studies, free-radical production, thiol oxidation and DNA-strand-break formation, *Biochemical Journal*. 301 (1994) 21–30. <https://doi.org/10.1042/bj3010021>.
- [10] A. Maroz, O. Brede, Reaction of radicals with benzoquinone—addition or electron transfer?, *Radiation Physics and Chemistry*. 67 (2003) 275–278. [https://doi.org/10.1016/S0969-806X\(03\)00051-3](https://doi.org/10.1016/S0969-806X(03)00051-3).
- [11] A. Fujimoto and T. Masuda. Chemical Interaction between Polyphenols and a Cysteinyl Thiol under Radical Oxidation Conditions. *Journal of Agricultural and Food Chemistry* 2012 60 (20), 5142-5151 DOI: 10.1021/jf3008822
- [12] M. De Lucia, L. Panzella, A. Pezzella, A. Napolitano, M. d’Ischia, Plant Catechols and Their S-Glutathionyl Conjugates as Antinitrosating Agents: Expedient Synthesis and Remarkable Potency of 5-S-Glutathionylpiceatannol, *Chem. Res. Toxicol.* 21 (2008) 2407–2413. <https://doi.org/10.1021/tx800283d>.
- [13] H. Karoui, N. Hogg, C. Fréjaville, P. Tordo, B. Kalyanaraman, Characterization of Sulfur-centered Radical Intermediates Formed during the Oxidation of Thiols and Sulfite by Peroxynitrite, *Journal of Biological Chemistry*. 271 (1996) 6000–6009. <https://doi.org/10.1074/jbc.271.11.6000>.
- [14] M.E. Mullins, J.S. Stamler, J.A. Osborne, J. Loscalzo, D.J. Singel, EPR spectroscopic characterization of biological thiyl radicals as PBN spin-trap adducts, *Appl. Magn. Reson.* 3 (1992) 1021. <https://doi.org/10.1007/BF03166170>.
- [15] D.I. Potapenko, E. G. Bagryanskaya, Y. P. Tsentalovich, V. A. Reznikov, T. L. Clanton, and V. V. Khramtsov. Reversible Reactions of Thiols and Thiyl Radicals with Nitron Spin Traps. *The Journal of Physical Chemistry B* 2004 108 (26), 9315-9324. DOI: 10.1021/jp049026t
- [16] D. N. Polovyanenko, V. F. Plyusnin, V. A. Reznikov, V. V. Khramtsov, and E. G. Bagryanskaya. Mechanistic Studies of the Reactions of Nitron Spin Trap PBN with Glutathionyl Radical. *The Journal of Physical Chemistry B* 2008 112 (15), 4841-4847. DOI: 10.1021/jp711548x
- [17] D. N. Polovyanenko, S. R. A. Marque, S. Lambert, L. Jicsinszky, V. F. Plyusnin, and E. G. Bagryanskaya. Electron Paramagnetic Resonance Spin Trapping of Glutathionyl Radicals by PBN in the Presence of Cyclodextrins and by PBN Attached to β -Cyclodextrin. *The Journal of Physical Chemistry B* 2008 112 (41), 13157-13162. DOI: 10.1021/jp8050164

- [18] S. Ito, T. Kato, K. Shinpo, K. Fujita, Oxidation of tyrosine residues in proteins by tyrosinase. Formation of protein-bonded 3,4-dihydroxyphenylalanine and 5-S-cysteinyl-3,4-dihydroxyphenylalanine., *Biochem J.* 222 (1984) 407–411.
- [19] A. Napolitano, S. Memoli, O. Crescenzi, G. Prota, Oxidative Polymerization of the Pheomelanin Precursor 5-Hydroxy-1,4-benzothiazinylalanine: A New Hint to the Pigment Structure, *J. Org. Chem.* 61 (1996) 598–604. <https://doi.org/10.1021/jo951149+>.
- [20] M.S. Cabeza, S.A. Guerrero, A.A. Iglesias, D.G. Arias, New enzymatic pathways for the reduction of reactive oxygen species in *Entamoeba histolytica*, *Biochimica et Biophysica Acta (BBA) - General Subjects.* 1850 (2015) 1233–1244. <https://doi.org/10.1016/j.bbagen.2015.02.010>.
- [21] T.W. Hart, Some observations concerning the S-nitroso and S-phenylsulphonyl derivatives of L-cysteine and glutathione, *Tetrahedron Letters.* 26 (1985) 2013–2016. [https://doi.org/10.1016/S0040-4039\(00\)98368-0](https://doi.org/10.1016/S0040-4039(00)98368-0).
- [22] W.M. Jones, J.B. Tapia, R.R. Tuttle, M.M. Reynolds, Thermogravimetric Analysis and Mass Spectrometry Allow for Determination of Chemisorbed Reaction Products on Metal Organic Frameworks, *Langmuir.* 36 (2020) 3903–3911. <https://doi.org/10.1021/acs.langmuir.0c00158>.
- [23] A.J. McGrath, G.E. Garrett, L. Valgimigli, D.A. Pratt, The redox chemistry of sulfenic acids, *J Am Chem Soc.* 132 (2010) 16759–16761. <https://doi.org/10.1021/ja1083046>.
- [24] R. Amorati, G.F. Pedulli, D.A. Pratt, L. Valgimigli, TEMPO reacts with oxygen-centered radicals under acidic conditions, *Chem. Commun.* 46 (2010) 5139–5141. <https://doi.org/10.1039/C0CC00547A>.
- [25] L. Valgimigli, K.U. Ingold, J. Lusztyk, Solvent Effects on the Reactivity and Free Spin Distribution of 2,2-Diphenyl-1-picrylhydrazyl Radicals(1), *J Org Chem.* 61 (1996) 7947–7950. <https://doi.org/10.1021/jo9608578>.
- [26] Gaussian 09 Citation
- [27] F. Neese, The ORCA program system, *WIREs Computational Molecular Science.* 2 (2012) 73–78. <https://doi.org/10.1002/wcms.81>.
- [28] F. Neese, Software update: the ORCA program system, version 4.0, *WIREs Computational Molecular Science.* 8 (2018) e1327. <https://doi.org/10.1002/wcms.1327>.
- [29] C. Adamo, V. Barone, Toward reliable density functional methods without adjustable parameters: The PBE0 model, *J. Chem. Phys.* 110 (1999) 6158–6170. <https://doi.org/10.1063/1.478522>.
- [30] J.-D. Chai, M. Head-Gordon, Long-range corrected hybrid density functionals with damped atom–atom dispersion corrections, *Phys. Chem. Chem. Phys.* 10 (2008) 6615–6620. <https://doi.org/10.1039/B810189B>.
- [31] J.M. Smith, Y. Jami Alahmadi, C.N. Rowley. Range-Separated DFT Functionals are Necessary to Model Thio-Michael Additions. *J Chem Theory Comput.* 2013 Nov 12;9(11):4860-5. doi: 10.1021/ct400773k.
- [32] Y. Zhao, D.G. Truhlar, The M06 suite of density functionals for main group thermochemistry, thermochemical kinetics, noncovalent interactions, excited states, and transition elements: two new functionals and systematic testing of four M06-class functionals and 12 other functionals, *Theor Chem Account.* 120 (2008) 215–241. <https://doi.org/10.1007/s00214-007-0310-x>.
- [33] G.E. Scuseria, C.L. Janssen, H.F. Schaefer, An efficient reformulation of the closed-shell coupled cluster single and double excitation (CCSD) equations, *J. Chem. Phys.* 89 (1988) 7382–7387. <https://doi.org/10.1063/1.455269>.
- [34] G.E. Scuseria, H.F. Schaefer, Is coupled cluster singles and doubles (CCSD) more computationally intensive than quadratic configuration interaction (QCISD)?, *J. Chem. Phys.* 90 (1989) 3700–3703. <https://doi.org/10.1063/1.455827>.
- [35] J.A. Pople, M. Head-Gordon, K. Raghavachari, Quadratic configuration interaction. A general technique for determining electron correlation energies, *J. Chem. Phys.* 87 (1987) 5968–5975. <https://doi.org/10.1063/1.453520>.
- [36] D.E. Woon, T.H. Dunning, Gaussian basis sets for use in correlated molecular calculations. III. The atoms aluminum through argon, *J. Chem. Phys.* 98 (1993) 1358–1371. <https://doi.org/10.1063/1.464303>.
- [37] E.R. Davidson, Comment on “Comment on Dunning’s correlation-consistent basis sets,” *Chemical Physics Letters.* 260 (1996) 514–518. [https://doi.org/10.1016/0009-2614\(96\)00917-7](https://doi.org/10.1016/0009-2614(96)00917-7).
- [38] E. Papajak, J. Zheng, X. Xu, H. R. Leverentz, and D. G. Truhlar Perspectives on Basis Sets Beautiful: Seasonal Plantings of Diffuse Basis Functions. *Journal of Chemical Theory and Computation* 2011 7 (10), 3027-3034. DOI: 10.1021/ct200106a

- [39] K.A. Peterson, T.B. Adler, H.-J. Werner, Systematically convergent basis sets for explicitly correlated wavefunctions: The atoms H, He, B–Ne, and Al–Ar, *J. Chem. Phys.* 128 (2008) 084102. <https://doi.org/10.1063/1.2831537>.
- [40] S. Miertuš, E. Scrocco, J. Tomasi, Electrostatic interaction of a solute with a continuum. A direct utilization of AB initio molecular potentials for the prevision of solvent effects, *Chemical Physics*. 55 (1981) 117–129. [https://doi.org/10.1016/0301-0104\(81\)85090-2](https://doi.org/10.1016/0301-0104(81)85090-2).
- [41] M. Cossi, G. Scalmani, N. Rega, V. Barone, New developments in the polarizable continuum model for quantum mechanical and classical calculations on molecules in solution, *J. Chem. Phys.* 117 (2002) 43–54. <https://doi.org/10.1063/1.1480445>.
- [42] G. Scalmani, V. Barone, K.N. Kudin, C.S. Pomelli, G.E. Scuseria, M.J. Frisch, Achieving linear-scaling computational cost for the polarizable continuum model of solvation, *Theor Chem Acc.* 111 (2004) 90–100. <https://doi.org/10.1007/s00214-003-0527-2>.
- [43] J. Tomasi, B. Mennucci, R. Cammi, Quantum mechanical continuum solvation models, *Chem Rev.* 105 (2005) 2999–3093. <https://doi.org/10.1021/cr9904009>.
- [44] A.K. Rappe, C.J. Casewit, K.S. Colwell, W.A.I. Goddard, W.M. Skiff, UFF, a full periodic table force field for molecular mechanics and molecular dynamics simulations, *J. Am. Chem. Soc.* 114 (1992) 10024–10035. <https://doi.org/10.1021/ja00051a040>.
- [45] D. M. York and M. Karplus. A Smooth Solvation Potential Based on the Conductor-Like Screening Model. *The Journal of Physical Chemistry A* 1999 103 (50), 11060-11079. DOI: 10.1021/jp992097l

CHAPTER 3

Oxygen uptake kinetics as a powerful tool to investigate polyphenol-oxidase (PPO) reaction and its inhibition.

Natural phenols as potent anti-melanogenic agents

Abstract

A new method for studying tyrosinase kinetics and its inhibition is described. It is based on oxygen sensing during the progress of tyrosinase reaction, taking advantage of the role of oxygen as the obliged oxidant in polyphenol oxidase chemistry. The method is matched to the conventional spectrophotometric approach. The stoichiometric ratio of O₂ uptake to dopachrome formation was 1.5 ± 0.2 for substrate L- tyrosine and 1.0 ± 0.1 for L-DOPA. With both methods, we reinvestigated mushroom tyrosinase inhibition by glabridin from *Glycyrrhiza glabra*. The two methods agreed showing mixed-type inhibition for monophenolase and diphenolase activities, at variance with previous literature. Average KI (KI') values for glabridin were 13.6 ± 3.5 (281 ± 89) nM and 57 ± 8 (1312 ± 550) nM, for monophenolase and diphenolase inhibition, respectively, with IC₅₀ of 80 ± 8 nM and 294 ± 25 nM, respectively, at 1 mM substrate. For reference kojic acid K_I (K_I') were 10.9 ± 8 (217 ± 55) μ M and 9.9 ± 1.4 (21.0 ± 5.2) μ M, for monophenolase and diphenolase, respectively, with respective IC₅₀ of 33 ± 8 μ M and 17 ± 3 μ M. Glabridin's activity is among the highest in nature, being about three orders of magnitude higher than previously reported.

To validate the method with other molecules defined from previous literature "tyrosinase inhibitors" it is applied to investigate the anti-tyrosinase activity of Bakuchiol. It is a phytochemical isolated from *Psoralea corylifolia* (Babki), which has gained very high interest in recent dermatological research as skin protectant, anti-age and depigmenting phytochemical. Combination of both oxygen sensing during tyrosinase reaction and UV-vis monitoring of dopachrome formation (475 nm), showed competitive inhibition with average K_I constant (μ M, 30 °C, pH 6.8) of 6.71 ± 1.23 and 1.15 ± 0.34 for monophenolase and diphenolase reactions respectively, with respective IC₅₀ 37.22 ± 5.18 and 6.91 ± 0.96 ~ at 1 mM substrate. In order to complete the analysis of the compound it has been associated other two different techniques. Firstly, the fluorescence spectroscopy to characterize the bonding type between the tyrosinase active site and Bakuchiol. Fluorescence quenching showed a single binding mode with formation constant K_a 1.02×10^6 M⁻¹. Secondly, we studied the antioxidant

activity of bakuchiol, since its combination with the anti-tyrosinase activity would complete the picture of its bioactivity. We used the inhibited autoxidation of styrene and cumene (PhCl, 30 °C) as a kinetic model in homogenous solution, which afforded inhibition constant $k_{inh} = 18.1 \pm 6.6$ ($10^4 \text{ M}^{-1}\text{s}^{-1}$, 30 °C). Inhibition of the autoxidation of MeLin in Triton™ X-100 micelles afforded instead $k_{inh} = 0.16 \pm 0.03$ ($10^4 \text{ M}^{-1}\text{s}^{-1}$, 37 °C). Stoichiometric factor was 1.9 ± 0.1 in both models. ReqEPR spectroscopy afforded the BDE(OH) as 81.7 ± 0.1 kcal/mol. Our results demonstrate that bakuchiol is a potent tyrosinase inhibitor with good antioxidant activity having major potential both in dermatological treatments and as natural food preservative against oxidation and food-browning

INTRODUCTION

3.1 Tyrosinase enzyme and its inhibition

3.1.1 Inhibition of melanin biosynthesis in the biomedical, cosmetic and food-safety fields

Melanin is a pigment that is produced by a variety of organisms, including humans, plants, and animals. It is synthesized from the oxidation and polymerization of phenolic precursors and is primarily regulated by the enzyme tyrosinase (TYR) [1]. Melanin is also involved in phenotypical expression. Its most important form is Eumelanin which is the dark pigment responsible for the color of skin, eyes and hair. Insertion of the sulfurated aminoacid cysteine causes the formation of red-colored pheomelanin. But beside the type of melanin, the actual level of biosynthesis of Eumelanin modulates the phenotypical color. Melanin has several important biological functions and properties, including providing protection from radiation, serving as an antioxidant [2], and protecting against neurodegeneration. It is also being studied for its potential use in the development of bioinspired materials [3] [4]. In addition to its protective functions, melanin can also be a problem when its production is dysregulated [5], leading to conditions such as hyperpigmentation, melasma, and photo-induced dyschromia. In the

food industry, the production of melanin-like pigments can lead to enzymatic browning [6] and other deterioration processes [7], such as changes in flavour and odour, and a loss of nutritional value [8] [9] [10]. Therefore, the inhibition of melanin production has become an important strategy in food preservation, as well as in the cosmetic and biomedical fields [11]. Several review articles have discussed in-depth some well-known and commercial skin-whitening agents, such as hydroquinone, kojic acid, arbutin, magnesium ascorbyl phosphate, licorice extract, aloesin, azelaic acid, soybean extract, and niacinamide [12]. Naturally occurring skin-whitening agents exert their effects by regulating melanin production through a number of mechanisms, including inhibiting the expression and activity of TYR and suppressing the uptake and distribution of melanosomes. In the cosmetics industry, since skin-whitening compounds from natural sources are usually more appealing to consumers, a greater demand exists for inhibitors of melanogenesis derived from plants that prevent hyperpigmentary disorders [13].

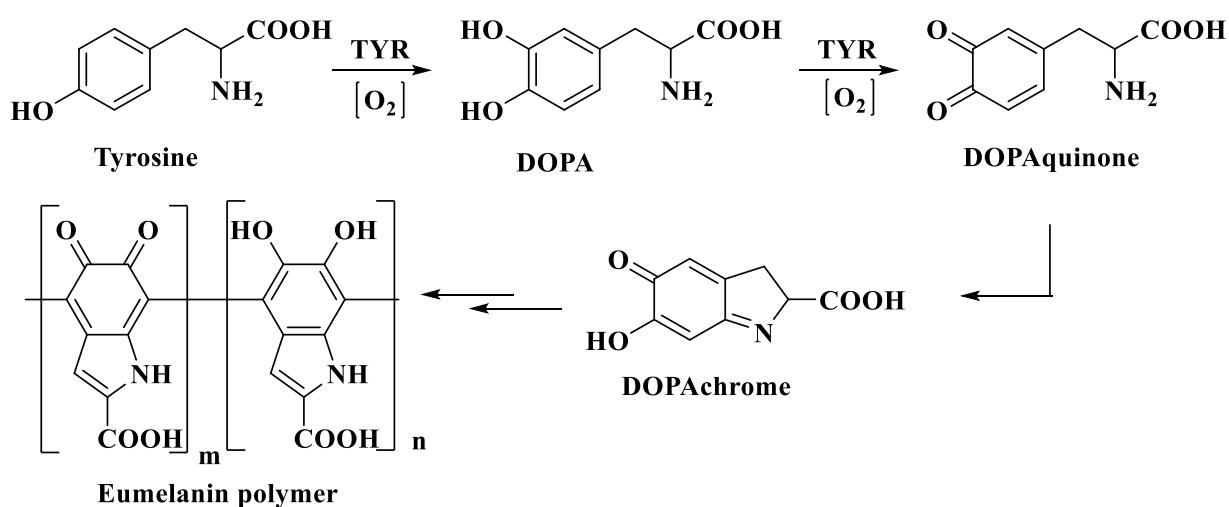


Fig. 3.1 Melanin biosynthesis

3.1.2 Tyrosinase enzyme

Tyrosinase is a polyphenol oxidase (PPO), a type-3 copper enzyme that is involved in the production of pigments in animals, plants, and fungi. It plays a key role in melanogenesis, which is the process by which the pigment is produced in the skin, hair, and eyes of animals. The enzyme has three forms, which are the deoxy-form, oxy-form, and met-form, and it catalyses two types of reactions: the ortho-hydroxylation of

monophenols to o-diphenols and the oxidation of o-diphenols to o-quinones [14]. Both these reactions use molecular oxygen as co-substrate [15]. The active site of tyrosinase contains two copper ions and three histidine residues, which are responsible for its catalytic activity. Tyrosinase is important in many biological processes, not limited to the development of skin, hair, and eye colour, but also extended to the ripening and browning of fruit, vegetables and animal food (*e.g.* shrimps).

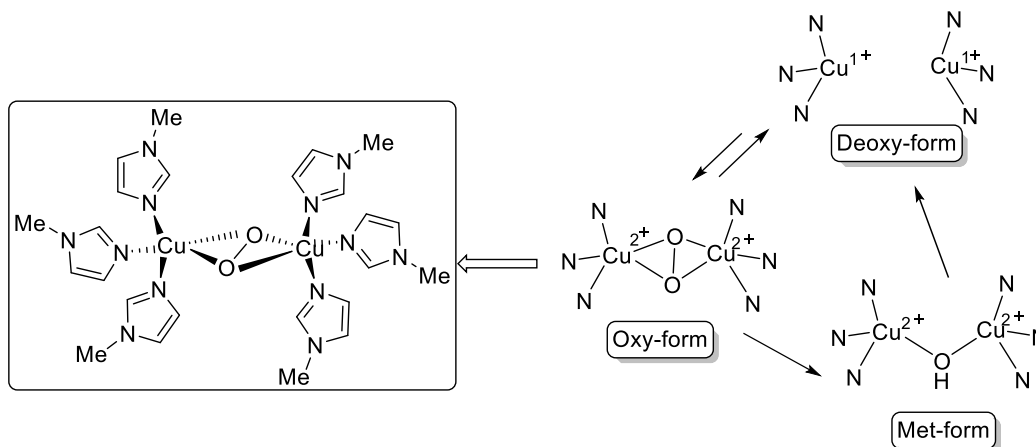


Fig. 3.2 Tyrosinase active site and its three forms.

Tyrosinase has two main activities named monophenolase activity and diphenolase activity, respectively. The monophenolase activity coincides with the conversion of monophenols into o-diphenols, while the diphenolase activity converts o-diphenols into o-quinones. These reactions are important in the process of melanogenesis, which is the production of pigment in animal or vegetal tissues. The active form of tyrosinase responsible for the monophenolase activity is the oxy-form, while both the oxy-form and met-form are involved in the diphenolase activity. From a kinetic perspective, it is well known that the monophenolase activity of tyrosinase shows a lag period before the formation of products is observed, this exists until a sufficient amount of catechol is produced [16]. The length of the lag time in the monophenolase reaction can be influenced by various factors, including the enzyme source, the concentration of monophenol, the enzyme concentration, and the presence of transition metal ions. Tyrosinase has been purified from a variety of species, including plants, animals, and

microbes, and mushroom tyrosinase (mTYR) from *Agaricus bisporus* has been extensively studied as a model system for the screening of tyrosinase inhibitors [17].

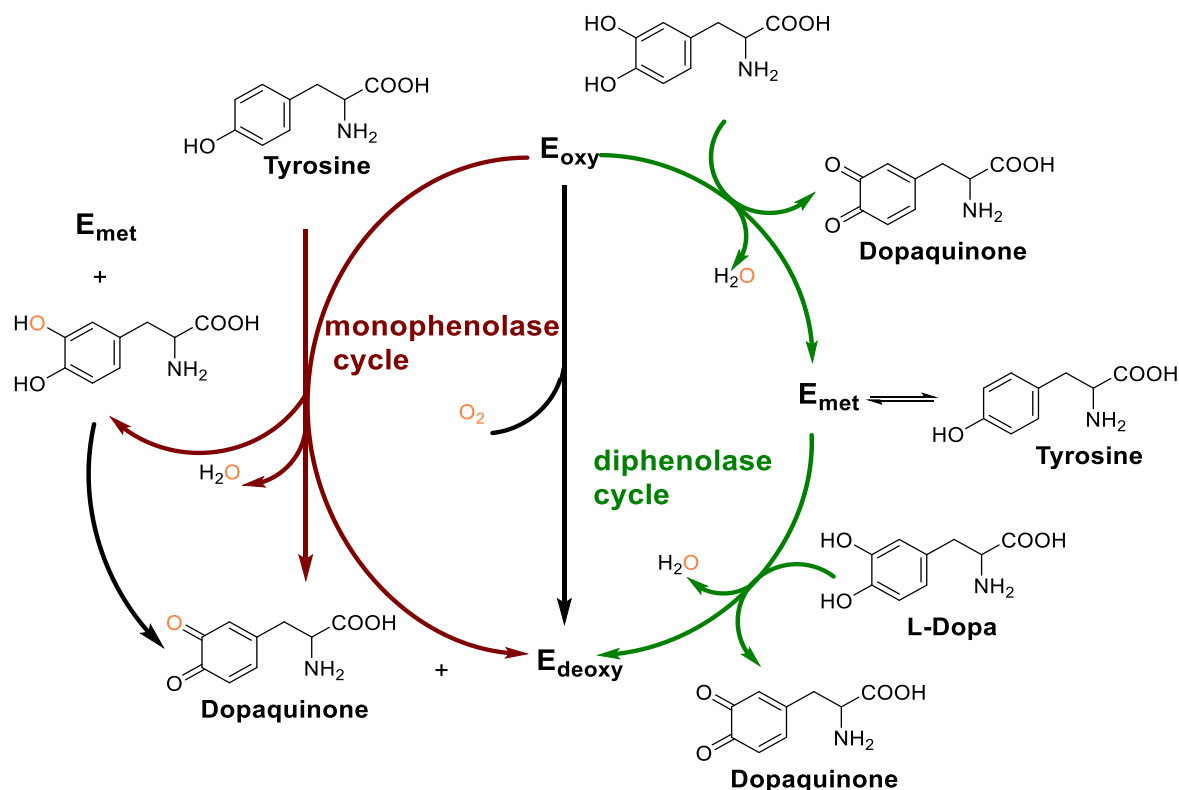


Fig. 3.3. Monophenolase and diphenolase catalytic activities of tyrosinase enzyme.

3.1.3 Enzyme inhibition mechanism

Enzyme inhibitors are substances that reduce the rate of an enzyme-catalyzed reaction by interacting with the enzyme, cofactor, or substrate. There are two main types of inhibitors: reversible and irreversible. Irreversible inhibitors form a covalent bond with the enzyme and inactivate it permanently, while reversible inhibitors can be separated from the enzyme to restore its activity. Reversible inhibitors can be further classified on the basis of their mechanism of inhibition and the effect they have on the enzyme's kinetic parameters. These types of reversible inhibition include *competitive*, *uncompetitive*, *noncompetitive*, and *mixed* inhibition [18]. Irreversible inhibitors are specific for tyrosinase and do not inactivate all proteins, instead, they work by altering the active site of the enzyme. They often contain reactive functional groups that modify amino acid residues in the enzyme, such as cysteine or L-tyrosine, which are essential

for its activity. Regardless of the exact mechanism of an enzyme reaction, a kinetic characterization often makes use of the simple Michaelis–Menten model:

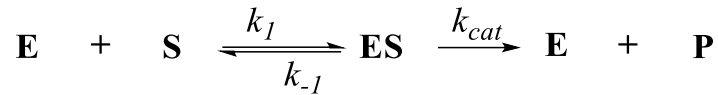


Fig. 3.4. basic one substrate enzyme kinetic model.

[E], [S] and [ES] are, respectively, the concentrations of the enzyme, substrate, and the enzyme-substrate complex at time t . Michaelis and Menten, in 1913, hypothesized that an equilibrium was obtained and maintained between E, S and ES. Therefore, a hyperbolic relationship (Eq. 3.1) exists between the initial velocity, V_0 , and initial substrate concentration [S], such that at a constant total enzyme concentration, [E]:

$$V_0 = \frac{d[\text{P}]}{dt} = V_{\max} \frac{[\text{S}]}{K_M + [\text{S}]} \quad (3.1)$$

This is referred to as the Michaelis-Menten equation. K_m is the Michaelis-Menten constant, which corresponds to the substrate concentration that gives half maximum velocity. V_{\max} is the limiting initial velocity, at any specific total enzyme concentration, under “saturating” substrate concentration. K_m is independent of enzyme concentration, while V_{\max} increases as the total concentration of the enzyme increases. The kinetic equations describing the different types of reversible inhibition and their behaviour is summarized in Table 3.1. For reversible inhibition, the full inhibition is usually obtained extremely rapidly since there is no chemical reaction involved where the dissociation constant for the reaction (k_{-1}/k_{+1}), is defined as the inhibitor constant, K_i .

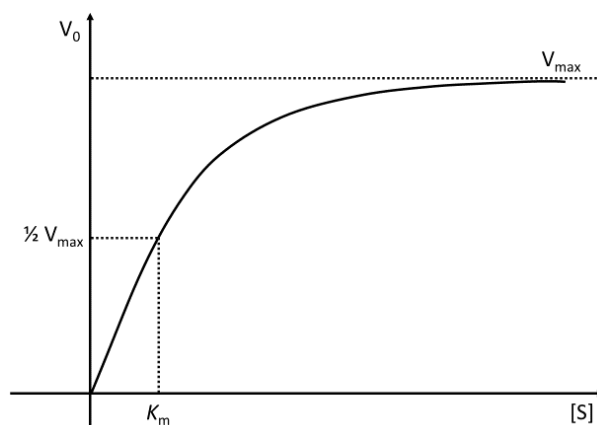


Fig. 3.5 Hyperbolic plot of Michaelis-Menten kinetic model.

Table 3.1. Relationships between apparent K_m , V_{\max} and the inhibition constant for different reversible inhibition types.

Type of inhibition	V^{app}	V^{app}/K_m^{app}	K_m^{app}
Competitive	V	$\frac{V/K_m}{1 + [I]/K_I}$	$K_m(1 + [I]/K_I)$
Mixed	$\frac{V}{1 + [I]/K_I}$	$\frac{V/K_m}{1 + [I]/K_I}$	$\frac{K_m(1 + [I]/K_I)}{1 + [I]/K_I}$
Non-competitive ^a	$\frac{V}{1 + [I]/K_I}$	$\frac{V/K_m}{1 + [I]/K_I}$	K_m
Uncompetitive	$\frac{V}{1 + [I]/K_I}$	V/K_m	$\frac{K_m}{1 + [I]/K_I}$

a) For pure non-competitive inhibition, $K_I = K_I'$

The Lineweaver-Burk plot is a linearized graphical representation of the Michaelis-Menten equation, which is a model of enzyme kinetics. The Michaelis-Menten equation describes the relationship between the rate of enzyme-catalyzed reactions (V) and the substrate concentration ($[S]$). The Lineweaver-Burk plot describes the variation of $1/V$ as a function of $1/[S]$ and it is also called the double-reciprocal plot. It allows to easily determine the values of the kinetic parameters V_{\max} and K_m from the slope and y-intercept of the plot, respectively (Eq. 3.2). V_{\max} is the maximum reaction rate, and K_m is the substrate concentration at which the reaction rate is half of its maximum. The

Lineweaver-Burk plot allows to easily compare the kinetic behaviour of different enzyme inhibitors, and offers a quick judgment of the inhibition type for reversible inhibitors.

$$\frac{1}{V_0} = \frac{K_m}{V_{max}} \frac{1}{[S]} + \frac{1}{V_{max}} \quad (3.2)$$

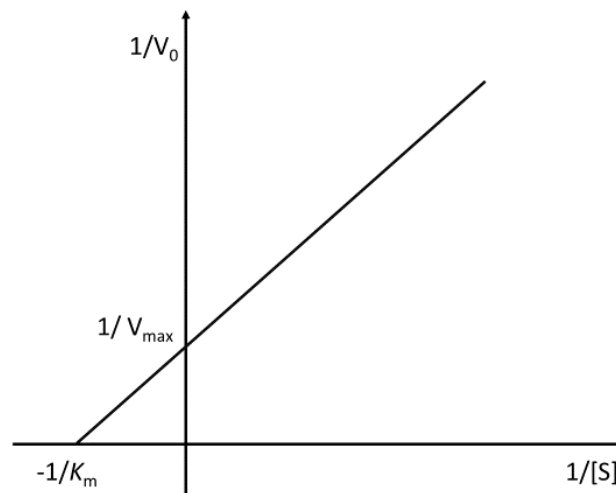


Fig. 3.6. Double reciprocal linear plot of Lineweaver-Burk kinetic model.

3.1.4 Types of reversible enzyme inhibitors

As previously mentioned, reversible enzyme inhibitors are defined competitive, uncompetitive, non-competitive, and mixed-type inhibitors [18] [19].

Competitive inhibitors bind to the same active site on the enzyme as the substrate, and they compete with the substrate for binding to the enzyme. As a result, the presence of a competitive inhibitor increases the substrate concentration required to reach V_{max} , but it does not affect the maximum reaction rate (V_{max}). The Lineweaver-Burk plot for a competitive inhibitor will have the same y-intercept as the plot for the enzyme without the inhibitor, but the slope will be steeper (i.e., K_m will be higher).

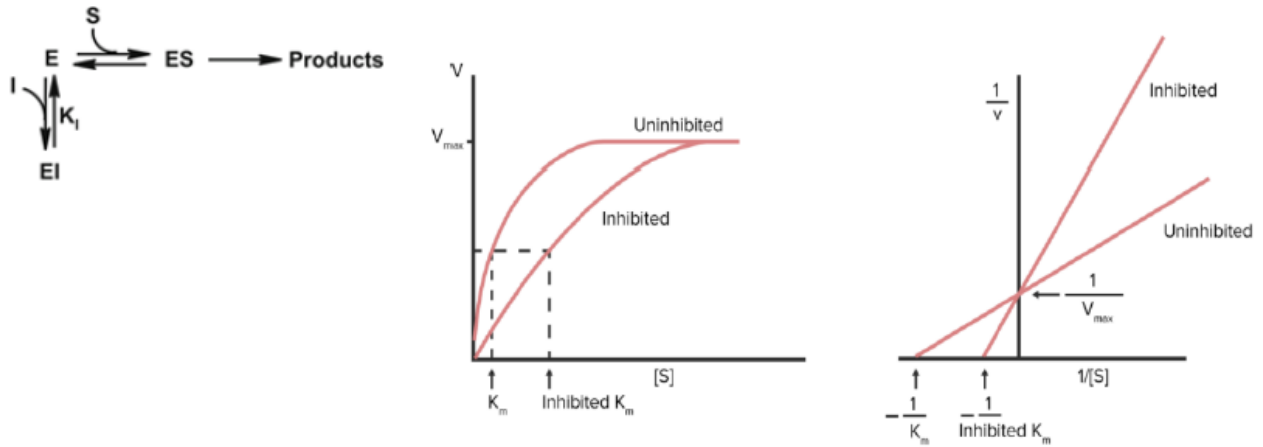


Fig. 3.7. Equilibria and kinetic plots representing interaction of a competitive inhibitor with the enzyme.

Uncompetitive inhibitors bind to a site on the enzyme that is distinct from the active site and only interacts with the enzyme-substrate complex, inhibiting the transformation. In the presence of an uncompetitive inhibitor, V_{\max} is reduced, and K_m is increased. The Lineweaver-Burk plot for an uncompetitive inhibitor will have the same slope and a higher y-intercept compared to the plot for the enzyme without the inhibitor.

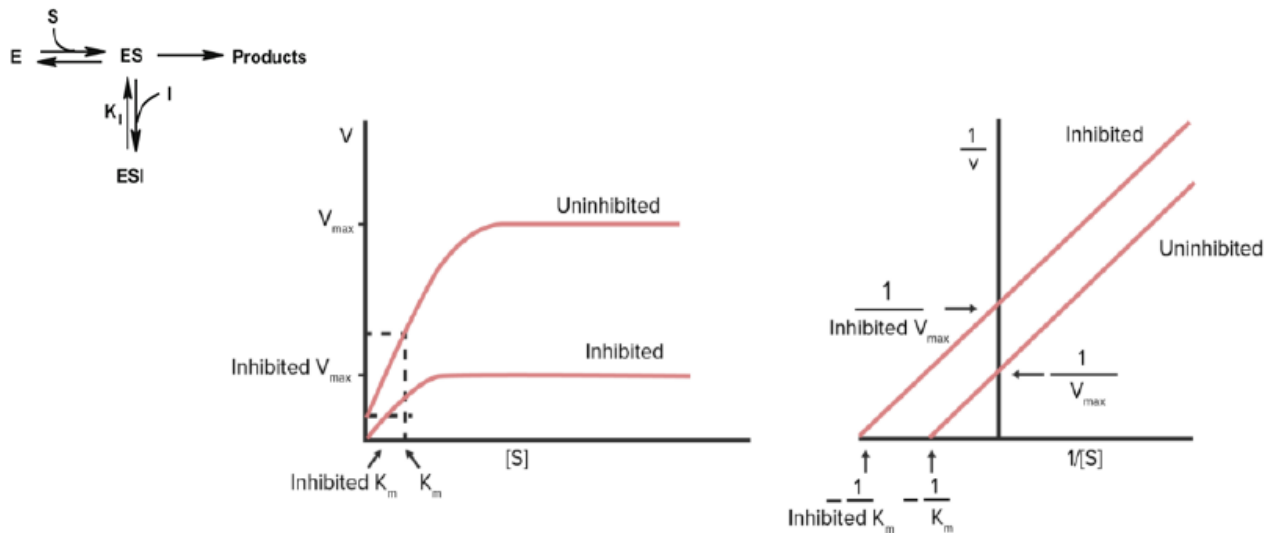


Fig. 3.8. Equilibria and kinetic plots representing interaction of an uncompetitive inhibitor with the enzyme.

Non-competitive inhibitors bind to a site on the enzyme that is distinct from the active site and inhibit the enzyme regardless of the substrate concentration. In the presence of a non-competitive inhibitor, V_{\max} is reduced, and K_m is unchanged. The Lineweaver-

Burk plot for a non-competitive inhibitor will have a higher y-intercept and a steeper slope compared the plot for the enzyme without the inhibitor.

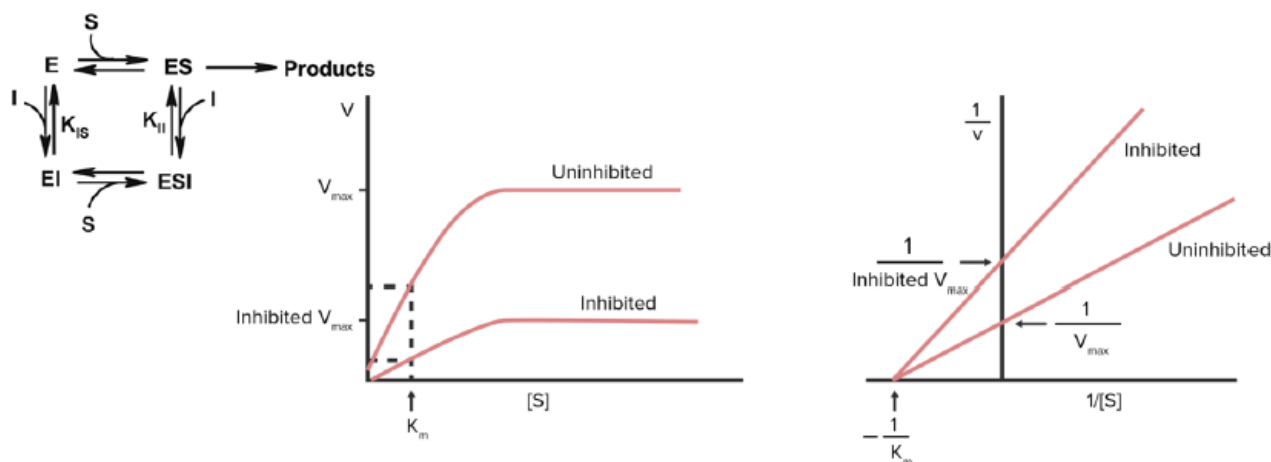


Figure 3.9. Equilibria representing interaction of a non-competitive inhibitor with the enzyme

Mixed reversible inhibitors behave both as competitive and as non-competitive inhibitors and the prevalence of the two effects depends on the substrate concentration. At high substrate concentrations, mixed inhibitors behave like competitive inhibitors, while at low substrate concentrations they behave like non-competitive inhibitors. The Lineweaver-Burk plot for a mixed inhibitor will have a slope and y-intercept that is intermediate between the plots for competitive and non-competitive inhibitors.

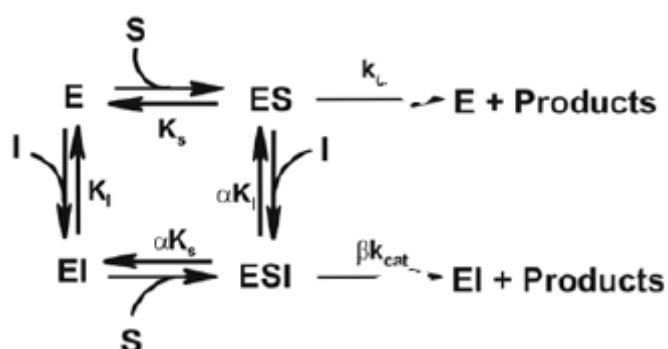


Fig. 3.10 Equilibria representing interaction of a mixed-type inhibitor with the enzyme.

The dissociation constant, K_I , is a measure of the strength of the interaction between the enzyme and the inhibitor. A smaller K_I value indicates a more potent inhibitor. The IC_{50} value, on the other hand, is a measure of the concentration of the inhibitor required

to achieve 50% inhibition of enzyme activity. It is often used to quantify inhibitors performance and often preferred to K_i owing to its more intuitive meaning and easier measurement. However, it is important to note that, unlike K_i , the IC_{50} value can vary depending on the concentration of substrate and other experimental conditions, so it is important to ensure that comparisons of IC_{50} values between inhibitors are made under similar experimental conditions. Non-competitive inhibitors also do not follow the same relationship between inhibition constant and inhibitor concentration, so it is important to take this into account when interpreting IC_{50} values for non-competitive inhibitors.

RESEARCH OBJECTIVES

Tyrosinase is an enzyme that plays a key role in the production of the pigment melanin in the skin. Excessive production of melanin can lead to hyperpigmentation disorders such as melasma, lentigines, and age spots. Inhibition of tyrosinase is therefore of interest for the prevention and treatment of hyperpigmentation and as a potential skin whitening agent in cosmetics [20]. Inhibitors of tyrosinase are also important in the preservation of food products to avoid so-called enzymatic browning. Clearly, having a robust and reliable approach to test tyrosinase inhibitors is of key importance in the search for new inhibitors, which represent another type of “antioxidants” compared to those working in the inhibition of autoxidation, described in chapter 1. The inhibitory activity of these compounds is often measured by monitoring the inhibited and uninhibited tyrosinase reaction using UV-Vis spectroscopy, which measures the accumulation of the coloured product dopachrome at 475 nm. In the reaction sequence, following diphenolase reaction, one half of *o*-dopaquinone spontaneously transforms to dopachrome, while the other half goes back to L-dopa [21].

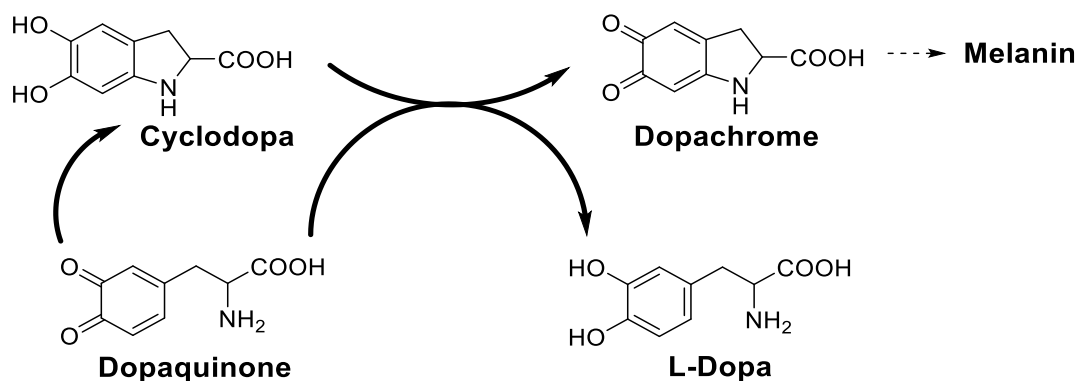


Figure 3.11. Non-enzymatic cyclization of dopaquinone to form dopachrome regenerating L-dopa.

However, since tyrosinase is an oxidative enzyme and oxygen is directly involved in the formation of L-dopa and dopaquinone, hence of dopachrome, this study can also use oximetry to measure the kinetics of oxygen consumption during the reaction, so to improve the reliability of the measurements. The goal of the study was primarily to set-up and validate a method to investigate tyrosinase inhibition using combined UV-Vis spectroscopy and oximetry. Second, the combined method was used to investigate relevant natural inhibitors that could also serve as lead compounds to design novel improved inhibitors.

To date, a large number of compounds with tyrosinase inhibition activity, of synthetic or natural origin, have been discovered [22]. Glabridin from *Glycyrrhiza glabra* (licorice) is reputedly a potent inhibitor of the enzyme tyrosinase [23]. It has been first extracted from liquorice roots and is also found in other botanical sources. Glabridin has been reported to have 15-fold higher activity against tyrosinase than kojic acid [24], and to be more effective than resveratrol and oxyresveratrol. It has been taken as a drug lead to develop novel synthetic inhibitors [25], and pharmaceutical-grade liquorice extracts standardized in glabridin are commercially available [26]. However, the literature on the actual activity of glabridin is largely confusing, with IC_{50} values ranging from 0.09 to 5.25 μ M for inhibition of tyrosinase with the substrate L-tyrosine [27] [28]. There is only one study that has addressed the mechanism of tyrosinase inhibition by glabridin, which was reported as non-competitive. Confusion about the

inhibitory activity of glabridin is even higher concerning the K_i values for inhibition of mushroom tyrosinase. The only report available in the literature indicated K_i values of 0.38 mM and 0.81 mM for monophenolase and diphenolase activities [29]. These values would indicate a quite modest activity, much lower than the reference inhibitor kojic acid, which is instead reported to be much less effective than glabridin. Therefore, owing to its importance, re-investigating glabridin activity was used as a model to set up and validate our new combined spectrophotometric-oxymetric approach. Beside validating the methods we also aimed at revising the mechanism and kinetics of glabridin as a reference for future studies and applications. We used kojic acid as the reference in our studies, since it perhaps the best known inhibitor of tyrosinase, and a highly effective positive control. The same study has been conducted with Bakuchiol thanks his increasing popularity as bioactive food component [30] [31] [32], and to the current high interest in plant-derived depigmenting compound [33] [34]. This study also investigated the antioxidant activity of bakuchiol using several techniques, including inhibited autoxidation studies in both homogenous solution and heterogeneous systems [35], and electron paramagnetic resonance [36]. They hypothesized that bakuchiol's anti-tyrosinase potency is higher than previously thought and that the mechanism of its antioxidant activity would require revision. It has also believed that bakuchiol has the potential to be a natural food preservative due to its ability to protect against both air oxidation and enzymatic food browning [37].

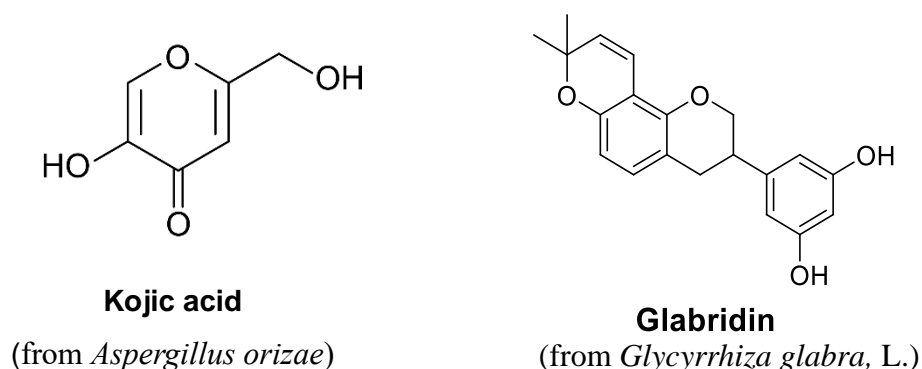


Fig. 3.12 Example of tyrosinase inhibitors molecules

RESULTS AND DISCUSSION

3.2 Matching the results from two different methodologies: parallel monitoring of the tyrosinase reaction by oximetry and spectrophotometry

(Published on Food Chemistry 2022 as DOI: <https://doi.org/10.1016/j.foodchem.2022.133423>)

The kinetics of tyrosinase monophenolase and diphenolase reactions can be investigated individually taking advantage of the fact that monophenolase is slower: therefore, if we incubate the enzyme with tyrosine as the substrate, we measure essentially the rate of monophenolase reaction. Instead by using L-DOPA as the substrate we can measure the rate of diphenolase reaction skipping the first step. In both cases the reaction proceeds spontaneously after the action of tyrosinase: dopaquinone cyclizes to cyclodopa which reacts with another dopaquinone to give back L-DOPA, which reenters the cycle, and DOPACHROME which has strong absorbance in the visible region allowing monitoring the reaction by spectrophotometry. This is the standard and best-established method to study tyrosinase activity and inhibition, but it relies on the detection of a late reaction product so it is subject to some limitations and artifacts. To overcome these problems it has been thought that since oxygen is the obliged reactant of both mono and diphenolase activity, it could be a new method of kinetic investigation based on real-time monitoring of the oxygen consumption during the reaction, using a miniaturized oxygen sensor based on infrared fluorescence quenching. In our idea the two methods could be matched for higher accuracy once the stoichiometry of oxygen consumption versus dopachrome formation has been defined.

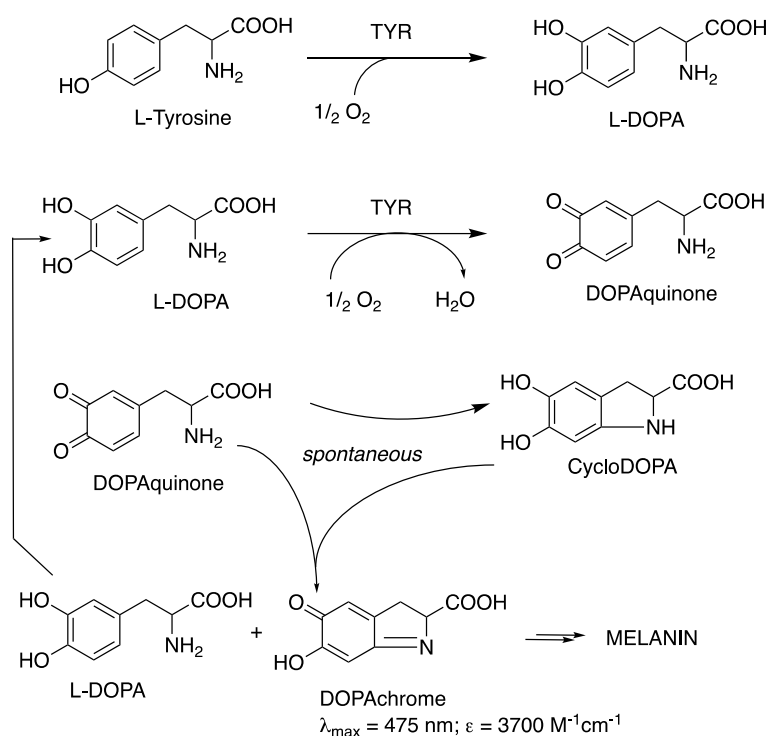


Figure 3.13. Spectrophotometrical measurement of mono and di-phenolase tyrosinase kinetics

The reaction was first monitored spectrophotometrically following the formation of dopachrome (DC) at 475 nm at 30 °C, according to the most established practice [6]. Measurements performed at fixed concentration of mTYR and variable concentration of substrate afforded the typical sigmoidal kinetic profile, with an initial lag time when the substrate was L-tyrosine. Plotting the initial rate of DC formation versus the substrate concentration showed good M-M behaviour (Fig. 3.14 A, C). Since tyrosinase activity is essentially an oxidation process operated by oxygen, where oxygen is directly involved into the production of late product DC, we set to also monitor the kinetics by parallel oximetry studies. In matched experiments performed in closed vials, we monitored the oxygen concentration as a function of time during the reaction progress, using a miniaturized oxygen sensor based on NIR fluorescence quenching (see paragraph 3.6 Experimental procedure for instrumental settings). Results are compared to those obtained by spectrophotometry in Fig. 3.14 (plots B and D).

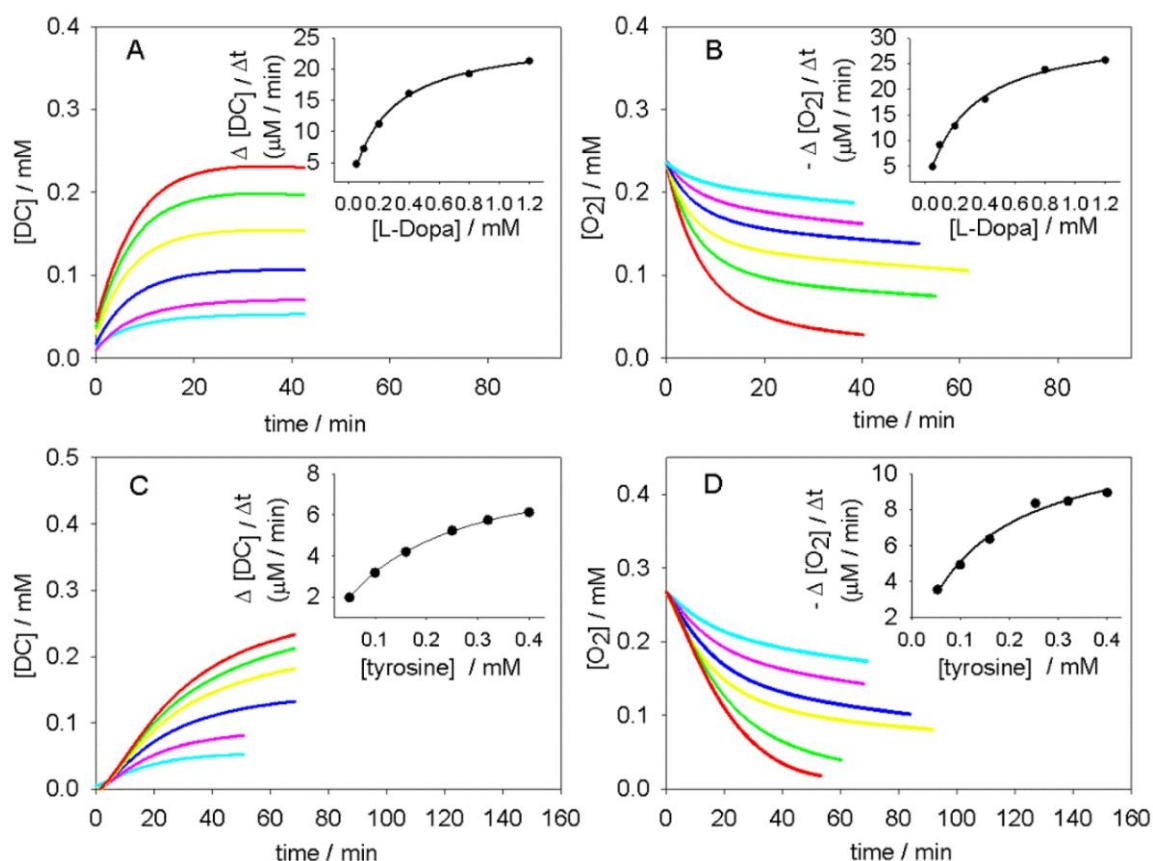


Fig. 3.14 Time-course of DC production and O₂ consumption during the oxidation of L-dopa (A, B) and L-tyrosine (C, D) catalyzed by tyrosinase (3.85 U/ml for L-dopa and 7.70 U/ml for L-tyrosine). The inserts are the initial rates of oxygen consumption (B, D) and dopachrome formation (A, C) during oxidation of both L-dopa (A and B) and L-tyrosine (A and B) with the corresponding non-linear fitting of Michaelis-Menten kinetics (solid lines).

It can be noted that the kinetic profile of oxygen consumption also follows the typical M-M behaviour, being complementary to the formation of dopachrome and suggesting that both methods are suited to monitor the reaction kinetics. This result was expected, since oxygen is the obliged oxidant in both cycles and it can be kinetically regarded as a substrate of tyrosinase. Our result also well matches the pioneering work by Naish-Byfield & Riley [38] showing Michaelis-Menten kinetic profiles of oxygen consumption (monitored electrochemically) during the oxidation of 4-hydroxyanisol by mTYR, and by Rodriguez-Lopez et al. [39] who showed complementarity between oxygen consumption (monitored electrochemically) and product accumulation during the mTYR oxidation of *tert*-butylcatechol.

Before quantitative analysis, it was however necessary to determine the stoichiometry of oxygen uptake compared to dopachrome formation. To do so we compared the initial

rate of dopachrome formation with that of oxygen uptake in matched experiments over a variety of experimental settings. The result showed in fig. 3.15 A-B explain clearly that when the substrate is L-DOPA, i.e. for the diphenolase reaction, the stoichiometric ratio is 1:1, while using tyrosine as the substrate, 1.5 molecules of oxygen are consumed per molecule of dopachrome formed. These results are in excellent agreement with previous studies where the electrochemical analysis of total oxygen consumption was compared to total dopachrome formation.

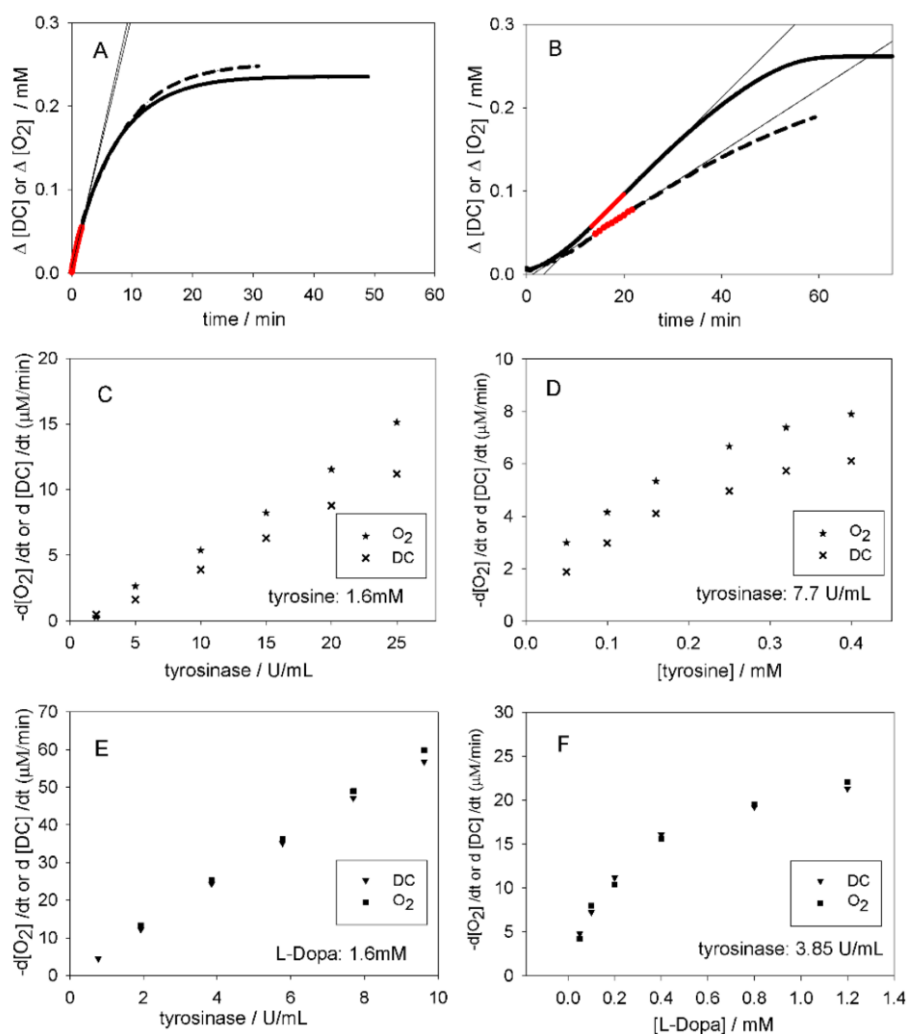


Fig. 3.15 (A, B) Representative traces of O_2 consumption (solid lines) and dopachrome (DC) formation (dashed lines) during the oxidation of L-DOPA 1.6 mM (A: tyrosinase 3.85 U/mL); and L-tyrosine 1.6 mM (B: tyrosinase 7.70 U/ml) at 30 °C, pH 6.8. Regression lines were drawn using the indicated (red) time-range. (C-F) Correlation of the stoichiometry of O_2 consumption to dopachrome (DC) production during oxidation of L-tyrosine (A, B) and L-DOPA (C, D), as a function of: (A, C) tyrosinase concentration at fixed substrate, and (B, D) substrate concentration at fixed enzyme.

The stoichiometry of oxygen consumption for tyrosinase-catalyzed oxidation of L-tyrosine to L-dopa is 0.5 mol O_2 per mol of L-tyrosine. However, the reaction goes on

to the subsequent steps converting L-DOPA to dopaquinone, which also consume 0.5 mol O₂, then dopaquinone converts spontaneously to dopachrome but one half is reduced back to L-dopa, requiring another 0.5 mol O₂ for re-oxidation [40]. To confirm the stoichiometric ratio we also extended the correlation of the initial rates of reaction to a broad range of enzyme and substrate concentrations by performing series of experiments at fixed substrate and variable enzyme activity, and at fixed enzyme activity and variable substrate concentration, using both L-DOPA alone and L-tyrosine alone as the substrate. We could confirm that the stoichiometric ratio of oxygen consumption to dopachrome formation was 1.0±0.1 and 1.5±0.2 (O₂ to DC) for substrate L-DOPA and L-tyrosine, respectively, over the whole range of experimental settings. (Fig. 3.15 C-F). It is also worth noting that these results are at variance with a study in which *tert*-butylphenol (TBP) and *tert*-butylcatechol (TBC) were used as substrate to assess oxygen consumption during monophenolase and diphenolase reaction, showing a variation of O₂/product stoichiometric ratio for very low substrate/enzyme concentration ratio. They suggest that the different outcome could be due to the higher stability in solution of the products formed from TBP/TBC, hence the exact stoichiometric ration might vary with the chosen substrates.

The kinetic measurements performed by the two approaches could then be compared on quantitative grounds. The initial rates of the reaction were analysed according to Michaelis-Menten equation and the K_m and V_{max} values for the monophenolase and diphenolase activity were obtained by non-linear regressions. For reaction with substrate L-tyrosine (monophenolase) K_m measured by spectrophotometry and by O₂ sensing was 0.18 ± 0.01 mM and 0.17 ± 0.02 mM, respectively, while V_{max} was 9.01 ± 0.12 μM/min and 8.45 ± 0.62 μM/min, respectively. Instead, for substrate L-DOPA (diphenolase) K_m from spectrophotometry and O₂ sensing was 0.26 ± 0.02 mM and 0.24 ± 0.02 mM, respectively, while V_{max} was 25.80 ± 0.53 μM/min and 24.18 ± 0.96 μM/min, respectively. The results are summarized in Table 3.2.

Table 3.2. Michaelis-Menten kinetics parameters measured both by UV-Vis spectrophotometry and by oximetry.

activity	substrate	dopachrome formation		oxygen consumption	
		K_m (mM)	V_{max} (M/min)	K_m (mM)	V_{max} (M/min)
monophenolase	L-tyrosine	0.184	9.0×10^{-9}	0.174	8.4×10^{-9}
diphenolase	L-DOPA	0.256	2.58×10^{-8}	0.214	2.40×10^{-8}

Given the higher rate of the diphenolase reaction, the V_{max} of this process was calculated at the beginning of the process (between $t=0$ and $t=3$ min) and monophenolase activity was evaluated between 5 and 20 min.

It can be noted that the two kinetic approaches afford results in excellent agreement, being identical within experimental error. Our data also match well with previous literature, *e.g.* Ros et al. [41] reported K_m of 0.168 mM and 0.272 mM respectively for monophenolase and diphenolase reaction, while Fenoll et al. [42] reported K_m as 0.25 mM and 0.28 mM for the two reactions. This provides good validation of our real-time oxygen consumption approach to investigate tyrosinase kinetics. To validate kinetics measurements we studied kojic acid as inhibitor of mTYR. Measurements were repeated under identical settings at fixed concentration of enzyme and, at each concentration of the inhibitor, a set of measurements was performed by varying the concentration of substrate. This afforded individual M-M plots for each concentration of inhibitor, both using L-tyrosine (monophenolase) and L-dopa (diphenolase) as the substrate. The entire set of measurements was repeated monitoring the reaction either with spectrophotometry or with O_2 sensing. Results are summarized in Fig. 3.16 and 3.17 for diphenolase and monophenolase reactions, respectively. The kinetics of DC formation and O_2 consumption were in excellent agreement and both sets of measurements revealed a good inhibition activity. Additionally, it has been found that inhibition of the enzyme was mixed-type with L-dopa as the substrate, and nearly competitive with L-tyrosine, which is in line with what has been reported in previous literature. Inhibition constants for mixed type inhibition (substrate = L-dopa) were $K_I = 9.91 \pm 1.42 \mu\text{M}$ and $K_I = 20.97 \pm 5.23 \mu\text{M}$, respectively, while competitive inhibition for substrate = L-tyrosine, was $K_I = 10.91 \pm 0.99 \mu\text{M}$. The K_I

was given by the average of different concentrations and the excellent agreement between the two methods can be evaluated from data in Table 3.3. Our results also agreed with previous literature, which validates our experimental approach and lends support to the reliability of subsequent findings [43].

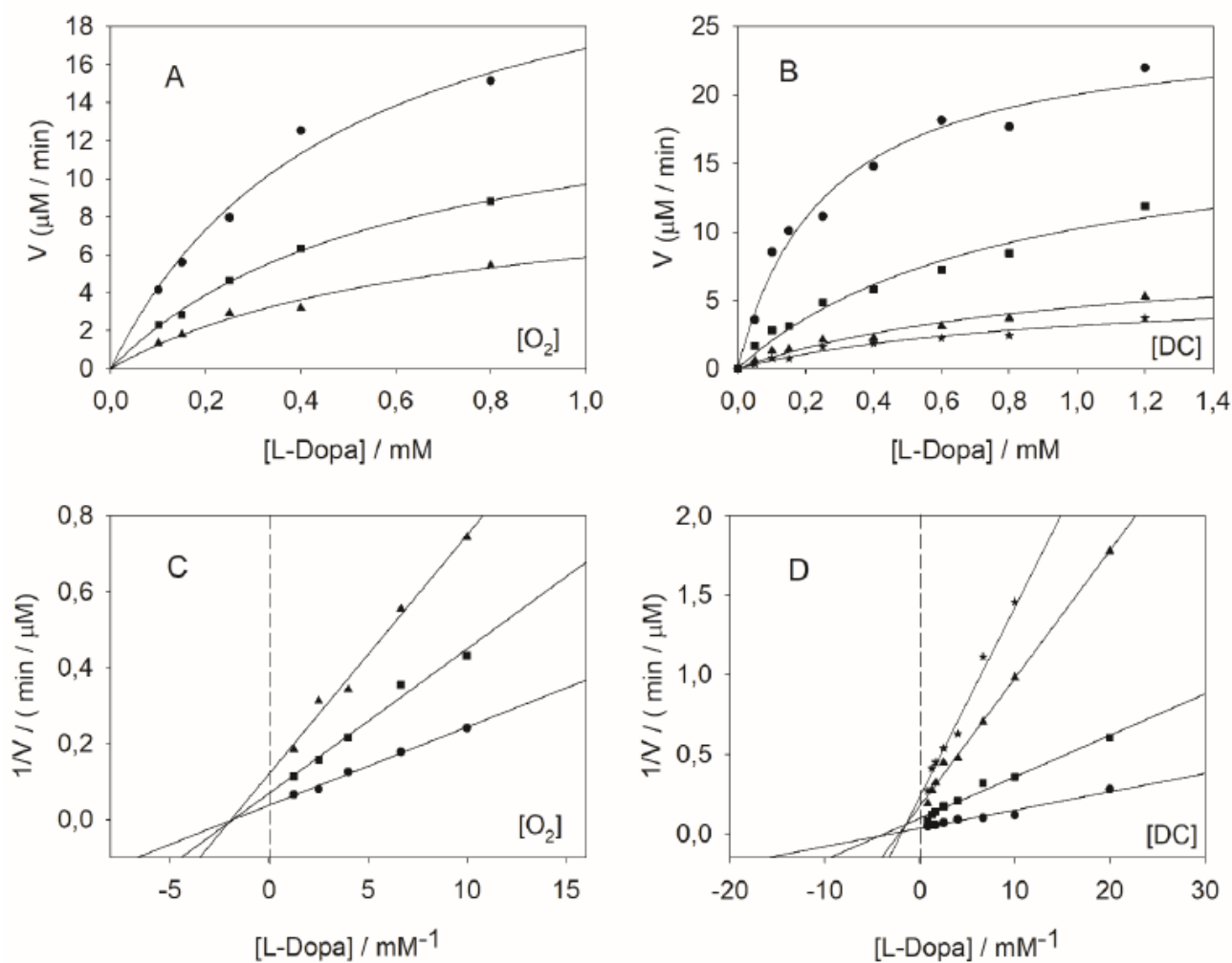


Fig. 3.16. Non-linear fittings (A and B) of Michaelis-Menten kinetics for kojic acid inhibition of diphenolase tyrosinase activity and (C and D) the corresponding Lineweaver–Burk linear fittings. Data were obtained both by oximetry (A, C) and UV-Vis spectrophotometry (B, D): (A, C) kojic acid concentrations: ●-0 μM , ■- 20 μM , ▲-50 μM ; (B, D) kojic acid concentrations: ●-0 μM , ■- 20 μM , ▲-50 μM , ★-100 μM . Enzyme concentration for substrate L-dopa was 3.85 U/ml, all experiments were conducted at pH 6.8 and 30°C. The rate of reaction V was evaluated from the initial portion (between $t=0$ and $t=2$ min) of the plot in each experiment.

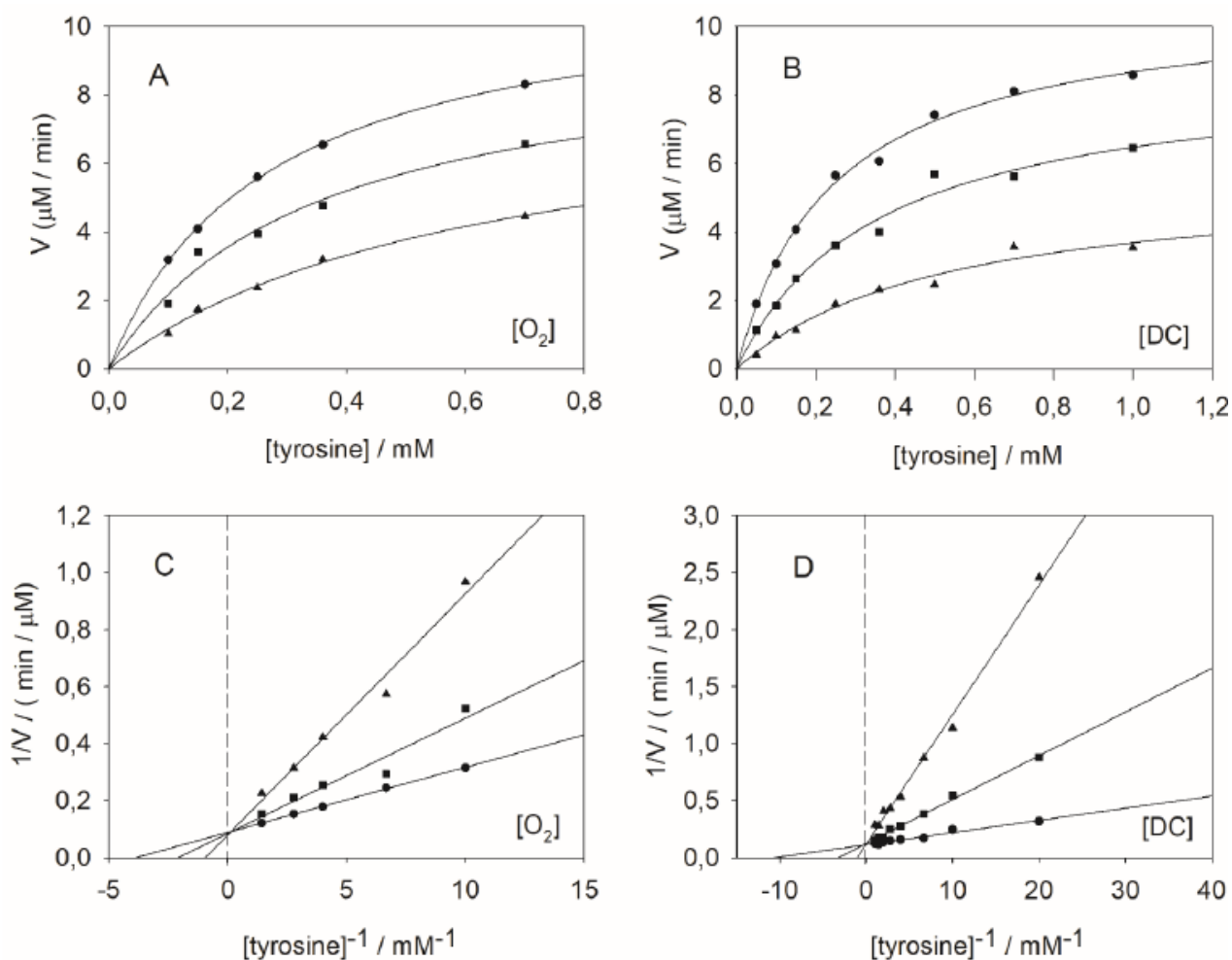


Fig. 3.17. Non-linear fittings (A and B) of Michaelis-Menten kinetics for kojic acid inhibition of monophenolase tyrosinase activity and (C and D) the corresponding Lineweaver–Burk linear fittings. Data were obtained both by oximetry (A, C) and UV-Vis spectrophotometry (B, D): (A, C) kojic acid concentrations: ●-0 nM, ■- 16 μM , ▲-25 μM ; (B,D) kojic acid concentrations: ●- 0 μM , ■- 10 μM , ▲- 30 μM . Enzyme concentration for substrate L-Tyrosine was 7.7 U/ml, all experiments were conducted at pH 6.8 and 30°C. The V of monophenolase activity was evaluated between 5 and 15 min.

Table 3.3. Kinetic parameters of tyrosinase activity inhibition by kojic acid at 30°C (pH= 6.8). Kinetics data were obtained by spectrophotometric monitoring of dopachrome (DC) or by real-time oxygen sensing (using the same procedure as for glabridin).

A. Kinetic parameters of tyrosinase diphenolase activity inhibition by kojic acid.								
	Dopachrome (DC) formation				Oxygen (O ₂) consumption			Average
[kojic acid] (μM)	0	20	50	100	0	20	50	
V_{\max} or V_{\max}^{app} (μM/min)	30.66 ± 1.74	13.2 ± 2.76	7.38 ± 1.8	5.07 ± 0.12	23.82 ± 3.6	13.62 ± 0.96	8.28 ± 1.34	
K_m or K_m^{app} (mM)	0.26 ±0.05	0.34 ±0.02	0.47 ±0.04	0.53 ±0.03	0.28 ±0.01	0.45 ±0.07	0.52 ±0.02	
$\alpha = (K_m^{\text{app}} \times \alpha') / K_m$		2.98	7.42	12.26		2.77	5.35	
$\alpha' = V_{\max} / V_{\max}^{\text{app}}$		2.32	4.17	6.04		1.73	2.88	
$K_I = [I] / (\alpha - 1)$ (μM)		10.08	7.79	8.89		11.30	11.50	9.91 ±1.42
$K_I = [I] / (\alpha' - 1)$ (μM)		15.12	15.79	19.85		27.48	26.62	20.97 ±5.23
B. Kinetic parameters of tyrosinase monophenolase activity inhibition by kojic acid.								
	Dopachrome (DC) formation			Oxygen (O ₂) consumption ^a			Average	
[kojic acid] (μM)	0	16	25	0	10	30		
V_{\max} or V_{\max}^{app} (μM/min)	8.94 ± 0.42	8.4 ± 0.66	7.98 ± 0.66	8.04 ± 0.96	7.5 ± 0.78	7.2 ± 0.48		
K_m or K_m^{app} (mM)	0.18 ± 0.02	0.36 ± 0.06	0.75 ± 0.12	0.26 ± 0.01	0.48 ± 0.09	1.07 ± 0.09		
$\alpha = (K_m^{\text{app}} \times \alpha') / K_m$		2.31	3.56		1.98	3.62		
$\alpha' = V_{\max} / V_{\max}^{\text{app}}$		1.06	1.12		1.07	1.12		
$K_I = [I] / (\alpha - 1)$ (μM)		12.25	9.78		10.17	11.45	10.91 ± 0.99	
$K_I = [I] / (\alpha' - 1)$ (μM)		266.67	208.33		142.85	250.00	216.96 ± 55.16	

Note: V_{\max} or V_{\max}^{app} refer to not inhibited and inhibited assays, respectively, and K_m or K_m^{app} refer to not inhibited and inhibited assays, respectively. Data were obtained both by UV-vis spectrophotometry and by oximetry method. V_{\max} or V_{\max}^{app} were calibrated by using the stoichiometry ratios 1.5 for O₂/DC for monophenolase reaction and 1.0 O₂/DC for diphenolase.

3.3 Inhibition kinetics by glabridin

(Published on Food Chemistry 2022 as DOI: <https://doi.org/10.1016/j.foodchem.2022.133423>)

We next investigated the kinetic of inhibition of both monophenolase and diphenolase activities by glabridin, using both spectrophotometry and oxygen uptake methods.

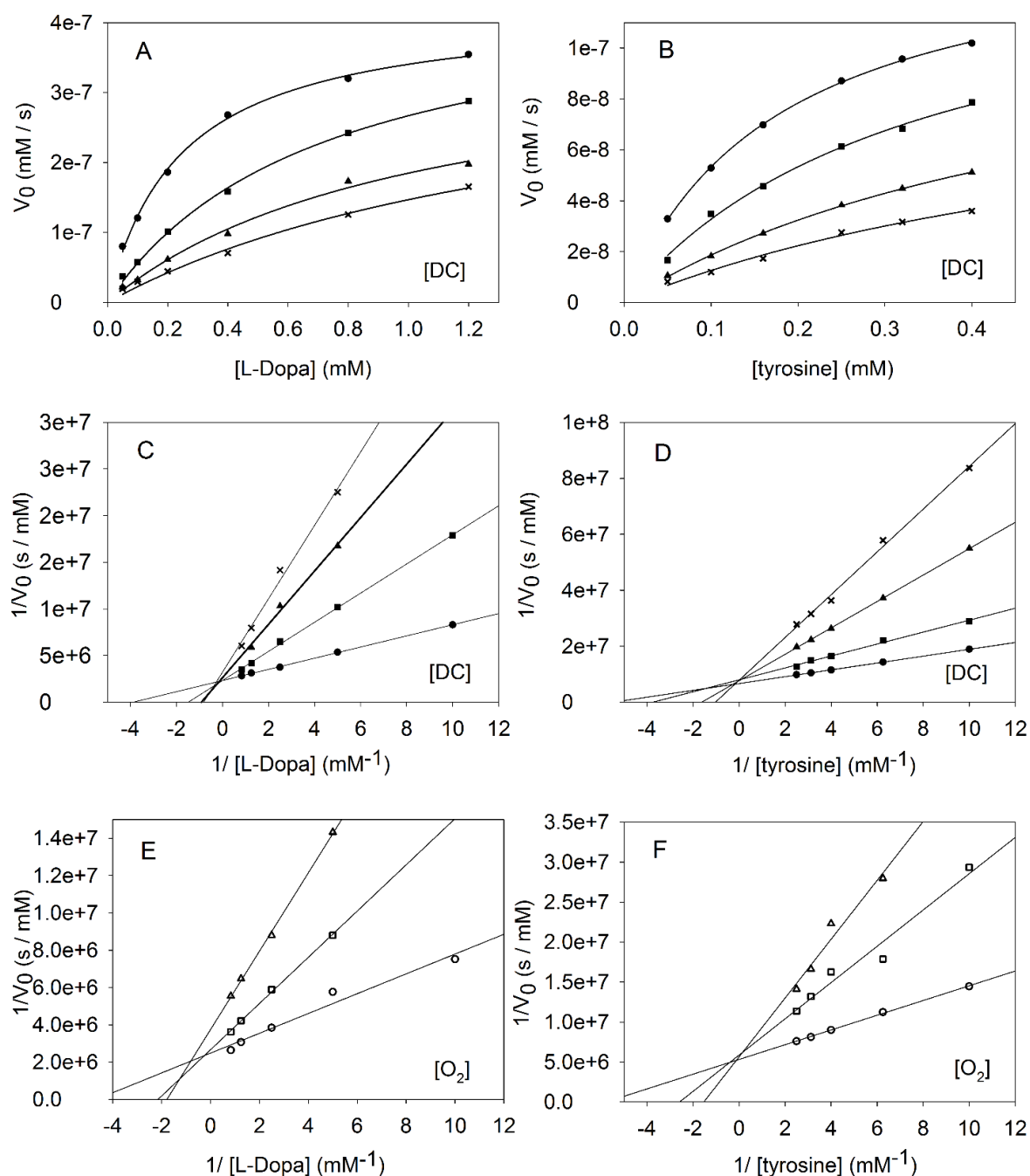


Fig. 3.18. Plots A and B are the non-linear fittings based on Michaelis-Menten kinetics of glabridin inhibition of monophenolase and diphenolase tyrosinase activity. Data were obtained by UV-Vis spectrophotometry: (A) diphenolase activity on L-Dopa, glabridin concentrations: ●-0 nM, ■- 90

nM, ▲-180 nM, ×-300 nM; (B) monophenolase activity on L-tyrosine, glabridin concentrations: ×-0nM, ▲- 15 nM, ■-37 nM, ●-50nM. (C) and (D) are the Lineweaver-Burk plots corresponding to A and B. (E) and (F) are the Lineweaver-Burk plots of glabridin inhibition on monophenolase and diphenolase activity studied by oximetry method: (E) diphenolase activity on L-Dopa, glabridin concentrations: ○-0nM, □-80nM, △-200nM; (F) monophenolase activity on L-tyrosine, glabridin concentrations: ○-0nM, □-20nM, △-40nM. Enzyme concentration for substrate L-dopa and L-tyrosine were 3.85 U/ml and 7.7U/ml respectively, all experiments were conducted at pH 6.5 and 30°C. Due to the higher rate of the diphenolase reaction, the V_{max} of this process was evaluated at the beginning of the process (between t=0 and t=2 min), the V_{max} of monophenolase activity was instead evaluated between 5 and 30 min.

The non-linear fittings of the Michaelis-Menten plots, and the linear Lineweaver-Burk plots [45] derived from the oximetry and spectrophotometry methods clearly showed that glabridin's mechanism of inhibition was not noncompetitive as previously reported, but nearly competitive instead. This means that glabridin is capable of binding in the enzyme active site with higher affinity than the substrate, instead of binding only out the active site of enzyme, causing a decrease in the apparent maximum reaction rate V_{max} , and no change in the apparent Michaelis-Menten constant K_m .

It has found that there is a minor variation of V_{max} , on increasing the concentration of the inhibitor, therefore the inhibition by glabridin was considered of mixed-type. This means that glabridin can interfere with both the free enzyme and enzyme-substrate (ES) complex, with two dissociation constants K_I and $K_{I'}$. This result is different from what was reported in the literature. We can define K_I and $K_{I'}$ as described as below.

$$K_I = \frac{[E][I]}{[EI]} \quad (3.3)$$

$$K_{I'} = \frac{[ES][I]}{[ESI]} \quad (3.4)$$

As described in Table 2.3, in order to determine K_I and $K_{I'}$ for a mixed inhibition from M-M kinetic treatment, it is necessary to introduce the parameters α and an α' , which are given as follows:

$$\alpha = \frac{K_m^{app}}{K_m} \alpha' \quad (3.5)$$

$$\alpha' = \frac{V_{max}}{V_{max}^{app}} \quad (3.6)$$

Where K_m and K_m^{app} are respectively is the Michaelis-Menten constant, (substrate concentration giving half-maximum rate) in the absence and in the presence of the inhibitor, and V_{max} and V_{max}^{app} are respectively the maximum rate measured in the absence and in the presence of the inhibitor. K_I and K_I' values can then be obtained from the following equations at each given concentration of the inhibitor [I].

$$\alpha = 1 + \left(\frac{[I]}{K_I}\right) \quad (3.7)$$

$$\alpha' = 1 + \left(\frac{[I]}{K_I'}\right) \quad (3.8)$$

The apparent M-M kinetics parameters K_m and K_m^{app} and α and an α' from data in Figure 3.18, are listed in Table 3.4 and Table 3.5, for substrate L-dopa and L-tyrosine respectively. The calculation of inhibition constants K_I and K_I' for various concentration of glabridin as the inhibitor are also collected in the Tables 3.4 and 3.5, for substrate L-dopa and L-tyrosine respectively. Also in this case, just like in the kojic acid example, the inhibitor constants have been obtained from the average of different concentrations.

Table 3.4. Kinetic parameters of tyrosinase diphenolase activity inhibition by glabridin. Kinetics data were obtained both by non-linear and linear regression fit (see experimental section) at different glabridin concentrations.

	Dopachrome (DC) formation				Oxygen (O ₂) consumption			average
[Glabridin] (nM)	0	90	180	300		80	200	
V_{max} or V_{max}^{app} (mM/s) ^a	4.30×10^{-7}	4.29×10^{-7}	3.79×10^{-7}	3.09×10^{-7}	4.03×10^{-7}	3.75×10^{-7}	2.67×10^{-7}	
K_m or K_m^{app} (mM)	0.26	0.67	1.08	1.21	0.21	0.47	0.56	
$\alpha = (K_m^{app} \times \alpha') / K_m$		2.17	4.79	6.58		2.34	3.95	
$\alpha' = V_{max} / V_{max}^{app}$		1.00	1.14	1.39		1.075	1.51	
$K_I = [I] / (\alpha - 1)$		77.24	47.54	53.75		59.86	67.71	61.22
$K_I' = [I] / (\alpha' - 1)$		39130.4	1337.7	766.13		1071.4	392.65	8539.7

V_{\max} or V_{\max}^{app} refer to not inhibited and inhibited assays, respectively, and K_m or K_m^{app} refer to not inhibited and inhibited assays, respectively. Data were obtained both by UV-Vis spectrophotometry and oximetry method.

Table 3.5. Kinetic parameters of tyrosinase monophenolase activity inhibition by glabridin. Kinetics data were obtained by non-linear and linear regression fit at different glabridin concentrations.

[Glabridin] (nM)	Dopachrome (DC) formation				Oxygen (O ₂) consumption ^a			average
	0	15	37	50	0	20	40	
V_{\max} or V_{\max}^{app} (mM/s)	1.50×10^{-7}	1.25×10^{-7}	1.30×10^{-7}	1.26×10^{-7}	1.40×10^{-7}	1.27×10^{-7}	1.32×10^{-7}	
K_m or K_m^{app} (mM)	0.18	0.27	0.61	0.97	0.17	0.39	0.65	
$\alpha = (K_m^{\text{app}} \times \alpha') / K_m$		1.74	3.86	6.25		2.46	3.99	
$\alpha' = V_{\max} / V_{\max}^{\text{app}}$		1.20	1.15	1.19		1.10	1.06	
$K_I = [I] / (\alpha - 1)$		20.21	12.95	9.53		13.70	13.37	13.95
$K_I = [I] / (\alpha' - 1)$		74.38	239.81	267.42		190.77	648.30	284.13

^a V_{\max} or V_{\max}^{app} were calibrated by using the stoichiometry ratio of 1.5 for O₂/DC (see 3.5.1).

The results from two different techniques, spectrophotometry and oximetry, were in agreement and indicated that glabridin inhibits both activities of the enzyme at very low concentrations (nanomolar). For most of its activity glabridin competes with substrate (L-tyrosine or L-DOPA) for the enzyme's active site in a classical competitive mode with K_I values of 13.63 ± 3.54 nM and 57.08 ± 8.32 nM, respectively. The inhibition is much stronger than previously reported. The values measured here support the reportedly the potent inhibition activity of glabridin, which outperforms kojic acid by 3 orders of magnitude for monophenolase inhibition and by 2 orders of magnitude for diphenolase inhibition. As previously indicated, IC_{50} is a measure of the concentration of an inhibitor that is needed to reduce the rate of an enzyme reaction to 50% of the value observed in the absence of the inhibitor. This

value is commonly reported in the literature as a way to compare the effectiveness of different inhibitors. It can be determined using a dose-response diagram and the Langmuir isotherm equation (Eq. 3.9). Results recorded in our study for Glabridin with the two techniques, oxygen uptake and spectrophotometry are collected in Table 3.6.

$$\frac{V_I}{V_0} = \frac{1}{1 + \frac{[I]}{IC_{50}}} \quad (3.9)$$

Table 3.6 IC₅₀ values calculated for mushroom tyrosinase inhibition by glabridin (at 30°C) at different concentrations of L-tyrosine and L-dopa substrates, both by spectrophotometric

From UV-Vis. monitoring at 475 nm (diphenolase)							
[L-dopa] (mM)	0.05	0.10	0.20	0.40	0.80	1.00	1.20
IC ₅₀ (nM)	80.9	81.6	96.4	114.0	229.7	255.1	292.6
Error (±std.dev.)	±0.5	±3.5	±8.9	±10.1	±9.9	±8.4	±12.6
From real-time O₂ sensing (diphenolase)							
[L-dopa] (mM)	0.05	0.10	0.20	0.40	0.80	1.00	1.20
IC ₅₀ (nM)	69.8	78.4	108.3	152.4	201.1	259.0	295.7
Error (±std.dev.)	±0.6	±4.1	±10.5	±3.7	±3.3	±15.7	±33.4
Averaged between O₂ sensing and UV-Vis (diphenolase)							
[L-dopa] (mM)	0.05	0.10	0.20	0.40	0.80	1.00	1.20
IC ₅₀ (nM)	75.4	80.0	102.3	133.2	220.9	257.0	294.2
Error (±std.dev.)	±5.6	±4.1	±11.4	±20.6	±11.5	±12.7	±25.3
From UV-Vis. monitoring at 475 nm (monophenolase)							
[L-tyrosine] (mM)	0.05	0.10	0.16	0.25	0.32	0.40	1.00
IC ₅₀ (nM)	16.50	21.0	22.8	29.3	31.6	38.4	84.0
Error (±std.dev.)	±0.2	±0.8	±2.4	±2.4	±4.1	±3.9	±6.9
From real-time O₂ sensing (monophenolase)							
[L-tyrosine] (mM)	0.05	0.10	0.16	0.25	0.32	0.40	1.00
IC ₅₀ (nM)	17.4	20.0	23.0	25.9	35.2	38.5	75.0
Error (±std.dev.)	±0.2	±0.9	±4.9	±1.6	±4.3	±2.8	±7.1
Averaged between O₂ sensing and UV-Vis (monophenolase)							
[L-tyrosine] (mM)	0.05	0.10	0.16	0.25	0.32	0.40	1.00
IC ₅₀ (nM)	16.9	20.5	22.9	27.6	33.4	38.5	79.5
Error (±std.dev.)	±0.5	±1.0	±3.9	±2.7	±4.6	±3.4	±8.3

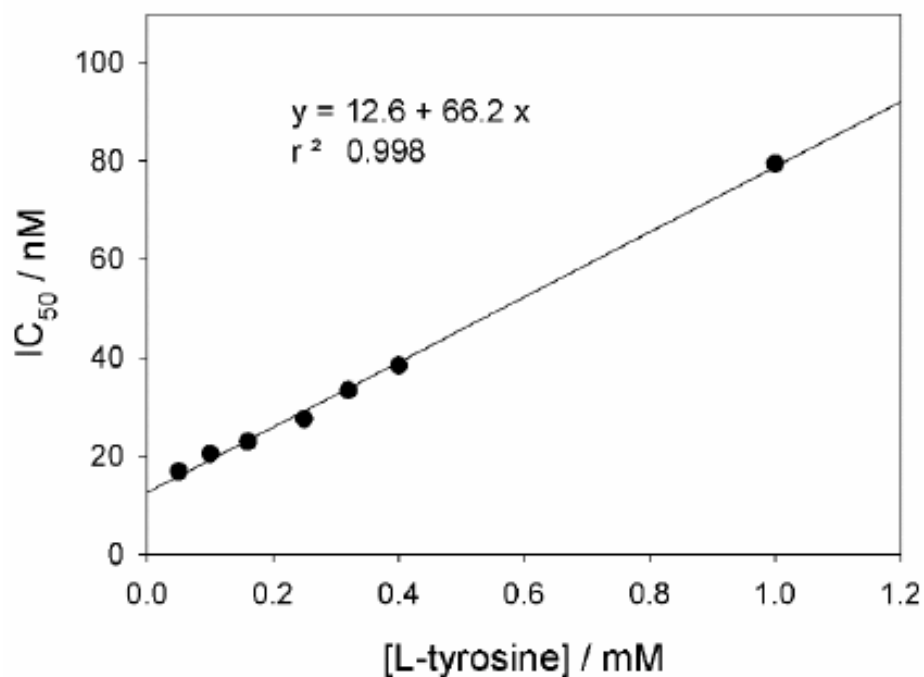


Fig. 3.19. Dependency on the concentration of substrate of IC₅₀ for glabridin in the inhibition of monophenolase activity of mushroom tyrosinase at 30°C (pH= 6.8), averaged between spectrophotometric monitoring of dopachrome and real-time O₂ sensing (data from Table 2.5).

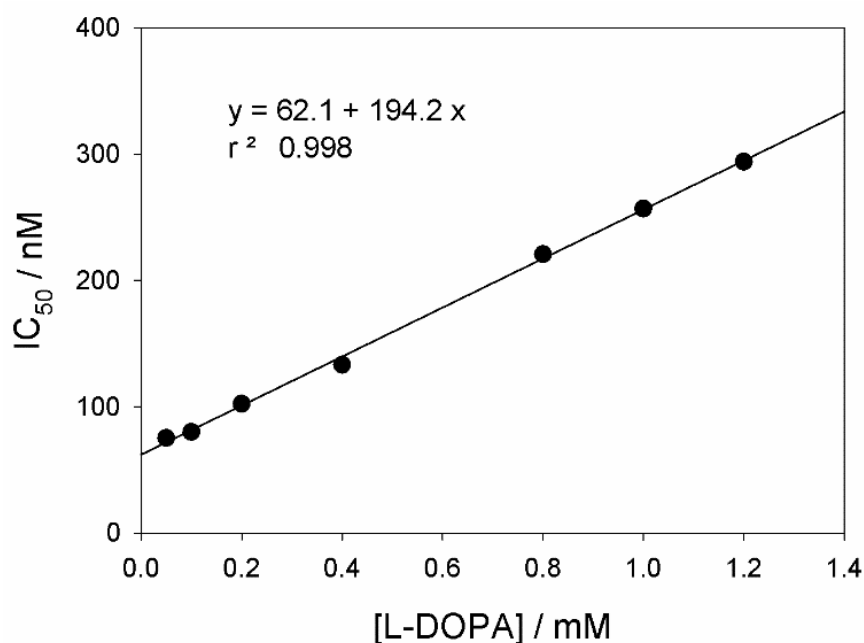


Fig. 3.20 Dependency on the concentration of substrate of IC₅₀ for glabridin in the inhibition of diphenolase activity of mushroom tyrosinase at 30°C (pH= 6.8), averaged between spectrophotometric monitoring of dopachrome and real-time O₂ sensing (data from Table 2.5).It can

be noted that the two techniques offered very similar results so that they could be combined to afford averages IC_{50} values for Glabidin in the inhibition of Tyrosinase monophenolase and diphenolase activities. It is worth stressing that IC_{50} values depend on the concentration of the substrate as it is illustrated in Fig. 3.19 and 3.20 for monophenolase and diphenolase reactions, respectively. This should not be overlooked when comparing the performance of different inhibitors.

To this end, we also measured IC_{50} values for kojic acid as a reference inhibitor and results, averaged between the two techniques, are collected in Table 3.7. Kojic acid also showed dependence of IC_{50} from the concentration of the substrate as demonstrated in Fig. 3.21 and 3.22.

Table 3.7 IC_{50} values calculated for mushroom tyrosinase inhibition by kojic acid (at 30°C; pH=6.8) at different concentrations of L-tyrosine and L-dopa substrates. The values came from the average results given by oximetry method and spectroscopy one .

[L-dopa] (mM)	0.1	0.15	0.40	0.60	0.80	1.00	1.20
IC_{50} (μ M)	9.4	8.3	12.1	12.5	15.8	17.0	19.9
Error (\pm std.dev.)	± 2.1	± 1.0	± 2.7	± 1.9	± 2.6	± 3.4	± 3.9
[L-tyrosine] (mM)	0.05	0.10	0.15	0.25	0.36	0.7	1.00
IC_{50} (μ M)	15.5	17.9	19.4	20.2	23.0	27.9	32.8
Error (\pm std.dev.)	± 3.5	± 2.9	± 3.8	± 2.4	± 5.2	± 4.4	± 6.5

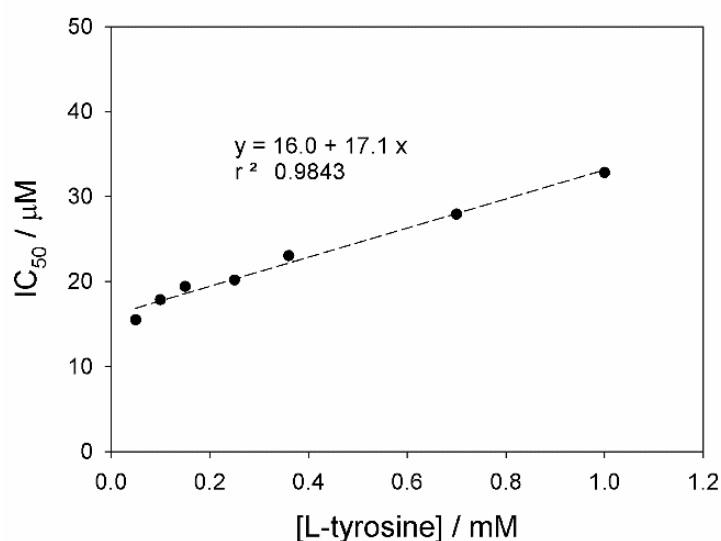


Fig. 3.21. Plot of IC_{50} vs the concentration of substrate (L-Tyrosine) for monophenolase inhibition of mushroom tyrosinase by Kojic acid at 30°C (data from Table 3.7).

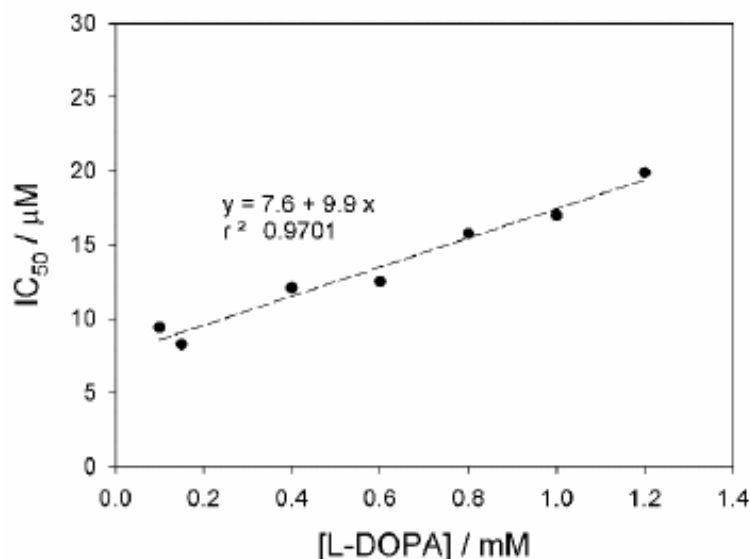


Fig. 3.22. Plot of IC_{50} vs the concentration of substrate (L-DOPA) for diphenolase inhibition of mushroom tyrosinase by Kojic acid at 30°C (data from Table 3.7)

Since both inhibitors have IC_{50} values that vary linearly with substrate concentration, comparison is only possible at the same concentration, i.e. under identical experimental settings. It can be noted that while for kojic acid IC_{50} values were in good agreement with previous literature, for Glabridin IC_{50} values were orders of magnitude smaller than previously reported, thereby indicating a much higher activity.

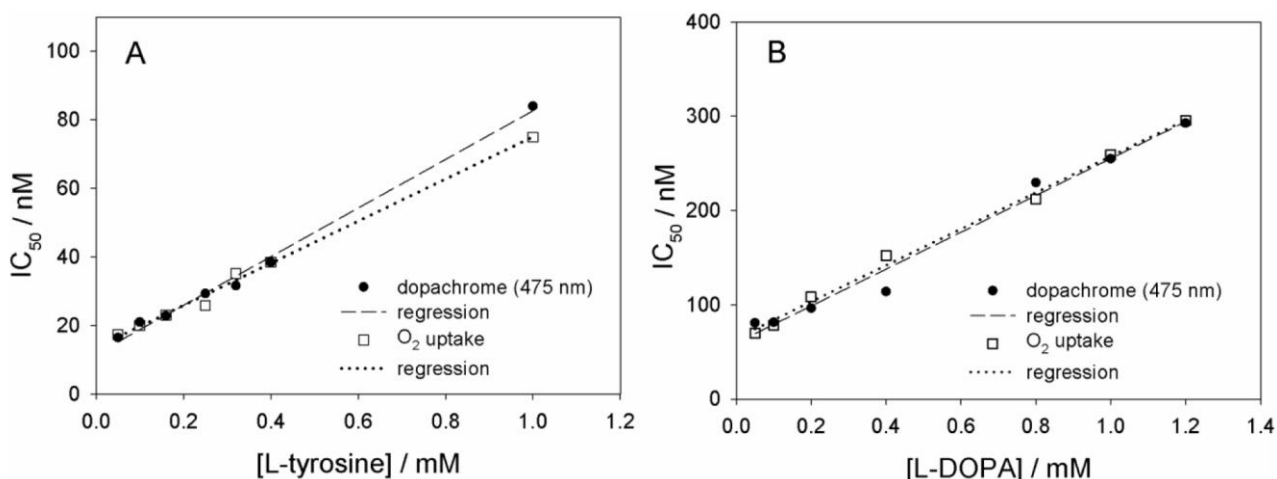


Fig. 3.23. Dependency of IC_{50} for glabridin inhibition of mTY on substrate concentration, both for monophenolase (A) and diphenolase (B) reactions. Data (Table 3.7) were obtained both by spectrophotometry and by oxygen sensing at 30 °C (pH = 6.8)

Indeed, glabridin has inhibition potency 3-orders of magnitude higher than kojic acid for monophenolase inhibition and 2-orders of magnitude higher than kojic acid for diphenolase inhibition, showing that glabridin is one of the most potent natural tyrosinase inhibitors currently known. This arises both from the analysis of the K_i values and from IC_{50} values, which show a remarkable consistency.

For competitive inhibitors like Glabridin, the linear relationship between the IC_{50} and substrate concentration is fully expected, as dictated by Cheng and Prusoff's equation. (Eq. 3.10).

$$IC_{50} = K_I + \frac{K_I}{[S] K_m} \quad (3.10)$$

This relationship is verified by plotting the IC_{50} values against substrate concentration either using averaged results from oximetry and spectrophotometry (Fig. 3.22 and 3.23) or by plotting the individual data from the two techniques as shown in Fig. 3.23. It also represents an independent method to obtain K_i values for Glabridin. Using the averaged plots, K_i values obtained by this method were 13 nM and 62 nM for monophenolase and diphenolase activities, respectively, in excellent agreement with data in Tables 3.4 and 3.5. This further supports our results and the reputation of Glabridin as one of the most effective natural tyrosinase inhibitors.

Certain molecules, known to have anti-tyrosinase activity, can also act as alternative substrates for tyrosinase enzyme. This is because tyrosinase enzyme is a polyphenol oxidase (PPO) enzyme which is not specific to just one substrate [46] [47]. This is especially true for inhibitors that can easily access the enzyme's active site such as competitive inhibitors and have a phenolic or polyphenolic structure. For example, Catechins, caffeic acid, ferulic acid, neohesperidin and other phenolic compounds have been reported to act as alternative substrates. It is also worth mentioning that since Glabridin is a phenolic compound, it cannot be excluded that it also acts as alternative

substrate and this has not been assessed before. To determine if Glabridin acts as an alternative substrate for tyrosinase enzyme, several experiments were conducted to ensure the absence of any interference in the kinetic analysis of tyrosinase inhibition. The methods used to determine this are the standard method of spectrophotometrically measuring enzyme kinetics and our new oxygen sensing approach. The results of these experiments carried out using glabridin as the substrate, without tyrosine or L-dopa, showed no development of absorbance at 475 nm when monitored spectrophotometrically and no oxygen uptake over 60 min when monitored by oxygen sensing method, which allows excluding that glabridin acts as an alternative substrate under the tested conditions.

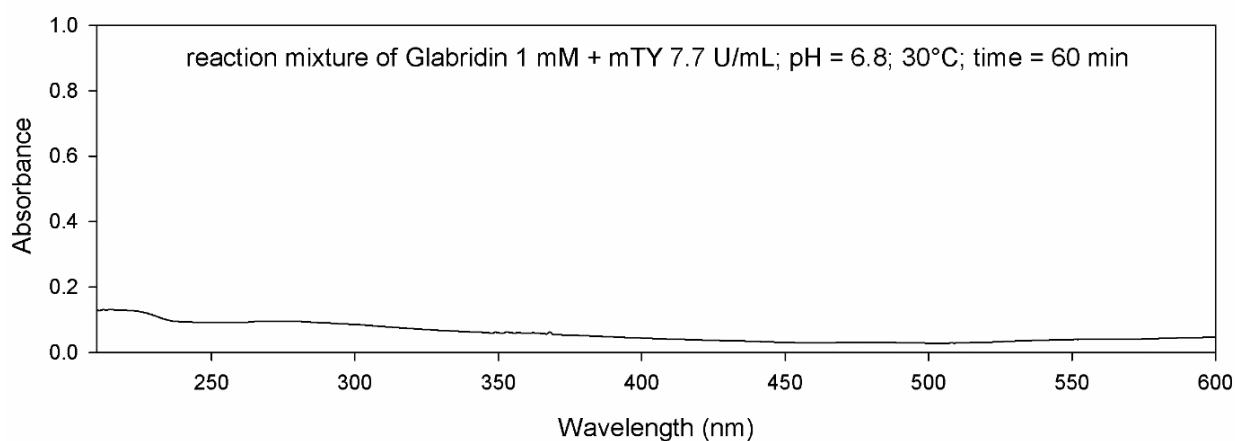


Fig. 3.24. UV-Vis. difference spectrum obtained by subtracting from the spectrum of the reaction mixture composed by mushroom tyrosinase (7.7.U/mL) and 1 mM glabridin incubated at 30° for 1 hour (pH=6.8), the spectrum of glabridin at the same concentration in the same medium. No change or development of significant absorbance suggests the absence of transformation of glabridin by the enzyme.

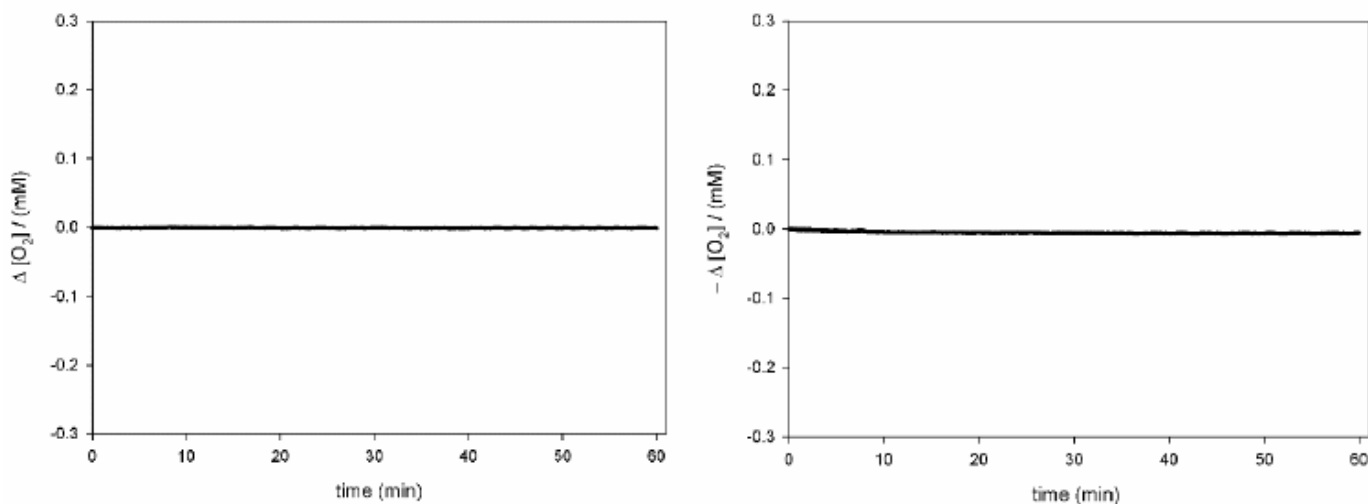


Fig. 3.25. Oxygen consumption recorded by incubating mushroom tyrosinase (7.7.U/mL) with 200 nM glabridin (left panel) and 1 mM glabridin (right panel) at 30° for 1 hour (pH=6.8), in the absence of other substrates. No detectable oxygen consumption indicates no transformation of glabridin by the enzyme.

3.4 Anti-tyrosinase and antioxidant activity of Bakuchiol

(Published in Food Chemistry 2022 as DOI: <https://doi.org/10.1016/j.foodchem.2022.134953>)

Psoralea corylifolia is an annual herb native to India and subtropical regions with a long history of use in traditional Chinese and Indian medicines. The seeds of the plant have been found to have high medicinal value due to the presence of bioactive phytochemicals including the meroterpene bakuchiol [48]. Studies have shown that bakuchiol has diverse bioactivities, including anti-inflammatory, antimicrobial, and anticancer effects, as well as protection against organ damage, diabetes, and anxiety and neurological disorders [49]. The main area of recent research has focused on bakuchiol's structural similarity with retinol (Vitamin A), which allows for mimic bioactivity in dermatological applications [50] such as anti-acne, anti-psoriasis, and anti-aging treatments [51]. Bakuchiol has also been found to have antioxidant activity and skin depigmenting activity, but the exact mechanisms for these effects are not fully understood. The study aims to investigate the kinetics of mushroom tyrosinase inhibition by bakuchiol to help understand the mechanism of its skin depigmenting

activity. Additionally, we investigated the antioxidant activity of bakuchiol by state-of-the-art inhibited autoxidation studies both in homogenous solution and in heterogeneous system and by electron paramagnetic resonance (EPR), so to complete the picture, affording the mechanism and absolute kinetics and thermodynamics of peroxy radical trapping

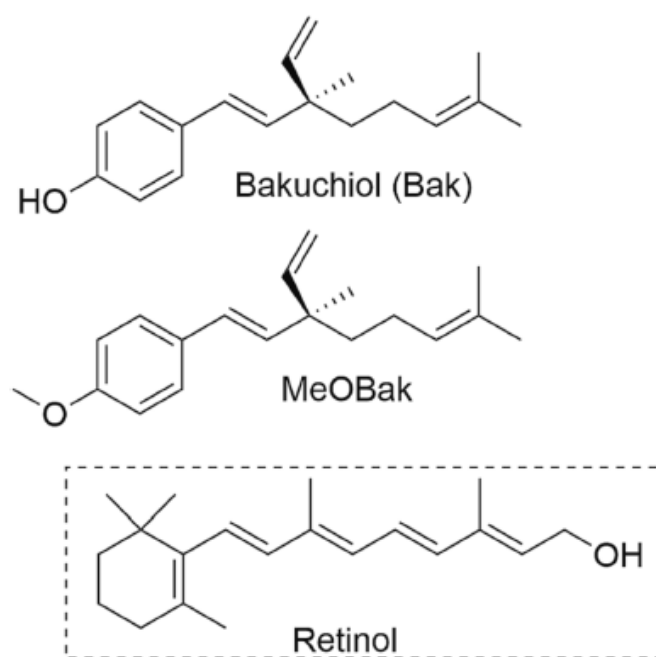


Fig. 3.26. Structure of bakuchiol and its OMe ether derivative compared to retinol.

3.4.1 Kinetics of mTYR inhibition

We used the same technique described in paragraph 3.3. The method was used to study the monophenolase and diphenolase reactions of mTYR at 30°C (pH 6.8) by monitoring the oxygen consumption during the oxidation of L-tyrosine to L-Dopa or of L-Dopa to dopaquinone, respectively. The results showed that bakuchiol significantly inhibited the mTYR reaction in the low micromolar range. The kinetics analysis performed using the Michaelis-Menten equation and the linearized double reciprocal Lineweaver-Burk plot showed that bakuchiol is a reversible competitive inhibitor of mTYR enzyme. This type of inhibition is indicated by the constancy of the V_{\max} , the maximum rate of enzyme reaction at saturating substrate concentration, and increase of the M-M constant K_m , the concentration of substrate required to produce

half-maximum reaction rate, with the concentration of the inhibitor. We also repeated the same study using the conventional spectrophotometric approach, monitoring the formation of dopachrome at 475 nm, as described in 3.3. The study confirmed the same findings. The results obtained by this method and by the oxygen sensing approach are in excellent agreement, as can be judged from the kinetic data reported in Table 3.8. The average inhibition constant K_i , the dissociation constant of the enzyme-inhibitor complex, was found to be $6.71 \pm 1.23 \mu\text{M}$ for monophenolase and $1.15 \pm 0.34 \mu\text{M}$ for diphenolase reactions, indicating high inhibition potency of bakuchiol. Measured K_i is lower than that of the reference inhibitor kojic acid, which was measured as $10.91 \mu\text{M}$ and $9.91 \mu\text{M}$ for monophenolase and diphenolase inhibition.

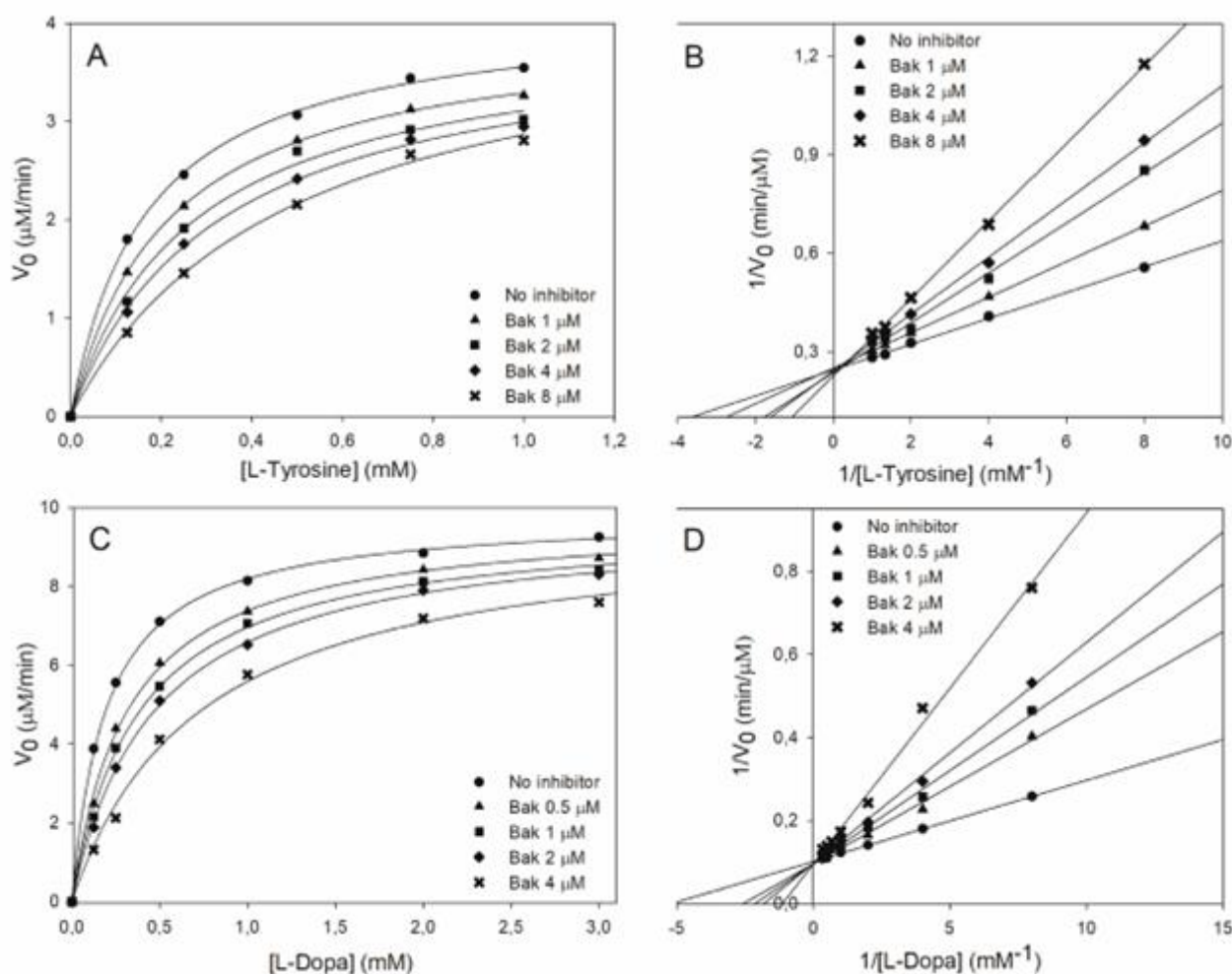


Figure 3.27 (A-D) Kinetics of mTYR reaction (30°C, pH 6.8) monitored by O_2 uptake, inhibited by bakuchiol, for (A, B) monophenolase reaction (substrate = L-Tyrosine; mTYR 1.6 U/mL) and (C, D) diphenolase reaction (substrate = L-DOPA, mTYR 0.8 U/mL). Graphs represent Michaelis-Menten hyperbolic plots (A, C) and Lineweaver-Burk linear plots (B, D) of the same experiments

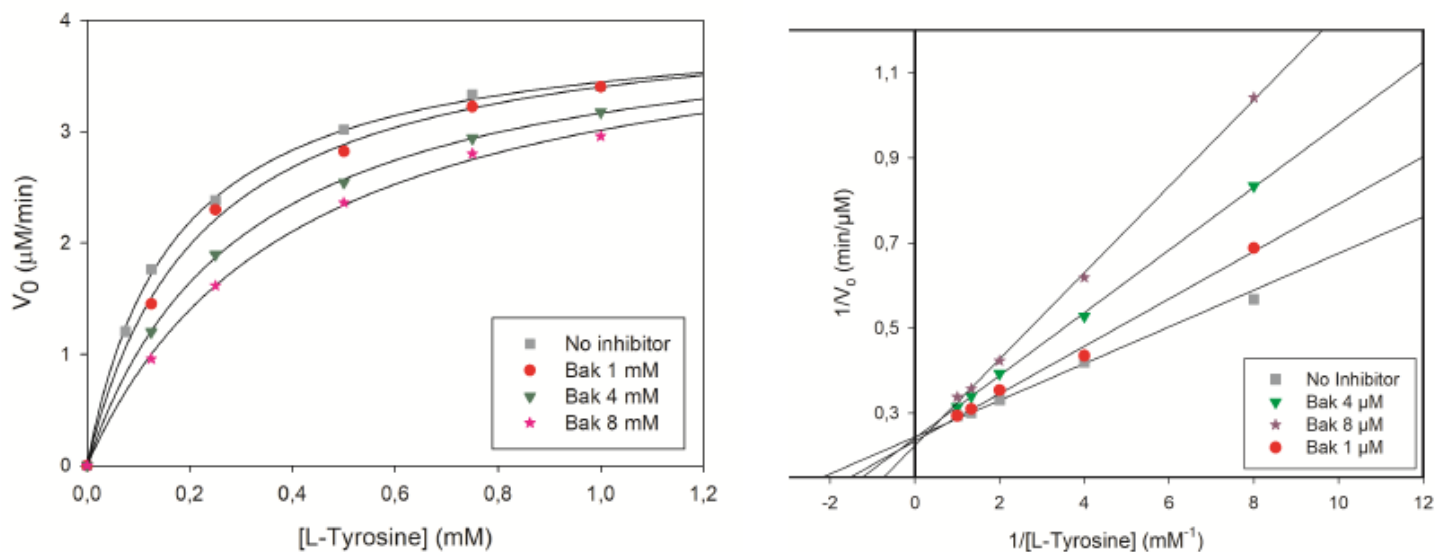


Figure 3.28. Kinetics of monophenolase reaction (substrate = L- Tyrosine) with 1.6 U/mL mushroom tyrosinase at 30°C (pH 6.8), inhibited by various concentrations of bakuchiol, monitored by UV-Vis spectrophotometry at 475 nm (dopachrome formation). The graphs represent Michaelis-Menten hyperbolic plots (left) and Lineweaver-Burk linear plots (right) of the same experiments.

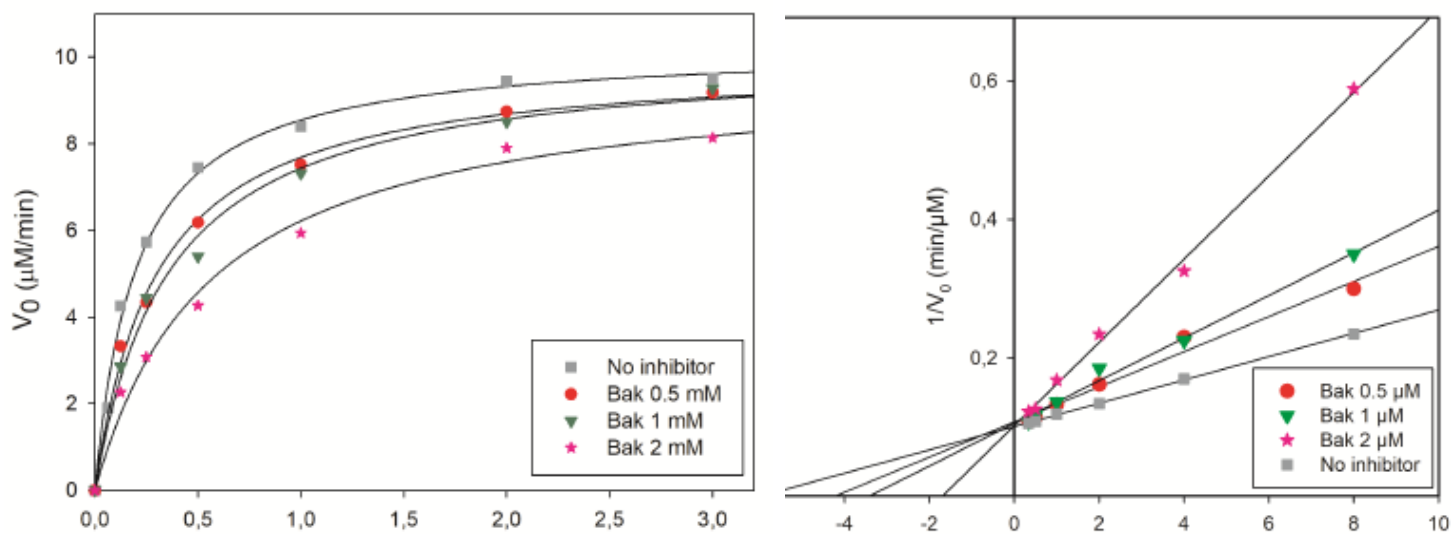


Figure 3.29. Kinetics of diphenolase reaction (substrate = L- DOPA) with 0.8 U/mL mushroom tyrosinase at 30°C (pH 6.8), inhibited by various concentrations of bakuchiol, monitored by UV-Vis spectrophotometry at 475 nm (dopachrome formation). The graphs represent Michaelis-Menten hyperbolic plots (left) and Lineweaver-Burk linear plots (right) of the same experiments.

The lower K_i values compared to kojic acid indicate higher inhibition potency, explaining the purported depigmenting activity of bakuchiol, and justifying the current high interest for this natural compound.

Table 3.8. Kinetic parameters of tyrosinase inhibition by bakuchiol at 30°C (pH = 6.8). Kinetic data were obtained by non-linear fitting of M-M plots at different bakuchiol concentrations, by O₂ sensing and UV-Vis spectrophotometry.^A

Monophenolase (substrate = L-tyrosine)					
O ₂ Uptake					
Bakuchiol (μM)	K_m or K_m^{app} (mM)	V_m or V_m^{app} (μM/min)	K_I (μM)	Average K_I (μM)	IC_{50} (μM)
					1 mM substr.
0	0.19 ± 0.02	4.20 ± 0.10	-		
1	0.21 ± 0.01	3.98 ± 0.25	8.04		
2	0.26 ± 0.03	3.96 ± 0.05	5.80	6.93	33.35
4	0.30 ± 0.02	4.02 ± 0.10	7.11	±0.93	±3.41
8	0.41 ± 0.04	4.00 ± 0.17	6.76		
UV-Vis Spectrophotometry (dopachrome formation)					
Bakuchiol (μM)	K_m or K_m^{app} (mM)	V_m or V_m^{app} (μM/min)	K_I (μM)	Average K_I (μM)	IC_{50} (μM)
					1 mM substr.
0	0.19 ± 0.02	4.11 ± 0.14	-		
1	0.22 ± 0.02	4.13 ± 0.16	5.92	6.49	41.09
4	0.30 ± 0.01	4.12 ± 0.07	6.48	±0.58	±3.12
8	0.40 ± 0.03	4.16 ± 0.13	7.07		
Averaged values (O₂ and UV-Vis)				6.71 ± 1.23	37.22 ± 5.18
Diphenolase (substrate = L-DOPA)					
O ₂ Uptake					
Bakuchiol (μM)	K_m or K_m^{app} (mM)	V_m or V_m^{app} (μM/min)	K_I (μM)	Average K_I (μM)	IC_{50} (μM)
					1 mM substr.
0	0.20 ± 0.01	9.84 ± 0.07	-		
0.5	0.32 ± 0.02	9.73 ± 0.17	0.81		
1	0.38 ± 0.02	9.62 ± 0.16	1.07	1.16	7.06
2	0.49 ± 0.03	9.75 ± 0.20	1.33	±0.28	±0.42
4	0.75 ± 0.09	9.82 ± 0.42	1.44		
UV-Vis Spectrophotometry (dopachrome formation)					
Bakuchiol (μM)	K_m or K_m^{app} (mM)	V_m or V_m^{app} (μM/min)	K_I (μM)	Average K_I (μM)	IC_{50} (μM)
					1 mM substr.
0	0.20 ± 0.02	10.26 ± 0.25	-		
0.5	0.30 ± 0.03	9.98 ± 0.24	1.03	1.13	6.76
1	0.36 ± 0.05	10.12 ± 0.38	1.26	±0.12	±0.73
2	0.56 ± 0.09	9.73 ± 0.51	1.11		
Averaged values (O₂ and UV-Vis)				1.15 ± 0.34	6.91 ± 0.96

^a V_{max} and K_m or V_{max}^{app} and K_m^{app} refer to not inhibited and inhibited assays, respectively.

IC₅₀ values for bakuchiol as an inhibitor of monophenolase and diphenolase enzymes were also measured using both O₂ uptake and spectrophotometry, as described in paragraph 3.4 for glabridin. The resulting IC₅₀ values for bakuchiol at a substrate concentration of 1 mM L-tyrosine or L-DOPA, averaged between the two techniques were 37.22 ± 5.18 μM for monophenolase and 6.76 ± 0.73 μM for diphenolase, while data recorded at other substrate concentrations are collected in Tables 3.9 and 3.10 . These values can be compared to those of a reference inhibitor, kojic acid, which had IC₅₀ values of 34.02 ± 5.51 μM and 16.86 ± 3.28 μM for monophenolase and diphenolase, respectively, at 1 mM substrate, in good agreement with previous studies.

Table 3.9. IC₅₀ values for bakuchiol inhibition of mTYR (30°C; pH 6.8) as a function of the concentration of the substrates L-Tyrosine (monophenolase reaction) and L-DOPA (diphenolase), measured by O₂ uptake kinetics.

[L-dopa] (mM)	0.125	0.25	0.50	1	2	3
IC₅₀ (μM)	1.90 ±0.11	2.44 ±0.18	4.01 ±0.25	7.06 ±0.42	12.96 ±1.12	18.46 ±1.47
[L-tyrosine] (mM)	0.125	0.25	0.50	1		
IC₅₀ (μM)	11.94 ±1.53	16.27 ±2.02	23.93 ±2.32	33.35 ±3.52		

Table 3.10. IC₅₀ values for bakuchiol inhibition of mTYR (30°C; pH 6.8) as a function of the concentration of the substrates L-Tyrosine (monophenolase reaction) and L-DOPA (diphenolase), measured by UV-Vis spectrophotometry (dopachrome formation at 475 nm).

[L-dopa] (mM)	0.125	0.25	0.50	1	2	3
IC₅₀ (μM)	1.83 ±0.09	2.54 ±0.15	3.94 ±0.31	6.76 ±0.73	12.39 ±1.02	18.02 ±1.23
[L-tyrosine] (mM)	0.125	0.25	0.50	1		
IC₅₀ (μM)	10.85 ±0.92	15.21 ±1.20	23.94 ±2.41	41.09 ±3.12		

3.4.2 Fluorescence quenching study

The quenching of intrinsic tryptophan fluorescence of mTYR by inhibitors can be used to confirm the nature of enzyme-inhibitor interaction [52]. In this study, the intrinsic tryptophan fluorescence of mTYR was measured range 290–500 nm (λ_{\max} 338 nm) upon excitation at 280 nm in the absence of inhibitor (F_0) and in the presence of increasing concentrations of bakuchiol, as the inhibitor, in a 50 mM phosphate buffer (pH 6.8). The fluorescence intensity (F) was found to decrease with increasing bakuchiol concentration, without any significant shift in the band maxima, indicating no major change in the conformation of the protein (Fig. 3.30). To evaluate the mechanism of quenching, static or dynamic, this quenching behaviour was analysed using the Stern-Volmer plot (Eq. 3.11) which relates the relative fluorescence intensity to the concentration of a quencher (Q).

$$F_0/F = 1 + k_q\tau_0[Q] = 1 + K_{SV}[Q] \quad (3.11)$$

The plot was found to be linear at low quencher concentrations and showed upward curvature at higher bakuchiol concentrations, indicating that the quenching is of the static type, i.e. the protein and the quencher form a non-emitting stable complex (Fig. 3.30 B). The constant obtained by fitting the plot in the linear region is the Stern-Volmer constant, K_{SV} . Using $\tau_0 = 10^{-8}$ s, which is the typical lifetime of the fluorophore in the absence of the quencher [53], the K_{SV} value obtained is $4.32 \times 10^5 \text{ M}^{-1}$ which is much greater than the maximum scatter collision quenching constant of dynamic quenchers with proteins, indicating that the static quenching mechanism is dominating. The apparent binding constant (K_a) and the number of binding sites (n) for complex formation between bakuchiol and mTYR were obtained by processing fluorescence data with Eq. 3.12.

$$\text{Log} [(F_0 - F)/F] = \text{Log}K_a + n\text{Log}[Q] \quad (3.12)$$

The results were $n = 1.06$ and $K_a = 1.02 \times 10^6 \text{ M}^{-1}$ indicating a single binding site and high affinity of complex formation, fully consistent with the results of enzyme inhibition.

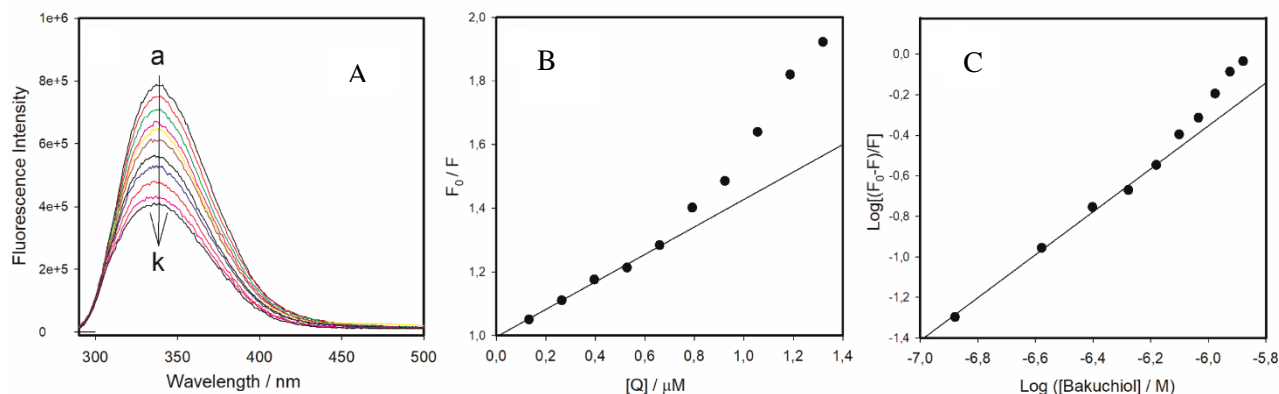
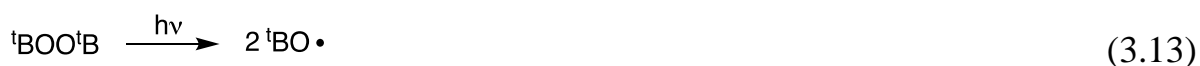


Fig. 3.30 Fluorescence emission spectra of mTYR (20 U/mL) in the absence (a) and the presence (b-k) of increasing concentration of bakuchiol up to 1.320 μM (A), the corresponding Stern-Volmer plot (B), and the log-log plot (eq. 3.12) relating fluorescence quenching to the number of binding sites (n) and complex formation constant K_a (C).

3.4.3 EPR and ReqEPR spectroscopy of bakuchiol phenoxyl radical

Since bakuchiol is regarded as an emerging natural treatment for skin-aging and age-related skin damage, beside the depigmenting activity, the investigation of its ability to quench chain-carrying peroxy radicals was judged important to understand its potential value.

Reaction of the O–H group with oxidizing or chain-carrying radicals (for example the one generated from *tert*-butylbenzene/ $^t\text{BOO}^t\text{B}$) to afford the corresponding stabilized phenoxyl radical is the key process sustaining the activity of phenolic antioxidants, hence we investigated the phenoxyl radical stability to shed more light on the antioxidant mechanism of bakuchiol.



Photolysis of di-*tert*-butylperoxide (TBP) in the presence of bakuchiol in the cavity of the EPR spectrometer generated alkoxy radicals that were trapped forming bakuchiol phenoxy radical, which was identified by its spectrum.

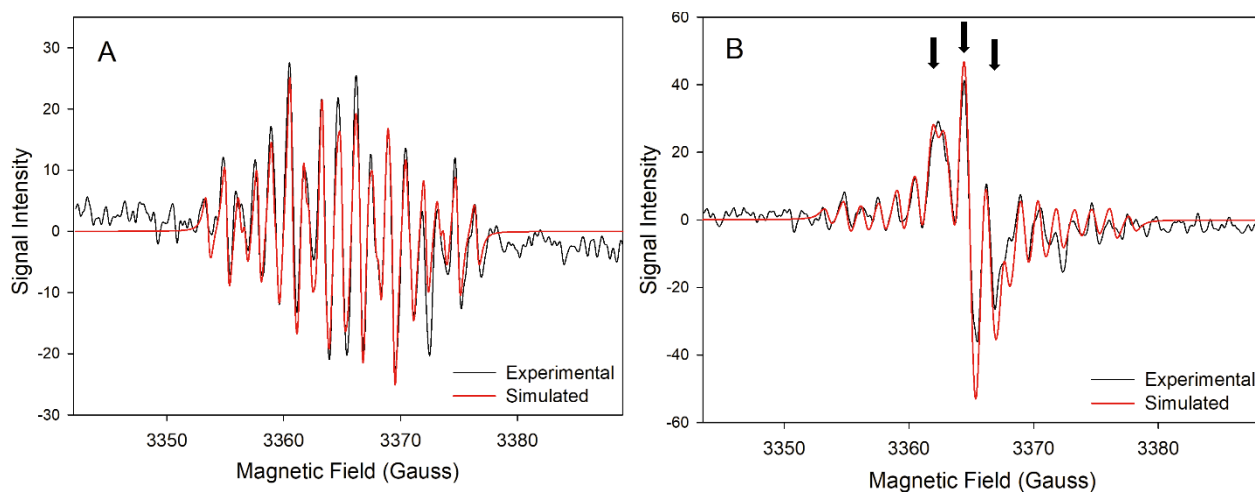


Fig. 3.31. EPR (X-band) spectrum recorded by photolyzing in the cavity of the spectrometer (in *tert*-butylbenzene/¹BOO¹B 9:1, at 30°C): (A) bakuchiol, (B) a mixture of bakuchiol and TBP 20:1. Simulations were obtained by Monte Carlo method using the parameters in Table 3.11. The spectral lines due to TBP• radical are indicated by an arrow (B): the resulting radical ratio was 1.26:1 (Bak•/TBP•).

It showed large hyperfine splitting constants (hfsc/Gauss, Table 3.11) due to coupling with the two *ortho* hydrogens (6.67 G) and with the *para* -CH= (7.05 G), and lower values for coupling with the hydrogen in vinylic position (3.27 G) and with the hydrogens in *meta*-position (1.94 G), in line with structurally related radicals [35,52, 53].

Table 3.11. EPR spectral parameters of bakuchiol phenoxyl radical, BDE(OH) determined by ReqEPR radical equilibration at 30°C in *tert*-butyl-benzene (n = 10).

<i>Thermodynamics of the -OH group</i>			
Radical	hfsc / Gauss ^a		<i>g</i> -factor
Bak(•)	6.67 (2H _{ortho}); 1.94 (2H _{meta}); 7.05 (H _{para}); 3.27 (H _{vinyl})		2.0041
TBP(•)	1.77 (2H _{meta}); 0.18 (18H)		2.0046
^U PhOH	^R PhOH	<i>K</i> _{eq}	BDE (Kcal/mol)
Bak	TBP	14.25 ± 2.07	81.7 ± 0.1

a. Hyperfine splitting constants in Gauss (=0.1 Tesla).

Accordingly, the *g*-factor = 2.0041 was typical of phenoxyl radicals and indicative of C/O coupling. Since the reactivity of phenols like bakuchiol with radicals, hence the antioxidant activity, is dictated by the bond dissociation enthalpy (BDE) of the O–H group, we measured it by the ReqEPR technique [54], [55] which consists in photolyzing the unknown phenol (^UPhOH = bakuchiol) in mixture with a reference phenol (^RPhOH) whose BDE(OH) is known, so to establish their equilibration (Eq. 3.15).



$$K_{eq} = \frac{[{}^U\text{PhOH}]}{[{}^R\text{PhOH}]} \times \frac{[{}^R\text{PhO}\cdot]}{[{}^U\text{PhO}\cdot]} \quad (3.16)$$

$$\Delta G^\circ = \Delta H^\circ - T\Delta S^\circ = -RT\ln K_{eq} \quad (3.17)$$

$$\text{BDE}({}^U\text{PhOH}) = \text{BDE}({}^R\text{PhOH}) - \Delta H^\circ \quad (3.18)$$

Measurement of the corresponding equilibrium constant (Eq. 3.16) is achieved by numerical simulation of the EPR spectrum obtained from the mixture, due to superimposition of the EPR signals of the two radicals, which affords their relative ratio (Fig. 3.31 B). This affords the ΔH of the reaction via (Eq. 3.17) under the reasonable assumption that the entropy change is negligible ($\Delta H \approx \Delta G$). Using 2,4,6-tri-*tert*-butylphenol (TBP) as the reference, the BDE(OH) of bakuchiol was determined

(Eq. 3.18) as 81.7 ± 0.1 kcal/mol (Table 3.11), which well justifies its good antioxidant activity (*vide infra*). Interestingly, this value is similar to that of the weakest OH group in (structurally related) resveratrol which, although not experimentally known, can be estimated as ~ 81.4 Kcal/mol by averaging the calculated (DFT) value (80.2 Kcal/mol) and the empirical value obtained by the group additivity rule (82.6 Kcal/mol) [56].

3.4.5 Antioxidant activity of bakuchiol in solution and in micelles

The antioxidant activity of bakuchiol was investigated by monitoring oxygen consumption during the controlled inhibited autoxidation of reference substrates, as illustrated in chapter 1, both in homogenous organic solution and in heterogenous micellar system. In organic solution (PhCl, 30°C) we studied the inhibited autoxidation of two well established oxidizable substrates, styrene and cumene, having largely different oxidation rates (k_p at 30°C is 41 and 0.34 M⁻¹s⁻¹, respectively) thereby affording complementary information. In the autoxidation of styrene initiated by AIBN, bakuchiol produced a slow-down of the oxidation, without a detectable inhibition period, which was observed instead for reference antioxidant α -tocopherol (TOH). This is due to the major difference in concentration between the oxidizable substrate and the antioxidant (six orders of magnitude), which severely challenges the apparent performance of the antioxidant. Analysis of the oxygen uptake plots was obtained using the following equations:

$$\tau = \frac{n[\text{Antiox.}]}{R_i} \quad (\text{Eq. 3.19})$$

$$-\frac{d[O_2]}{dt} = \frac{k_p[\text{Substrate}]R_i}{nk_{inh}[\text{Antiox}]} \quad (\text{Eq. 3.20})$$

$$\frac{R_0}{R_{inh}} - \frac{R_{inh}}{R_0} = \frac{nk_{inh}[\text{Antiox}]}{\sqrt{2k_t R_i}} \quad (\text{Eq. 3.21})$$

The inhibition rate constant – the rate constant for trapping alkylperoxy radicals – k_{inh} of $2.20 \times 10^5 \text{ M}^{-1}\text{s}^{-1}$ (Table 2.9) was obtained, which was about one order of magnitude lower than that of TOH ($k_{\text{inh}} = 3.2 \times 10^6 \text{ M}^{-1}\text{s}^{-1}$), nature's premiere lipid soluble antioxidant. The absence of a distinct inhibition period did not produce information on the stoichiometric factor n , i.e. the number of peroxy radicals trapped by one molecule of antioxidant. This was instead obtained by studying the inhibited autoxidation of cumene. Due to the lower value of k_p , cumene gave clear inhibition periods in the presence of micromolar bakuchiol, which were proportional to its concentration (Figure 3.32 B), allowing to determine n as 1.9 ± 0.1 , which is the typical value (about $n = 2$) expected for a monophenolic antioxidant.

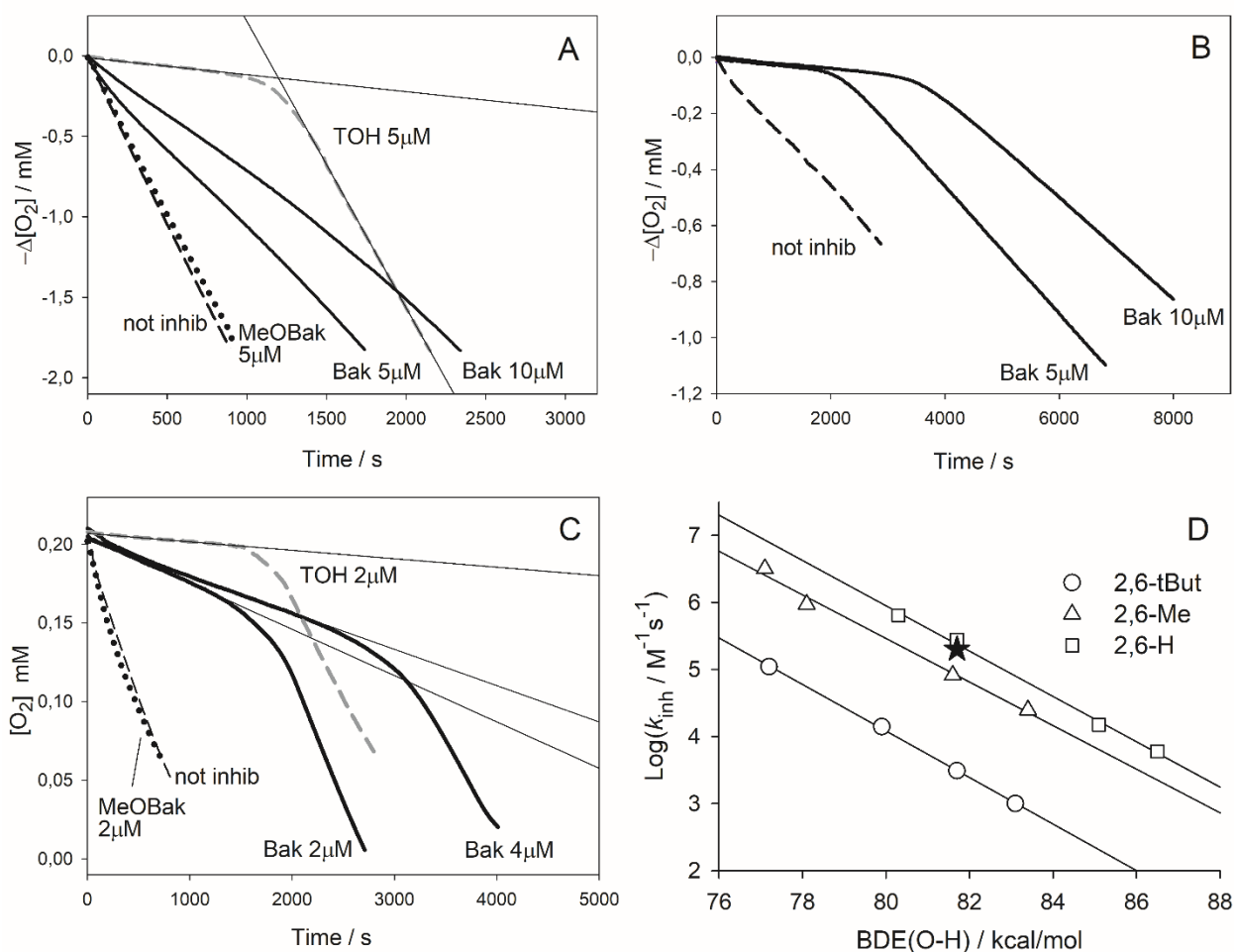


Fig. 3.32 Oxygen consumption plots recorded during the autoxidation of 4.3 M styrene in PhCl (A), and 3.6 M cumene in PhCl (B), both initiated by AIBN (0.05 M) at 30°C, or of 2.74 mM MeLin in 8 mM Triton X-100 micelles initiated by 5 mM AAPH at 37°C, pH 7 (C), without inhibitors (dashed line) or in the presence of bakuchiol, or MeOBak, or TOH as indicated. Thin lines represent the regression of the inhibited periods.

In panel (D) Evans-Polanyi correlation of the rate constant k_{inh} (at 30°C) for trapping ROO• radicals by

phenols with 2,6 (*ortho*) substituents of different size vs their BDE(OH). The data point of bakuchiol is indicated by a full star (★).

The inhibition constant $k_{\text{inh}} = 1.42 \times 10^5 \text{ M}^{-1}\text{s}^{-1}$ is in good agreement with that measured with styrene, standing for the reliability of both our measurements. The resulting averaged (styrene and cumene) value for k_{inh} of bakuchiol in PhCl solution was $1.8 \times 10^5 \text{ M}^{-1}\text{s}^{-1}$. This value, although lower than reference TOH, is identical within experimental error to that of well-established antioxidant resveratrol ($2.0 \times 10^5 \text{ M}^{-1}\text{s}^{-1}$ at 30 °C).

The antioxidant activity in heterogeneous systems was investigated using the autoxidation of methyl linoleate (MeLin, 2.74 mM) in Triton™ X-100 micelles (8 mM) initiated by water soluble AAPH at 37 °C, which is a well-validated kinetic model [58]. Bakuchiol gave distinct inhibition of the autoxidation, whose duration was proportional to its concentration. Comparison with TOH showed almost identical duration of the inhibition which afforded the stoichiometric factor as $n = 1.9 \pm 0.1$, in accordance with the value recorded in organic solution.

The inhibition constant was obtained from the slope of the inhibited period by eq. 3.20 as $k_{\text{inh}} = (1.6 \pm 0.3) \times 10^3 \text{ M}^{-1}\text{s}^{-1}$. For comparison, reference TOH under the same experimental settings afforded $k_{\text{inh}} = (1.5 \pm 0.2) \times 10^4 \text{ M}^{-1}\text{s}^{-1}$ in good agreement with literature using the same kinetic model. As also found in homogeneous solution, bakuchiol traps peroxy radical in micelles about one order of magnitude slower than TOH; however, it is interesting to note that its antioxidant activity in micelles is almost identical to that recently reported for resveratrol ($1.5 \times 10^3 \text{ M}^{-1}\text{s}^{-1}$ at 37° pH 7).

3.4.6 Antioxidant activity of bakuchiol O-methyl derivative MeOBak

Since a previous study [49, 52] suggested that bakuchiol antioxidant activity is due only in part to the phenolic –OH group, while the terpenic chain in 4-position also contributes by trapping radicals, we synthesized the protected methyl ester of Bakuchiol (MeOBak) derivative by O-methylation of bakuchiol, and tested it as an antioxidant in parallel autoxidation studies, using the oxidation of styrene in

chlorobenzene solution and of MeLin in Triton™ X-100 micelles as model systems. When tested under experimental settings identical to those used of native Bak, MeOBak showed no inhibition of the autoxidation of styrene (Fig. 3.32 A,C) similarly, no protection was observed in the autoxidation of MeLin in micelles where oxygen consumption plots obtained with MeOBak as the inhibitor were practically identical to those obtained without antioxidant. This allows to exclude the direct involvement of the terpene chain in the antioxidant activity of bakuchiol under our experimental settings (*vide infra*).

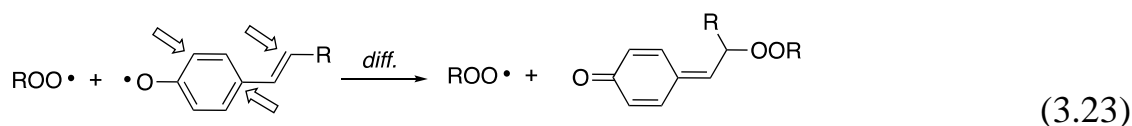
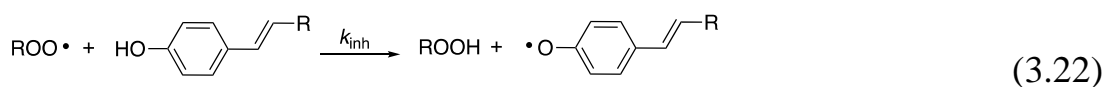
3.4.7 Discussion

Kinetic studies on tyrosinase inhibition carried out in parallel using real-time O₂ sensing and spectrophotometric monitoring of dopachrome yielded perspective results that support each other and show major inhibition efficacy by bakuchiol, even in the low micromolar range, in contrast to a previous report that indicated very modest inhibition, even at concentrations of 1 mg/mL. Inhibition is competitive for both the monophenolase and diphenolase reactions, with M-M related inhibition constant K_i of 6.71 1.23 M and 1.15 0.34 M, respectively, indicating higher inhibition potency for the diphenolase reaction - lower values indicate higher activity. K_i values determined in kinetic studies, which represent the enzyme-inhibitor complex's dissociation constant, are completely consistent with the K_a value of $1.02 \cdot 10^6 \text{ M}^{-1}$ determined by fluorescence quenching, which represents the apparent formation constant for such complex. Interestingly, K_i values are lower than those we previously measured for reference inhibitor kojic acid (10.91 μM and 9.91 μM for monophenolase and diphenolase inhibition respectively), indicating higher bioactivity of bakuchiol.

Although less robust in quantifying inhibition potency due to their reliance on substrate and enzyme concentration, IC_{50} values support bakuchiol's high anti-tyrosinase activity. In the tested concentration range, values measured by O₂ sensing ranged from 12-33 μM for monophenolase inhibition to 2-18 μM for diphenolase inhibition. Values obtained by spectrophotometry were also in good agreement. Taking 1 mM substrate

as reference setting for comparison and using averaged results from O₂ sensing and spectrophotometry, IC₅₀ values measured here for kojic acid indicate similar activity for monophenolase inhibition (34.02 μM vs 37.22 μM), while for diphenolase inhibition bakuchiol (IC₅₀ = 6.76 μM) was sensibly more effective than kojic acid (IC₅₀ = 16.86 μM). This is at variance with a previous study reporting IC₅₀ values of bakuchiol 18-folds higher than kojic acid for diphenolase inhibition, and indicates higher anti-tyrosinase activity of bakuchiol than previously expected.

Kang et al. [58] reported that an extract of *P. corylifolia* containing 77% bakuchiol reduced melanin biosynthesis in normal human epidermal melanocytes and the activity was attributed to reduction of tyrosinase enzyme expression and to reduction of TRP-1, TRP-2 and SOX-9 supporting proteins in melanocytes, without significant toxicity. The study showed also a downregulation of melanocyte dendrites formation, necessary to the transfer of melanosomes to keratinocytes as part of the normal skin pigmentation process. Our results indicate an additional complementary mechanism for the depigmenting activity outlined in that study: the potent inhibition of tyrosinase reaction. This completes the picture and allows better understanding of bakuchiol's depigmenting activity. Most important, it opens to new applications of bakuchiol (*vide infra*). Being a phenolic compound, the antioxidant activity of bakuchiol is expectedly dictated by its ability to quench chain-carrying peroxy radicals to the corresponding hydroperoxide, by formal H-atom transfer from the phenolic OH (Eq. 3.22). Inhibited autoxidation studies indicated a stoichiometric factor $n \sim 2$ (1.9 ± 0.1) both in organic solution and in aqueous micelles; therefore, a second peroxy radical is trapped by the resulting phenoxyl radical, i.e. by addition to the aromatic ring in conjugated positions (arrows in Eq. 3.23), or possibly by addition in the conjugated ethylene group (19).



Trapping of the second ROO• however does not determine the antioxidant activity, which is regulated by rate-determining reaction eq. 3.22. Since the BDE(OH) of the alkylhydroperoxides is 88.6 kcal/mol, our measurement of the BDE(OH) of bakuchiol by ReqEPR as 81.7 kcal/mol affords the ΔH° of reaction eq. 2.21 as -6.9 kcal/mol, which justifies bakuchiol's efficient trapping of ROO• radicals ($k_{\text{inh}} = 1.8 \times 10^5 \text{ M}^{-1}\text{s}^{-1}$ in PhCl solution at 30°C). Indeed, the BDE(OH) value of bakuchiol can be correlated to its reactivity via linear Evans-Polanyi relationships between $\log(k_{\text{inh}})$ and BDE(OH), which are well established for phenolic antioxidants. A plot built using literature data for differently substituted phenols in apolar organic solution, shows parallel correlation lines that differ for the bulkiness of substituents in *ortho*-position to the reactive OH group, i.e. they depend on steric factors. Bakuchiol perfectly fits in the correlation line for phenols lacking *ortho* substituents, implying that its reactivity with peroxy radicals is due entirely to the reaction of the phenolic OH group with peroxy radicals, while the terpenoid chain would influence the overall reactivity only by stabilizing the phenoxy radical and lowering the BDE(OH).

Our findings are at variance with a previous study which attributed part of the antioxidant activity of bakuchiol to the terpenoid chain. This conclusion was drawn mainly for the finding that the O-methylated derivative (MeOBak) reacted with thiyl radicals (by H-abstraction in the allyl positions) forming detectable transient species. However, the reaction of the side chain with some radical does not mean necessarily produce inhibition of autoxidation if the formed C-centered radical (R•) rapidly reacts with oxygen to form an alkylperoxy radical ROO• that propagates the oxidative chain. Indeed, when we prepared MeOBak and tested it as an antioxidant both in the autoxidation of styrene in solution and of MeLin in micelles, results showed that MeOBak had no antioxidant activity in either system, confirming that bakuchiol's antioxidant activity is entirely derived from the phenolic OH.

Previous studies from our research group identified an additional mechanism by which terpenoid compounds might express antioxidant activity, i.e. by enhancing the chain-

termination reaction [58]. However, this has some importance only at much higher concentrations and depending on the exact experimental conditions, hence it does not come into action under the settings in which the ROO• trapping by the phenolic –OH drives the antioxidant behavior.

The lower antioxidant activity of bakuchiol in micelles compared to apolar organic solution (k_{inh} of $1.6 \times 10^3 \text{ M}^{-1}\text{s}^{-1}$ vs $1.8 \times 10^5 \text{ M}^{-1}\text{s}^{-1}$) is well-known feature of any phenolic antioxidant and it is observed also with reference TOH (k_{inh} from $3.2 \times 10^6 \text{ M}^{-1}\text{s}^{-1}$ to $1.5 \times 10^4 \text{ M}^{-1}\text{s}^{-1}$). It is caused in part by H-bonding of the phenolic OH group at the water-lipid interface, and in part by rate-limiting exchange of radicals and antioxidants among micellar particles. It is worth noting that the antioxidant activity of bakuchiol matches that of the well-known antioxidant resveratrol in both apolar organic solutions and aqueous micelles, which increases interest in bakuchiol's potential applications. The presence of good antioxidant activity as well as high tyrosinase inhibiting activity fully justifies bakuchiol's interest in topical skin-care treatments, such as anti-photoaging, and meets a growing demand for plant-derived compounds with such bioactivity. Most intriguingly, our findings point to bakuchiol's previously untapped potential as a natural food preservative. Not only bakuchiol outperforms reference kojic acid as tyrosinase inhibitor, it also outperforms by over one order of magnitude the efficacy in peroxy radical trapping of ubiquitous food preservative butylated hydroxytoluene (BHT, $k_{\text{inh}} \sim 1 \times 10^4 \text{ M}^{-1}\text{s}^{-1}$ at 30°C in PhCl), promising much improved protection against oxidative damage combined with excellent protection from enzymatic food-browning.

EXPERIMENTAL PART

3.5 Materials and method

3.5.1 Materials

(*S*)-(+)-Bakuchiol (4-[(3*S*,1*E*)-3-ethenyl-3,7-dimethylocta-1,6-dien-1-yl]phenol; 99%) was from Cymit Quimica (Barcellona, Spain). Tyrosine ($\geq 98\%$), L-DOPA (3,4-

dihydroxy-L-phenylalanine; $\geq 98\%$), kojic acid (5-hydroxy-2-hydroxymethyl-4H-4-pyranone; $\geq 98.5\%$) Glabridin ($\geq 98\%$), water, acetonitrile, methanol (HPLC grade) were purchased from Sigma-Aldrich (St. Louis, MO, USA). Commercial mushroom tyrosinase (EC 1.14.18.1, activity = 3130 units/mg) was purchased from Sigma-Aldrich and used without further purification. Fresh mTYR solutions were prepared every day and tyrosinase activity was analyzed spectrophotometrically to adjust solutions to fixed tyrosinase Sigma units for consistent results. Briefly, one Sigma unit corresponds to the amount that will cause an increase in absorbance at 280 nm of 0.001 per minute at pH 6.8 in a 3 mL reaction mixture containing L-tyrosine. Sigma units were used throughout this study. One Sigma unit corresponds to 1.65×10^{-4} international units (I.U.) for monophenolase activity and to 2.24×10^{-2} I.U. for diphenolase activity. AAPH (2,2'-azobis(2-methylpropionamide) dihydrochloride), methyl linoleate ($\geq 98\%$) and Triton™ X-100, were used as received. AIBN (2,2' -Azobis(isobutyronitrile); 98%) was recrystallized from methanol, while 2,4,6-tri-*tert*-butylphenol (TBP, 98%) was recrystallized from hexane. Stock solutions of AAPH or AIBN in the desired solvents were prepared immediately prior to use and/or maintained for maximum 2h or 4h, respectively, at 4°C between subsequent uses, to avoid significant decomposition. Cumene (98%) and styrene ($\geq 99\%$) were purified by double percolation through silica and activated basic alumina columns. Solvents and other chemicals were of the highest grade commercially available (Sigma-Aldrich, Merck, VWR; Milan, Italy) and were used as received.

3.5.2 *kinetics evaluation of tyrosinase reaction by UV-Vis spectrophotometer*

Kinetic evaluation of monophenolase and diphenolase inhibition of tyrosinase with or without inhibitors was carried out using UV-Vis spectrophotometry at 30°C in a Thermo Scientific (Milan, Italy) Biomate 5 coupled with a Heto DBT Hetotherm (Birkerød, Denmark) thermostating water circulator for temperature control. The samples were analyzed in polystyrene micro cuvettes (≥ 1.5 mL, $l = 1$ cm, 12.5×12.5

×45 mm). Absorbance of dopachrome was measured at 475 nm from 20 min to 60 min (1 scan / 55s) reading the solution against a reference cuvette containing all reaction components except the substrate, which was replaced with potassium phosphate buffer (50 mM, pH 6.8). Absorbance variation *vs* time at different substrate concentration allowed to obtain initial velocity ($V = \Delta A / \Delta \text{min}$) which was converted in $\mu\text{M}/\text{min}$ according Lambert-Beer law as follows¹ : $V (\mu\text{M}/\text{min}) = V (\Delta A / \Delta \text{min}) \times 10^6 / \epsilon_{\lambda_{\text{max}}} \times l$. The molar extinction coefficient (ϵ) for dopachrome at $\lambda_{\text{max}} = 475 \text{ nm}$ is $3700 \text{ M}^{-1} \text{ cm}^{-1}$ and UV path (l) was 1 cm. Michaelis-Menten parameters (K_m e V_{max}) were obtained processing initial velocity *vs* substrate concentration data by nonlinear regression using Sigmaplot software.

The effect of inhibition of monophenolase activity was evaluated at fixed tyrosinase units at varying substrate concentrations testing reactions without and with inhibitors. Given the difficulty to maintain the activity of enzyme, the tyrosinase activity was analysed at the beginning of every integral week during the experimental period according to supplier indications, in order to adjust to fixed tyrosinases units for different substrates. Briefly, Sigma unit corresponds to the amount that will cause an increase in absorbance at 280 nm of 0.001 per minute at pH 6.8 in a 3 mL reaction mixture containing L-tyrosine. Sigma units were used thoroughly in this study.

3.5.3 kinetic evaluation of tyrosinase reaction by oximetry

Kinetic evaluation of tyrosinase monophenolase and diphenolase kinetics or inhibition by inhibitors was carried out using oximetry at 30°C by the oxygen sensor (Pyrosience Bremen, Germany) immersed in a water bath controlled by Heto DBT Hetotherm (Birkerød, Denmark). The samples were contained in stirred 2.4 mL glass flasks, immersed in a water bath. The oxygen consumption was recorded every second, and all reaction components were maintained as those set for UV–vis spectrophotometry. The raw data collected directly from the oxygen sensor is a percentage (P) of the

saturation oxygen concentration in the sample, corresponding to 0.236 mM at 30 °C which reflects in the sensor reading as 20 % (P_0). Thus, the oxygen concentration during the time course of the enzymatic oxidation of L-dopa or L-tyrosine were converted into mM/s by the following equation: $[O_2]$ (mM) = percentage \times 0.236 (mM) / 20%.

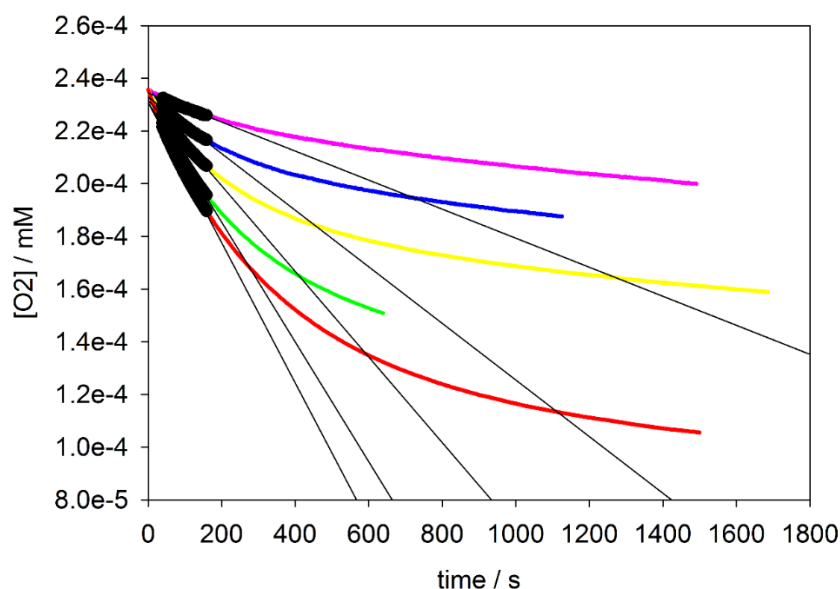


Figure 3.33 Example of the time progresses of O_2 consumption during the oxidation of L-dopa at different initial concentration from 0.1 mM (purple line) to 1.2 mM (red line), inhibited by glabridin (80 nM). The black lines are the linear regression (V_0) for every L-dopa concentration, taken in the highlighted time range (40s to 160s).

Table 3.12 Raw data of initial rates obtained from the linear fitting by Sigamplot software of initial rates of oxygen consumption for different L-dopa concentrations.

[L-dopa] (mM)	0.1	0.2	0.4	0.8	1.2
$V_0 = \text{slope of } O_2 \text{ uptake (mM/s)}$	5.71×10^{-8}	1.14×10^{-7}	1.70×10^{-7}	2.37×10^{-7}	2.63×10^{-7}

The non-linear analysis was conducted by non-linear fitting of initial velocity V_0 as a function of L-dopa concentration with the hyperbolic equation $y = \frac{a x}{b + x}$ using sigmaplot software, where y, x, a and b represent V_0 , [S], V_{\max} and K_m respectively. The results of fitting are shown in Figure 2.30.

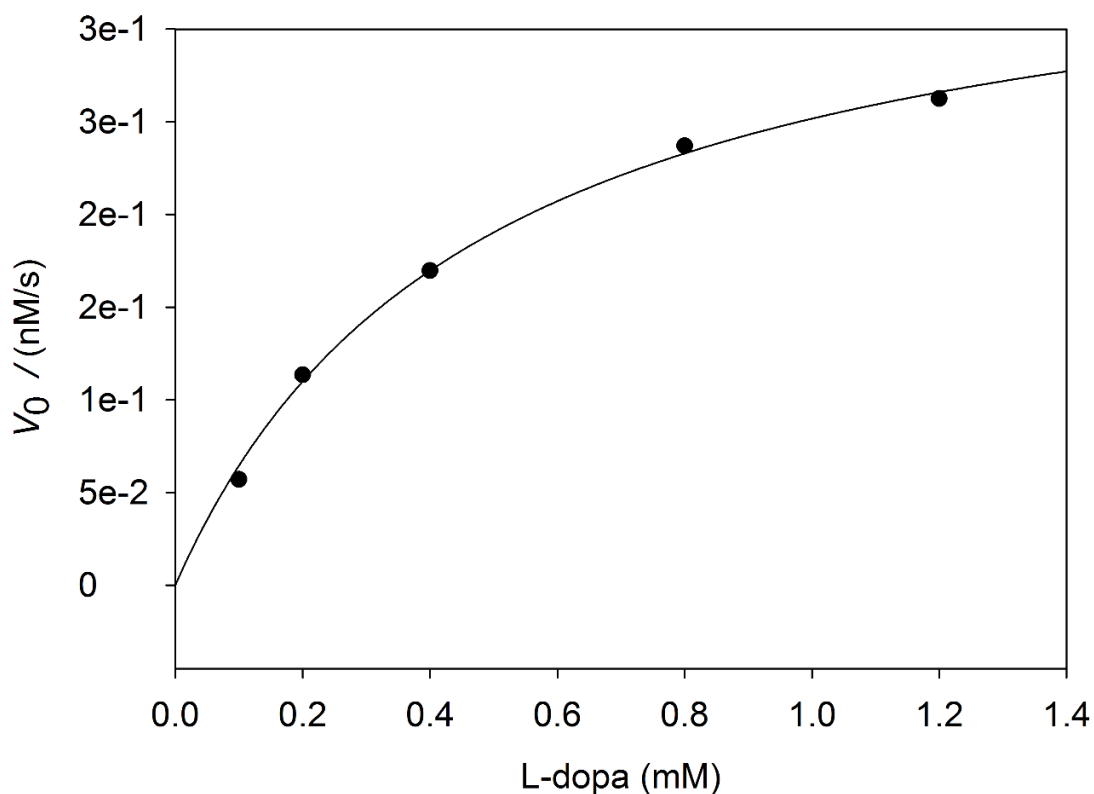


Figure 3.34. Initial rates of oxygen consumption during tyrosinase catalyzed oxidation of L-dopa and the corresponding non-linear fitting to Michaelis-Menten kinetics.

The results from the non-linear fitting by Sigmaplot is shown below:

Results for the Overall Best-Fit Solution:

R	Rsqr	Adj Rsqr	Standard Error of Estimate
0.9983	0.9967	0.9956	5.6658E-009

Coefficient

a	3.7521E-007
b	0.4749

where the value of a and b represent V_{\max}^{app} and K_m^{app} , respectively.

Identical kinetic data collection and treatment was applied when using L-tyrosine as the substrate and either in the absence of inhibitor or for each concentration of glabridin.

3.5.4 Setup of the real-time oxygen sensing equipment

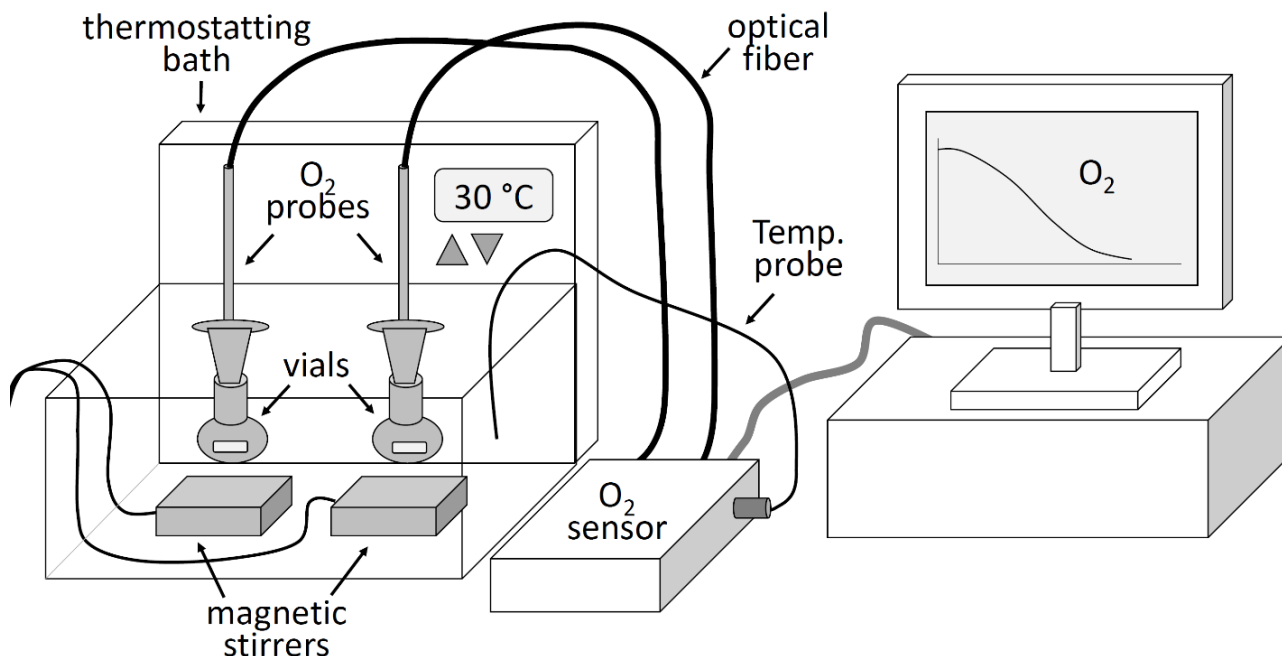


Fig. 3.35 The equipment setup

The equipment was set up using a commercial two channels Optical Oxygen Meter FireSting-O₂ (model FSO2-2) connected via optical fibers to two IR fluorescence oxygen sensor probes (Robust type) contained in a 3 mm o.d. stainless-steel needle (Pyrosience GmbH, Bremen, Germany). The samples were contained in 2.4 mL glass flasks hand-made by a local scientific glass blower, sealed with a conical PP cap through which the O₂ sensor is inserted (after drilling the cap along the main axis) so that the sensor tip is protruding for about 3-4 mm inside the flask and is air-tight sealed. On closing the flask, care is taken to leave no air bubble, so that the entire volume is occupied by the (air-saturated) aqueous reaction mixture. The sample flask is provided with a PTFE-coated stirring bar and is completely submerged in a water bath controlled by Heto DBT HeteroTherm (Birkerød, Denmark) thermostating unit. Mixing is provided by submerged sealed magnetic stirrers MixDrive 1XS controlled by an external Mix Control (2mag AG, Munchen, Germany). The oxygen meter is connected to a temperature sensor (immersed in the water bath) for automatic correction of the sensor

response, and to a PC via USB port for data collection. The O₂ sensor probes are designed and indicated by the manufacturer for use in aqueous solution, in the bare form, i.e. without any protection. Since the content in organic material in our samples was very limited, in principle the probes could be used, as indicated, without protection. However, on performing multiple measurements with the same probes, we noted a progressive loss in sensitivity with time, which we attributed to the deposition of thin layers of insoluble melanin on the surface of the polymeric matrix containing the fluorescent dye, in the sensor tip (only the lower surface is exposed to the solution, while the rest of the matrix is protected by the stainless-steel structure of the probe). Such loss of performance could not be overcome by accurate cleaning of the surface without causing damage to the probe itself. Therefore, we decided to protect the tip of the probe by coating with a polymeric membrane, which would allow sufficient permeability to oxygen to produce no interference with the kinetic measurements.

In order to protect the oxygen probe, several polymeric membranes were comparatively tested in reference kinetic assays for oxygen consumption, namely: 1) the time-course of oxygen concentration in a freshly prepared solution of 8 mM Na₂SO₃ in distilled water; 2) the autoxidation of 10% (v/v) tetrahydrofuran (THF) in aqueous phosphate buffer (pH 7.4) initiated by the thermal decomposition of 50 mM azobisamidinopropane dihydrochloride (AAPH) at 30°C; 3) the autoxidation of 0.15% (w/v) soy lecithin in aqueous phosphate buffer (pH 7.4) initiated by 75 mM AAPH at 30°C. Tested membranes were: a) silicon 500 μm; b) LDPE 100 μm; c) LDPE 25 μm; d) LDPE/HDPE 12 μm; e) Teflon® (PTFE) 100 μm; f) Teflon® (PTFE) 76 μm. Among them, d) and f) offered the best compromise between oxygen permeability and mechanical properties: both offered no significant barrier to the consumption of oxygen at rates of ca. 0.1 mM/s, with measured rates of oxygen consumption differing less than 5% with respect to the bare (uncoated) probe. Teflon® (PTFE) 76 μm was selected for our kinetic measurements with tyrosinase for its inertness. To guarantee reproducible measurements with no interference of the membrane, we found it is important to have both sides of the membrane “hydrated” *i.e.* in contact with water so

that the diffusion of O₂ through the membrane follows the path water-membrane-water. To this end, we always took care of leaving a thin layer of buffered water (the same medium used for kinetic measurements) between the membrane and the lower (sensitive) surface of the oxygen probe. To do so, we applied a drop of buffer solution on the membrane and used it to obtain intimate adhesion of the membrane itself to the tip of the probe, then we fixed the membrane tightly in place with an O-ring, applied with the help of a micropipette tip (*e.g.* Gilson type), taking care of leaving no air bubble between the membrane and the tip of the probe. The membrane could be (gently) washed externally after every use and was replaced every day or every second day of experiments. The same instrumental setting was also used to monitor oxygen consumption during autoxidation studies in micellar systems in water.

3.5.5 Autoxidation studies in homogenous solution

Autoxidation experiments were performed in a two-channel oxygen uptake apparatus, based on a Validyne DP 15 differential pressure transducer built in our laboratory [161]. In a typical experiment, an air-saturated solution of the oxidizable substrate containing AIBN (0.01-0.1M) was equilibrated at 30 °C with an identical reference solution containing excess 2,2,5,7,8-pentamethyl-6-hydroxychromane (PMHC, 25 mM). After equilibration, and when a constant O₂ consumption was reached, a stock solution of the antioxidant (typically 1.0 mM in PhCl) was injected in the sample flask, so to reach the desired concentration in the range 1-20 μM in the sample flask. The oxygen consumption in the sample was measured after calibration of the apparatus from the differential pressure recorded with time between the two channels. Initiation rates, R_i , were determined for each condition in preliminary experiments by the inhibitor method, where τ is the length of the inhibition period, using TOH as a reference antioxidant.

The inhibition rate constant for peroxy radical trapping k_{inh} was obtained from oxygen consumption plots by eqs. 2.19 or 2.20, where k_p , and $2k_t$, are the rate constants for chain propagation and termination of the substrate, R_0 and R_{inh} are respectively the rate

of oxygen consumption ($-d[\text{O}_2]/dt$) in the absence and presence of the antioxidant, while n is the stoichiometric factor, *i.e.* the number of peroxy radicals trapped by one molecule of antioxidant. Styrene ($k_p = 41 \text{ M}^{-1}\text{s}^{-1}$; $2k_t = 4.2 \times 10^7 \text{ M}^{-1}\text{s}^{-1}$, at 30°C) and cumene ($k_p = 0.34 \text{ M}^{-1}\text{s}^{-1}$; $2k_t = 4.5 \times 10^4 \text{ M}^{-1}\text{s}^{-1}$, at 30°C) were used as the oxidizable substrates [59].

3.5.6 Autoxidation studies in aqueous micelles

Measurements were performed as previously described [58], with modifications. In a typical experiment, 2.5 mL of air-saturated buffered (PBS, 50 mM, pH 7.4) aqueous dispersion of MeLin (final concentration 2.74 mM) in TritonTM X-100 (final concentration 8 mM) micelles were prepared by vortex mixing, then adding a freshly prepared stock solution of AAPH (final concentration 5 mM), immediately followed by addition 4-16 μL of a (0.5-1 mM) stock solution of the antioxidant in acetonitrile (final concentration of 2-8 μM) at room temperature. After brief additional vortex stirring (5-10 sec.) the mixture used to fill in a sealed 2.4 mL glass vial provided with a PTFE-coated stirring bar. The sample was equilibrated at 37°C in a thermostatted bath equipped with a sealed magnetic stirrer and O_2 consumption was recorded. Oxygen concentration was monitored with the same equipment described for mTYR kinetics and data were similarly treated by the equation: $V \text{ (M/s)} = V \text{ (}\Delta P/\Delta t\text{)} \times 0.210 \times 10^{-3} / P_0$, where P_0 is the initial 20% O_2 saturation reading that corresponds to 0.210 mM at 37°C . Oxygen consumption in the presence of the antioxidant was compared with that recorded with identical reference mixtures lacking the antioxidant. The inhibition rate constant was obtained from oxygen consumption plots by Eqs. 3.19-3.21, as described for autoxidation studies in homogenous solution, using $k_p = 36 \text{ M}^{-1}\text{s}^{-1}$ for MeLin in micelles.

3.5.7 EPR measurements

Deoxygenated *tert*-butylbenzene solutions containing the phenols (0.01-0.001 M) and di-*tert*-butyl peroxide (10% v/v) were sealed under nitrogen in a suprasil quartz EPR

tube. The sample was inserted in the thermostatted (30°C) cavity of an X-band EPR spectrometer and photolyzed with a mercury-xenon lamp (240-400 nm, max 4500 mW/cm²). Spectra were recorded with the following settings: modulation amplitude 0.1-1 Gauss, sweep width 60 Gauss, modulation frequency 100 kHz, frequency 9.76 GHz, sweep time 60s, microwave power 0.1-1 mW. Measured *g*-factors, were corrected with respect to that of the perylene radical cation in concentrated H₂SO₄ (*g* = 2.00258). When using mixtures of TBP and bakuchiol in ReqEPR experiments, the molar ratio of the two equilibrating radicals was obtained from the EPR spectra and used to determine the equilibrium constant, *K*_{eq}. Different irradiation power levels (20% to 100%) and different ratios of the two phenols were tested to guarantee that the two species were at the equilibrium. Spectral parameters and relative radical concentrations were determined by comparison of the digitized experimental spectra with computer simulated ones, as previously described [57].

3.5.8 Statistical analysis

Each measurement was performed at least in triplicate. Values of *V*_{max} and *V*_{max}^{app}, and of *K*_m and *K*_m^{app} in the absence and presence of inhibitors were determined from non-linear regression of M-M plots based on 5-6 concentrations of the substrate, which were analysed by Shapiro-Wilk Test with significance set at *P* ≤ 0.05. Results are expressed as regression value ± standard error.

References

- [1] M. d'Ischia, K. Wakamatsu, F. Cicoira, E. Di Mauro, J.C. Garcia-Borron, S. Commo, I. Galván, G. Ghanem, K. Kenzo, P. Meredith, A. Pezzella, C. Santato, T. Sarna, J.D. Simon, L. Zecca, F.A. Zucca, A. Napolitano, S. Ito, Melanins and melanogenesis: from pigment cells to human health and technological applications, *Pigment Cell Melanoma Res.* 28 (2015) 520–544. <https://doi.org/10.1111/pcmr.12393>.
- [2] Y. Guo, A. Baschieri, F. Mollica, L. Valgimigli, J. Cedrowski, G. Litwinienko, R. Amorati, Hydrogen Atom Transfer from HOO. to ortho-Quinones Explains the Antioxidant Activity of Polydopamine, *Angewandte Chemie International Edition.* 60 (2021) 15220–15224. <https://doi.org/10.1002/anie.202101033>.
- [3] M. d'Ischia, A. Napolitano, A. Pezzella, P. Meredith, M. Buehler, Melanin Biopolymers: Tailoring Chemical Complexity for Materials Design, *Angewandte Chemie International Edition.* 59 (2020) 11196–11205. <https://doi.org/10.1002/anie.201914276>.
- [4] S. Roy, J.W. Rhim. New insight into melanin for food packaging and biotechnology applications. *Crit Rev Food Sci Nutr.* 2022;62(17):4629-4655. doi: 10.1080/10408398.2021.1878097.
- [5] E. Nicolaidou, A.D. Katsambas, Pigmentation disorders: hyperpigmentation and hypopigmentation, *Clinics in Dermatology.* 32 (2014) 66–72. <https://doi.org/10.1016/j.clindermatol.2013.05.026>.
- [6] K.M. Moon, E.-B. Kwon, B. Lee, C.Y. Kim, Recent Trends in Controlling the Enzymatic Browning of Fruit and Vegetable Products, *Molecules.* 25 (2020) 2754. <https://doi.org/10.3390/molecules25122754>.
- [7] O. Martínez-Alvarez, M. Elvira López-Caballero, P. Montero, M. del Carmen Gómez-Guillén, The effect of different melanosis-inhibiting blends on the quality of frozen deep-water rose shrimp (*Parapenaeus longirostris*), *Food Control.* 109 (2020) 106889. <https://doi.org/10.1016/j.foodcont.2019.106889>.
- [8] X. Song, M. Ni, Y. Zhang, G. Zhang, J. Pan, D. Gong, Comparing the inhibitory abilities of epigallocatechin-3-gallate and gallic acid against tyrosinase and their combined effects with kojic acid, *Food Chemistry.* 349 (2021) 129172. <https://doi.org/10.1016/j.foodchem.2021.129172>.
- [9] Q. Yu, L. Fan, Understanding the combined effect and inhibition mechanism of 4-hydroxycinnamic acid and ferulic acid as tyrosinase inhibitors, *Food Chemistry.* 352 (2021) 129369. <https://doi.org/10.1016/j.foodchem.2021.129369>.
- [10] L.-L. Shao, X.-L. Wang, K. Chen, X.-W. Dong, L.-M. Kong, D.-Y. Zhao, R.C. Hider, T. Zhou, Novel hydroxypyridinone derivatives containing an oxime ether moiety: Synthesis, inhibition on mushroom tyrosinase and application in anti-browning of fresh-cut apples, *Food Chemistry.* 242 (2018) 174–181. <https://doi.org/10.1016/j.foodchem.2017.09.054>.
- [11] L. Panzella, A. Napolitano, Natural and Bioinspired Phenolic Compounds as Tyrosinase Inhibitors for the Treatment of Skin Hyperpigmentation: Recent Advances, *Cosmetics.* 6 (2019) 57. <https://doi.org/10.3390/cosmetics6040057>.
- [12] T.-S. Chang, Natural Melanogenesis Inhibitors Acting Through the Down-Regulation of Tyrosinase Activity, *Materials.* 5 (2012) 1661–1685. <https://doi.org/10.3390/ma5091661>.
- [13] W. Qian, W. Liu, D. Zhu, Y. Cao, A. Tang, G. Gong, H. Su. Natural skin-whitening compounds for the treatment of melanogenesis (Review). *Exp Ther Med.* 2020 Jul;20(1):173-185. doi: 10.3892/etm.2020.8687. Epub 2020 Apr 24. PMID: 32509007; PMCID: PMC7271691.
- [14] Y.-J. Kim, H. Uyama, Tyrosinase inhibitors from natural and synthetic sources: structure, inhibition mechanism and perspective for the future, *CMLS, Cell. Mol. Life Sci.* 62 (2005) 1707–1723. <https://doi.org/10.1007/s00018-005-5054-y>.
- [15] Á. Sánchez-Ferrer, J. Neptuno Rodríguez-López, F. García-Cánovas, F. García-Carmona, Tyrosinase: a comprehensive review of its mechanism, *Biochimica et Biophysica Acta (BBA) - Protein Structure and Molecular Enzymology.* 1247 (1995) 1–11. [https://doi.org/10.1016/0167-4838\(94\)00204-T](https://doi.org/10.1016/0167-4838(94)00204-T).
- [16] J.N. Rodríguez-López, J. Tudela, R. Varón, F. García-Carmona, F. García-Cánovas, Analysis of a kinetic model for melanin biosynthesis pathway., *Journal of Biological Chemistry.* 267 (1992) 3801–3810. [https://doi.org/10.1016/S0021-9258\(19\)50597-X](https://doi.org/10.1016/S0021-9258(19)50597-X).
- [17] S. Zolghadri, A. Bahrami, M.T. Hassan Khan, J. Munoz-Munoz, F. Garcia-Molina, F. Garcia-Canovas, AA. Saboury. A comprehensive review on tyrosinase inhibitors. *J Enzyme Inhib Med Chem.* 2019 Dec;34(1):279-309. doi: 10.1080/14756366.2018.1545767. PMID: 30734608; PMCID: PMC6327992.
- [18] T.-S. Chang, An Updated Review of Tyrosinase Inhibitors, *International Journal of Molecular Sciences.* 10 (2009) 2440–2475. <https://doi.org/10.3390/ijms10062440>.

- [19] R.S. Ochs, Understanding Enzyme Inhibition, *J. Chem. Educ.* 77 (2000) 1453. <https://doi.org/10.1021/ed077p1453>.
- [20] T. Robin, S. Reuveni, M. Urbakh, Single-molecule theory of enzymatic inhibition, *Nat Commun.* 9 (2018) 779. <https://doi.org/10.1038/s41467-018-02995-6>.
- [21] K.A. Cayce, A.J. McMichael, S.R. Feldman, Hyperpigmentation: an overview of the common afflictions, *Dermatol Nurs.* 16 (2004) 401–6, 413–6; quiz 417.
- [22] M.J. Peñalver, A.N.P. Hiner, J.N. Rodríguez-López, F. García-Cánovas, J. Tudela, Mechanistic implications of variable stoichiometries of oxygen consumption during tyrosinase catalyzed oxidation of monophenols and o-diphenols, *Biochimica et Biophysica Acta (BBA) - Protein Structure and Molecular Enzymology.* 1597 (2002) 140–148. [https://doi.org/10.1016/S0167-4838\(02\)00264-9](https://doi.org/10.1016/S0167-4838(02)00264-9).
- [23] S. Zolghadri, A. Bahrami, M.T. Hassan Khan, J. Munoz-Munoz, F. Garcia-Molina, F. Garcia-Canovas, A.A. Saboury, A comprehensive review on tyrosinase inhibitors, *Journal of Enzyme Inhibition and Medicinal Chemistry.* 34 (2019) 279–309. <https://doi.org/10.1080/14756366.2018.1545767>.
- [24] O. Nerya, J. Vaya, R. Musa, S. Izrael, R. Ben-Arie, S. Tamir, Glabrene and Isoliquiritigenin as Tyrosinase Inhibitors from Licorice Roots, *J. Agric. Food Chem.* 51 (2003) 1201–1207. <https://doi.org/10.1021/jf020935u>.
- [25] K. Yamauchi, T. Mitsunaga, I. Batubara, Isolation, Identification and Tyrosinase Inhibitory Activities of the Extractives from *Allamanda cathartica*, *Natural Resources.* 2 (2011) 167–172. <https://doi.org/10.4236/nr.2011.23022>.
- [26] W. Jirawattanapong, E. Saifah, C. Patarapanich, Synthesis of glabridin derivatives as tyrosinase inhibitors, *Arch. Pharm. Res.* 32 (2009) 647–654. <https://doi.org/10.1007/s12272-009-1501-x>.
- [27] Y. Tamura, The History of Licorice Applications in Maruzen Pharmaceuticals Co., Ltd., IntechOpen, 2017. <https://doi.org/10.5772/65962>.
- [28] Y.M. Kim, J. Yun, C.-K. Lee, H. Lee, K.R. Min, Y. Kim, Oxyresveratrol and Hydroxystilbene Compounds: INHIBITORY EFFECT ON TYROSINASE AND MECHANISM OF ACTION *, *Journal of Biological Chemistry.* 277 (2002) 16340–16344. <https://doi.org/10.1074/jbc.M200678200>.
- [29] C. Li, T. Li, M. Zhu, J. Lai, Z. Wu, Pharmacological properties of glabridin (a flavonoid extracted from licorice): A comprehensive review, *Journal of Functional Foods.* 85 (2021) 104638. <https://doi.org/10.1016/j.jff.2021.104638>.
- [30] B. Chopra, A.K. Dhingra, K.L. Dhar, *Psoralea corylifolia* L. (Buguchi) — Folklore to modern evidence: Review, *Fitoterapia.* 90 (2013) 44–56. <https://doi.org/10.1016/j.fitote.2013.06.016>.
- [31] R.K. Chaudhuri, K. Bojanowski, Bakuchiol: a retinol-like functional compound revealed by gene expression profiling and clinically proven to have anti-aging effects, *Int J Cosmet Sci.* 36 (2014) 221–230. <https://doi.org/10.1111/ics.12117>.
- [32] B.J. West, I. Alabi, S. Deng, A Face Serum Containing Palmitoyl Tripeptide-38, Hydrolyzed Hyaluronic Acid, Bakuchiol and a Polyherbal and Vitamin Blend Improves Skin Quality, *Journal of Cosmetics, Dermatological Sciences and Applications.* 11 (2021) 237–252. <https://doi.org/10.4236/jcda.2021.113020>.
- [33] A. Mahdavi, N. Mohammadsadeghi, F. Mohammadi, F. Saadati, S. Nikfard, Evaluation of inhibitory effects of some novel phenolic derivatives on the mushroom tyrosinase activity: Insights from spectroscopic analyses, molecular docking and in vitro assays, *Food Chemistry.* 387 (2022) 132938. <https://doi.org/10.1016/j.foodchem.2022.132938>.
- [34] R. Amorati and L. Valgimigli. Methods To Measure the Antioxidant Activity of Phytochemicals and Plant Extracts. *Journal of Agricultural and Food Chemistry* 2018 66 (13), 3324-3329. DOI: 10.1021/acs.jafc.8b01079.
- [35] R. Amorati, G.F. Pedulli, L. Valgimigli, H. Johansson, L. Engman, Organochalcogen Substituents in Phenolic Antioxidants, *Org. Lett.* 12 (2010) 2326–2329. <https://doi.org/10.1021/ol100683u>.
- [36] Y.-Z. Zhu, K. Chen, Y.-L. Chen, C. Zhang, Y.-Y. Xie, R.C. Hider, T. Zhou, Design and synthesis of novel stilbene-hydroxypyridinone hybrids as tyrosinase inhibitors and their application in the anti-browning of freshly-cut apples, *Food Chemistry.* 385 (2022) 132730. <https://doi.org/10.1016/j.foodchem.2022.132730>.
- [37] T.-S. Chang, H.-Y. Ding, S.S.-K. Tai, C.-Y. Wu, Mushroom tyrosinase inhibitory effects of isoflavones isolated from soygerm koji fermented with *Aspergillus oryzae* BCRC 32288, *Food Chemistry.* 105 (2007) 1430–1438. <https://doi.org/10.1016/j.foodchem.2007.05.019>.
- [38] S. Naish-Byfield, P.A. Riley, Oxidation of monohydric phenol substrates by tyrosinase. An oximetric study, *Biochemical Journal.* 288 (1992) 63–67. <https://doi.org/10.1042/bj2880063>.

- [39] J. Rodríguez-López, J. Ros-Martínez, R. Varón, F. García-Cánovas, Calibration of a Clark-type oxygen electrode by tyrosinase-catalyzed oxidation of 4-tert-butylcatechol, *Analytical Biochemistry*. 202 (1992) 356–360. [https://doi.org/10.1016/0003-2697\(92\)90118-Q](https://doi.org/10.1016/0003-2697(92)90118-Q).
- [40] S. Mondal, A. Thampi, and M. Puranik. Kinetics of Melanin Polymerization during Enzymatic and Nonenzymatic Oxidation. *The Journal of Physical Chemistry B* 2018 122 (7), 2047-2063 DOI: 10.1021/acs.jpcc.7b07941
- [41] J. Ros, J. Rodríguez-López, F. García-Cánovas, Tyrosinase: kinetic analysis of the transient phase and the steady state, *Biochimica et Biophysica Acta (BBA) - Protein Structure and Molecular Enzymology*. 1204 (1994) 33–42. [https://doi.org/10.1016/0167-4838\(94\)90029-9](https://doi.org/10.1016/0167-4838(94)90029-9).
- [42] L.G. Fenoll, J.N. Rodríguez-López, F. García-Sevilla, P.A. García-Ruiz, R. Varón, F. García-Cánovas, J. Tudela, Analysis and interpretation of the action mechanism of mushroom tyrosinase on monophenols and diphenols generating highly unstable o-quinones, *Biochimica et Biophysica Acta (BBA) - Protein Structure and Molecular Enzymology*. 1548 (2001) 1–22. [https://doi.org/10.1016/S0167-4838\(01\)00207-2](https://doi.org/10.1016/S0167-4838(01)00207-2).
- [43] J.S. Chen, C. Wei, R.S. Rolle, W.S. Otwell, M.O. Balaban, M.R. Marshall, Inhibitory effect of kojic acid on some plant and crustacean polyphenol oxidases, *J. Agric. Food Chem.* 39 (1991) 1396–1401. <https://doi.org/10.1021/jf00008a008>.
- [44] Enzymes, n.d. <https://books.google.com/books/about/Enzymes.html?hl=it&id=jj4HEAAAQBAJ>
- [45] S.-Y. Seo, V.K. Sharma, N. Sharma, Mushroom tyrosinase: Recent prospects, *Journal of Agricultural and Food Chemistry*. 51 (2003) 2837–2853. <https://doi.org/10.1021/jf020826f>.
- [46] F. Mayr, S. Sturm, M. Ganzera, B. Waltenberger, S. Martens, S. Schwaiger, D. Schuster, H. Stuppner, Mushroom Tyrosinase-Based Enzyme Inhibition Assays Are Not Suitable for Bioactivity-Guided Fractionation of Extracts, *J. Nat. Prod.* 82 (2019) 136–147. <https://doi.org/10.1021/acs.jnatprod.8b00847>.
- [47] F. Alam, G.N. Khan, M.H.H.B. Asad, *Psoralea corylifolia* L: Ethnobotanical, biological, and chemical aspects: A review, *Phytotherapy Research*. 32 (2018) 597–615. <https://doi.org/10.1002/ptr.6006>.
- [48] K.Y. Oh, J.H. Lee, M.J. Curtis-Long, J.K. Cho, J.Y. Kim, W.S. Lee, K.H. Park, Glycosidase inhibitory phenolic compounds from the seed of *Psoralea corylifolia*, *Food Chemistry*. 121 (2010) 940–945. <https://doi.org/10.1016/j.foodchem.2010.01.022>.
- [49] T.P.A. Krishna, B. Edachery, S. Athalathil, Bakuchiol – a natural meroterpenoid: structure, isolation, synthesis and functionalization approaches, *RSC Adv.* 12 (2022) 8815–8832. <https://doi.org/10.1039/D1RA08771A>.
- [50] L. Mátyus, J. Szöllösi, A. Jenei, Steady-state fluorescence quenching applications for studying protein structure and dynamics, *Journal of Photochemistry and Photobiology B: Biology*. 83 (2006) 223–236. <https://doi.org/10.1016/j.jphotobiol.2005.12.017>.
- [51] H. Johansson, D. Shanks, L. Engman, R. Amorati, G.F. Pedulli, L. Valgimigli. Long-lasting antioxidant protection: a regenerable BHA analogue. *J Org Chem.* 2010 Nov 19;75(22):7535-41. doi: 10.1021/jo101239c.
- [52] G. Brigati, M. Lucarini, V. Mugnaini, G.F. Pedulli, Determination of the Substituent Effect on the O–H Bond Dissociation Enthalpies of Phenolic Antioxidants by the EPR Radical Equilibration Technique, *J. Org. Chem.* 67 (2002) 4828–4832. <https://doi.org/10.1021/jo025755y>.
- [53] R. Amorati, F. Ferroni, G.F. Pedulli, L. Valgimigli, Modeling the Co-Antioxidant Behavior of Monofunctional Phenols. Applications to Some Relevant Compounds, *J. Org. Chem.* 68 (2003) 9654–9658. <https://doi.org/10.1021/jo0351825>.
- [54] M.C. Kang, J.-W. Lee, T.H. Lee, L. Subedi, H.M. Wahedi, S.-G. Do, E. Shin, E.-Y. Moon, S.Y. Kim, UP256 Inhibits Hyperpigmentation by Tyrosinase Expression/Dendrite Formation via Rho-Dependent Signaling and by Primary Cilium Formation in Melanocytes, *International Journal of Molecular Sciences*. 21 (2020) 5341. <https://doi.org/10.3390/ijms21155341>.
- [55] A. Baschieri, M.D. Ajvazi, J.L.F. Tonfack, L. Valgimigli, R. Amorati, Explaining the antioxidant activity of some common non-phenolic components of essential oils, *Food Chemistry*. 232 (2017) 656–663. <https://doi.org/10.1016/j.foodchem.2017.04.036>.
- [56] R. Amorati, G.F. Pedulli, L. Valgimigli, Kinetic and thermodynamic aspects of the chain-breaking antioxidant activity of ascorbic acid derivatives in non-aqueous media, *Org. Biomol. Chem.* 9 (2011) 3792–3800. <https://doi.org/10.1039/C1OB05334E>.

- [57] A. Baschieri, R. Pizzol, Y. Guo, R. Amorati, and L. Valgimigli. Calibration of Squalene, p-Cymene, and Sunflower Oil as Standard Oxidizable Substrates for Quantitative Antioxidant Testing *Journal of Agricultural and Food Chemistry* 2019 67 (24), 6902-6910 DOI: 10.1021/acs.jafc.9b01400
- [58] L. Valgimigli, M. Valgimigli, S. Gaiani, G.F. Pedulli, L. Bolondi, Measurement of oxidative stress in human liver by EPR spin-probe technique, *Free Radical Research*. 33 (2000) 167–178. <https://doi.org/10.1080/10715760000300721>.

ACKNOWLEDGMENTS

My deepest acknowledgments are addressed to Prof. Luca Valgimigli, supervisor of this thesis and Prof. Riccardo Amorati, for the support and the indispensable help provided for the realization of these projects and for the availability always demonstrated during the three years of doctorate. The supervision and the responsibilities I was given, have been chosen in perfect combination for encouraging my personal and professional growth at the best. I would also like to thank Dr. Ya Fang Guo, Dr. Cecilia Poderi and Dr. Andrea Baschieri for the immense support and for transmitting to me his enthusiasm for chemistry and research. A part of my award are then reserved to the researchers I had the pleasure to work with: in particular Dr. Adrian Konopko, Alessio Cremonini and Fabio Mollica who was my colleagues at the beginning of my PhD and Dr. Irene Coralli, Dr. Rosalinda Sciacca and Seyedeh Rojin Shariati Pour, my Tecnopolo colleagues, whose support was fundamental in the years, Prof. Derek Pratt and all his research group, who gave me the opportunity not only to perform part of my research abroad, but also provided me the best personal and professional environment to work in. Lastly, I would like to give special thanks to the University of Bologna for giving me the opportunity and the indispensable materials to accomplish this path.

